MoES/P.O.(Seismo)/1(270)/AFM/2015
Ministry of Earth Sciences
(Seismology Division)

Prithvi Bhavan,
Lodhi Road,
New Delhi – 110003
Dated: 11/12/2015
14

# SANCTION ORDER

Project Title: **Financial assistance for the research project entitled, Integrated Project on Active Fault Mapping in Kachchh Basin, Western India**

Coordinator: **Prof. L. S. Chamyal, Department of Geology, The Maharaja Sayajirao University of Baroda Vadodara-390002.**

**Co-Coordinator: Dr. Mithila Verma, Ministry of Earth Sciences, New Delhi-110003.**

Approval of the President is hereby conveyed under Rule 20 of the Delegation of Financial Power Rules, 1978, for the above-mentioned project at a total cost of ₹**3,07,50,660/- (Rupees three crore seven lakh fifty thousand six hundred and sixty only**), for a period of five years under Seismicity & Earthquake Precursors Program, AO no. MoES/P.O.(Seismo)/8(7)/2007 date 24/09/2012 followed by revised A.O. of even No. dated 14/07/2015. The component vise items of expenditure for which the total allocation of ₹**3,07,50,660/-** has been approved are given below:

**COMPONENT –I** : M. S. University of Baroda, Vadodara
**P. I. :** Prof. D. M. Maurya, Department of Geology

| ITEM/ BUDGET | 1st Year | 2nd Year | 3rd Year | 4th Year | 5th Year | Total (Rs.) |
|---|---|---|---|---|---|---|
| A. Recurring | | | | | | |
| 1. Salary\wages<br>a) JRF (Two)<br>@ 25,000/- p.m. +HRA | 7,00,000 | 7,00,000 | 7,00,000 | 7,00,000 | 7,00,000 | 35,00,000 |
| b)Field-cum-Laboratory Assistant (One) @7,000 consolidated) | 84,000 | 84,000 | 84,000/- | 84,000 | 84,000 | 4,20,000 |
| 2. Consumables | 1,00, 000 | 1,00, 000 | 1,00, 000 | 1,00, 000 | 1,00, 000 | 5,00,000 |
| 3. Travel | 1,00,000 | 1,00,000 | 1,00,000 | 1,00,000 | 1,00,000 | 5,00,000 |
| 4. Contingency | 75, 000 | 75, 000 | 75, 000 | 75, 000 | 75, 000 | 3,75,000 |
| B. Over head | 25,000 | 25,000 | 25,000 | 25,000 | 25,000 | 1,25,000 |
| Total (A+B) | **10,84,000** | **10,84,000** | **10,84,000** | **10,84,000** | **10,84,000** | **54,20,000** |

14/12/15

COMPONENT – II
P. I.: M. S. University of Baroda, Vadodara
Prof. Prafulla K. Jha, Department of Physics

| ITEM/ BUDGET | 1st Year | 2nd Year | 3rd Year | 4th Year | 5th Year | Total (Rs.) |
|---|---|---|---|---|---|---|
| A. Recurring | | | | | | |
| 1. Salary\wages<br>a) JRF (One)<br>@ 25,000/- p.m. +HRA | 3,60,000 | 3,60,000 | 3,60,000 | 3,60,000 | 3,60,000 | 18,00,000 |
| 2. Consumables | 50, 000 | 50,000 | 50,000 | 30,000 | 20,000 | 2,00,000 |
| 3. Travel | 50, 000 | 50,000 | 50, 000 | 50, 000 | 50, 000 | 2,50,000 |
| 4. Contingency | 1,00, 000 | 50,000 | 50,000 | 50,000 | 50,000 | 3,00,000 |
| Total | 5,60,000 | 5,10,000 | 5,10,000 | 4,90,000 | 4,80,000 | 25,50,000 |

COMPONENT – III
P. I.: Institute of Seismological Research (ISR), Gandhinagar
Dr. Girish Chandra Kothyari

| ITEM/ BUDGET | 1st Year | 2nd Year | 3rd Year | 4th Year | 5th Year | Total (Rs. |
|---|---|---|---|---|---|---|
| A. Recurring | | | | | | |
| 1. Salary\wages<br>a) JRF (One)<br>@ 25,000/- p.m. +HRA | 3,60,000 | 3,60,000 | 3,60,000 | 3,60,000 | 3,60,000 | 18,00,000 |
| 2. Consumables | 1,00,000 | 1,00,000 | 50,000 | 25,000 | 25,000 | 3,00,000 |
| 3. Travel | 1,00,000 | 1,00,000 | 1,00,000 | 1,00,000 | 1,00,000 | 5,00,000 |
| 4. Other cost | 1,50,000 | 50,000 | 50,000 | 25,000 | 25,000 | 3,00,000 |
| B. Non Recurring | | | | | | |
| 1) Equipments<br>a) Laptop<br>b) Color Printer<br>c) Distometer | 73,000<br>50,000<br>1,00,000 | --<br>--<br>-- | --<br>--<br>-- | --<br>--<br>-- | --<br>--<br>-- | 73,000<br>50,000<br>1,00,000 |
| B.Overhead | 25,000 | 25,000 | 25,000 | 25,000 | 25,000 | 1,25,000 |
| Total (A+B) | 9,58,000 | 6,35,000 | 5,85,000 | 5,35,000 | 5,35,000 | 32,48,000 |

COMPONENT – IV
P. I.: Indian Institute of Technology (IIT), Kanpur & LDCE, Ahmedabad
Dr. Javed Malik, Dept of Civil Engineering

| Item | BUDGET (in Rupees) | | | | | |
|---|---|---|---|---|---|---|
| | 1st Year | 2nd Year | 3rd Year | 4th Year | 5th Year | Total |
| A. Recurring | | | | | | |
| 1. Salaries/wages<br>a) JRF (One)<br>@ 25,000/- p.m. +HRA | 3,60,000 | 3,60,000 | 3,60,000 | 3,60,000 | 3,60,000 | 18,00,000 |
| 2. Consumables | 1,00,000 | 1,00,000 | 1,00,000 | 1,00,000 | 1,00,000 | 5,00,000 |
| 3. Travel | 1,00,000 | 1,00,000 | 1,00,000 | 1,00,000 | 1,00,000 | 5,00,000 |
| 4. Other costs | 2,00,000 | 2,00,000 | 1,00,000 | 1,00,000 | 1,00,000 | 7,00,000 |

| | | | | | | |
|---|---|---|---|---|---|---|
| and total (A+B) | 7,85,000 | 7,85,000 | 6,85,000 | 6,85,000 | 6,85,000 | 36,25,000 |

P.I.: Dr. Gadhavi Mahendrasinh Shivraj, Dept of Civil Engineering

| Item | BUDGET (in Rupees) | | | | | Total |
|---|---|---|---|---|---|---|
| | 1st Year | 2nd Year | 3rd Year | 4th Year | 5th Year | |
| A. Recurring | | | | | | |
| 1. Consumables | 1,00,000 | 50,000 | 50,000 | 50,000 | 50,000 | 3,00,000 |
| 2. Travel | 1,00,000 | 50,000 | 50,000 | 50,000 | 50,000 | 3,00,000 |
| 3. Other costs | 1,00,000 | 50,000 | 50,000 | 50,000 | 50,000 | 3,00,000 |
| B. Overhead | 25,000 | 25,000 | 25,000 | 25,000 | 25,000 | 1,25,000 |
| Grand total (A+B) | 3,25,000 | 1,75,000 | 1,75,000 | 1,75,000 | 1,75,000 | 10,25,000 |

COMPONENT – V KSKV Kachchh University, Bhuj- Kachchh

P. I.: Dr. Mahesh G. Thakkar, Dept. of Earth and Environmental

| Item | BUDGET (in Rupees) | | | | | Total |
|---|---|---|---|---|---|---|
| | 1st Year | 2nd Year | 3rd Year | 4th Year | 5th Year | |
| A. Recurring | | | | | | |
| 1. Salaries/wages a) JRF (One) @ 25,000/- p.m. +HRA | 3,60,000 | 3,60,000 | 3,60,000 | 3,60,000 | 3,60,000 | 18,00,000 |
| 2. Consumables | 1,50,000 | 1,50,000 | 75,000 | 75,000 | 75,000 | 5,25,000 |
| 3. Travel | 1,00,000 | 75,000 | 75,000 | 75,000 | 75,000 | 4,00,000 |
| 4. Other cost | 2,00,000 | 2,00,000 | 1,00,000 | 1,00,000 | 1,00,000 | 7,00,000 |
| B. Overhead | 25,000 | 25,000 | 25,000 | 25,000 | 25,000 | 1,25,000 |
| Grand total (A+B) | 8,35,000 | 8,10,000 | 6,35,000 | 6,35,000 | 6,35,000 | 35,50,000 |

COMPONENT – VI Institute of Seismological Research (ISR), Gandhinagar

P. I.: Dr. Kapil Mohan

| Item | BUDGET (in Rupees) | | | | | Total |
|---|---|---|---|---|---|---|
| | 1st Year | 2nd Year | 3rd Year | 4th Year | 5th Year | |
| A. Recurring | | | | | | |
| 1. Salaries/wages a) JRF (Two) @ 25,000/- p.m. +HRA | 7,20,000 | 7,20,000 | 7,20,000 | 7,20,000 | 7,20,000 | 36,00,000 |
| 2. Consumables | 1,50,000 | 1,50,000 | 1,50,000 | 75,000 | 75,000 | 6,00,000 |
| 3. Travel | 1.50,000 | 1,50,000 | 1,50,000 | 1,50,000 | 1,50,000 | 7,50,000 |
| 4. Other cost | 50,000 | 50,000 | 50,000 | 50,000 | 50,000 | 2,50,000 |
| Grand total | 10,70,000 | 10,70,000 | 10,70,000 | 9,95,000 | 9,95,000 | 52,00,000 |

COMPONENT – VII
P. I.:

Institute of Seismological Research (ISR), Gandhinagar
Dr. Rakesh Dumka

| ITEM/ BUDGET | 1st Year | 2nd Year | 3rd Year | 4th Year | 5th Year | Total (Rs.) |
|---|---|---|---|---|---|---|
| A. Recurring | | | | | | |
| 1. Salary/ wages a) JRF (One) @ 25,000/- p.m. +HRA | 3,60,000 | 3,60,000 | 3,60,000 | 3,60,000 | 3,60,000 | 18,00,000 |
| 2. Consumables | 1,00,000 | 50,000 | 50,000 | 50,000 | 50,000 | 3,00,000 |
| 3. Travel | 1,00,000 | 1,00,000 | 75,000 | 75,000 | 75,000 | 4,25,000 |
| 4. Contingency | 1,50,000 | 75,000 | 75,000 | 50,000 | 50,000 | 4,00,000 |
| B. Non-recurring | | | | | | |
| 1. Computer (Work-station) | 2,00,000 | – | – | – | – | 2,00,000 |
| 2. Laptop (1) | 75,000 | | | | | 75,000 |
| 3. Printer (1) | 16,500 | | | | | 16,500 |
| 4. Batteries (36) | 1,91,160 | | | | | 1,91,160 |
| Grand total | 11,92,660 | 5,85,000 | 5,60,000 | 5,35,000 | 5,35,000 | 34,07,660 |

COMPONENT – VIII
P. I.:

KSKV Kachchh University, Bhuj- Kachchh-370001
Dr. Subhash Bhandari, Dept. of Earth and Environmental

| ITEM/ BUDGET | 1st Year | 2nd Year | 3rd Year | 4th Year | 5th Year | Total (Rs.) |
|---|---|---|---|---|---|---|
| A. Recurring | | | | | | |
| 1. Salary/ wages a) JRF (One) @ 25,000/- p.m. +HRA | 3,60,000 | 3,60,000 | 3,60,000 | 3,60,000 | 3,60,000 | 18,00,000 |
| 2. Consumables | 1,00,000 | 50,000 | 50,000 | 50,000 | 50,000 | 3,00,000 |
| 3. Travel | 75,000 | 75,000 | 75,000 | 50,000 | 50,000 | 3,25,000 |
| 4. Contingency | 1,00,000 | 50,000 | 50,000 | 50,000 | 50,000 | 3,00,000 |
| Grand total | 6,35,000 | 5,35,000 | 5,35,000 | 5,10,000 | 5,10,000 | 27,25,000 |

2. Sanction of the President authority is also hereby conveyed to the payment of ₹74,44,660/- (₹16,44,000/- to the **Registrar, M. S. University of Baroda, Vadodara;** ₹32,20,660/- to the **Director General, Institute of Seismological Research, Raisan, Gandhinagar, Gujarat;** ₹7,85,000 to the **Director Indian Institute of Technology , Kanpur;** ₹3,25,000 to the **Principal L.D. College of Engineering, Navrangpura, Ahmedabad;** ₹14,70,000/- to the **Registrar, KSKV Kachchh University, Bhuj- Kachchh)** as first installment. The component vise break-up of the same would be as follows:

| Item/Component | COMP-I | COMP-II | COMP III | COMPO - IV | | COMP - V | COMP - VI | COMP-VII | COMP-VIII |
|---|---|---|---|---|---|---|---|---|---|
| A. RECURRING | MSU | MSU | ISR | IITK | LDCE | KSKV KU | ISR | ISR | KSKV KU |
| Salary | 784000 | 360000 | 360000 | 360000 | — | 360000 | 720000 | 360000 | 360000 |
| Consumables | 100000 | 50000 | 100000 | 100000 | 100000 | 150000 | 150000 | 100000 | 100000 |
| Travel | 100000 | 50000 | 100000 | 100000 | 100000 | 100000 | 150000 | 100000 | 75000 |

| | | | | | | | | | |
|---|---|---|---|---|---|---|---|---|---|
| Contingency / Other Cost | 75000 | 100000 | 150000 | 200000 | 100000 | 200000 | 50000 | 150000 | 100000 |
| B. Non-recurring | -- | -- | 223000 | – | | -- | -- | 482660 | -- |
| C. Overhead | 25000 | -- | 25000 | 25000 | 25000 | 25000 | | | |
| Total (A+B+C) | **1084000** | **560000** | **958000** | **785000** | **325000** | **835000** | **1070000** | **1192660** | **635000** |

3. The said amount in para 2, will be drawn by DDO, MoES and will be disbursed to the Registrar, M. S. University of Baroda, Vadodara; Director General, Institute of Seismological Research, Raisan, Gandhinagar, Gujarat; Director Indian Institute of Technology , Kanpur; Principal L.D. College of Engineering, Navrangpura, Ahmedabad; and Registrar, KSKV Kachchh University, Bhuj- Kachchh through RTGS as per following details:

**M.S, University**

| | | |
|---|---|---|
| Name of the Bank | : | Bank of Baroda |
| Type of Account | : | Current Account |
| IFSC Code | : | BARB0MSUNIV |
| Account No. | : | 02010200000020 |
| MICR No. | : | 390012019 |
| Branch Name | : | Bank of Baroda, Campus Branch, Fatehganj, Baroda |

**ISR Component**

| | | |
|---|---|---|
| Name of the Bank | : | Oriental Bank of Commerce |
| IFSC Code | : | ORBC0100933 |
| Account No. | : | 09332091000067 |
| MICR No. | : | 380022008 |
| Branch Name | : | Oriental Bank of Commerce, Sector 11, Suman Tower, Gandhinagar-11 |

**IIT, Kanpur**

| | | |
|---|---|---|
| Name of the Bank | : | State Bank of India. |
| Type of Account | : | Current Account |
| IFSC Code | : | SBIN0001161 |
| Account No. | : | 10426002126 |
| MICR No. | : | 208002041 |
| Branch Name | : | IIT Kanpur Branch |

**L.D. College of Engineering, Ahmedabad**

| | | |
|---|---|---|
| Name of the Bank | : | State Bank ofIndia |
| Type of Account | : | Savings Account |
| IFSC Code | : | SBIN0002651 |
| Account No. | : | 30769133013 |
| MICR No. | : | 380002017 |
| Branch Name | : | Gujarat University |

**KSKV Kachchh University, Ahmedabad**

| | | |
|---|---|---|
| Name of the Bank | : | Union Bank of India |
| Type of Account | : | Savings Account |
| IFSC Code | : | UBIN0535061 |
| Account No. | : | 350602010804560 |
| MICR No. | : | 370026051 |
| Branch Name | : | Bhuj Branch, Jubilee Circle, Bhuj Kachchh-370001 |

14/12/15

4. The expenditure involved is debit able to Demand No.31 Ministry of Earth Sciences

| | |
|---|---|
| 3455 | - Meteorology (Major Head) |
| 00.001 | - Direction & Administration |
| 07 | - Seismological and Geosciences (SAGE) |
| 07.00.31 | - Grants-in-aid-General for the year 2015-16 (Plan) |

5. Sanction of the grant is subject to the conditions as detailed in the enclosed Guidelines for Implementing Research Project.

6. Overhead expenses are meant for the host institute towards the cost for providing infrastructural facilities and benefits to the staff employed in the project, etc.

7. The provisions of GFR 211(1) relating to U.C.'s for the fund released are not applicable at this stage since the said institute would be receiving the grant for the aforesaid purpose for the first time.

8. As per rule 212(1) of GFRs, the account of the Grantee institution shall be open to inspection by sanctioning authority/audit whenever the institute is called upon to do so.

9. It is desirable to have MoES nominee in the selection process for recruitment of JRF/SRF/RA/Scientists in the project.

10. The position of project staff is co-terminus with the duration of the project & MoES would have no liability towards such manpower costs beyond the duration of the project.

11. The assets acquired wholly or substantially out of government grants by the implementing agencies will not be disposed off without obtaining the prior approval of MoES.

12. All the future correspondence regarding the project may be addressed to Adviser & Head Geosciences/Seismology Division.

13. Amount released for the project may be kept in a separate interest earning account of M. S. University of Baroda, Vadodara; Director General, Institute of Seismological Research, Gandhinagar; Indian Institute of Technology, Kanpur; L.D. College of Engineering, Ahmedabad; and KSKV Kachchh University, Kachchh.

14. Data acquired under the project needs to be sent to Ministry regularly and it should not be shared with any private agency/foreigner, without prior approval of MoES.

15. The expenditure has been entered into ECR register at Page No.26, Sl. No.77 .

16. This issues under the powers delegated to this Ministry and with the concurrence of IF Division of MoES, vide Dy. No.850/IFD/15 dated 24/11 /2015 and approval of Secretary vide Dy.No.734 /Secy/15 dated 26/11/2015.

14/12/15

**(Kailash Chand)**
**Under Secretary to the Govt. of India**

To,

The Pay & Accounts Officer, MoES, New Delhi.

Copy forwarded for information and necessary action to:

1. The Principal Director of Audit, Scientific Department, III Floor, AGCR Building, IP Estate, New Delhi-110002.
2. Registrar, M. S. University of Baroda, Vadodara.
3. Prof. L. S. Chamyal, Department of Geology, The Maharaja Sayajirao University of Baroda Vadodara-390002.
4. Dr. Mithila Verma, Ministry of Earth Sciences, New Delhi-110003.
5. Prof. D. M. Maurya, Department of Geology, The Maharaja Sayajirao University of Baroda Vadodara-390002.
6. Prof. Prafulla K. Jha, Department of Physics, The Maharaja Sayajirao University of Baroda Vadodara-390002.
7. Director General, Institute of Seismological Research, Raisan, Gandhinagar, Gujarat.
8. Dr. Girish Chandra Kothyari, Institute of Seismological Research, Next to petroleum University, Raisan, Gandhinagar-382009, Gujarat.
9. Dr. Kapil Mohan, Institute of Seismological Research, Next to petroleum University, Raisan, Gandhinagar-382009, Gujarat.
10. Dr. Rakesh Dumka, Institute of Seismological Research, Next to petroleum University, Raisan, Gandhinagar-382009, Gujarat.
11. Director, Indian Institue of Technology, Kanpur-208016.
12. Dr. Javed Malik, Dept. of Civil Engineering, Indian Institue of Technology, Kanpur-208016.
13. Principal L.D. College of Engineering, Navrangpura, Ahmedabad
14. Dr. Gadhavi Mahendrasinh Shivraj, Dept of Civil Engineering, L. D. College of Engineering, Navrangpura, Ahmedabad-380015.
15. Registrar, KSKV Kachchh University, Bhuj- Kachchh.
16. Dr. Subhash Bhandari, Dept. of Earth and Environmental, KSKV Kachchh University, Bhuj-Kachchh-370001
17. Dr. Mahesh G. Thakkar, Dept. of Earth and Environmental, KSKV Kachchh University, Bhuj-Kachchh-370001
18. Cash Section, MoES, New Delhi, *with two spare copies of the sanction for making necessary payment to the grantee.*
19. Controller of Account, MoES, New Delhi.
20. Head, Geosciences/Seismology Division, MoES, New Delhi.
21. Sanction Folder/ File copy.

K. Chand 14/12/15

**(Kailash Chand)**
**Under Secretary to the Govt. of India**

No.SR/FST/ES-I/2018/29(C)
GOVERNMENT OF INDIA
MINISTRY OF SCIENCE & TECHNOLOGY
DEPARTMENT OF SCIENCE & TECHNOLOGY
R & D (Infrastructure) DIVISION

Technology Bhawan
New Mehrauli Road
New Delhi -110016

23rd September, 2019

ORDER

Subject: Financial assistance (1st installment) to the Department of Earth and Environmental Science, Krantiguru Shyamji Krishna Verma Kanchchh University, Bhuj-Kachchh, Gujarat under FIST Program.

Sanction of the President is hereby accorded to the approval of the aforesaid project at a total cost of Rs. 1,37,00,000/- (Rupees One Crore and thirty seven lakh only) for 5 years The detailed breakup of the grant for General as well as Capital Component are given below:

To strengthen the research facilities in the Department

Capital Assets: Rs. 125 L

E–Rs. 125 L [i) Carbon-Sulphur Analyzer, Analyzer, Biological Microscope, Microbial Incubator, Horizontal Lamina Chamber, 3 no Weighing Machine, Temperature Controlled Rotary Shaker, 25 no Petrological Microscopes, 2 no Streozoom Microscopes, Temperature Controlled Rotary Shaker)- Rs 95.0L, ii) acquiring Drone for Aeria Mapping, Soil Coring Kit, Drills for cleaning fossils, Sieve Shaker- Rs 30.0L]

General Components: Rs. 12.0 L

M– Rs. 12.0 L

Total : Rs. 137 Lakh

2. The total budget recommended for 5 years has been phased as below: (Rs. In lakh)

| Budget Heads | 1st year | 2nd year | 3rd year | 4th year | 5th year | Total |
|---|---|---|---|---|---|---|
| Equipment | 95.0 | 30.0 | - | - | - | 125.0 |
| Maintenance | - | 2.0 | 3.0 | 3.0 | 4.0 | 12.0 |
| Total | 95.0 | 32.0 | 3.0 | 3.0 | 4.0 | 137.0 |

3. Sanction of the President is also accorded to the release of Rs. 95,00,000/- (Rupees Ninety five lakh only) to the Registrar, Krantiguru Shyamji Krishna Verma Kanchchh University, Bhuj-Kachchh, Gujarat. under FIST Program as a 1st installment of the grant in 2019–2020 under `creation of capital assets' head for the maximum cost of the aforesaid Equipment including (9.4%) Custom Duty & other duties under the `Equipment'. The break-up of the 1st installment grant released now would be `Equipment': Rs. 95.0 lakh for procurement of Equipment mentioned above [Equipments of Foreign Origin to be acquired on FE Terms only and should not include charges for any comprehensive Maintenance and training personnel from the vendors during procurement process].

4. The Department/Institute will appropriately limit the expenditure within the sanctioned amount in case of any expected excess expenditure. The Department is requested to utilize the released funds in first one year from the date of sanction order.

5. This sanction is subject to the condition that the grantee organisation will furnish to the Department of Science & Technology, financial year wise Utilization Certificate (UC) in the proforma prescribed as per GFR 2017 and audited statement of expenditure (SE) along with up to date progress report at the end of each financial year duly reflecting the interest earned / accrued on the grants received under the project. This is also subject to the condition of submission of the final statement of expenditure utilization certificate and project completion report within one year from the scheduled date of completion of the project.

6. The grantee organisation will have to enter & upload the Utilization Certificate in the PFMS portal besides sending it in physical form to this Division with UC id genrated in PFMS Portal The subsequent/final instalment will be released only after confirmation of the acceptance of the UC by the Division and entry of previous Utilization Certificate in the PFMS.

Contd..2/

भारतीय अन्तरिक्ष अनुसंधान संगठन
अन्तरिक्ष विभाग
भारत सरकार
अन्तरिक्ष भवन
न्यू बी ई एल रोड, बेंगलूर – 560 231, भारत
दूरभाष : +91 80 2341 5474
फैक्स :

इसरो ISRO

Indian Space Research Organisation
Department of Space
Government of India
Antariksh Bhavan
New BEL Road, Bangalore - 560 231, India
Telphone : +91 80 2341 5474
Fax :

Dr. S. Seetha
Programme Director, SSPO

Telephone: 080-23416271/22172074
Fax: 080 – 23419190
E-mail: seetha@isro.gov.in

August 8, 2016

ISRO/SSPO/MOM-AO/2016-17

Dear Dr. Subhash Bhandari,

**Subject:** **Research proposal under Mars Orbiter Mission – Announcement of opportunity – release of fund - reg.**

This has reference to your submission of the research proposal **"An appraisal of fluvio-tectonic geomorphic set-up of Syria Planusm and Solis Planum provenance in Syria-Thaumasia, Mars"** for funding under Mars Orbiter Mission Announcement of Opportunity (MOM-AO). The domain experts in Department of Space have reviewed the proposal. I wish to inform you that, Chairman, ISRO/Secretary, DOS has approved the following:

1. Funding of the project under MOM-AO for a period of 3 years at a total outlay of ₹ 21,48,520 (Rupees Twenty One Lakhs Forty Eight Thousand Five Hundred Twenty Only) towards meeting the expenditure of the project (budget details enclosed).
2. Release of grant of ₹ 11,00,000 (Rupees Eleven Lakhs only) towards meeting the first year expenditure of the project.

The approval is subject to fulfillment of the following:

a. You will have to submit Annual Progress Report (APR), at the end of the year, indicating the progress of the work accomplished during the first year (to enable renewal of the project for second year). One copy of report should be sent to Shri Satadru Bhattacharya, MOM-AO Coordinator, Planetary Sciences Division, BPSG/EPSA, Space Applications Centre, Jodhpur-Tekra, Ambawadi Vistar P.O.Ahmedabad-380 015, India and two copies to the undersigned.

b. You will have to submit two copies of the Fund Utilization Certificate (FUC) and Audited Accounts Statement (AAS) on completion of the **first** year of the project (to enable renewal of the project for **second** year). **The FUC and AAS** should be sent to the Pay & Accounts Officer, Department of Space, Antariksh Bhavan, New BEL Road, Bengaluru 560 231 with a copy to Shri Satadru Bhattacharya, MOM-AO Coordinator, Planetary Sciences Division, BPSG/EPSA, Space Applications Centre, Jodhpur-Tekra, Ambawadi Vistar P.O.Ahmedabad-380 015, and to the undersigned.

c. In addition, on conclusion of the project, you will have to send a comprehensive report covering total project activities and final fund utilization certificate.

You are requested to send the enclosed Grant-in-Aid bill and Electronic Transfer Mandate Form duly filled and signed in original to the Pay and Accounts Officer, Department of Space, Antariksh Bhavan, New BEL Road, Bengaluru 560 231 with a copy to the undersigned for releasing the grants to Registrar, KSKV Kachchh University, Bhuj, Gujarat.

The Department of Space will issue financial sanction order for the approved grant to you very soon.

As per the revised fellowship norms, you have to appoint a candidate for JRF with PG Degree in Basic Science with NET or equivalent qualification or Graduate Degree in Professional course with NET/GATE or equivalent qualification or PG Degree in Professional course (ME/M.Tech.) as JRF. You may kindly intimate us and send the details of JRF after appointment.

With Regards,

Yours sincerely,

S Seetha

(S.Seetha)

Encl: Budget table
Grant-in-aid bill
Electronic Transfer Form
FUC Form

Dr. Subhash Bhandari
Associate Professor
KSKV Kachchh University
Near Changleswar Mahadev Temple
Mudra Road, Kachchh Dist.
Bhuj, Gujarat - 370001

CC: Scientific Secretary, ISRO
Shri Satadru Bhattacharya, SAC, Ahmedabad
Registrar, KSKV Kachchh University, Bhuj, Gujarat

| Project Title :An appraisal of fluvio-tectonic geomorphic set-up of Syria Planusm and Solis Planum provenance in Syria-Thaumasia, Mars | | | | | |
|---|---|---|---|---|---|
| Principal Investigator : Dr. Subhash Bhandari, Associate Prof. KSKV Kachchh University, Bhuj, Gujarat | | | | | |
| Sl. No | Head of Account | Years | | | Total Budget Approved (in Rs.) |
| | | 2016-2017 (in Rs.) | 2017-2018 (in Rs.) | 2018-2019 (in Rs.) | |
| 1 | Services (salary for JRF) @ Rs. 25000/- (+10% HRA) | 3,60,000 | 3,60,000 | 4,03,200 | **11,23,200** |
| 2 | Travel | 40,000 | 50,000 | 40,000 | **1,30,000** |
| 3 | Materials Computer and Accessories - Rs.150000 Softwares - Rs.400000 | 5,50,000 | 0 | 0 | **5,50,000** |
| 4 | Contingency | 50,000 | 50,000 | 50,000 | **1,50,000** |
| | Sub Total | 10,00,000 | 4,60,000 | 4,93,200 | **19,53,200** |
| Institutional Charges @10% to a Max Rs. 3 lakhs | | 1,00,000 | 46,000 | 49,320 | **1,95,320** |
| Total | | 11,00,000 | 5,06,000 | 5,42,520 | **21,48,520** |

PLOS ONE

RESEARCH ARTICLE

# Discovery of the first ichthyosaur from the Jurassic of India: Implications for Gondwanan palaeobiogeography

**Guntupalli V. R. Prasad[1]*, Dhirendra K. Pandey[2], Matthias Alberti[3], Franz T. Fürsich[4], Mahesh G. Thakkar[5], Gaurav D. Chauhan[5]**

**1** Department of Geology, Centre for Advanced Studies, University of Delhi, Delhi, India, **2** Earth and Planetary Sciences Group, Manipal Center for Natural Sciences, Manipal University, Manipal, Karnataka, India, **3** Institut für Geowissenschaften, Christian-Albrechts-Universität zu Kiel, Kiel, Germany, **4** GeoZentrum Nordbayern, Friedrich-Alexander-Universität Erlangen-Nürnberg, Erlangen, Germany, **5** Department of Earth and Environmental Science, KSKV Kachchh University, Bhuj, India

* guntupalli.vrprasad@gmail.com

Check for updates

OPEN ACCESS

**Citation:** Prasad GVR, Pandey DK, Alberti M, Fürsich FT, Thakkar MG, Chauhan GD (2017) Discovery of the first ichthyosaur from the Jurassic of India: Implications for Gondwanan palaeobiogeography. PLoS ONE 12(10): e0185851. https://doi.org/10.1371/journal.pone.0185851

**Editor:** William Oki Wong, Institute of Botany, CHINA

**Received:** February 16, 2017

**Accepted:** September 20, 2017

**Published:** October 25, 2017

**Copyright:** © 2017 Prasad et al. This is an open access article distributed under the terms of the Creative Commons Attribution License, which permits unrestricted use, distribution, and reproduction in any medium, provided the original author and source are credited.

**Data Availability Statement:** All relevant data are available within the paper.

**Funding:** GVRP acknowledges research grant from J.C.Bose National Fellowship (Grant No.SR/S2/JCB-14/2010) of the Science and Engineering Research (SERB), New Delhi for this work. MA greatly acknowledges financial support by the Alexander von Humboldt Foundation. The funders had no role in study design, data collection and analysis, decision to publish, or preparation of the manuscript.

## Abstract

An articulated and partially preserved skeleton of an ichthyosaur was found in the Upper Jurassic (Upper Kimmeridgian) Katrol Formation exposed at a site south of the village Lodai in Kachchh district, Gujarat (western India). Here we present a detailed description and inferred taxonomic relationship of the specimen. The present study revealed that the articulated skeleton belongs to the family Ophthalmosauridae. The new discovery from India further improves the depauperate fossil record of ichthyosaurs from the former Gondwanan continents. Based on the preserved length of the axial skeleton and anterior part of the snout and taking into account the missing parts of the skull and postflexural region, it is suggested that the specimen may represent an adult possibly reaching a length of 5.0–5.5 m. The widespread occurrence of ophthalmosaurids in the Upper Jurassic deposits of western Tethys, Madagascar, South America and India points to possible faunal exchanges between the western Tethys and Gondwanan continents through a southern seaway.

## Introduction

Ichthyopterygia is a highly successful group of marine reptiles that appeared in the Early Triassic (Olenekian) from a possible diapsid ancestral lineage, survived until the middle Late Cretaceous (Late Cenomanian) and had a worldwide distribution [1, 2]. Though the diversity of ichthyosaurs suffered heavily during the end-Triassic mass extinction, they recovered in the earliest part of the Jurassic Period as evident from a large number of articulated and exceptionally preserved specimens reported from England, Germany and North America [3, 4]. However, their disparity had never recovered after the Triassic-Jurassic mass extinction [4]. Traditionally, all the Early Jurassic ichthyosaurs were considered to have been replaced during the Middle Jurassic by the ophthalmosaurids, a new clade of ichthyosaurs that appeared at the Aalenian-Bajocian boundary and survived into the Cretaceous [3, 5]. But the recent discovery

**Competing interests:** The authors have declared that no competing interests exist.

**Abbreviations:** AMNH, American Museum of Natural History; DUGF/, Delhi University, Department of Geology fossil collection numbers; KGMV, Kachchh Geological Museum Vertebrate Fossil catalogue numbers; RUC2016IKH, Rajasthan University 2016 collection from Kas Hill section.

of a basal thunnosaurian from Iraq demonstrated that non-ophthalmosaurid ichthyosaurs of Late Triassic radiation event survived into the Cretaceous [6]. In comparison to the Early Jurassic, the fossil record of Middle Jurassic ichthyosaurs is less known. The fossil record for the Late Jurassic is relatively better known and has been improving in recent years with many new discoveries coming from South America [5, 7–9], North America [10], and Europe [11–13].

Due to the extensive collections of ichthyosaurs from the UK and mainland Europe, historically the research on ichthyosaurs was biased towards the Laurasian continents. In the former Gondwanaland, the Jurassic ichthyosaur fossil record is very limited with most reports coming from the Middle and Upper Jurassic strata of Argentina [5, 7–9]. Until now, Jurassic ichthyosaurs have been reported from the Aalenian-Bajocian and Tithonian-Berriasian strata of Argentina [5, 7–9, 14–17], Tithonian of Chile [18], Tithonian of Madagascar [19], Rhaetian-Sinemurian of New Zealand [20], and Late Kimmeridgian-Middle Tithonian of Antarctica [21, 22]. Despite their widespread occurrence in the Jurassic, no ichthyosaur has been documented from the Jurassic of India until now.

In India, ichthyosaur remains have been reported previously from the Lower Cretaceous (Upper Albian—Middle Cenomanian) Karai Formation of the Cauvery Basin in South India [23–26]. But these finds are known primarily by a few isolated vertebrae and teeth. However, Lydekker [24] assigned a few complete and partially complete vertebrae to a new species *Ichthyosaurus indicus* because of a deep concavity of the centra. *I. indicus* was considered nomen dubium by McGowan and Motani [3]. Five complete adult and juvenile teeth from the same formation were assigned to *Platypterygius indicus* because of the morphological similarity of the teeth to *Platypterygius* and proximity of the two ichthyosaur fossil sites within the Karai Formation [25]. Zammit [27] observed that tooth forms similar to that of *Platyptrerygius* also occur in *Brachypterygius* and thus suggested that the placement of teeth from the Karai Formation in *P. indicus* is tentative. Later reviews of *Platypterygius* species have shown that the vertebrae reported by Lydekker are referable to Ichthyosauria indet. as they lack diagnostic characters. Further it was felt that among the teeth only DUGF/41 can be referred to subfamily Platypterygiinae gen. indet. because of its square rooted cross-section and the rest should be placed in the order Ichthyosauria fam. indet. [1, 28]. Although India hosts extensive marine Jurassic deposits both in the Himalayan and peninsular Indian (Kachchh, Jaisalmer) regions, until now no ichthyosaur remains have been documented from this time interval.

The Jurassic succession of the Kachchh Basin preserves rocks ranging in age from Aalenian to Tithonian but has yielded only a few marine reptiles. One plesiosaurian vertebra associated with a few fragmentary rib bones was documented from the Upper Tithonian to Neocomian Bhuj Formation from a site near Umia (Amiya) village and was assigned to *Thaumatosaurus indicus* Lydekker [29]. Bardet et al. [30] described 19 articulated vertebrae recovered from the lower part of the Katrol Formation corresponding to the *Katrolensis* Ammonite Zone, equivalent of the Beckeri Zone of the Western Tethys, as representing the plesiosaur family Cryptoclididae. They also redescribed a plesiosaur mandibular symphysis from the Lower Cretaceous Bhuj Formation, Kachchh, housed in the Indian Museum, Kolkata. This specimen, initially referred to *Thaumatosaurus indicus* [23, 31], was reassigned to *Simolestes indicus* [30]. Two large skulls of Callovian marine crocodiles putatively identified as *Steneosaurus* were also reported from marls of the Chari Formation underlying the Dhosa Oolite about 10 km southwest of Bhuj [32]. The relative scarcity of marine reptiles from the Jurassic deposits of India seems to be an artifact of sampling bias rather than of preservation potential of the fossils as these marine sequences have not been prospected in the past with a focused objective of recovering vertebrate fossils. During a field campaign carried out in January and February 2016, we discovered a partially preserved ichthyosaur skeleton (KGMV-0501) in the Upper Jurassic (Upper Kimmeridgian) Katrol Formation south of Lodai village (N 23˚ 22.391', E 69˚ 54.690'),

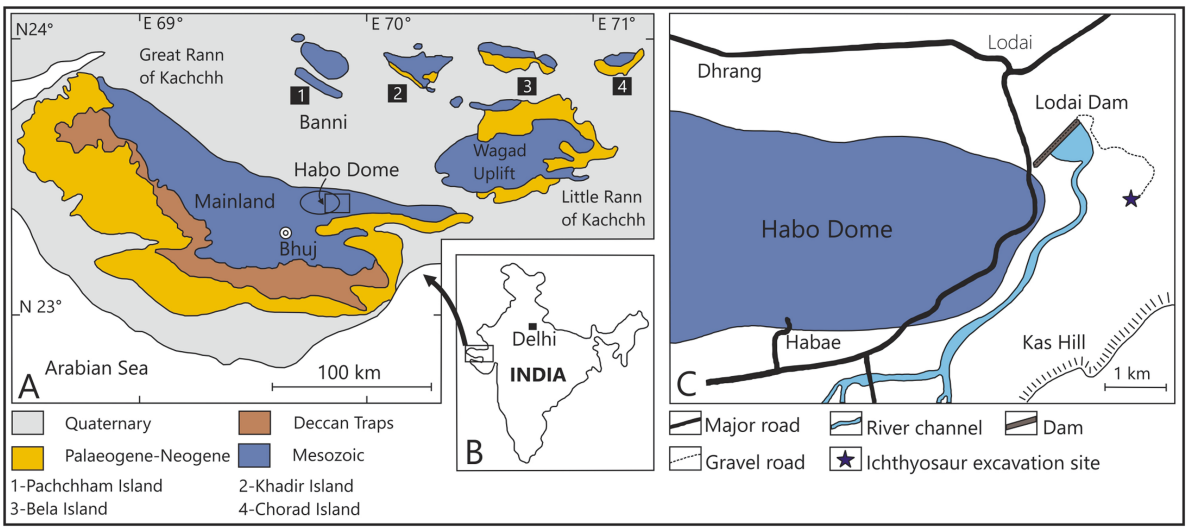


**Fig 1. Geological and location map of the Upper Jurassic ichthyosaur site of Kachchh, western India.** A. Geological map of the Kachchh region (modified after Fürsich et al. [39]), B. Inset map of India showing the location of Kachchh. C. Location map of the ichthyosaur site.

https://doi.org/10.1371/journal.pone.0185851.g001

about 30 km northeast of Bhuj in the Kachchh district, western India (Fig 1). KGMV-0501 represents the first Jurassic ichthyosaur and the first articulated ichthyosaur skeleton from the Mesozoic strata of India and is one of the few ichthyosaur finds from the former Gondwanaland. In this paper, a preliminary description of the newly discovered skeleton is presented and its dietary adaptations as well as palaeobiogeographic significance are discussed.

## Geological setting and age

The Kachchh Basin is a pericratonic E-W oriented rift basin on the western margin of India, which was formed during Late Triassic rifting between India and Africa [33]. In the Kachchh region, Jurassic rocks are exposed in three areas, the Kachchh Mainland, the Island Belt (Pachchham, Khadir, Bela and Chorad) within the salt marshes of the Great Rann of Kachchh, and the Wagad Uplift in its eastern part (Fig 1).

The Mesozoic rocks of Kachchh were first described by Wynne [34]. However, it was Waagen [35] who divided these rocks into four subdivisions viz., Patcham, Chari, Katrol and Umia Series in ascending order. Subsequently, many revised classifications have been proposed for the Jurassic stratigraphy of Kachchh but the names proposed by Waagen [35] survived as formal lithostratigraphic units until now. According to Fürsich et al. [36], the Jurassic sequence of Kachchh commences with an initial phase of continental sedimentation of Late Triassic to Early Jurassic age. Following this phase of terrestrial sedimentation, marine depositional environments prevailed in the basin from the Bajocian to Aptian with a hiatus in sedimentation from the upper part of the Oxfordian to the lower part of Kimmeridgian [37, 38]. The Kimmeridgian in the Kachchh basin is represented by a thick succession of siliciclastics belonging to the Katrol Formation. In the early Middle to Late Kimmeridgian, shallow-marine to mid shelf conditions prevailed throughout the basin [39].

The basal sandstones of the Katrol Formation on the Kachchh Mainland yielded ammonites of late Early to Late Kimmeridgian age at a number of localities. The present ichthyosaur has been found within the lower Katrol Formation together with a number of ammonites belonging to *Katroliceras lerense* Spath, 1931 and *Katroliceras* sp. (Fig 2). This index fossil indicates

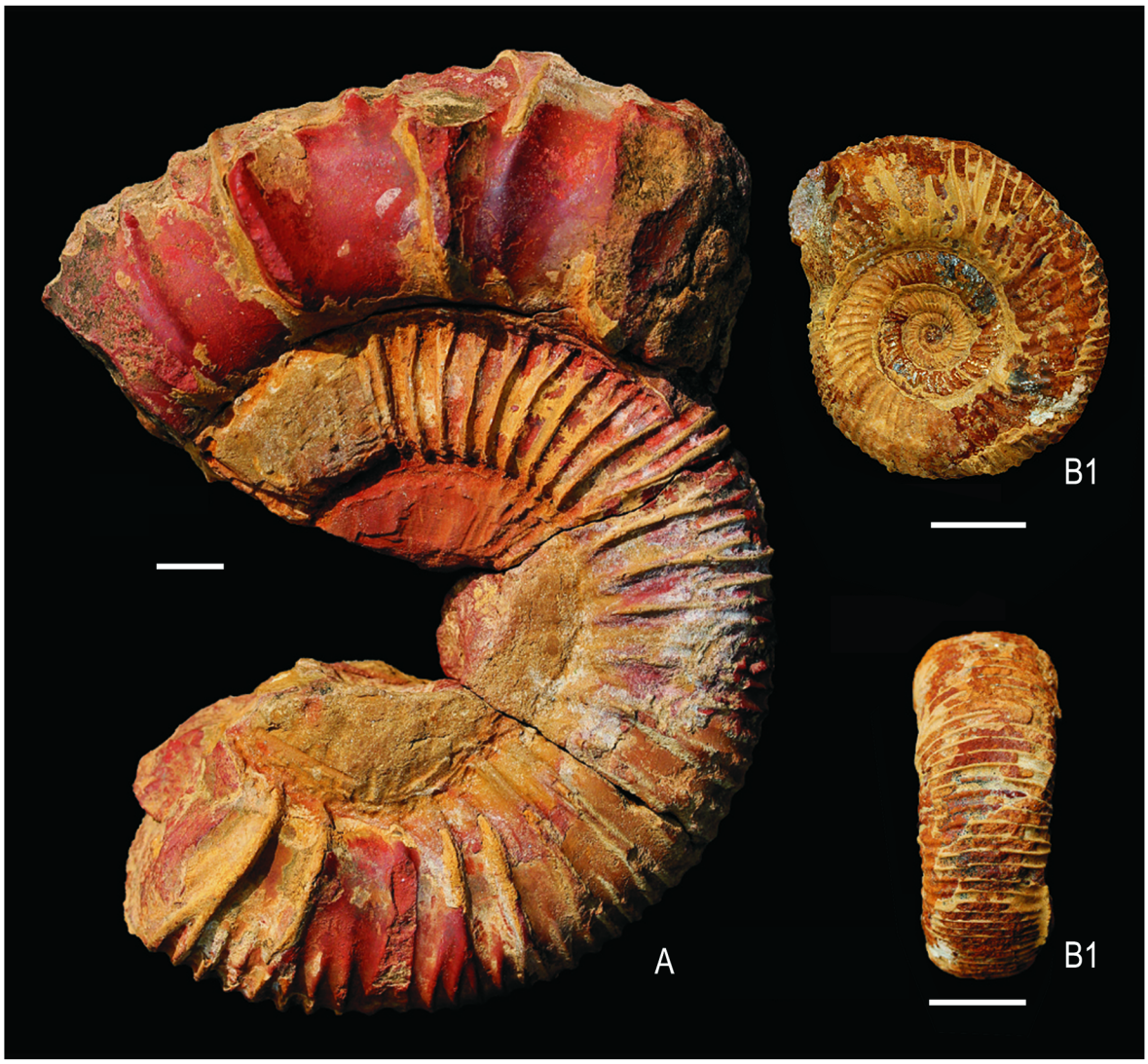


**Fig 2.** *Katroliceras lerense* Spath, 1931 (RUC2016IKH 01) in lateral view (A). Inner whorl of *Katroliceras* sp. (RUC2016IKH 02) (B1-B2) from the lower Katrol Formation (Upper Kimmeridgian) at the study site in lateral (B1) and ventral (B2) views. Scale bars equal 1 cm.

https://doi.org/10.1371/journal.pone.0185851.g002

the Katrolensis Zone of the Upper Kimmeridgian [40], which corresponds to the Beckeri Zone of the north Tethyan margin [41].

## Material and methods

Field investigations carried out by a team comprising the present authors and students of Delhi University and KSKV Kachchh University during the months of January and February 2016 resulted in the discovery of a fossil vertebrate yielding horizon in the Upper Kimmeridgian Katrol Formation to the south of Lodai village near Bhuj town, Gujarat, India (Fig 1). During a full scale excavation at this fossil site, the vertebral column, ribs, neural spines, gastralia and two associated fins were found in articulation. Additionally, a part of the snout representing the premaxilla was found at the anterior end of the preserved vertebral column and a few isolated teeth, vertebrae, jaw fragments, and other bone fragments were found scattered

around the excavation site. The skeleton is encased in a hard, ferruginous nodular matrix whereas the ribs are preserved in a soft shale. The vertebral column preserved a portion of the cervical region, the entire dorsal region, and a part of the pre-flexural region and measures 3.6 m. Taking into consideration of 36 cm long preserved premaxillary bone, missing skull region and the postflexural vertebrae, it is inferred that the complete skeleton may have measured between 5.0 and 5.5 m in length. The axial skeleton and two paddles were collected in six plaster jackets. Before making the plaster jackets, photographs of the axial skeleton and associated paddles were taken using a Canon EOS 60D Camera. Also, the fragmented ribs were collected separately after taking photographs and making rough sketches. Line drawings of the two inferred forefins, isolated vertebrae, and the vertebral column were made from photographs. The specimens described here are deposited in the Geological Museum of the Department of Earth and Environmental Science, Krantiguru Shyamji Krishna Verma Kachchh University, Bhuj, Kachchh District, Gujarat, India and bear accession numbers KGMV 0501–0512. The present work was an integral part of a completed Government of India (Science and Engineering Research Board, New Delhi) funded research grant (SR/S2//JCB-14/2010) to GVRP.

## Mode of preservation

KGMV 0501 is found in a horizontal position on the bedding plane of greenish-yellow silty shales. The skeleton was lying on its left lateral surface exposing its right lateral side. One of the fins, inferred as the left forefin, was lying close to the anterior part of the vertebral column in its natural position. However, no bones of the pectoral girdle were found, but they may have been buried in the rock matrix underneath the ribs and vertebrae. A second fin of nearly the same size as the left forefin is found close to the tail bend. As the hindfins are highly reduced in post-Middle Jurassic ichthyosaurs and based on the size similarity of this fin to that of the anterior fin it is regarded here as most likely the right forefin. No bones of the girdle were found attached to the fin. This fin appears to have been displaced from its natural position before the axial skeleton rested on the sea floor as its proximal end is ventrally pointing with respect to the axial skeleton, whereas its distal end with fin elements is partially covered under the vertebral column. Some of the distal fin elements can be seen protruding dorsally above the vertebrae. Though no skull was found, an anterior part of the snout representing the premaxilla was found in a vertical position at the anterior end of the vertebral column. The skull may be present in one of the plaster jackets, but preparation is required. Articulated, highly fragmented ribs and gastralia lie on the ventral side of the vertebral column. The postfexural vertebrae are not preserved.

From the vertically positioned anterior part of the premaxilla, it is inferred that the animal after death nose-dived into the soft sediment with the skull going down into the substrate in a vertical position. Once the skull landed vertically in the substratum, the body was laid on its lateral side. The teeth in the premaxilla were dislodged from their natural position after death. Differential preservation of the skeleton with a major part remaining intact (anterior premaxilla, vertebral column and left forefin), one displaced possible right forefin, and non-preservation of hindfins, pectoral and pelvic girdles and part of the posterior tail bones may be interpreted in terms of scavenging, reworking, and partial burial of the skeleton with the exposed parts being subjected to disarticulation and decomposition [42]. The vertebral column is embedded in maroon-coloured ferruginous concretions. The nearly intact vertebral column indicates that the concretionary ferruginous coating of the skeleton took place following its burial below the sediment and this happened at least a few centimeters below the sediment-water interface. Possibly this prevented the disarticulation of the skeleton by any scavenger or by epifaunal activity. During its excavation ammonoid shells and belemnite rostra were found

within the greenish-yellow shales of the Katrol Formation. The presence of ammonoids and belemnites indicate that the sediments were deposited under fully marine conditions.

## Systematic Palaeontology

Superorder Ichthyopterygia Owen, 1840
Order Ichthyosauria de Blainville, 1835
Family Ophthalmosauridae Baur, 1887
Ophthalmosauridae gen. et sp. indet.
(Figs 3–12)

### Referred material

Partially preserved skeleton (KGMV 0501) consisting of premaxilla, articulated vertebrae, left forefin, and? right forefin. Two fairly well-preserved teeth (KGMV 0502–0503), one posterior caudal vertebra (KGMV 0504), three postflexural caudal vertebrae (KGMV 0505–0507), three isolated phalanges (KGMV 0508–0510) and two mandibular fragments (KGMV 0511–0512) found scattered around the articulated skeleton are considered to belong to KGMV 0501.

### Stratigraphic horizon, age and locality

Greenish-yellow shales of the Katrol Formation representing the Katrolensis Zone of the Upper Kimmeridgian age [40] exposed near Lodai village (N23˚22.391': E69˚54.690'), 30 km northeast of Bhuj, Kachchh District, Gujarat (western India).

### Description

The studied specimen comprises a large, partial skeleton that is mostly articulated (KGMV 0501). The preserved skeletal remains include an incomplete premaxilla, articulated vertebrae of cervical, dorsal and pre-flexural regions, left forefin, possible right forefin all in articulation and isolated teeth, vertebrae of posterior caudal and postflexural regions, and phalanges possibly belonging to the articulated skeleton. Some of the anterior vertebrae, many of the caudal vertebrae and perhaps the pelvic remains are missing. The fin lying close to the vertebral column anteriorly is the left forefin in its original position with only a slight dislocation from the axial skeleton (Fig 3). The posteriorly located fin, lying close to the tail just near the posterior ribs, possibly represents the right forefin. Despite its position, the latter is regarded as a displaced right forefin because hindfins became highly reduced in Jurassic and Cretaceous ichthyosaurs [43].

**Premaxilla.** The incomplete premaxillary bone is 36 cm in length (Fig 4A1–4A3). The preserved bone represents the part of the premaxilla anterior to the nasal and up to the tip of the snout. It has a rounded dorsal surface and semi-circular cross-section (Fig 5). Both the right and left labial faces of the premaxilla bear a longitudinal groove (fossa premaxillaris) with a few nutrient foramina opening into its floor discretely and coalescing with it posteriorly (Fig 4A2–4A3). This fossa lies about 1.5 cm above the dental groove. The premaxilla is a semi-cylindrical bone each side having an outer facial and inner palatal part. The naturally sectioned premaxilla (8 fragments) offers 16 transverse sections for study (Fig 5). In transverse section, the facial part of the bone is semi-lunate in shape with a convex outer face and concave inner face (Fig 5). The facial pair of bones meets along the midline and forms the arch of the snout. Together with the outward diverging curved ends of the palatal bones, the semi-lunate facial bones enclose a lozenge-shaped canal in the midline that persists from the preserved distal part to the anterior end of the premaxilla. This canal, interpreted as a direct continuation of

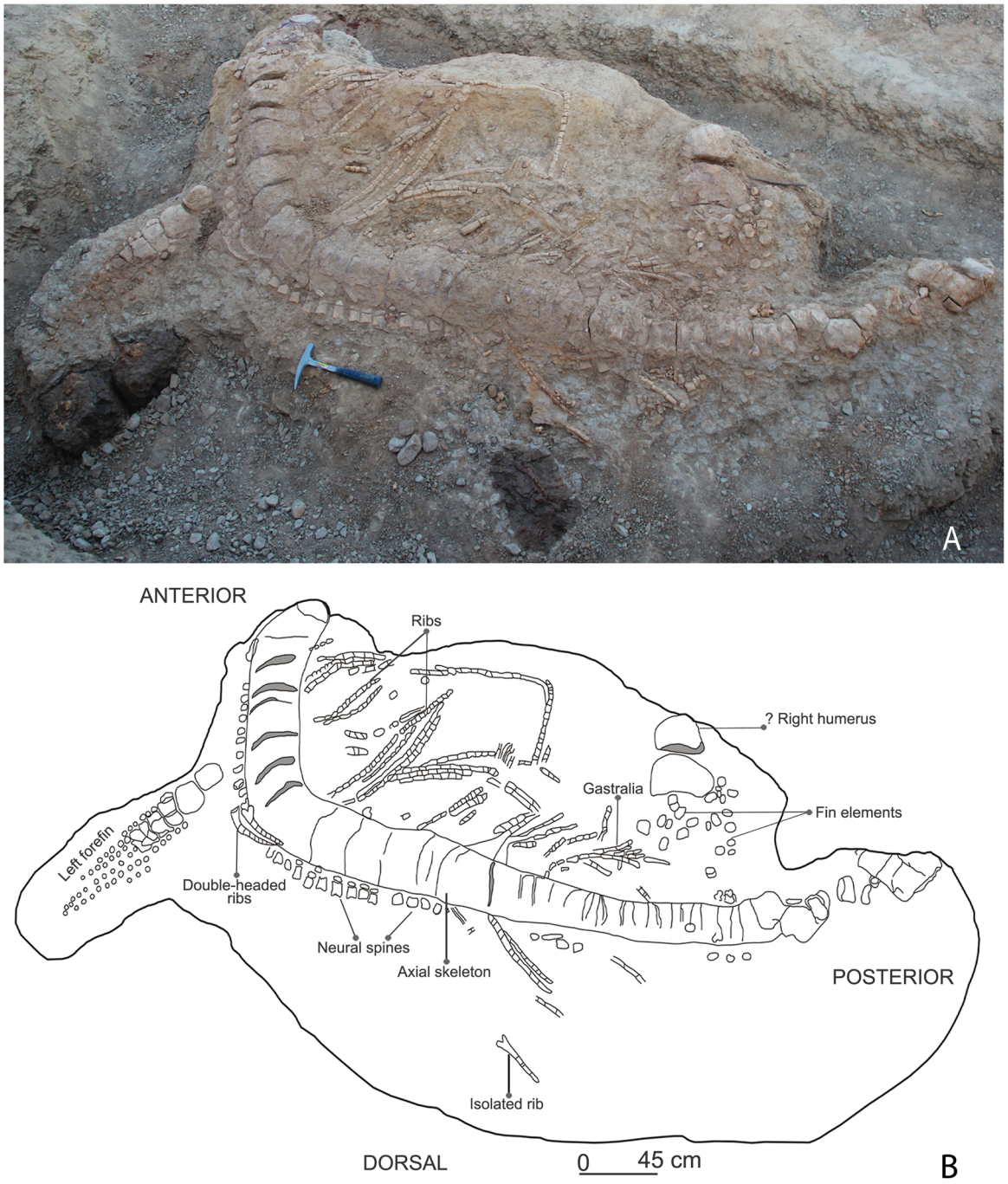


**Fig 3. Field photograph (A) accompanied with a sketch (B) of the excavated ichthyosaur skeleton in the Katrol Formation near Lodai village, Kachchh, India.**

https://doi.org/10.1371/journal.pone.0185851.g003

the cranial cavity [44], decreases in size anteriorly. In all preserved natural transverse sections, the two bones of the palatal process are not separated from the facial part. The palatal process occurs in the form of two curved vertical plates that enlarge at their ventral extremities into rounded, club-like structures (Fig 5). In the ventral face, the lower ends of the palatal process are rounded, closely approximated in the middle.

**Fig 4. Anterior part of the premaxilla of Ophthalmosauridae gen. et sp. indet.** (KGMV 0501) in ventral (A1), left lateral (A2) and right lateral (A3) views. Scale bar equals 10 cm.

https://doi.org/10.1371/journal.pone.0185851.g004

The broad groove between the palatal process and the facial part on either side is broad, deep and holds one tooth each (in cross section) (Figs 4A1–4A2 and 5). The teeth are held loosely in this dentigerous groove, which is oriented more vertically in the anterior part and becomes laterally oriented posteriorly. The exposed ventral surface of the premaxilla displays at least eight teeth in each half of the bone. But all the teeth are only partially preserved, small in size and oriented anteroposteriorly with their pointed ends slanting posteroventrally. In most cases, their tips are broken. This may be an artifact of post-mortem dislocation of the teeth from their vertical positions. In one transverse section, cross-sections of replacement teeth dorsal to the mature teeth have also been noticed (Fig 5). The posterior teeth are oriented slightly more laterally than the anterior ones. The state of preservation indicates that the teeth were lost or broken prior to burial.

**Teeth.** One of the preserved teeth in the premaxilla is very robust (preserved height = 34 mm, maximum basal diameter = 17 mm) and has a worn rounded apex (Fig 6A1). This tooth has a slight lingually curved crown, a short and smooth acellular cementum layer and an oval cross-section. It shows enamel spalling on its labial face close to the apex (Fig 6A3) and extensive longitudinal enamel spalling on its lingual face that extends from the apex to nearly its base (Fig 6A4). The lingual longitudinal enamel spalling also exhibits obliquely oriented coarse grooves (Fig 6A5). The longitudinal fluting of this tooth is relatively coarse. Though not many teeth are preserved in the premaxilla, they appear to decrease in size towards the front. Most of the premaxillary teeth have broken tips (Fig 6B). However, it is unclear if the damage is due to

**Fig 5. Anterior part of the premaxilla of Ophthalmosauridae gen. et sp. indet.** (KGMV 0501) showing cross sections at posterior (left) and anterior (right) ends of the premaxilla at different segments of the bone. Scale bars equal 2.2 cm for the middle picture and 2 cm for the left and right pictures.

https://doi.org/10.1371/journal.pone.0185851.g005

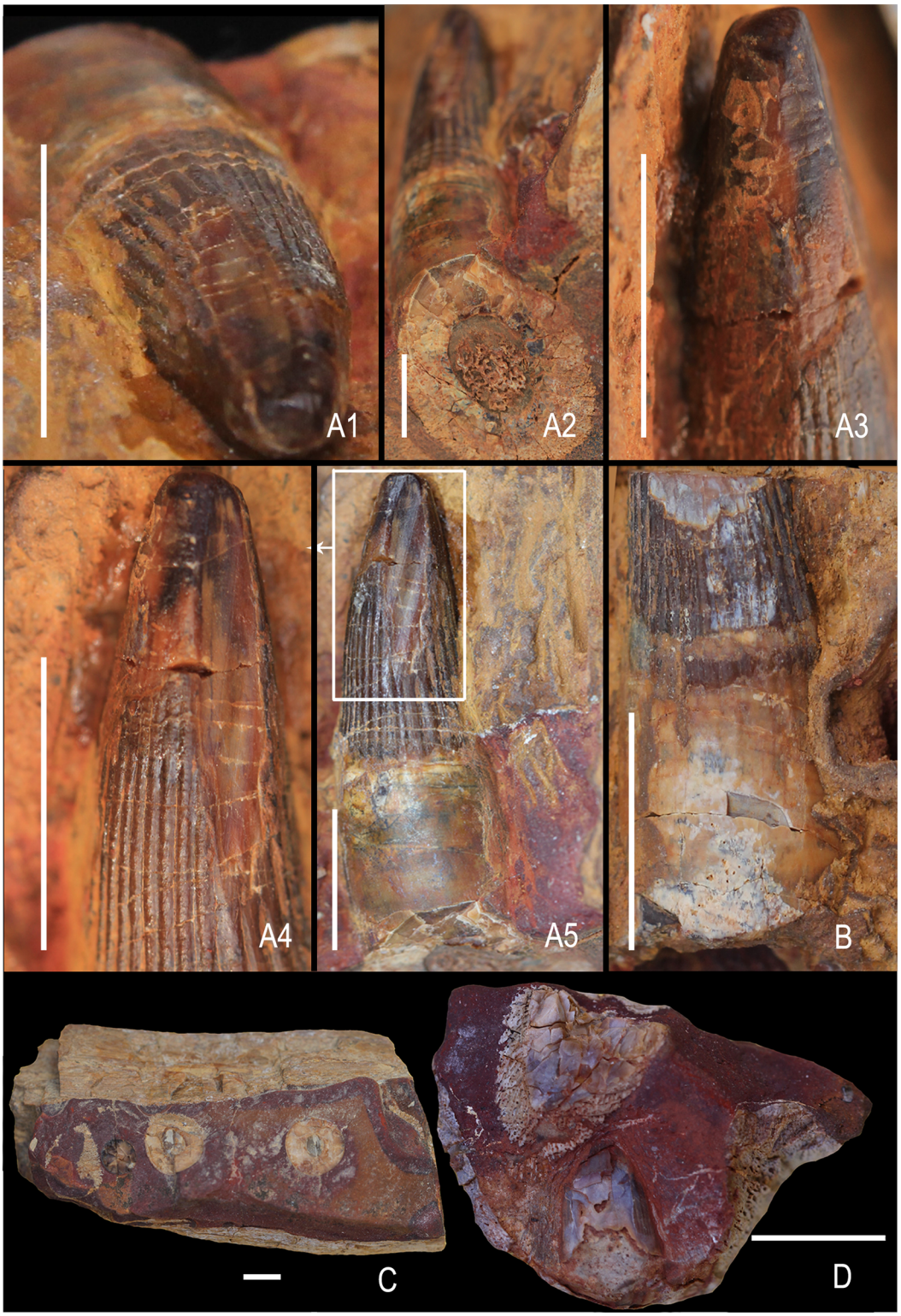


**Fig 6. Ophthalmosauridae gen. et sp. indet.** A1-A5, premaxillary tooth showing wear facet in apical view (A1), basal cross-section (A2), enamel spalling in the apicolabial region (A3), longitudinal enamel spalling on the linguolateral facet (A4), obliquely oriented grooves on the longitudinally spalled enamel (A5). A second premaxillary tooth showing breakage in the apical region (B), a mandibular fragment showing circular cross-section of teeth (KGMV 0511) (C), a small fragment of jaw showing an erupting tooth beneath an aged tooth (KGMV 0512) (D). Scale bars equal 1 cm.

https://doi.org/10.1371/journal.pone.0185851.g006

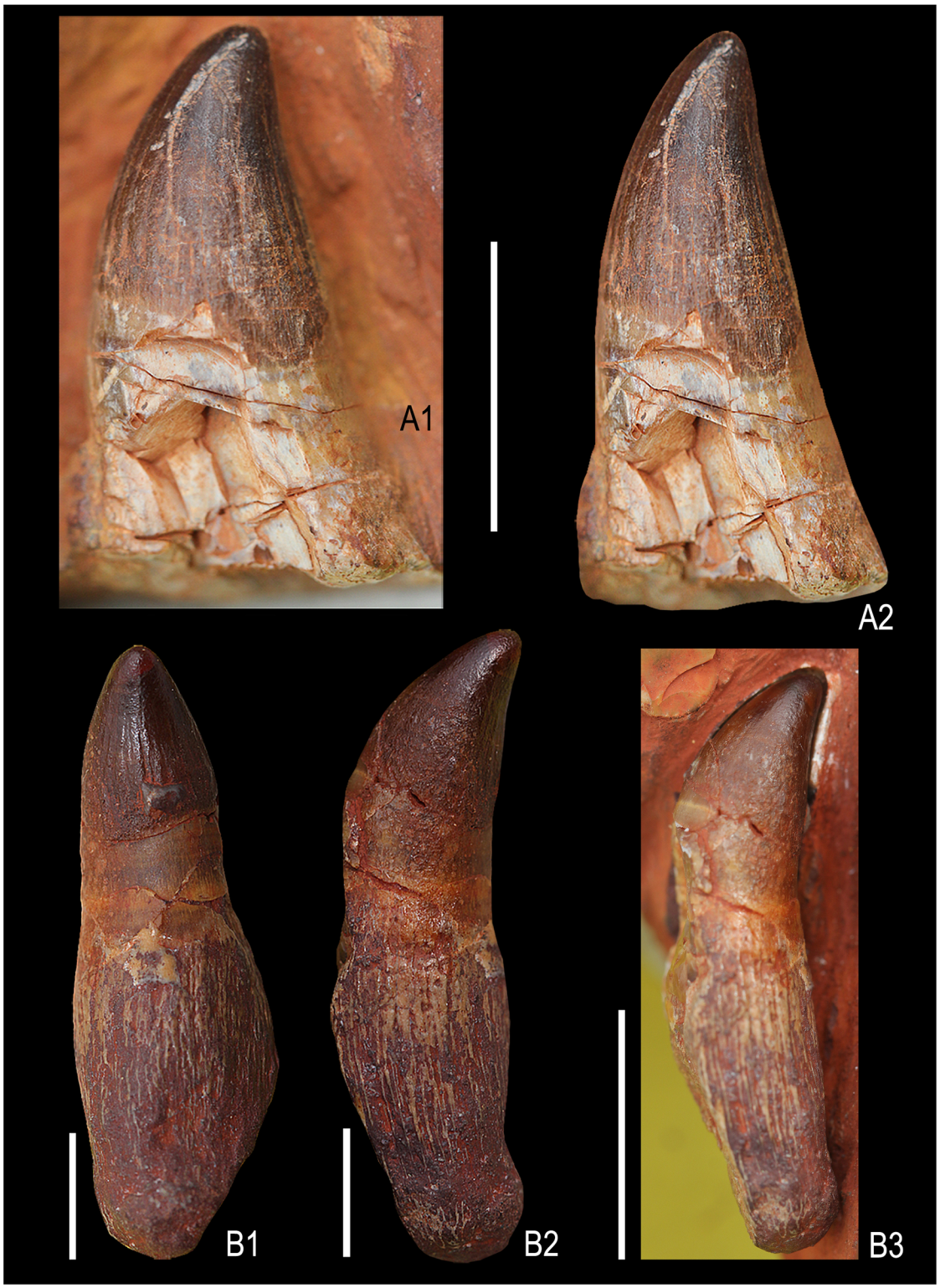


**Fig 7. Isolated teeth of Ophthalmosauridae gen. et sp. indet.** Lateral view of a tooth embedded in ferruginous matrix (KGMV 0502) (A1), the same tooth with edges improved by photoshop (A2). A second tooth (KGMV 0503) in lingual view (B1), lateral view (B2), embedded in ferruginous matrix before extraction (B3). Scale bars equal 1 cm.

https://doi.org/10.1371/journal.pone.0185851.g007

post-mortem taphonomic processes or related to food processing. In one of the mandibular fragments (KGMV 0511), the broken teeth show a circular cross-section (Fig 6C).

Two teeth (KGMV 0502–0503) were found on the surface at the excavation site close to the anterior end of the articulated axial skeleton and probably belong to this specimen. KGMV 0503, the better preserved of the two teeth, has a crown with longitudinal striations that do not reach the apex, smooth and short acellular cementum (dentine) layer, and the basal elongated and flaring, porous cellular cementum with fine longitudinal ridges (Fig 7B1–7B3). In this tooth, the basal cellular cementum layer is nearly half of the total height of the tooth (crown height = 9 mm, height of acellular cementum = 7 mm, height of cellular cementum = 15 mm). The apex of the crown is smoothened by wear. Though KGMV 0503 has a long root with basal longitudinal striations, the shape of the basal cross-section cannot be deciphered, as the root is longitudinally broken (Fig 7B1–7B3). As this tooth has no strongly expanded root base as in *Platypterygius*, its cross-section may have been circular or oval in shape. KGMV 0502 is similar to KGMV 0503 in the morphology of its crown and smooth dentine layer, but its basal cellular cementum layer is not preserved (Fig 7A1 and 7A2). At the junction of the crown and acellular cementum, the tooth is inflated and the dentine-covered area is flaring ventrally and slightly compressed transversely rendering an elliptical basal cross section. In KGMV 0502, a longitudinal scratch mark extending from the tip to the middle of the crown possibly represents a wear surface (abrasion).

**Axial skeleton.** The preserved length of the axial skeleton is 3.6 m (Fig 3). The vertebral column is embedded in a hard ferruginous matrix and as a result no diagnostic characters to clearly differentiate the cervical vertebrae from dorsal or caudal vertebrae are observed. The description of the vertebral column is, therefore, not possible until the specimen is prepared. However, short and wide neural spines can be seen dorsally in the anterior and middle parts of the preserved axial skeleton (Fig 3). Since the preserved axial skeleton includes the region just behind the skull and extends up to the tail bend, it is anticipated that several cervical, all the dorsal and most of the pre-flexural vertebrae are present.

One large and three small vertebrae were collected as float during the excavation of the articulated skeleton. Based on the criteria used by McGowan and Motani [3] and Kirton [45], the isolated vertebrae from the Lodai ichthyosaur site can be identified as posterior caudal and postflexural vertebrae.

One specimen (KGMV 0504) of the present collection of isolated vertebral centra can confidently be identified with posterior caudal vertebra. KGMV 0504 is anteroposteriorly flattened and disc-like (length of the centrum = 2.7 cm) (Figs 8A1–8A5 and 9B1–9B4). In the anterior and posterior views, the centrum is sub-quadrangular in outline with a slightly broader ventral side (at the level of rib facet) (8.7 cm) than the dorsal side (8 cm). The height of the centrum at the level of neural arches is 7.8 cm. The rib facet is a broad and elevated ridge that extends over the entire length of the centrum slightly below its mid-height and bears a rounded pit anteriorly (Fig 9B2). The anterior face of the centrum is, to a large extent, concealed by the matrix except in the dorsal half where a part of the preceding centrum is preserved. The neural arches are in the form of low and narrow ridges and enclose a wide (2.5 cm) neural canal. The thick anterior and posterior edges enclosing a spindle-shaped depressed area in the mid-ventral face of the centrum are interpreted as the haemal arches.

There are three centra in the Kachchh ichthyosaur collection, which can be referred to the postflexural vertebrae (Figs 9A1–9A3 and 10A1–10C2). KGMV 0505, the best preserved of the three centra, has a width of 1.6 cm, height of 1.8 cm and length of 1.3 cm. The centra are small in size, elliptical in anterior and posterior views, biconcave, slightly compressed laterally and higher than transversely wide. Their dorsal surfaces are comparatively shorter than their ventral surfaces. The facets for neural arches are low, ridge-like, and transversely wide in the

**Fig 8. Ophthalmosauridae gen. et sp. indet.** A1-A5 posterior caudal vertebra (KGMV 0504) in posterior (A1), anterior (A2), ventral (A3), dorsal (A4) and lateral views (A5) showing rounded facet for a rib. B1-B2. isolated proximal phalanx (KGMV 0508) in dorsal or ventral (B1) and lateral (B2) views. C1-C2. isolated distal phalanx (KGMV 0509) in dorsal or ventral (C1) and lateral (C2) views. Scale bars equal 1 cm.

https://doi.org/10.1371/journal.pone.0185851.g008

middle. There are no facets for ribs on these vertebrae. Similarly, no facets for haemal arches are present on the ventral face of the centra.

**Ribs.** One proximal shaft of an isolated rib lying dorsally and near to the posterior end of the vertebral column is double-headed and has an elliptical cross-section (Fig 3A and 3B). The

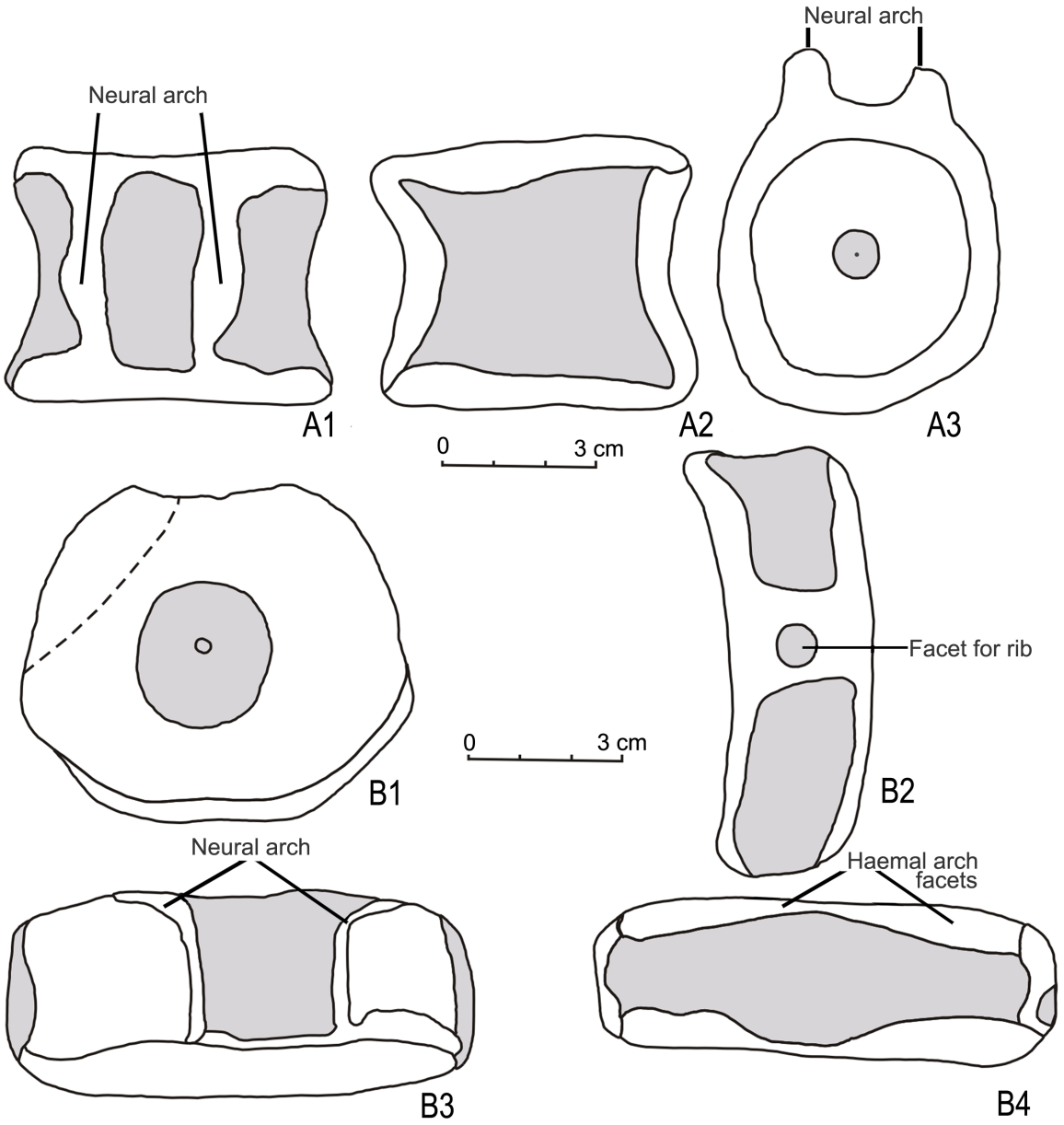


**Fig 9. Ophthalmosauridae gen. et sp. indet.** Line drawings of post-flexural caudal vertebra (KGMV 0505) (A1-A3) in dorsal (A1), lateral (A2), and anterior or posterior (A3) views. Line drawings of posterior caudal vertebra (KGMV 0504) (B1-B4) in posterior (B1), lateral (B2), dorsal (B3) and ventral (B4) views.

https://doi.org/10.1371/journal.pone.0185851.g009

remaining ribs lie on the ventral side of the axial skeleton and are attached to the vertebrae, relatively thin, laterally compressed and highly fragmented. Many of the ribs occurring articulated in the anterior region are double- headed. The shafts of the ribs are flattened and grooved both anteriorly and posteriorly rendering a cross-sectional shape of '8'. Ribs near the presacral region are shorter, slender, and have elliptical to spherical cross-sections. In majority of the ribs, only proximal parts are preserved. The length of the longest preserved rib is 100 cm.

**Neural spines.** Except for the posterior region beyond the displaced? right forefin, the neural spines are preserved all along the dorsal surface of the vertebral column (Fig 3A and 3B).

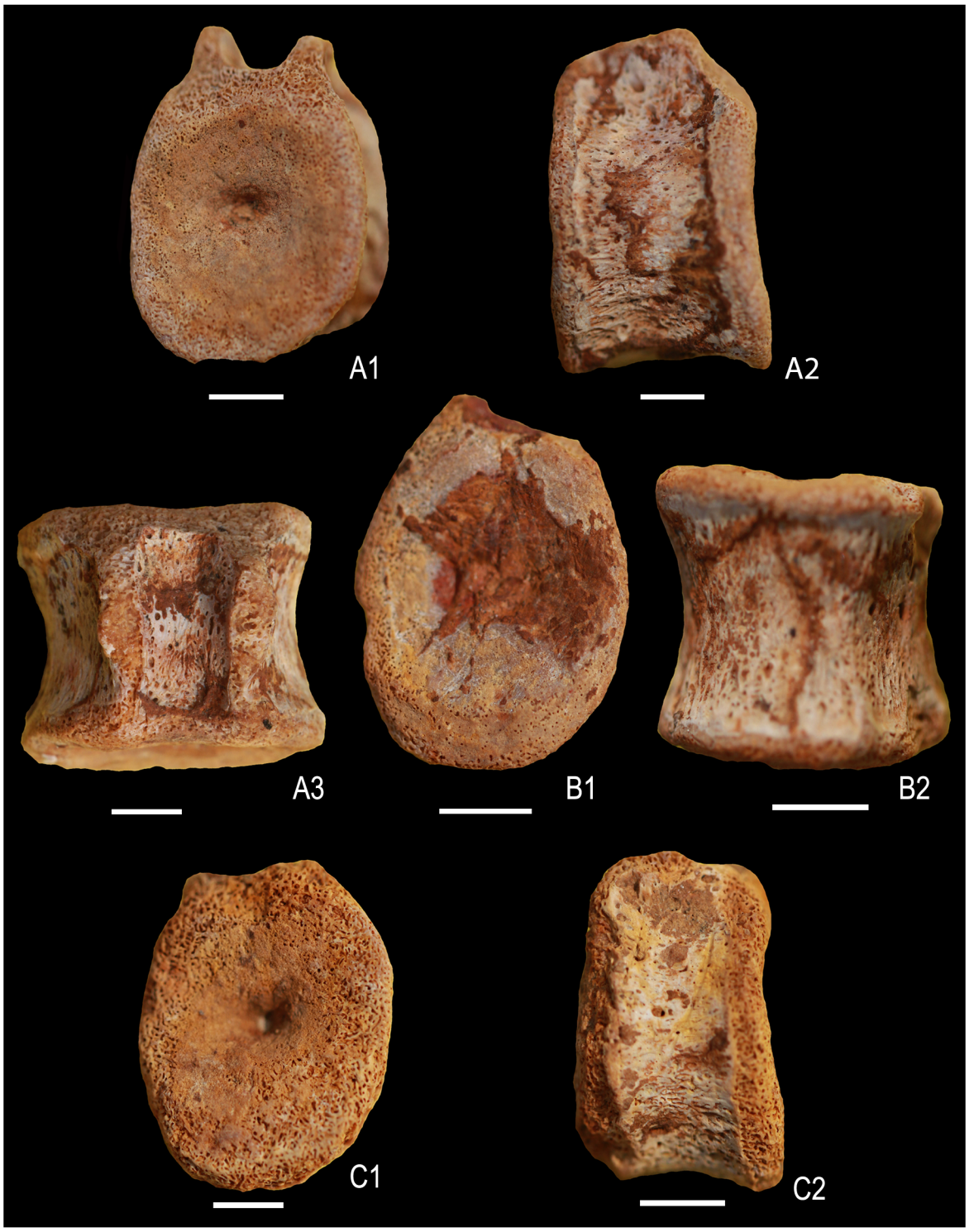


**Fig 10. Post-flexural caudal vertebrae of Ophthalmosauridae gen. et sp. indet (A1-C2).** A1-A2 (KGMV 0505), anterior or posterior view (A1), lateral view (A2), dorsal view (A3). B1-B2 (KGMV 0506), anterior or posterior view (B1), ventral view (B2). C1-C2 (KGMV 0507), anterior or posterior view (C1), lateral view (C2). Scale bars equal 1 cm.

https://doi.org/10.1371/journal.pone.0185851.g010

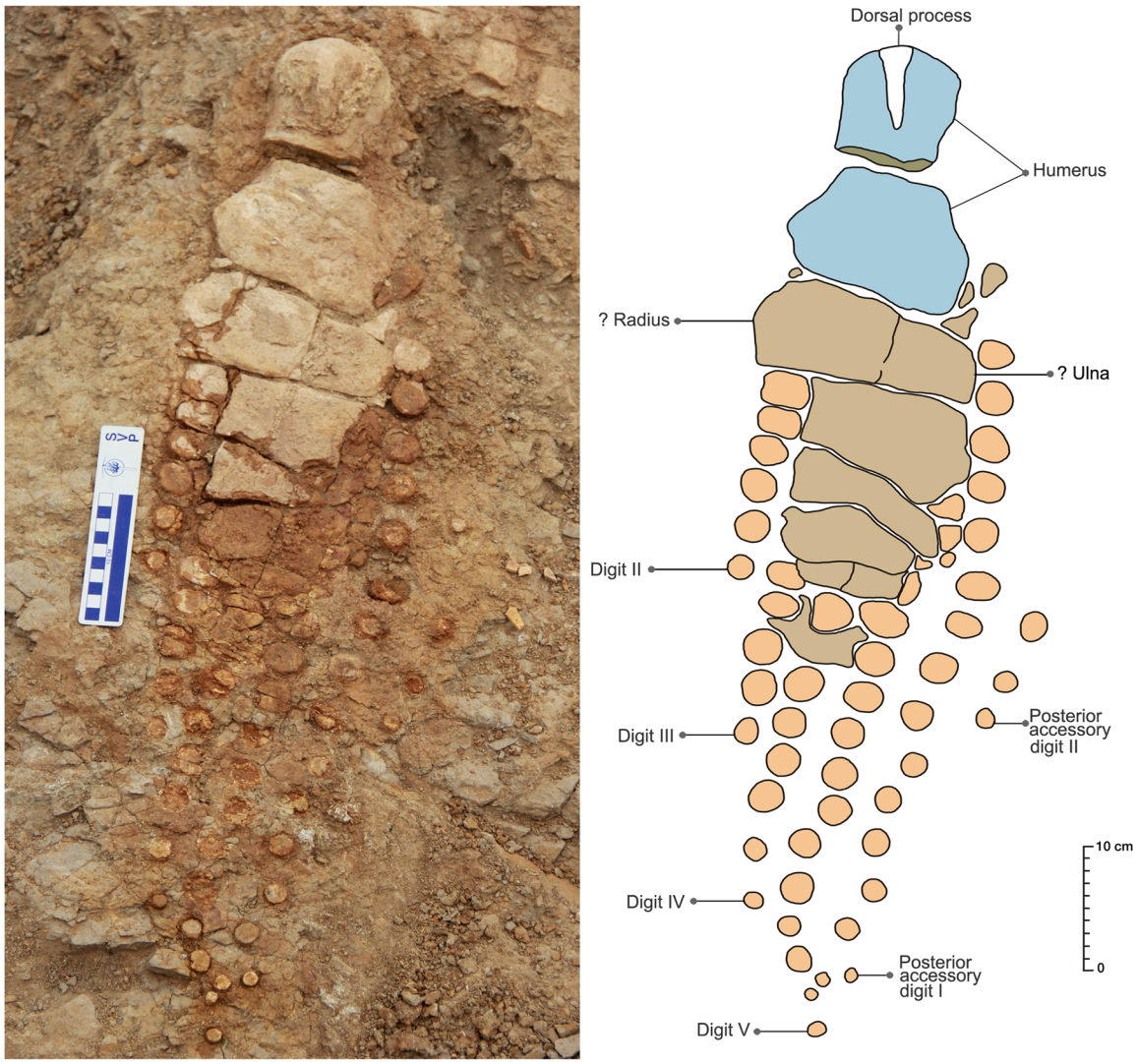


**Fig 11. Close-up view of the left forefin accompanied with a sketch.**

https://doi.org/10.1371/journal.pone.0185851.g011

They are short, rectangular in shape with their long axis directed dorsally, decrease in size posteriorly, and occur well-separated from the vertebral centra.

**Gastralia.** A few clustered, short, rod-like bones of gastralia are found in the posterior region of the skeleton just anterodorsal to the preserved? right forefin (Fig 3A and 3B). They are cylindrical in outline and are also highly fractured as in the case of ribs. These bones are thinner than the ribs.

**Left forefin.** The exposed surface of the left forefin (Fig 11) is considered as dorsal as the humerus has a prominent dorsal process that extends distally one-third of the proximodistal length of the humerus. The dorsal process is positioned at equidistance from its anterior and posterior margins. The proximal extremity of the humerus is rounded in outline, while its distal end is moderately expanded anteroposteriorly. The anterior margin of the humeral shaft is moderately concave, whereas its posterior margin is slightly concave or nearly straight. The distal articular face is nearly straight except for a short, deflected facet anteriorly. There is a slight concavity in the middle of the distal face where the radius comes into contact with the

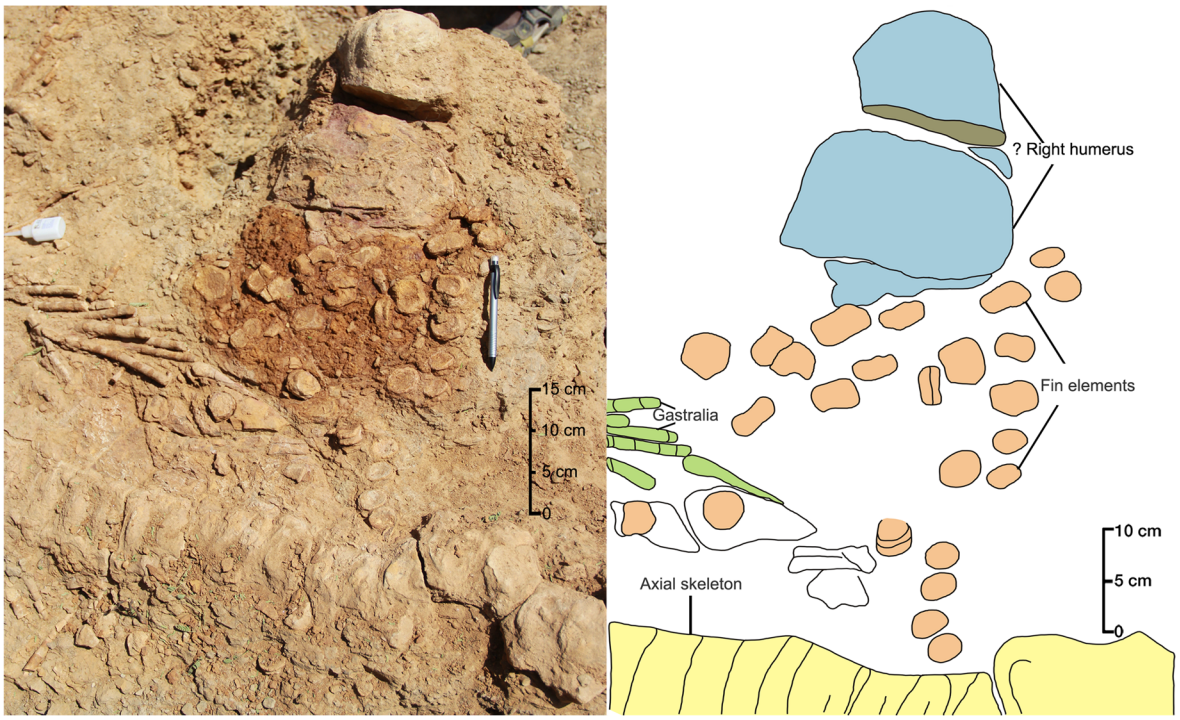


**Fig 12. Close-up view of the ?right forefin accompanied with a sketch.**

https://doi.org/10.1371/journal.pone.0185851.g012

humerus. The short obliquely oriented facet at its anterodistal end is possibly for articulation with the pre-radial element. Distal to the humerus, there are two large, rectangular elements, the anterior one being larger proximodistally as well as anteroposteriorly than the posterior one. Whether these elements represent the radius and ulna or it is the matrix that conceals these proximal fin elements will be clear only when the specimen is fully prepared. The sutures between the proximal elements of the forefin cannot be determined because of the poor contrast between the matrix and the bone. Post-depositional break-up of bones (longitudinal breaks) due to weathering further complicates their identification. Because of the concealment of the proximal part of the fin by the rock matrix, the proximal and distal carpals and metacarpals, which are crucial for generic identification, are not exposed. The fin is substantially long (80 cm) and slender (Table 1). Spherical disc-like phalanges are arranged in six rows. There appear to be four primary digits that begin distal to the metacarpals, and extend to the distal end of the fin. There are two accessory digits located posterior to the primary digits. The actual number of phalanges in the primary digits cannot be counted as their proximal ends are buried beneath the matrix. The anterior-most digit has only six exposed spherical elements that are located quite proximal to the other three primary digits. This could be a pre-axial digit or Digit

**Table 1. Measurements of the humerus and left forefin.** The measurements were taken from the proximal end of the humerus to the last phalanx including the break in the humerus and gaps between the phalanges.

| | **Proximodistal length** | **Maximum anteroposterior width** | |
|---|---|---|---|
| **Left forefin** | 80 cm | 19 cm | |
| | **Proximodistal length** | **Width of proximal end** | **Width of distal end** |
| **Humerus** | 25.5 cm | 9.0 cm | 14.5 cm |

https://doi.org/10.1371/journal.pone.0185851.t001

II. The primary Digit III shows only five exposed phalanges and extends slightly distal to the Digit II. The fourth primary digit (Digit IV) has seven exposed phalanges and extends near to the distal end. The fifth primary digit (Digit V) extends to the distal-most part of the fin and has 12 exposed phalanges. The first posterior accessory digit is very long and starts from the posteroproximal end of the forefin. It has 15 spherical elements, which decrease in size distally. The second posterior accessory digit is located at the mid-length of the fin and has only three very small, disc-like phalanges. In the pre-axial digit or Digit II, the proximal two exposed phalanges appear to be rectangular in outline. It is, therefore, quite possible that the proximal most phalanges of the digits are rectangular or anteroposteriorly elongated. Majority of the exposed phalanges are clearly spherical in outline and gradually decrease in size distally. Though the phalanges are not closely packed in each digit, the individual digits are clearly differentiated from each other. The distal part of the forefin is posteriorly curved.

**?Right forefin.** There is a second fin (Fig 12) located at the posterior end of the skeleton. The proximal bone of this fin is morphologically comparable to the humerus of the left forefin. Although the bone has a thick ferruginous coating concealing most of the morphological features, it appears to have a deltopectoral crest. This bone occurring at the posterior end of the articulated vertebral column has its distal extremity pointing towards the vertebral column rather than away from it. Therefore, it is inferred that this fin was displaced from its original position after the death of the animal. Its larger size is highly unusual for a pelvic fin because Late Jurassic ichthyosaurs had highly reduced hindfins [43]. The fin elements distal to the humerus are dislocated from their natural position and many of them are rectangular in shape. But half of the preserved phalanges, which are more distal in position and some located dorsoventral to the posterior presacral vertebrae, are ovoid or spherical in shape. The isolated rectangular phalanges recovered from the surface have a central groove all along the periphery of the bone. These rectangular elements may represent proximal elements of the fin.

**Phalanges.** Three isolated phalanges were surface-collected from the site of the articulated skeleton (KGMV 0508–0510). One of them is rectangular in outline (KGMV 508), dorsoventrally thick and most likely a proximal one (Fig 8B1 and 8B2). Two of them (KGMV 0509–0510) are comparatively small in size and disc-like (Fig 8C1 and 8C2) possibly representing the distal elements.

## Discussion

The Callovian and post-Callovian ichthyosaurs are generally included in the family Ophthalmosauridae [8, 9, 46–50], although Fischer et al. [6] reported a non-ophthalmosaurid ichthyosaur from the Early Cretaceous of Iraq. Keeping in view their chronostratigraphic position (Kimmeridgian Stage), the described specimens are referred to post-Liassic ophthalmosaurids. This conclusion further receives support from the presence of a stout dorsal process on the humerus of the forefin. This character has been viewed as a synapomorphy of Ophthalmosauridae in several phylogenetic analyses [8,10, 49, 51, 52]. The presence of an anterior accessory element articulating with the humerus was also considered as characteristic of ophthalmosaurids [11]. The amphicoelous isolated vertebrae from Kachchh are quite distinct from those of weakly amphicoelous vertebrae of platypterygiine ophthalmosaurids.

The documented fossil record of Middle-Late Jurassic ichthyosaurs is highly skewed towards the western Tethys (Anglo-Paris Basin), North America, and Northern Europe (Norway, Russia). But recent reports of ophthalmosaurid ichthyosaurs from Argentina, Mexico, Cuba, Madagascar, Australia and now from India clearly indicate that the apparent restricted distribution is due to poor sampling in these parts of the world. In their classic work, McGowan and Motani [3] considered five genera and 14 species of ophthalmosaurids as valid. Since

**Table 2. Stratigraphic and geographic distribution of Middle and Late Jurassic ophthalmosaurid ichthyosaurs.**

| NAME OF THE TAXON | FORMATION & GEOGRAPHIC LOCATION | AGE |
|---|---|---|
| *Caypullisaurus bonapartei* [7] | Vaca Muerta Formation, Neuquén Basin, Argentina | Berriasian—Tithonian |
| *Palvennia hoybergeti* [11] | Agardhfjellet Formation, Svalbard, Norway | Tithonian |
| *Ophthalmosaurus* cf. *O. icenicus* [54] | La Caja Formation, Mexico | Tithonian |
| *Cryopterygius kristiansenae* [11] | Agardhfjellet Formation, Svalbard, Norway | Tithonian |
| *Cryopterygius kielanae* [55] | Kcynia Formation, Central Poland | Tithonian |
| *Undorosaurus gorodischensis* [56] | Volga Region and Moscow Region, Russia | Tithonian |
| *Undorosaurus trautscholdi* [57] | Mnevniki, Moscow, Russia | Tithonian |
| *Arthropterygius* sp. [9] | Vaca Muerta Formation, Neuquén Basin, Argentina | Tithonian |
| *Arthropterygius* sp. [13] | Parmes Formation, Russia | Middle Tithonian |
| *Janusaurus lundi* [12] | Agardhfjellet Formation, Svalbard, Norway | early Middle Tithonian |
| *Aegirosaurus leptospondylus* [58, 59] | Solnhofen Formation, Germany | Early Tithonian |
| *Nannopterygius enthekiodon* [60] | Kimmeridge Clay Formation, Dorset, England | Kimmeridgian |
| *Brachypterygius extremus* [61] | Kimmeridge Clay Formation, Dorset, England | Kimmeridgian |
| *Arthropterygius chrisorum* [10, 62] | Ringnes Formation, Melville Island, Northwest Territories, Canada | Kimmeridgian—Oxfordian |
| *Ophthalmosaurus natans* [63] | Sundance Formation, USA | Oxfordian—Callovian |
| *Ophthalmosaurus icenicus* [64] | Oxford Clay, England | Callovian |
| *Mollesaurus periallus* [15] | Los Molles Formation, Neuquén Basin, Argentina | Bajocian |

https://doi.org/10.1371/journal.pone.0185851.t002

then many new taxa have been reported from different parts of the world taking the list to 20 genera and 27 species [53]. Until now the Middle-Late Jurassic members of Ophthalmosauridae are known by 11 genera and 15 species (Table 2).

A squared root cross-section of *Platypterygius*, *Undorosaurus*, *Brachypterygius* and *Maiaspondylus* [56, 65, 66] was considered as a synapomorphy of platypterygiine ichthyosaurs [67]. A comparison of the ichthyosaur teeth from Kachchh is made with isolated ichthyosaur tooth (DUGF/41) from the Upper Albian—Middle Cenomanian Karai Formation of the Cauvery Basin, South India, assigned to Platypterygiinae gen. indet. [28]. The tooth of Platypterygiinae gen. indet. (Fig 13A1 and 13A2) is distinctly different from those of the studied specimens in having a comparatively short and less curved crown, and strongly basally expanded root with a rectangular cross-section. The Kachchh specimens with a rounded to oval root cross-section thus fall within the primitive ophthalmosaurine clade of the Ophthalmosauridae [67].

The little morphological information that could be deciphered from the proximal part of the left forefin distal to the humerus in its current state of preparation limits its comparison with other known ophthalmosaurids, but still some general conclusions can be made. In general, the outline of the forefin, being elongated and narrow anteroposteriorly, is comparable to that of *Aegirosaurus* from the Early Tithonian of Germany [59]. The humerus of *Aegirosaurus* is widest at the distal end as in the Kachchh specimen [59]. However, *Aegirosaurus* has a broad and distally less extended dorsal process situated at the proximal end of the humerus, an angulated distal margin, and more tightly packed fin elements which are to a large extent rectangular in outline. *Cryopterygius kristiansenae* from the Tithonian of Svalbard, Norway [11], has also a narrow and long fin. In *Cryopterygius*, however, the dorsal process of the humerus arises from the postaxial margin and its long axis trends anterodistally towards the midline and the fin is slightly asymmetrical.

In the morphology of the humerus, the Kachchh specimen differs from most members of the family Ophthalmosauridae in having a narrow proximal end narrower than a moderately

**Fig 13. Isolated tooth of Platypterygiinae gen. indet.** (DUGF/41) from the Upper Albian—Middle Cenomanian Karai Formation, Cauvery Basin, South India in lingual view (A1) and lateral view (A2). Scale bars equal 1 cm.

https://doi.org/10.1371/journal.pone.0185851.g013

broad distal end and a nearly straight distal end obliquely oriented to the long axis of the forefin as compared to the angulated facets separated by a ridge in the middle in most ophthalmosaurids. The humerus of the left forefin (KGMV 0501) with a well constricted mid-shaft and a distal end more anteroposteriorly expanded than the proximal end differs from that of *Arthropterygius*, *Undorosaurus*, *Cryopterygius*, *Janusaurus*, *Sveltonectes*, *Maiaspondylus* and *Platypterygius*. In *Caypullisaurus*, the distal end of the humerus is obliquely oriented to the long axis with a short angulation at the anterodistal end and the fin is long as in the Kachchh specimen ([7]: fig.5). However, the fin elements are rectangular and closely packed in *Caypullisaurus* [7]. In the Kachchh specimen, the distal humerus has three recognizable facets as in *O. icenicus*, *Brachypterygius*, *Arthropterygius*, *Caypullisaurus*, *Undorosaurus*, *Aegirosaurus*, *Janusaurus*, *Platypterygius* and *Acamptonectes* [7, 12, 45, 56, 59, 67] as compared to two facets in *Cryopterygius*, *Nannopterygius* and *Sveltonectes* [68]. In fact, the distal humerus of *Arthropterygius* compares well with that of the Kachchh specimen in possessing two relatively large facets

for ulna and radius and a small, obliquely oriented preaxial facet [13]. But in *Arthropterygius*, a median crest separates the ulna from the radius.

The better-preserved left forefin of the Kachchh specimen has six digits as in *Cryopterygius*, *Aegirosaurus* and *Brachypterygius*. The phalanges of this specimen are rounded, widely spaced and dorsoventrally thick as in Ophthalmosauridae and their closest sister taxon *Chacaicosaurus* [68]. In many ophthalmosaurids, such as *Caypullisaurus*, *Platypterygius*, *Brachypterygius*, *Aegirosaurus* and *Maiaspondylus*, the fin elements are rectangular in outline and tightly packed [68]. In the wide spacing of elements (loose packing) and their rounded shape (particularly in the distal region), the left forefin of KGMV 0501 compares well with that of *Ophthalmosaurus icenicus* though the fin is broader in its middle, distal to the epipodials in the latter. The distal end of the humerus is also nearly straight in *O. icenicus* as in the Kachchh specimen though angulated posteriorly in the former. The relatively dorsoventrally thick elements of the fins are characteristic of the family Ophthalmosauridae [3]. However, the tentatively identified right forefin has dorsoventrally thick, rectangular phalanges proximally and rounded phalanges distally. The exposed phalanges in the left forefin are rounded in shape, while the shape of proximal elements appear to be rectangular but most of this area is concealed beneath the matrix. Thick proximal elements and the unnotched anterior facet of the elements on the leading edge of the fins are regarded as synapomorphies of Ophthalmosauridae and *Chacaicosaurus* [68].

In its shape, transverse width and height proportions, and location of the single rib facet slightly below the mid-height, KGMV 0504 compares very well with the one figured by Kirton ([45]: fig.20 h-j) as a posterior caudal vertebral centrum of *Ophthalmosaurus icenicus* from the Oxford Clay. However, McGowan and Motani [3] noted that isolated vertebrae, and their shape variation, are to be used taxonomically with caution.

## Dental wear and dietary preference

Besides using to distinguish between different groups of ichthyosaurs [69] and sometimes as an important taxonomic criterion [70], tooth shapes have been widely used in the past to deduce the preference of the animal for a particular prey or varied preys [69, 71]. Based on the shape of the tooth apex, wear pattern, presence or absence of cutting edges, as well as shape and size of the crown, Massare [71] defined seven feeding types or guilds for Mesozoic marine reptiles viz., crush guild, crunch guild, smash guild, pierce I guild, pierce II guild, general guild, and cut guild.

The two isolated teeth (KGMV 0502–0503) found on the surface close to the skeleton are embedded in the maroon-coloured ferruginous matrix and their surfaces were exposed during preparation. These teeth have finely fluted crowns with blunt conical apices and do not show any apical wear except for a rugose appearance and smoothening. KGMV 0502 displays a narrow strip (ribbon-like) of longitudinal wear on the enamel of the crown on its labiolateral face. Preliminary preparation of the premaxilla exposed one nearly complete large tooth (Fig 6A2). It has a worn (smooth), leveled tip (Fig 6A1), and a small spalled enamel on the labial face close to the apex (Fig 6A3). It also exhibits an oval or lenticular longitudinal spalled enamel surface extending from the apex to nearly the base of the crown on its lingual face (Fig 6A4). An interesting feature of this spalled wear facet of the enamel is the presence of two coarse longitudinal grooves that are oriented oblique to the wear surface (Fig 6A5). This kind of wear surfaces has not been reported in any of the known ichthyosaurs until now.

Dental wear surfaces due to attrition (tooth/tooth contact) or abrasion (tooth/food contact) on teeth are not very common in non-mammalian tetrapods [72]. While studying dental occlusion in *Dakosaurus*, a metriorhynchid crocodile from the Late Jurassic of Europe, Young

et al. [72] noticed three types of wear: (1) apical wear or spalling of teeth or breakage of tip suggesting large prey or abrasive food that may include bone or both, and enamel spalling present on the labial or lingual surface of the tooth in the form of a discrete ovoid or triangular facet that begins at the apex of the crown and extends basally; (2) macroscopic wear along the mesial and distal carinae of the teeth that extends from the apex and terminates at variable distance from the base or occasionally extending along the whole length of the carinae; (3) semi-circular macroscopic wear present at the base of the crown and formed during the final phase of occlusion when the apex of the opposing tooth comes into contact with the base of the crown.

In case of the premaxillary tooth of the Kachchh specimen, the apex is not broken but worn flat. There is another in-situ tooth in the premaxilla that shows a broken crown apex (Fig 6B). It is, however, difficult to assess whether this was a post-mortem breakage or the result of abrasion with hard prey as a few other teeth in the premaxilla have broken tips. Enamel spalling is present on the labial face close to the apex. Similarly, a longitudinal ovoidal spalling of the enamel begins at the apex and extends very close to the base of the crown. The longitudinal wear strip found in KGMV 0502 may in fact represent the early stage of apical spalling. However, Young et al. [72] have not observed the obliquely oriented longitudinal grooves of the studied premaxillary tooth on spalled enamel surfaces of *Dakosaurus*. In contrast, the wear surfaces on the mesial and distal carinae and the semi-circular wear facet at the base of the crown characteristic of marine metriorhynchid crocodiles are not present on the premaxillary tooth of KGMV 0501. Examination of mosasaur, plesiosaur and ichthyosaur skeletons housed at the AMNH by Young et al. [72] revealed apical spalling in many instances as in the Kachchh specimen, but no wear on the mesial and distal carinae was noticed [72].

According to the definition of Massare [71], the teeth from Kachchh with an acute but rounded and polished apex are similar to the morphology of smash and crunch guilds. Enamel spalling is caused by the impact between the tooth and prey (an unusually hard substance such as bone) in the same axis in which the jaw closes [73], or by breaking the prey items into smaller pieces. The robustness of the teeth preserved in the premaxilla and extensive enamel spalling on one of the surfaces indicates that the teeth were used to grasp a prey with hard exterior such as armoured fish, crustaceans, and thick-shelled ammonites as in the case of the crunch guild of Massare [52, 71]. Robust teeth with intense tooth wear, frequent apical tooth breakage and enamel spalling are generally observed in top-tier predators [69]. Therefore, the wear pattern observed in the premaxillary tooth from Kachchh, which has not been earlier reported in ichthyosaurs, indicates that the animal was feeding on a very hard, abrasive prey and might have been a top-tier predator.

## Palaeobiogeographic significance

Middle and Late Jurassic ichthyosaurs primarily represented by ophthalmosaurids have been widely documented from the western Tethys (England, France and Germany), the Boreal region (Russia, Norway) and North America [3]. However, prospecting for Mesozoic vertebrate faunas in Gondwanan continents in recent years has corrected this bias towards Laurasian continents to some extent. Many discoveries of ichthyosaur fossils from Argentina [7, 9, 14, 15, 17], Chile [74], Antarctica [21, 22], Madagascar [19] and New Zealand [20] have improved the Gondwanan fossil record.

The Jurassic ichthyosaurs from South America (Argentina and Chile) are shown to be closely related to those from the Tethys region [18, 74]. Based on the common occurrence of the same genera and species of marine invertebrates in both regions [75–79], teleost fishes [80], herpetofauna [81], as well as marine reptiles [7, 54, 82] it has been suggested that the Caribbean or Hispanic Corridor connecting the eastern Pacific Ocean with the western Tethys

through the Central Atlantic facilitated faunal dispersals between the two regions during the Late Jurassic [83–85].

However, a second dispersal route extending from Iraq-Kurdistan, East Africa, western India, Mozambique, Madagascar, and eastern Antarctica to the interconnected rift grabens (Rocas Verdes Basin) of southern Patagonia was also suggested based on the presence of similar bivalve, belemnite and ammonoid faunas in the Upper Jurassic rocks of these areas [76, 86]. The latter sea route has been designated as the Trans-Erythrean Seaway [87], Indo-Madagascan Seaway [88], South African Rocas Verdes Seaway [74], or Indo-Austral Seaway [85]. Currently, the timing of formation of this Trans-Gondwana Seaway is not well constrained. Though there is clear evidence for the prevalence of marine conditions in the early Middle Jurassic time from East Africa, Madagascar, and western India [89–94], Mozambique might have remained in contact with East Antarctica for a longer time, opening only in the Late Jurassic as evidenced by the formation of the first oceanic crust in the Mozambique Channel [95–97]. It has been proposed that this channel, which connected eastern Africa with the southern Andes along Antarctica, had been in existence since the Callovian, but became fully operational only from the Tithonian onwards [98]. Zverkov et al. [13] based on the common occurrence of *Arthropterygius* in Northern Europe, Argentina and Canada suggested that the southern seaway might have become operational by the Late Tithonian and Berriasian.

The Jurassic succession of the Kachchh Basin contains marine fauna that is very similar to that of Madagascar and therefore belongs to the Ethiopian or Indo-Madagascan faunal province. Based on the study of nautiloids, Halder [99] suggested that during the early stage of marine transgression Kachchh was an isolated basin promoting the evolution of endemic species. By the Late Bathonian, a two-way migration was possible between the Mediterranean Tethys and the Indo-Madagascan province. Finally, most species were common to both provinces in the Oxfordian and the Tethyan shallow shelf [100] was the primary migration route between these provinces.

In the Jurassic fauna of Kachchh, there are several examples of episodic faunal exchanges between the Indo-Madagascan and the Mediterranean provinces. These include the Callovian reineckeiids [101], *Indosphinctes*, Oxfordian *Larcheria* [102], Kimmeridgian *Nebrodites* and Late Kimmeridgian—Early Tithonian *Hybonoticeras* [103]. The appearance of ammonid genera characteristic of different palaeobiogeographic provinces, such as *Tithopeltoceras* and *Durangites* of the Mediterranean Province and *Himalayites* of the Mediterranean Tethys and Indo-Madagascan Province in the Late Tithonian fauna of Kachchh has been explained in terms of interprovincial migrations facilitated by high sea level [104–107]. Many of the ostracod taxa reported from the Callovian-Oxfordian Chari Formation and lower part of the Kimmeridgian Katrol Formation also demonstrate close affinities to those of Rajasthan (western India), Madagascar, Tanzania and central Saudi Arabia thus favouring faunal exchanges between the western Tethys and the Indo-Madagascan Province as early as in Oxfordian-Kimmeridgian time [108].

A two-way marine dispersal route between Kachchh and the Andes Basin via Madagascar and South Africa has also been visualized in view of the occurrence of *Corongoceras* cf. *C. lotenoense* in the Tithonian of Kachchh and *Virgatosphinctes*, *Blanfordiceras*, *Spiticeras* in the Andes [76, 106]. Similarly, *Megacucullaea*, a bivalve, considered to be endemic to the Indo-Madagascan Province, reached the Andes in the Late Jurassic [76, 104, 107].

Prior to the present ichthyosaur discovery, a cryptoclidid plesiosaur, a Middle-Late Jurassic plesiosaur widely known from western Europe, was documented from the Upper Jurassic Katrol Formation [30]. This marine reptile also supports the existence of faunal interchanges between the Indo-Madagascan and western Tethys provinces in the Late Jurassic (Kimmeridgian). Based on the temperature minimum recorded from the early Late Oxfordian of

Kachchh, it was suggested that the widening of the Trans-Gondwanan Seaway may have led to increased upwelling in the Malagasy Gulf and to a cooling recorded in the oxygen isotopes of belemnites and other marine invertebrates from Kachchh [38]. While describing an ophthalmosaurid ichthyosaur forefin and basioccipital from the Tithonian of Madagascar, Fernández [19] also indicated that this marine reptile find might support the southern Trans-Gondwana route. The present report of a partially preserved skeleton belonging to an ophthalmosaurid ichthyosaur underscores the fact that ichthyosaurs had a wide geographic distribution as previously suggested [109]. Further, the presence of ophthalmosaurid ichthyosaurs in the Upper Jurassic strata of western India, Madagascar, Argentina and Chile with close affinities to those of the western Tethys in addition to the reported presence of ichthyosaurs in the Jurassic of Antarctica [21, 22] supports the possible existence of a Trans-Gondwana dispersal route (Fig 14) as early as in the Kimmeridgian as suggested earlier on the basis of invertebrate fossils. Though the circuitous trans-Pacific migration route along the Caribbean Seaway for the dispersal of ophthalmosaurids from the western Tethys to Indo-Madagascan province is not impossible, the Trans-Gondwana route is the most parsimonious one in light of additional existing evidence from bivalves, cephalopods and plesiosaurs. A more clear picture on the southern biogeographic connections will emerge as and when the phylogenetic relationships of KGMV-0501 with the Upper Jurassic ophthalmosaurids is precisely established.

## Conclusions

The present ichthyosaur find represents the first nearly complete articulated skeleton of an ichthyosaur from India and the first record from the Jurassic of India. It further expands our knowledge on morphological diversity and geographic distribution of Late Jurassic ophthalmosaurids, their dietary habits and palaeobiogeography. At present, the specimen cannot be positively identified with known Jurassic ichthyosaur taxa from other parts of the world because of its encrustation in ferruginous rock matrix, which conceals much of the morphological information. In its dental characters and vertebral and forefin morphology, KGMV 0501 is referable to the ichthyosaur family Ophthalmosauridae. However, the currently available limited number of characters is inadequate to establish generic or species level relationships within the family. In general, the morphology of humerus and forefin indicate close similarities with *Ophthalmosaurus*, *Arthropterygius* and *Aegirosaurus*.

The preserved axial skeleton measures 3.6 m in length. If the partially preserved snout (36 cm), the missing posterior skull region and post-flexural tail are taken into account, the ichthyosaur from Kachchh may have had an estimated length of 5.0–5.5 m. In this respect, it may represent an adult animal that was comparatively large in size with respect to other Late Jurassic ichthyosaurs [7, 59]. Its state of preservation indicates that the animal landed on the sea floor vertically on its snout, while the rest of the body later fell on its side. The body has also been subjected to limited displacement and disarticulation following its deposition on the sediment surface possibly due to scavenging or reworking. The wear pattern on the teeth suggests that the animal was adapted for feeding on a hard and abrasive prey.

Although the taxonomic position of the Kachchh ichthyosaur within the family Ophthalmosauridae is unresolved at the moment, it represents one of the few ichthyosaur finds from the Jurassic of the least explored former Gondwanaland. It adds to the already known ichthyosaur discoveries of Argentina, Madagascar, New Zealand, Australia, Antarctica and Chile thereby improving the fossil record of this group of marine reptiles from the former Gondwanaland. The presence of ophthalmosaurid ichthyosaurs in the Upper Jurassic of India, Madagascar and South America implies that a marine seaway possibly connected the western Tethys

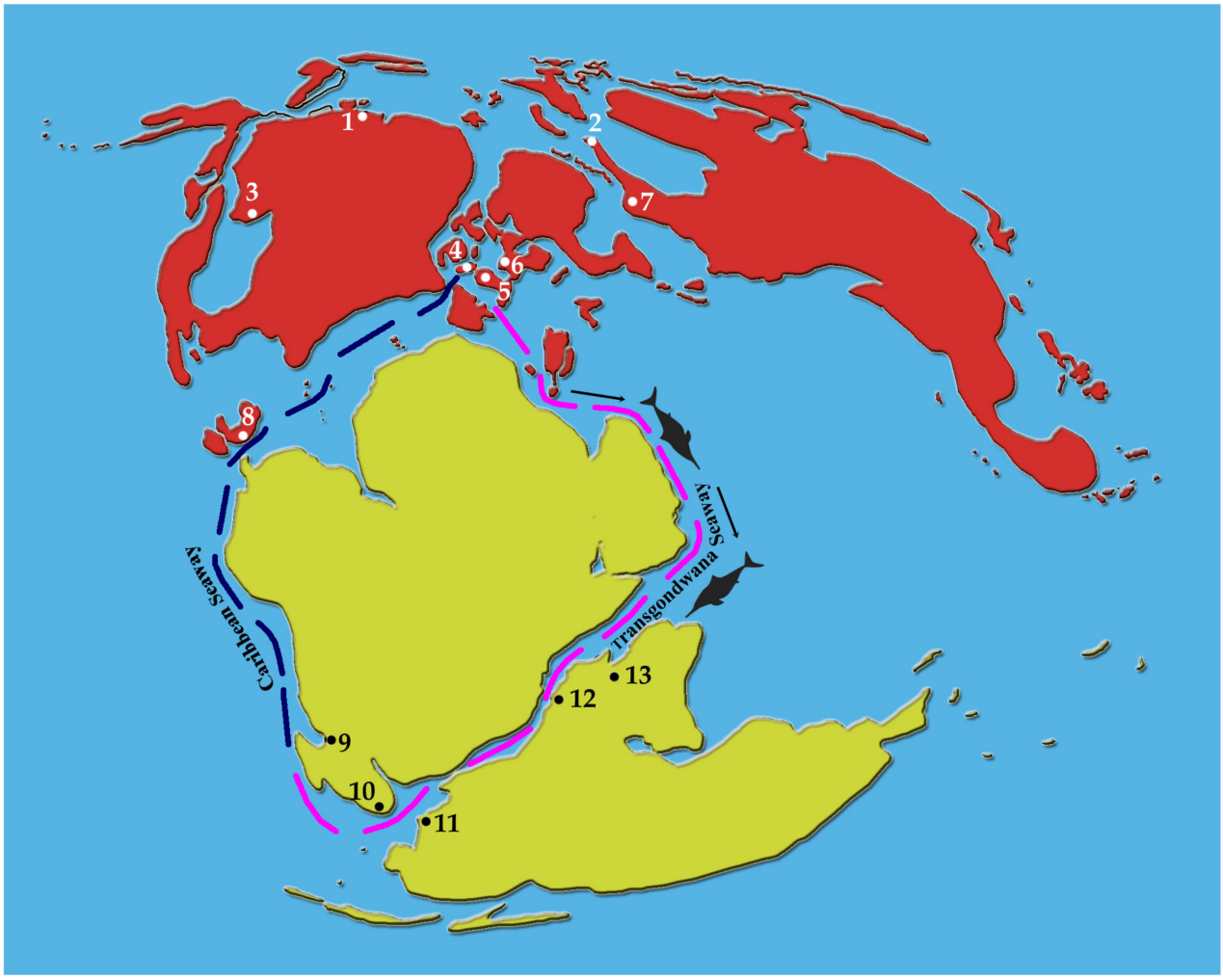


**Fig 14. Late Jurassic world palaeogeographic map showing the distribution of Middle and Late Jurassic ophthalmosaurids (adopted from fig 3 of Fernández [19]).** 1. Canada (*Arthropterygius*), 2. Norway (*Cryopterygius*, *Brachypterygius*, *Palvennia*, *Janusaurus*), 3. USA (*Ophthalmosaurus*), 4. England (*Ophthalmosaurus*, *Brachypterygius*, *Nannopterygius*), 5. Germany (*Aegirosaurus*), 6. Poland (*Cryopterygius*), 7. Russia (*Ophthalmosaurus*, *Brachypterygius*, *Arthropterygius*, *Undorosaurus*), 8. Mexico (*Ophthalmosaurus*, *Brachypterygius*), 9. Argentina (*Ophthalmosaurus*, *Caypullisaurus*, *Arthropterygius*), 10. Chile (Ophthalmosauridae indet.), 11. Antarctica (Ichthyosauria *incertae sedis*), 12. Madagascar (Ophthalmosauridae indet.), 13. India (Ophthalmosauridae indet.). The inferred sea route along which faunal interchanges may have taken place between the western Tethys and the southern Indian Ocean is shown in magenta colour.

https://doi.org/10.1371/journal.pone.0185851.g014

with South America via the Indian Ocean in the Late Jurassic facilitating faunal exchanges between Europe and Gondwanan continents. Identification of the Kachchh specimen below family level is crucial for understanding its phylogenetic relationships to contemporaneous taxa from the former Gondwanaland and Laurasia and consequent palaeobiogeographic connections. The articulated nature of the Kachchh ichthyosaur and the previous record of plesiosaur remains from the Kimmeridgian and Tithonian rocks of the Kachchh Mainland further indicates that focused research in remote areas of Kachchh may lead to more exciting finds in the future.

## Acknowledgments

We express our sincere thanks to Dean Lomax and two other anonymous reviewers for their critical and helpful comments on the manuscript. Thanks are also due to M.S. Thanglemmoi, Vaibhav Miglani and Raman Umamaheswaran for field assistance during the excavation of the skeleton and S.D. Biju, Sonali, L.Ranjit Singh, K. Deepak Singh, and Harsha Dhiman of Delhi University for their help in making the figures and formatting the text. We also acknowledge a number of graduate students from the Department of Earth and Environmental Science, KSKV Kachchh University, Bhuj, for their assistance during the field excavation. We also thank Marta S. Fernández for suggestions on the digits of the forefin.

## Author Contributions

**Conceptualization:** Guntupalli V. R. Prasad, Dhirendra K. Pandey, Matthias Alberti, Franz T. Fürsich.

**Data curation:** Guntupalli V. R. Prasad.

**Formal analysis:** Guntupalli V. R. Prasad.

**Funding acquisition:** Guntupalli V. R. Prasad.

**Investigation:** Guntupalli V. R. Prasad, Dhirendra K. Pandey, Matthias Alberti, Franz T. Fürsich.

**Methodology:** Guntupalli V. R. Prasad.

**Project administration:** Guntupalli V. R. Prasad, Dhirendra K. Pandey, Matthias Alberti, Franz T. Fürsich, Mahesh G. Thakkar, Gaurav D. Chauhan.

**Resources:** Guntupalli V. R. Prasad, Matthias Alberti.

**Supervision:** Guntupalli V. R. Prasad, Dhirendra K. Pandey, Matthias Alberti, Franz T. Fürsich, Mahesh G. Thakkar, Gaurav D. Chauhan.

**Validation:** Guntupalli V. R. Prasad.

**Visualization:** Guntupalli V. R. Prasad, Dhirendra K. Pandey, Matthias Alberti, Franz T. Fürsich.

**Writing – original draft:** Guntupalli V. R. Prasad.

**Writing – review & editing:** Guntupalli V. R. Prasad, Dhirendra K. Pandey, Matthias Alberti, Franz T. Fürsich, Mahesh G. Thakkar.

## References

1. Fischer V, Bardet N, Benson RBJ, Arkangelsky MS, Friedman M. Extinction of fish-shaped marine reptiles associated with reduced evolutionary rates and global environmental volatility. Nature Communications. 2016; 7:10825/ https://doi.org/10.1038/ncomms10825/www.nature.com/naturecommunications. PMID: 26953824
2. Ji C, Jiang D-Y, Motani R, Rieppel O, Hao W-C, Sun Z-Y. Phylogeny of the Ichthyopterygia incorporating recent discoveries from South China. Journal of Vertebrate Paleontology. 2015.
3. McGowan C, Motani R. Part 8. Ichthyopterygia. In: Sues H-D, editor. Handbook of Paleoherpetology. München: Verlag Dr. Friedrich Pfeil; 2003. pp. 1–175.
4. Thorne PM, Ruta M, Benton MJ. Resetting the evolution of marine reptiles at the Triassic-Jurassic boundary. PNAS. 2011; 20:8339–8344.
5. Fernández MS. Ophthalmosauria (Ichthyosauria) forefin from the Aalenian-Bajocian boundary of Mendoza province, Argentina. Journal of Vertebrate Paleontology. 2003; 23:691–694.

6. Fischer V, Appleby RM, Naish D, Liston J, Riding JB, Brindley S, et al. A basal thunnosaurian from Iraq reveals disparate phylogenetic origins for Cretaceous ichthysaurs. Biology Letters. 2013; 9: 20130021. http://dx.doi.org/10.1098/rsbl.2013.0021. PMID: 23676653
7. Fernández MS. A new ichthyosaur from the Tithonian (Late Jurassic) of the Neuquén Basin, northwestern Patagonia, Argentina. Journal of Paleontology. 1997a; 71:479–484.
8. Fernández MS. Redescription and phylogenetic position of Caypullisaurus (Ichthyosauria: Ophthalmosauridae). Journal of Paleontology. 2007; 81:677–681.
9. Fernández MS, Maxwell EE. The genus *Arthropterygius* Maxwell (Icthyosauria: Ophthalmosauridae) in the Late Jurassic of the Neuquén Basin, Argentina. Geobios. 2012; 45:535–540.
10. Maxwell EE. Generic reassignment of an ichthyosaur from the Queen Elizabeth Islands, Northwest Territories, Canada. Journal of Vertebrate Paleontology. 2010; 30:403–415.
11. Druckenmiller PS, Hurum JH, Knutsen EM, Nakrem HA. Two new ophthalmosaurids (Reptilia: Ichthyosauria) from the Agardhfjellet Formation (Late Jurassic: Volgian/Tithonian), Svalbard, Norway. Norwegian Journal of Geology. 2012; 92:311–339.
12. Roberts AJ, Druckenmiller PS, Saetre GP, Hurum JH. A new Upper Jurassic ophthalmosaurid ichthyosaur from the Slottsmøya Member, Agardhfjellet Formation of Central Spitsbergen. PLoS ONE. 2014; 9(8): e103152. https://doi.org/10.1371/journal.pone.0103152 PMID: 25084533
13. Zverkov NG, Arkhangelsky MS, Pardo-Pérez JM, Beznosov PA. On the Upper Jurassic ichthyosaur remains from the Russian North. Proceedings of the Zoological Institute RAS. 2015; 319(1):558–588.
14. Fernández MS. A new long snouted ichthyosaur from the early Bajocian of Neuquén Basin (Argentina). Ameghiniana. 1994; 31:291–297.
15. Fernández MS. A new ichthyosaur from the Los Molles Formation (Early Bajocian), Neuquén basin, Argentina. Journal of Paleontology. 1999; 73:677–681.
16. Fernández MS. Late Jurassic ichthyosaurs from the Neuquén Basin, Argentina. Historical Biology. 2000; 14:133–136.
17. Fernández MS, Talevi M. Ophthalmosaurian (Ichthyosauria) records from the Aalenian—Bajocian of Patagonia (Argentina): an overview. Geological Magazine. 2014; 151:49–59.
18. Pardo-Peréz J, Frey E, Stinnesbeck W, Fernández MS, Rivas L, Salazar C, et al. An ichthyosaurian forefin from the Lower Cretaceous Zapata Formation of southern Chile: Implications for morphological variability within *Platypterygius*. Palaeobiodiversity and Palaeoenvironments. 2012; 92:287–294.
19. Fernández MS. On the paleogeographical distribution of the Callovian and Late Jurassic ichthyosaurs. Journal of Vertebrate Paleontology. 1997b; 17: 752–754.
20. Zammit M. Australasia's first Jurassic ichthyosaur fossil: an isolated vertebra from the Lower Jurassic Arataura Formation of North Island, New Zealand. Alcheringa. 2011; 35(3):341–343.
21. Whitham AG, Doyle P. Stratigraphy of the Upper Jurassic Lower Cretaceous Nordenskjöld Formation of eastern Graham Land, Antarctica. Journal of South American Earth Sciences. 1989; 2(4):371–384.
22. Hikuroa DCH. Second Jurassic marine reptile from the Antarctic Peninsula. Antarctic Science. 2009; 21(2):169–170.
23. Lydekker R. Fossil Reptilia and Batrichia. Palaeontological Indica Series.Palaeontologica Indica Series. 1879; IV(1): 1–36.
24. Lydekker R. Note on the classification of the Ichthyopterygia with a notice of two new species. Geological Magazine 3rd Series. 1888; 5:309–314.
25. Underwood CJ. Goswami A, Prasad GVR, Verma O, Flynn JJ. Marine vertebrates from the 'mid' Cretaceous (early Cenomanian) of South India. Journal of Vertebrate Paleontology. 2011; 31:539–552.
26. Ayyasami K, Elamparuthi S, Gowtham B. An ichthyosaur vertebra from the Cretaceous (Middle Cenomanian) Karai Formation, southern India. Journal Geological Society of India. 2016; 87:706–708.
27. Zammit M. Cretaceous ichthyosaurs: Dwindling diversity, or the empire strikes back? Geosciences. 2012; 2:11–24.
28. Fischer V. Taxonomy of Platypterygius campylodon and the diversity of the last ichthyosaurs. PeerJ; 2016 4:e2604. https://doi.org/10.7717/peerj.2604 PMID: 27781178
29. Verma KK, Satsangi PP, Srivastava S, Mehra S. On a plesiosaurian vertebra from the upper Gondwanas of Kutch, Gujarat, India. In: Laskar B, Raja Rao CS, editors. Fourth International Gondwana Symposium, Proceedings and Papers (India 1977). Calcutta: 1979. pp. 217–220.
30. Bardet N, Mazin JM, Cariou E, Enay R, Krishna J. Les Plesiosauria du Jurassique supérieur de la province de Kachchh (Inde). Comptes Rendus de l'Académie des Sciences de Paris 313, 1991; Série.II:1343–1347.

31. Lydekker R. Notices of new and other Vertebrata from Indian Tertiary and Secondary rocks. Records of the Geological Survey of India. 1877; 10:41.

32. Phansalkar VG, Sudha G, Kadkikar AS. Giant marine reptilian skulls from the Jurassic of Kachchh, Gujarat. Current Science. 1994; 67(6): 460–461.

33. Biswas SK. Stratigraphy and sedimentary evolution of the Mesozoic basin of Kutch, Western India. In: Tandon SK, Pant CC, Casshyap SM, editors. Stratigraphy and sedimentary evolution of western India. Nainital: Gyanodaya Publications; 1991. pp.74–103.

34. Wynne AB. Memoir of the geology of Kutch to accompany the map compiled by A.B. Wynne and F. Fedden during the seasons of 1867–68 and 1868–69. Memoirs of the Geological Survey of India. 1872; 9(1):1–293.

35. Waagen W. The Jurassic fauna of Cutch. Memoirs of the Geological Survey of India, Palaeontologia Indica. 1873–1875; 9:1–247.

36. Fürsich FT, Singh IB, Joachimski M, Krumm S, Schlirf M, Schlirf S. Palaeoclimate reconstructions of the Middle Jurassic of Kachchh (western India): an integrated approach based on palaeoecological, oxygen isotopic, and clay mineralogical data. Palaeogeography, Palaeoclimatology, Palaeoecology. 2005; 217:289–309.

37. Fürsich FT. Environmental distribution of trace fossils in the Jurassic of Kachchh (western India). Facies. 1998; 39:243–272.

38. Alberti M, Fürsich FT, Pandey DK. The Oxfordian isotope record ($\delta^{18}O$, $\delta^{13}C$) of belemnites, brachiopods, and oysters from the Kachchh Basin (western India) and its potential for palaeoecologic, palaeoclimatic and palaeogeographic reconstructions. Palaeogeography, Palaeoclimatology, Palaeoecology. 2012; 344–345:49–68.

39. Fürsich FT, Alberti M, Pandey DK. Stratigraphy and palaeoenvironments of the Jurassic rocks of Kachchh—Field Guide. Beringeria. 2013; 7:1–174. 28.

40. Krishna J, Pathak DB, Pandey B. Quantum refinement in the Kimmeridgian ammonoid chronology in Kachchh (India). GeoResearch Forum. 1996; 1–2: 195–204.

41. Krishna J, Pandey B, Ojha JR. *Gregoryceras* in the Oxfordian of Kachchh (India): diverse eventful implications. Geobios. 2009; 42:197–208.

42. Martill DM. Soupy substrates: a medium for the exceptional preservation of ichthyosaurs of the Posidonia Shale (Lower Jurassic) of Germany. Kaupia. 1993; 2:77–97.

43. Delsett LL, Roberts AJ, Druckenmiller PS, Hurum JH. A new ophthalmosaurid (Ichthyosauria) from Svalbard, Norway, and evolution of the ichthyopterygian pelvic girdle. PLoS ONE. 2017; 12(1): e0169971. https://doi.org/10.1371/journal.pone.0169971 PMID: 28121995

44. Sollas WJ. The skull of *Ichthyosaurus* studied in serial sections. Philosophical Transactions of the Royal Society of London. 1916; Series B 208: 62–126.

45. Kirton AM. A review of British Upper Jurassic ichthyosaurs. Ph.D. Thesis, University of Newcastle upon Tyne. 1983. 239 p. http://ethos.bl.uk/OrderDetails.do?uin=uk.bl.ethos.344855.

46. Motani R. On the evolution and homology of ichthyosaurian forefins. Journal of Vertebrate Paleontology. 1999a; 19:28–41.

47. Maisch MW, Matzke AT. The Ichthyosauria. Stuttgarter Beiträge zur Naturkunde, Serie B. 2000; 298:1–159.

48. Sander PM. Ichthyosauria: their diversity, distribution, and phylogeny. Paläontologische Zeitschrift. 2000; 74:1–35.

49. Druckenmiller PS, Maxwell EE. A new lower Cretaceous (lower Albian) ichthyosaur genus from the Clearwater Formation, Alberta, Canada. Canadian Journal of Earth Sciences. 2010; 47:1037–1053.

50. Maisch MW. Phylogeny, systematics, and origin of the Ichthyosauria—the state of the art. Palaeodiversity. 2010; 3:151–214. 66.

51. Motani R. Phylogeny of the Ichthyopterygia. Journal of Vertebrate Paleontology. 1999b; 19: 473–496.

52. Fischer V, Clément A, Guiomar M, Godefroit P. The first definite record of a Valanginian ichthyosaur and its implication for the evolution of post-Liassic Ichthyosauria. Cretaceous Research. 2011b; 32:155–163.

53. Fernández MS, Campos L. Ophthalmosaurids (Ichthyosauria: Thunnosauiria): Alpha taxonomy, clades and names. In: Fernández M, Herrera Y, editors. Reptiles Extinctos—Volumen en Homenaje a Zulma Gasparini. Publicacion Electronica de la Asociacion Paleontologica Argentina. 2015; 15(1):20–30.

54. Buchy MC. First record of *Ophthalmosaurus* (Reptilian: Ichthyosauria) from the Tithonian (Upper Jurassic) of Mexico. Journal of Paleontology. 2010; 84(1):149–155.

55. Tyborowski D. A new ophthalmosaurid ichthyosaur from the Late Jurassic of Owadów-Brzezinki Quarry, Poland. Acta Palaeontologica Polonica. 2016; 61(4): 791–803

56. Efimov VM. A new family of ichthyosaurs, the Undorosauridae fam. nov. from the Volgian stage of the European part of Russia. Paleontological Journal. 1999; 33(2):174–181.

57. Arkhangelsky MS, Zverkov NG. On a new ichthyosaur of the genus *Undorosaurus*. Proceedings of the Zoological Institute. 2014; 318(3): 187–196.

58. Wagner A. Beschreibung einer fossilen Schildkröte und etlicher anderer Reptilien-Ueberreste aus den lithographischen Schiefern und dem Gründsandsteine von Kelheim. Abhandlungen der Mathematische-Physikalischen Classe der königlich bayerischen Akademie der Wissenschaften. 1853; 7 (1):239–264.

59. Bardet N, Fernández MS. A new ichthyosaur from the Upper Jurassic Lithographic Limestones of Bavaria. Journal of Paleontology. 2000; 74(3): 503–511.

60. Hulke JW. Note on an Ichthyosaurus (I. enthekiodon) from Kimmeridge Bay, Dorset. Quarterly Journal of the Geological Society of London. 1871; 27:440–441.

61. Boulenger GA. On a new species of ichthyosaur from Bath. Proceedings of the Zoological Society of London. 1904; 1904(1):424–426.

62. Russell DA. Jurassic marine reptiles from Cape Grassy, Melville Island, Arctic Canada. The Geology of Melville Island, Arctic Canada. Geological Survey of Canada Bulletin. 1993; 450:195–201.

63. Marsh OC. A new order of extinct reptiles (Sauranodonta) from the Jurassic Formation of the Rocky Mountains. American Journal of Science. 1879; Series 3(17):85–86.

64. Seeley HG. On the pectoral arch and forelimb of *Ophthalmosaurus*, a new ichthyosaurian genus from the Oxford Clay. Quartely Journal of the Geological Society of London. 1874; 30:699–707.

65. Bardet N. Dental cross-sections in Cretaceous Ichthyopterygia: Systematic implications. Geobios. 1990; 23:169–172.

66. Maxwell EE, Caldwell MW. Evidence for a second species of the ichthyosaur Platypterygius in North America: a new record from the Loon River Formation (Lower Cretaceous) of northwestern Canada. Canadian Journal of Earth Sciences. 2006; 43:1291–1295.

67. Fischer V, Maisch MW, Naish D, Liston J, Kosma R, Joger U, et al.New ophthalmosaurid ichthyosaurs from the Early Cretaceous of Europe demonstrate extensive ichthyosaur survival across the Jurassic—Cretaceous boundary. PLoS ONE. 2012; 7(1):e29234. https://doi.org/10.1371/journal.pone.0029234 PMID: 22235274

68. Fischer V, Masure E, Arkhangelsky MS, Godefroit P. A new Barremian (Early Cretaceous) ichthyosaur from western Russia. Journal of Vertebrate Paleontology. 2011a; 31:1010–1025.

69. Fischer V, Bardet N, Guiomar M, Godefroit P. High diversity in Cretaceous ichthyosaurs from Europe prior to their extinction. PLoS ONE. 2014; 9(1):e84709. https://doi.org/10.1371/journal.pone.0084709 PMID: 24465427

70. Lomax DR. A new leptonectid ichthyosaur from the Lower Jurassic (Hettangian) of Nottinghamshire, England, UK, and the taxonomic usefulness of the ichthyosaurian coracoid. Journal of Systematic Palaeontology. 2016; http://dx.doi.org/10.1080/14772019.2016.1183149.

71. Massare JA. Tooth morphology and prey preference of Mesozoic marine reptiles. Journal of Vertebrate Paleontology. 1987; 7:121–137.

72. Young MT, Brusatte SL, Beatty BL, Andrade MB, Desojo JB. Tooth-on-tooth interlocking occlusion suggests macrophagy in the Mesozoic marine crocodylomorph *Dakosaurus*. The Anatomical Records. 2012; 295:1147–1158.

73. Schubert BW, Ungar PS. Wear facets and enamel spalling in tyrannosaurid dinosaurs. Acta Palaeontologica Polonica. 2005; 50:93–99.

74. Shultz MR, Fildani A, Suarez M. Occurrence of the Southernmost South American Ichthyosaur (Middle Jurassic—Lower Cretaceous), Parque Nacional Torres del Paine, Patagonia, Southernmost Chile. Palaios. 2003; 18:67–73.

75. Hallam A. Early and Mid-Jurassic molluscan biogeography and the establishment of the central Atlantic seaway. Palaeogeography, Palaeoclimatology, Palaeoecology. 1983; 43:181–193.

76. Riccardi AC. Jurassic and Cretaceous marine connections between the Southeast Pacific and Tethys. Palaeogeography, Palaeoclimatology, Palaeoecology. 1991; 87:155–189.

77. Ballent SC, Whatley R. The distribution of the Mesozoic ostracod genus Procytherura Whatley, palaeogeographical implications with special reference to Argentina. Alcheringa. 2000; 24:229–242.

78. Aberhan M. Bivalve palaeobiogeography and the Hispanic Corridor: time of opening and the effectiveness of a proto-Atlantic seaway. Palaeogeography, Palaeoclimatology, Palaeoecology. 2001; 165:375–394.

79. Damborenea SE. Hispanic Corridor: Its evolution and the biogeography of bivalve molluscs. GeoResearch Forum. 2000; 6:369–380.

80. Arratia G. The Jurassic and the early history of the teleosts. In: Arratia G, Viohl G, editors. Mesozoic Fishes—Systematics and Paleoecology. München: Verlag Dr. Friedrich Pfeil; 1996. pp. 243–259.

81. Gasparini Z. Marine Reptiles of the circum-Pacific region. In: Westermann G, editor. The Jurassic of the Circum-Pacific. Cambridge: Cambridge University Press, World and Regional Geological Series; 1992. pp. 361–364.

82. Fernández MS, Iturrade-Vinent M. An Oxfordian Ichthyosauria (Reptilia) from Viñales, Western Cuba: Paleobiogeographic significance. Journal of Vertebrate Paleontology. 2000; 20(1):191–193.

83. Gasparini Z. A new Oxfordian pliosaurid (Plesiosauria, Pliosauridae) in the Caribbean Seaway. Palaeontology. 2009; 52:661–669.

84. Gasparini Z, Fernández M, de la Fuente M, Salgado L. Reptiles marinos jurásicos y cretácicos de la Patagonia argentina: Su aporte al conocimiento de la herpetofauna mesozoica. Asociación Paleontológica Argentina Publicación Especial. 2007; 11:125–136.

85. Salazar C. The Jurassic-Cretaceous boundary (Tithonian—Hauterivian) in the Andean Basin of central Chile: Ammonites, bio- and sequence stratigraphy and palaeobiogeography. Heidelberg: Ruprecht-Karls Universität; 2012. 388 p.

86. Leanza HA. The Tithonian ammonite genus Chigaroceras Howarth (1992) as a bioevent marker between Iraq and Argentina. GeoResearch Forum. 1996; 1–2:451–458.

87. Arkell WJ. Jurassic Geology of the World. Edinburgh: Oliver and Boyd, 1956. 806 p.

88. Cecca F. Palaeobiogeography of Tethyan ammonites during the Tithonian (latest Jurassic). Palaeogeography, Palaeoclimatology, Palaeoecology. 1999; 147:1–37.

89. Pandey DK, Fürsich FT. Bajocian (Middle Jurassic) Age of the Lower Jaisalmer Formation of Rajasthan, western India. Newsletters on Stratigraphy. 1994; 30:75–81. 36.38. 39.41.

90. Förster R. The geological history of the sedimentary basin of southern Mozambique, and some aspects of the origin of the Mozambique Channel. Palaeogeography, Palaeoclimatology, Palaeoecology. 1975; 17:267–287.

91. Singh CSP, Jaitly AK, Pandey DK. First report of some Bajocian—Bathonian (Middle Jurassic) ammonoids and the age of oldest sediments from Kachchh, W. India. Newsletters on Stratigraphy. 1982; 11 (1):37–40.

92. Krishna J. An overview of the Mesozoic stratigraphy of Kachchh and Jaisalmer basins. Journal of the Palaeontological Society of India. 1987; 32:136–49.

93. Ali Kassim M, Carmignani L, Conti P, Fantozzi PL. Geology of the Mesozoic—Tertiary sedimentary basins in southwestern Somalia. Journal of African Earth Sciences. 2002; 34:3–20.

94. Geiger M, Clark DN, Mette W. Reappraisal of the timing of the breakup of Gondwana based on sedimentological and seismic evidence from the Morondava Basin, Madagascar. Journal of African Earth Sciences; 2004; 38:363–381.

95. Rabinowitz PD, Coffin MF, Falvey D. The separation of Madagascar and Africa. Science. 1983; 220:67–69. https://doi.org/10.1126/science.220.4592.67 PMID: 17736163

96. Veevers JJ. Gondwanaland from 650–500 Ma assembly through 320 Ma merger in Pangea to 185–100 Ma breakup: supercontinental tectonics via stratigraphy and radiometric dating. Earth-Science Reviews. 2004; 68:1–132.

97. Martin AK. Gondwana break-up via double-saloon-door rifting and seafloor spreading in a backarc basin during subduction rollback. Tectonophysics. 2007; 445:245–272.

98. Enay R. Paleobiogeographie des Ammonites des Jurassique Terminal (Tithonique/Volgien/Portlandien S.L.) et Mobilite Continentale. Geobios. 1972; 5(4): 355–407.

99. Halder K. Diversity and biogeographic distribution of Jurassic nautiloids of Kutch, India, during the fragmentation of Gondwana. Journal of African Earth Sciences. 2000; 311:175–185.

100. Cairou E. Ammonites of the Callovian and Oxfordian. In: Hallam A, editor. Atlas of Palaeobiogeography. Amsterdam: Elsevier; 1973. pp. 287–295.

101. Cairou E, Krishna J. The Tethyan Reineckeiinae of Kachchh and Jaisalmer (West India): Systematic biostratigraphic and biogeographic implications. Palaeontographica A. 1988; 203:149–170.

102. Krishna J, Melendez G, Pandey B, Pathak DB. Characterization of the ammonite genus Larcheria (Middle Oxfordian) in Kachchh (India): Paleontology, biostratigraphic and paleobiogeographic evaluation in context of north Tethyan occurrences. Comptes Rendus de l'Académie des Sciences de Paris. 1995; 321(2a):1187–1193.

103. Krishna J, Pathak DB. Late Lower Kimmeridgian—Lower Tithonian virgatosphinctins of India: Evolutionary succession and biogeographic implications. Geobios. 1993; 15:227–238.

**104.** Shome S, De S, Roy P, Bardhan S, Das SS. Ammonites as biological stopwatch and biogeographical blackbox—a case study from the Jurassic-Cretaceous boundary (150 Ma) of Kutch, Gujarat. Current Science. 2004; 86(1):197–202.

**105.** Shome S, Bardhan S, De S. Record of *Tithopeltoceras* (Ammonoidea) from the Tithonian of Kutch, India and its stratigraphic and paleobiogeographic significance. Journal of Paleontology. 2005; 79(3): 619–624.

**106.** Bardhan S, Shome S, Roy P. Biogeography of Kutch ammonites during the Latest Jurassic (Tithonian) and a global paleobiogeographic overview. In: Landman NH, Davis RA, Mapes RH, editors. Cephalopod Present and Past: New Insights and Perspectives. Dordrecht: Springer; 2007. pp. 375–395.

**107.** Shome S, Bardhan S. A new Late Tithonian ammonite assemblage from Kutch, Western India. Journal of the Palaeontological Society of India. 2009; 54(1):1–18.

**108.** Khosla SC, Jakhar SR, Mohammed MH. Ostracodes from the Jurassic beds of Habo Hill, Kachchh, Gujarat, India. Micropaleontology. 1997; 43(1):1–39.

**109.** McGowan C. Further evidence for the wide geographical distribution of ichthyosaur taxa (Reptilia: Ichthyosauria). Journal of Paleontology. 1978; 52:1155–1162.

Planetary and Space Science 240 (2024) 105826

Contents lists available at ScienceDirect

Planetary and Space Science

journal homepage: www.elsevier.com/locate/pss

# The Luna structure, India: A probable impact crater formed by an iron bolide

K.S. Sajinkumar [a,*,1], S. James [a,1], G.K. Indu [a,b], Saranya R. Chandran [a], Devika Padmakumar [a], J. Aswathi [a], S. Keerthy [a], M.N. Praveen [c], N. Sorcar [d], J.K. Tomson [d], Anil Chavan [e,f], Subhash Bhandari [e], M. Satyanarayanan [g], R. Bhushan [f], A. Dabhi [f], Y. Anilkumar [a]

[a] Department of Geology, University of Kerala, Thiruvananthapuram, 695 581, Kerala, India
[b] University College, Thiruvananthapuram, 695 031, Kerala, India
[c] Geological Survey of India, Bengaluru, 560 111, India
[d] National Centre for Earth Science Studies, Thiruvananthapuram, 695 011, Kerala, India
[e] Department of Earth and Environmental Science, K.S.K.V. Kachchh University, Bhuj, 370 001, India
[f] Physical Research Laboratory, Navrangpura, Ahmedabad, 380 009, India
[g] CSIR-National Geophysical Research Institute, Hyderabad, 500 007, India

ARTICLE INFO

*Keywords:*
Luna
Meteorite impact crater
Iron bolide
Ejecta field
Radiocarbon dating

ABSTRACT

The Luna structure of India has been rumored to be an impact crater for more than a decade without any convincing evidence. This structure (1.5–1.8 km) is prominently visible in the low-lying Banni Plains of the tectonically active Kutch Basin as a circular morphological feature with a less-prominent rim. Luna area is strewn with melt-like rocks having high specific gravity and displaying wide range of magnetic properties. It contains minerals like wüstite, kirschsteinite, ulvöspinel, hercynite, and fayalite. The whole rock analysis denotes PGE enrichment, with notably higher average concentrations of Ru (19.02 ppb), Rh (5.68 ppb), Pd (8.64 ppb), Os (6.03 ppb), Ir (10.63 ppb) and Pt (18.31 ppb). The target is not exposed at Luna, owing to the overlying thick sequence of Quaternary sediments. The mineralogical and geochemical signatures points to an impact into a target, which is rich in clay with elevated calcium and silica (sand/silt) content. Geochemical data suggests an iron or stony-iron meteorite as the potential projectile at Luna. The silt layer containing plant remnants, underlying the strewn layer, yielded a radiocarbon age of 6905 years, making Luna the biggest crater to result from an iron bolide within the last 10,000 years.

## 1. Introduction

Impact cratering, a fundamental process of the Solar System, is innately tied to the modification of planetary and satellite surfaces (Shoemaker, 1983; Melosh, 1989; French, 1998; Osinski and Pierazzo, 2013). The process led to the formation of hundreds of thousands impact craters across planetary bodies. A large number of craters could have been expected on Earth today, if not for the active plate tectonics and geomorphic processes (Grieve, 1987, 2001; Gottwald et al., 2020; Schmieder and Kring, 2020). However, majority of the impact craters expected across the oceanic crust (younger than 280 Ma) remains unexposed (James et al., 2022a). In addition, the inaccessibility of polar regions considerably limits the crater discoveries, although new craters are uncovered by intense exploration like the Hiawatha glacier of Greenland (cf. Kjær et al., 2018). Similarly, the relatively lesser advanced state of crater studies in Asia, Africa, and South America further hindered crater identification in these regions. Currently, Earth preserves only 201 impact craters (Osinski et al., 2022). It is now known that impact cratering has played an important role through solar system history, such as the formation of Moon (Canup and Asphaug, 2001; Daly, 1946), the evolution of primitive crust (Maruyama and Santosh, 2017; Santosh et al., 2017), ocean vaporization events (Zahnle and Sleep, 1996; Svetsov, 2005), emplacement of large igneous provinces (Osinski et al., 2018, 2022), genesis of economic mineral and hydrocarbon resources (Grieve, 2005; Reimold et al., 2005; James et al., 2022b), mass extinctions (Grieve and Kring, 2007; Osinski et al., 2022), and

* Corresponding author.
*E-mail address:* sajinks@keralauniversity.ac.in (K.S. Sajinkumar).
[1] These authors contributed equally to this work.

https://doi.org/10.1016/j.pss.2023.105826
Received 1 April 2023; Received in revised form 17 November 2023; Accepted 1 December 2023
Available online 6 December 2023
0032-0633/© 2023 Elsevier Ltd. All rights reserved.

large-scale environmental and climatic changes (e.g. Chicxulub Impact Event) (Schulte et al., 2010; Scotese et al., 2021; James et al., 2023) among others. Hitherto, terrestrial impact craters continue to be the research hotspots for geologists and planetary scientists. Osinski et al. (2022) has comprehensively detailed the surge in the number of confirmed impact craters since 1960s following the discovery of shock features. Over the past decade, several structures have been confirmed as impact craters like Jeokjung-Chogye Basin (Lim et al., 2021), Yallalie (Cox et al., 2019) and Summanen (Plado et al., 2018), while promising structures are still being investigated.

In this study, we introduce the Luna structure (23°42′16″ N; 69°15′35′E) with 1.5–1.8 km diameter, as a potential hypervelocity impact crater (Fig. 1). The structure remains submerged (and inaccessible) for a greater part of the year owing to its presence in the low-lying Banni Plains of the Kutch Basin of western India. Interestingly, the Luna region was one amongst the several settlements linked to the ancient Harappan Civilization (7000-1900 BP) (Possehl, 2002; Makwana et al., 2021). The impact origin of the structure was suspected by Karanth (2006), though no convincing evidence of impact was provided except for the mere mention of the presence of stishovite and coesite from erratic samples collected from the vicinity of Luna. Although some other works have also hinted at impact origin of the Luna structure (Chavan et al., 2022; Indu et al., 2022), but none have provided convincing evidence. Hence, the quest for unravelling the Luna structure was initiated. We present strong petrographic, mineralogical, and geochemical evidence to confirm the impact origin of Luna structure, along with an age estimate. The confirmation of the Lunar structure will not only increase the count of craters known in India (other Indian craters being Dhala, Ramgarh, Lonar (cf. Osinski et al., 2022; Li et al., 2018; Keerthy et al., 2019; Chandran et al., 2022, 2023; Aneeshkumar et al., 2022)), but it will also motivate impact crater and planetary science studies in India.

## 2. Luna geomorphology and regional geology

The Luna structure is carved on the salt marshes of the active Kutch Basin. The Luna structure is composed of a crater rim and floor (Fig. 2a and b). The structure has an E-W diameter of 1.5 km and N–S diameter of 1.8 km. The crater rim has an elevation of 6 m (above mean sea level (AMSL)) in the east and 7 m in the west. The crater floor is at 0.5 m AMSL. As the surrounding Banni Plains have an elevation of 2.5–3.5 AMSL, the crater rim is at an average elevation of 3.5 m above the surrounding plains (Fig. 2c). Despite this, the crater is frequently flooded, and hence, remains inaccessible owing to the unique regional geomorphology of the surroundings. The crater floor is covered by thick Quaternary sediment blanket underlain by Tertiary sedimentary rocks. The sediments at the crater floor manifest as mud cracks due to desiccation during the drier summer months.

The rifted Kutch Basin, sandwiched between the North Kathiawar Fault and the Nagar Parkar faults, is an active depositional area (Biswas, 2016a). Studies suggest that the sediments were deposited during the early, syn, and post-rift stages of basin formation (Desai and Biswas, 2018). The initial rifting episode during Jurassic led to the development of E-W trending extensional faults in the Neoproterozoic basement (Biswas, 2016a, 2016b; Desai and Biswas, 2018). The rift infilling during the Mesozoic is comprised of fossil-rich felsic sediments (Biswas, 2016a). During 66-65 Ma, the Indian Plate drifted over the Reunion Hotspot, and the emplacement of Deccan flood basalts occurred as the terminal lithological units of the Mesozoic (Pillai et al., 2017). The Paleogene-Neogene transgressive sedimentary sequences were deposited over Deccan basalts in the post-rift sag basin (Biswas, 2016a). During Quaternary, the basin experienced hinterland sedimentation in Banni Plains and Rann (both half-grabens) (Roy and Merh, 1982; Ngangom et al., 2017; Kumar et al., 2021; Dabhi et al., 2022a, 2022b). It is in the Banni plains, an extremely low-lying (3–12 AMSL; Maurya et al., 2016) flat terrain, composed of unconsolidated soft sediments that the Luna structure is situated. The Banni Plains constitute Quaternary clay and silt-dominated sediments, indicative of fluvio-marine conditions (Sant et al., 2017; Singh and Kar, 2001). The sediments at the Banni Plains are clayey silt (increased terrestrial input post 1.9 ka) and clay (marine deposition post 9.3 ka, peaked at 6.0-2.0 ka marine transgression) (Sant et al., 2017; Singh and Kar, 2001). The diverse clay varieties noted at Banni Plains ascertain it as an active depocenter. The Banni Plains are dominated by smectite, derived from the Deccan Volcanic Province; illite and chlorite from the Himalayan sediments and kaolinite from the Kutch Mainland Hills (Sant et al., 2017).

## 3. Methodology

### 3.1. Field investigation and surface sampling

Field investigations were carried in three different phases between 2019 and 2022, coinciding with the dry conditions at Luna. Even in the driest conditions, when significant crater floor was exposed, the thick Quaternary sediments within the structure acted as hindrance for

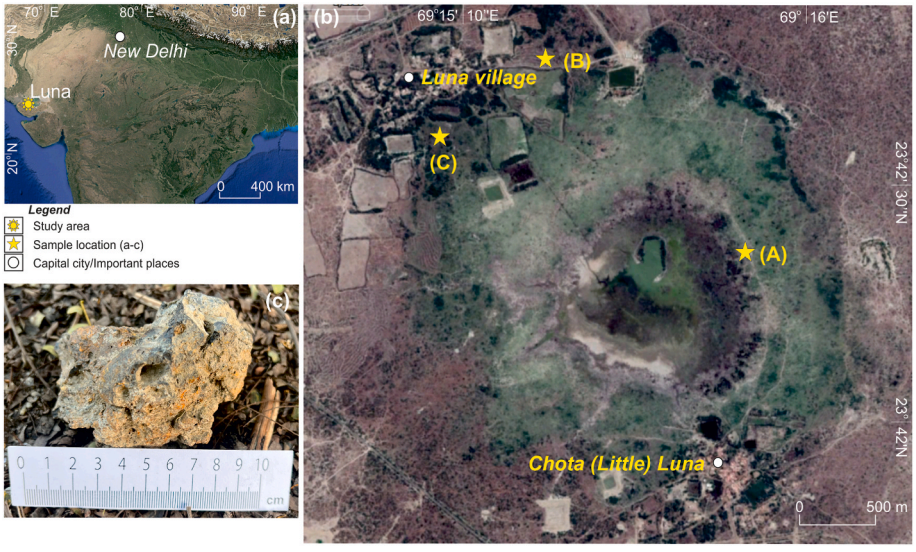


**Fig. 1.** (a) Location map of Luna structure in Gujarat, India (b) Aerial view of Luna with depiction of a typical circular shape (c) A impact melt-like rock sample from Luna (Source of (a) and (b): Google Earth).

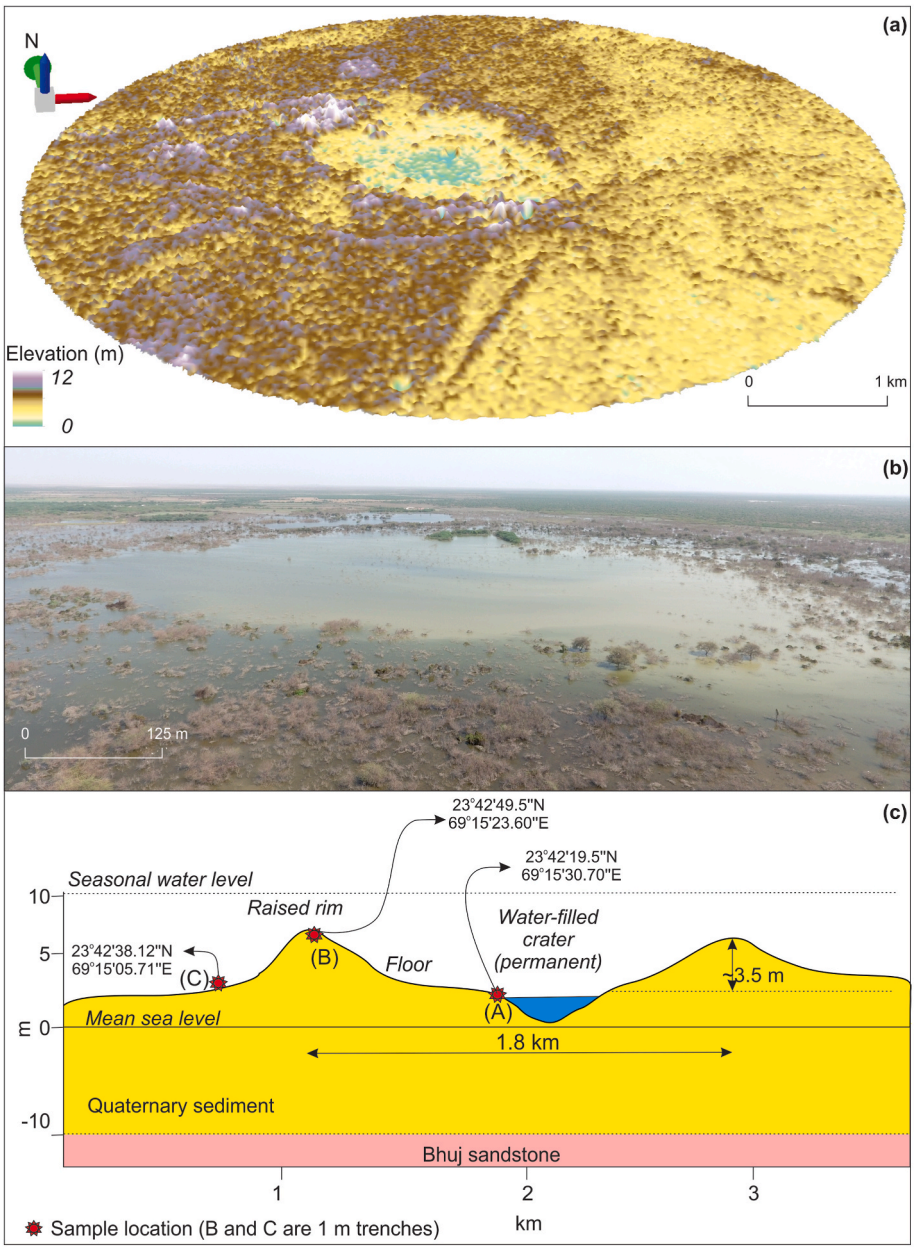


**Fig. 2.** (a) 12.5 m resolution TanDEM-X elevation data of Luna structure (b) UAV image of Luna revealing the circularity of the structure (c) Cross-section of the Luna structure with locations of sample collection (A), (B) and (C).

sample collection. Furthermore, the collection of Quaternary sediments itself is not reliable since the same is transported from different regions (during annual flooding episodes) and therefore, is not innate to the structure itself. Hence, the focus was on collecting suspected melt fragments (SMF) around the crater structure. The samples were recovered mainly from three locations: (A) crater floor (B) raised rim and (C) regions within 200 m from the rim (Fig. 2c; Supplementary Material 1). The samples at (A) occur erratically on the surface; whereas the samples at (B) and (C) were collected from trenches of 1 m depth. The SMF at (B) and (C) are constrained within a 30 cm thick layer, which in turn is overlain by a ~10 cm thick sediment layer and underlain by thick silt deposits.

The samples were classified based on magnetic property, specific gravity, vesicularity, and colour (Supplementary Material 1). A total of 342 SMF were collected and classified as magnetic (206) and non-magnetic (136). Keeping the magnetic character as the primary parameter (measured with respect to attraction to a hand-held magnet), the samples were further classified as porous and non-porous (based on visual interpretation), wherein the specific gravities were measured (Supplementary Material 1). Representative samples were subjected to different analyses, to arrive conclusions on potential impact origin of the Luna structure.

### 3.2. Methodology for petrographic, mineralogical, geochemical analyses and radiocarbon dating

Representative samples were selected for different analysis as all 342 SMF could not be individually analysed. A total of 15 polished thin sections were studied using Leica DM2700P polarizing (reflecting) microscope and Olympus CX 31 binocular polarizing microscope housed at the Department of Geology, University of Kerala, India. Scanning Electron Microscopy (SEM)-EDX Carl Zeiss EVO 18 Secondary Electron Microscope equipped with a CL detector, BSE (Back-scattered Electron), EDS (Energy dispersive X-Ray) of 5–300,000× magnification housed at

Central Laboratory for Instrumentation and Facilitation (University of Kerala, India) was employed for mineralogical studies. The analyses at all points were performed under 18 kV accelerating voltage and 20 nA probe current, and a working distance of 19 mm. BSE images of the polished thin sections were acquired using Hitachi SU-70 Field Emission Gun (FEG) SEM (equipped with a Schottky emitter) housed at the Planetary and Space Science Centre (PASSC), University of New Brunswick, Canada. Electron probe microanalyzer (EPMA) of CAMECA SXFiveTactics instrument at the National Centre for Earth Science Studies (NCESS), Kerala, India, was used for obtaining wavelength dispersive spectroscopy (WDS) of SMF. The instrument was operated with 15 kV accelerating voltage, 20 nA beam current, and 1 μm beam diameter. Respective background intensities were measured on both sides of the peak for half the peak times. Data reduction has been carried out using X-Phi method. The analytical protocol is followed after Sorcar et al. (2021).

The major oxides, trace elements, rare earth element (REE), and platinum group of element (PGE) composition in representative samples were determined at National Geophysical Research Institute (NGRI), Hyderabad, India. For geochemical analyses, the samples were pulverized using a jaw crusher followed by size reduction to a fine powder in an agate mortar. Major oxides were determined by X-ray Fluorescence (XRF) spectroscopy (Phillips®MAGIXPRO Model 2440) using pressed sample pellets, following the methodology by Krishna et al. (2007). For trace element determination including REE and high field strength elements (HFSE), the samples were dissolved in reagent grade HF:$HNO_3$ acid mixture in Savillex®screw top vials, following a closed digestion procedure (Satyanarayanan et al., 2018). The samples were analysed by High Resolution Inductively Coupled Plasma Mass Spectrometry (HR-ICP-MS) (Nu ATTOM®, Nu Instruments, UK). Internal drift was corrected using $^{103}Rh$ as an internal standard whereas external drift was corrected by repeated analysis of geochemical reference materials BHVO-1 and BCR-1 (USGS), JB-2 and JB-3 (GSJ, Japan) (Govindaraju, 1994; Jochum et al., 2005); the same were used as calibration standards. The precision of major oxides and trace element analysis is found to be −3% and 5% RSD, respectively. The sample preparation for PGE analysis was carried out by NiS fire assay method with tellurium co-precipitation followed by HR-ICP-MS based analysis (Balaram et al., 2006). The samples were washed, dried, pulverized and sieved to 60 mesh size consistencies, with fine powdering carried out through an acetone-cleansed agate mortar to avoid siderophile contamination. The compositional measurements were made for PGE while maintaining a 300 R; wherein <5% RSD for ng/mL level PGE was observed (Satyanarayanan et al., 2018). The accuracy of the measurements was determined through comparisons with reference materials WMG-1, WMS-1A, SARM-47, and PTC-1A. The detection limits (in ppb) are of the order: 1.2 for Os, Ir, Ru; 0.5 for Pt, Rh and 1.9 for Pd; while the precision on the raw counts was <5% RSD for all the measured PGEs.

Radiocarbon dating was performed in the Accelerator Mass Spectrometer (AMS) facility at the Physical Research Laboratory - Accelerator Unit for Radioisotope Studies (PRL-AURiS), Ahmedabad, India. A total of 500 g of silt was collected from two points in the trench (C) for radiocarbon dating. The analysis followed the methodologies stated by Bhushan et al. (2019a,b). A quantity of 10 mg, from both the samples, were graphitized, along with the graphitization of standards and intercomparison samples. The silt samples and standards were exposed to the graphite (OxII) target. Radiocarbon measurements were carried out at 1 MV terminal voltage and beam current of 20–40 μA. The data was calibrated utilizing the Calib 8.2 (INTCAL20) with appropriate age correction.

## 4. Results

### 4.1. Physical characteristics of suspected melt fragments (SMF)

SMF collected from the Luna structure have dimensions ranging from a few mm to several cm, with the majority being 2–5 cm in length, and a few samples are larger than 10 cm. It displays diverse physical characteristics. Majority of the collected SMF appear glassy (aphanitic) without any visible crystals (Fig. 3a). A few SMF exhibit flow patterns on the surface (Fig. 3b) and have smooth, undulating surfaces (Fig. 3c). Most SMF are vesicular (Fig. 3d). The specific gravities of these 342 SMF are within the range of 1.7–5 g/cm$^3$, with an average of 3.7 g/cm$^3$.

### 4.2. Petrographical and mineralogical characteristics of Luna samples

SMFs are observed to show different textures, both in optical photomicrographs and BSE images. The photomicrograph of IL3 (Fig. 4a) shows the presence of angular to rounded vesicles. The photomicrograph of IL13 (Fig. 4b) and BSE images of SL2 (Fig. 4c) denotes occurrence of two minerals, wherein the darker matrix entails bright dendrites. The SEM-EDS of both SL2 and IL13 (Supplementary Material 2) points to the potential presence of quasi-randomly oriented wüsite dendrites (parallel bars arranged at 90°), dispersed within a silicate matrix of kirschsteinite. WDS data confirms the presence of wüsite and kirschsteinite in SL2 (Table 1, Supplementary Material 3). In sample SL2, wüsite has an average composition of $(Fe_{0.91}Mn_{0.04}Mg_{0.03}Al_{0.01})O$, meanwhile kirschsteinite has an average composition of $(Fe_{0.70}Ca_{0.51}Al_{0.28}K_{0.12}Mn_{0.11}Mg_{0.07}Na_{0.05}P_{0.03})Si_{0.96}O_4$. Sample SL5 depicts relatively limited presence of wüstite and kirschsteinite (Fig. 4d). The average WDS-determined composition of wüstite is $(Fe_{0.94}Mn_{0.02}Mg_{0.02}Al_{0.01})O$ and kirschsteinite is $(Fe_{0.78}Ca_{0.76}Al_{0.19}K_{0.08}Mg_{0.06}Mn_{0.05}Na_{0.06}P_{0.03})Si_{0.96}O_4$ (Table 1, Supplementary Material 3). Sample SL5 also depicts the presence of silica, with an average composition of $(Si_{0.99}Fe_{0.01})O_2$ (Table 1, Supplementary Material 3). In SL10, ulvöspinel ($(Fe_{1.79}Ti_{0.70}Al_{0.48}Mg_{0.04}Mn_{0.01}Mg_{0.01}Si_{0.01}Ti_{0.70})O_4$), hercynite ($(Fe_{1.06}Ti_{0.06}Mg_{0.05}Mn_{0.01}Al_{1.83})O_4$) and fayalite ($(Fe_{1.79}Mg_{0.13}P_{0.03}Mn_{0.02}\ Al_{0.02}Ti_{0.01}Ca_{0.01})Si_{0.96}O_4$) were identified (Table 1, Supplementary Material 3). In BSE images of SL10, the larger subhedral grains of ulvöspinel are present in conjunction with relatively anhedral fayalite grains. Fayalite depicts a homogenous composition across many grains, with compositional zoning in some larger grains. Hercynite grains occur in close proximity with fayalite grains (Fig. 4e). Lastly, in the BSE image of SL11, the presence of plagioclase feldspar (labradorite/bytownite), ilmenite, olivine (series), ulvöspinel and silica are identified through WDS (Fig. 4f) (Table 1, Supplementary Material 3).

### 4.3. Assessment of potential geochemical indicators of projectile contribution

The average major oxide concentrations of SMF are as follows: $SiO_2$ (40.47%), $Fe_2O_3$ (31.785%), CaO (9.90%), $Al_2O_3$ (6.58%), $P_2O_5$ (3.95 %), $K_2O$ (1.44%), MgO (1.165%), $TiO_2$ (1.04%), $Na_2O$ (0.49 %) and MnO (0.25%) (Table 2). Cr concentration of Luna samples range in 39.54–149.66 ppm, Co in 10.44–72.581 ppm and Ni in 8.412–57.825 ppm (Table 2). IL2A, IL6 and IL16 depict Cr enrichment relative to crustal average of 135 ppm (cf. Rudnick and Gao, 2014), and IL2A, IL13 and IL16 depicts Co enrichment relative to crustal average of 26.6 ppm (cf. Rudnick and Gao, 2014). The samples exhibit exceedingly high PGE content, with average concentration of Ru (19.02 ppb), Rh (5.68 ppb), Pd (8.64 ppb), Os (6.03 ppb), Ir (10.63 ppb) and Pt (18.31 ppb) (Table 2). Based on the above geochemical signatures, similarities between certain samples are noted. IL12 and IL13 share compositional similarities for all oxides and elements except $Fe_2O_3$, CaO, V, Cr, Cu, Co, Zn, Rb, Sr, Y, Zr, Ba, Ru and Ir (Table 2). IL2A and IL3 show remarkable compositional similarity for major oxides (avg. difference in concentrations (ADC): 0.14 wt%), but high compositional differences among REE (ADC: 10.3 ppm) and very high differences among remaining non-PGE trace elements (ADC: 82.9 ppm).

**Fig. 3.** Physical characteristics of Luna samples (a) with glassy appearance (b) flow patterns and undulating surfaces (c)smooth flow patterns (d) plenty of vesicles.

### *4.4. Probable age of impact event as revealed by radiocarbon dating*

The radiocarbon dating was performed on plant remnants from two separate sediment fractions (silt), collected from the 1 m deep trench at location C. Two samples were collected from depths of 0.5 (SL T2) and 1 m (SL T1), which occur below the layer of Luna SMF (Fig. 5). The silt layer at 1 m depth was dated at 7971 years (median age), while the layer sampled at 0.5 m yielded a median age of 6905 years.

## 5. Discussion

### *5.1. A look into potential target and impactor types*

#### *5.1.1. Potential target type*

In impact cratering scenarios, the resultant mineralogy holds several clues to the target and projectile types, especially in cases with no direct exposures of the target. The Luna samples contain minerals uncommon to natural terrestrial settings, such as kirschsteinite and wüstite, and with other minerals like ulvöspinel, hercynite, and fayalite. Kirschsteinite (silicate phase) and wüstite (metallic phase) are ubiquitous in samples (Table 1, Supplementary Material 2, 4). Kirschsteinite, a variety of Ca-rich olivine (CaO >20 wt%), is generally reported from angrites, CV chondrites and iron meteorites (Sokol et al., 2002). Folco and Mellini (1997) notes that kirschsteinite crystallizes from silica-undersaturated melts at high temperatures (>450 °C), under reducing conditions (cf. Ganino et al., 2017; Ganino and Libourel, 2017). During impact events, kirschsteinite is expected to form when an iron-projectile impacts a carbonate-dominated mixed-target (Sokol et al., 2002; Hamann, 2018). The Banni Plains at Luna is expected to be rich in organic matter ($CaCO_3$, smectite clay; Sant et al., 2017) and silicates (avg. $SiO_2$ of Luna is 40.47%). We suggest that the impact-induced high temperatures initiate carbonate phase decomposition and oversee reactions between (Ca-rich) silicate melt and target, with the reactions terminating with the formation of Ca–Fe rich silicates (e.g., kirschsteinite), which precipitates from the melt at relatively lower temperatures (cf. Hamann, 2018). Wüstite (FeO) forms under strong reducing conditions (low oxygen fugacity) when $Fe^{3+}$ phase gets reduced to $Fe^{2+}$ at high temperatures (>570 °C) (Bruce and Hancock, 1969; Badyukov and Raitala, 2012; Henrichs et al., 2020). Lukanin and Kadik (2007) supplements the same by noting that reduced phases are sustained in high temperature impact melts. The presence of oxide spinel group also points to a potential impact origin at Luna. The coexistence of Al-rich hercynite and Al-poor ulvöspinel, and even fayalite, points to the presence of oxide spinel solid solution (Morrison and Hazen, 2021). Morrison and Hazen (2021) state that the oxide spinel group is characteristic of non-chondritic meteorites. Hercynite can result from high temperature (1000–1600°C; Välja et al., 2019) shock metamorphism of argillaceous sediments (cf. Deer et al., 2013). Although hercynite is not a shock indicator mineral, it is reported in impact melts of Henbury (Ding and Veblen, 2004), Wanapitei (Dressler et al., 1997), Chesapeake Bay (Wittmann et al., 2009), Bosumtwi (Välja et al., 2019), Popigai (Whitehead et al., 2002) and K/Pg boundary (Kyte and Bostwick, 1995). Furthermore, hercynite is indicative of silica-poor environment (Abbott et al., 2005), meanwhile the presence of ilmenite and ulvöspinel is indicative of a reducing environment (Cameron, 1970). As the Banni Plains is an active depocenter in a transitional (fluvio-marine) phase, a sedimentary target rich in clay and silicates can be expected at the Luna structure. Moreover, the presence of olivine, feldspar and silica indicates the target-projectile mixing.

The geochemical comparisons drawn between Banni Plain sediments (Makwana et al., 2021) and Luna samples substantiate the above observations. Firstly, the high $Fe_2O_3$ (avg: 31.8 wt%), low $Na_2O$ (avg.: 0.49 wt%) and $K_2O$ (avg.: 1.44 wt%) concentrations of Luna samples contrast with the low $Fe_2O_3$ (avg.: 5.2 wt%), high $Na_2O$ (avg.: 1.2 wt%) and high $K_2O$ (avg.: 2.8 wt%) of Banni sediments from Bhuj-Khavda road (BKR) (Makwana et al., 2021; ~46 km from Luna, sediment age: 5 ka to present day) (Supplementary Material 4). Meanwhile, $Al_2O_3$, CaO and $TiO_2$ concentrations of Luna samples depict wide range of values (lower, higher and within the BKR range). Considering BKR sediments as representative to the target sediments at Luna structure, the enrichment in iron owes to an external contribution like an asteroid/meteorite (cf. Dence, 1971). Meanwhile, the notable decrease in $Na_2O$ and $K_2O$ of Luna samples relative to BKR samples might result from the consumption of Na and K during target-projectile interactions.

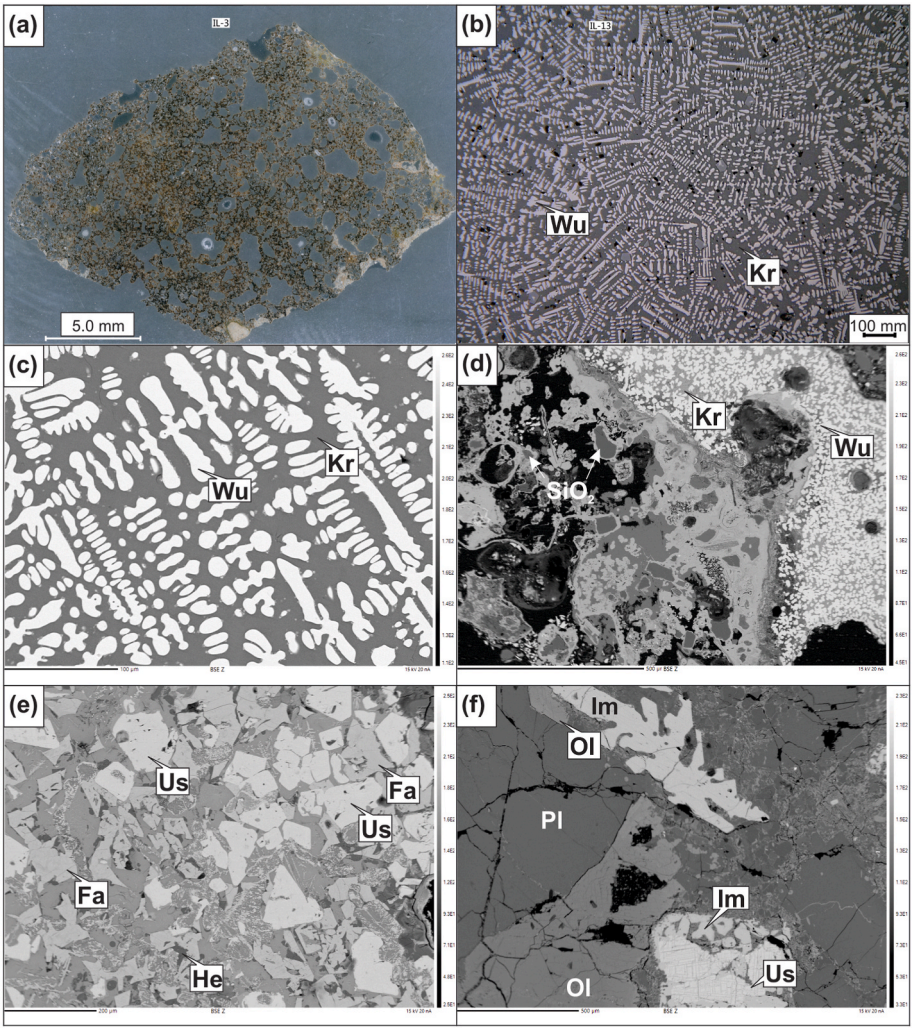


**Fig. 4.** (a) Photomicrograph of IL3 depicting vesicles (b) Photomicrograph (reflected) image of IL13 consisting of wüsite (Wu) lamellae in kirschsteinite (Kr)-bearing silicate matrix (c) BSE-SEM images of wüsite lamellae in kirschsteinite-bearing silicate matrix of mineral phases in SL2 (d) BSE image of wüsite and kirschsteinite along with silica in SL5. Sharp distinction can be noted between wüsite-kirschsteinite and $SiO_2$ (e) Combination of different mineral like ulvöspinel (Us), fayalite (Fa), and hercynite (He) in SL10 (f) Ilmenite (Im), ulvöspinel (Us) olivine (Ol) and plagioclase (Pl) association in SL11.

*5.1.2. Potential projectile type*

The projectile nature at Luna is evaluated through assessment of siderophile and PGE concentrations of Luna SMF, different meteorite groups, and impact melts from select impact craters. For the average continental crust, specific range for Ni/Ir (560–5250) and Cr/Ir (1260–9250) are noted (Goderis et al., 2013). Ni/Ir ratios (659–12633) for all Luna samples are higher than the crustal range, and for four samples (IL2A, IL6,IL13, IL16) the Cr/Ir ratios (11,600–32700) occur above the range (Fig. 6a, Supplementary Material 5). As continental crust is a notable contributor for Ni and Cr, the above ratios can be misleading and PGE concentrations were compared. Chondrite-normalized PGE-patterns of Luna samples, terrestrial impactites, Morasko Irons, Gebel Kamil Meteorite and bulk continental crust reveals that the PGE concentrations of Luna samples, meteorites and terrestrial impactites are higher than bulk continental crust values (Fig. 6b, Supplementary Material 6). Gebel Kamil Meteorite and Morasko Irons have highest PGE concentrations owing to sustained geochemical intactness of meteorites, potentially resulting from minimum possible interaction with the target. The elemental variation trends of Luna, Rochechouart (Tagle et al., 2009), Sääksjärvi (Tagle et al., 2009) and Gardnos (Goderis et al., 2009) are similar, with notable enrichment of Ru and Rh (less mobile), and depletion of Pt and Pd (more mobile). Wabar impactite (Mittlefehldt et al., 1992) depicts Ru and Pd depletion, and Ir, Pt and Au enrichment. It is noteworthy that the PGE concentrations of Luna samples are higher than all impactites, and is only lesser relative to the two meteorites- Gebel Kamil and Morasko Irons (found at the impact sites of respective craters). Hence, Fig. 6b implies the non-terrestrial nature of Luna samples, and henceforth, the Luna samples will be termed as Luna impactites.

Firstly, to identify the projectile at Luna, comparison of PGE concentrations of different impactites and 89 different meteorites were done (Supplementary Material 6). The chondrite normalized PGE patterns depict the deviation of the Luna impactites from the flat PGE patterns characteristic of chondrites (Goderis et al., 2013) (Fig. 7a). Hence, the projectile at Luna is non-chondritic. Amongst PGE, Ir and Ru are least mobile, meanwhile Pt and Pd are the most mobile when subject to post-impact modification (Tagle and Hecht, 2006; Goderis et al., 2013). Here, the inter-elemental ratio between a mobile and relatively immobile entity is noted (Fig. 7b). Firstly, Luna impactites have the highest Ru/Pt ratios (avg.:1.18) among all impactites (0.48–0.90), except Rochechouart (1.21) (Tagle et al., 2009). We also observe that the Morasko Irons (IAB iron; Kracher et al. (1980)) and Gebel Kamil Meteorite (ungrouped ataxite (19.8 wt% Ni) (D'Orazio et al., 2011)) are clustered at highly elevated values corresponding to other meteorites (MetBase).

Ir concentration of Luna impactites fall within the range of

**Table 1**
Table depicting microprobe data of Luna SMF (suspected melt fragments). The samples SL2, SL5 and SL10 are melt samples, whereas SL11 contains sporadically. In each sample, for a given mineral, a representative data along with the average composition. Oxides are provided in wt%.

| WDS Spots | SL2 | | | | SL5 | | | | | | SL10 | | | | | | SL11 | | | | | | | |
|---|---|---|---|---|---|---|---|---|---|---|---|---|---|---|---|---|---|---|---|---|---|---|---|---|
| | Kirschsteinite | | Wüstite | | Kirschsteinite | | Wüstite | | Silica | | Ulvospinel | | Fayalite | | Hercynite | | Ilmenite | | Feldspar | | Olivine | | Silica | Ulvospinel |
| | 46/1 | Avg. | 15/1 | Avg. | 10/1 | Avg. | 4/1 | Avg. | 16/1 | Avg. | 187/1 | Avg. | 121/1 | Avg. | 120/1 | Avg. | 45/1 | Avg. | 86/1 | Avg. | 87/1 | Avg. | 79/1 | 104/1 |
| F | 0.06 | 0.06 | 0.01 | 0 | 0.07 | 0.07 | 0.01 | 0 | 0 | 0 | 0.04 | 0.01 | 0.04 | 0.04 | 0.01 | 0 | 0.02 | 0.02 | 0 | 0.01 | 0 | 0.01 | 0.03 | 0.02 |
| Na2O | 0.88 | 0.89 | 0 | 0.01 | 0.61 | 0.98 | 0.03 | 0.02 | 0 | 0.01 | 0.01 | 0.02 | 0.04 | 0.01 | 0 | 0.01 | 0.04 | 0.01 | 3.88 | 4.62 | 0 | 0.33 | 0 | 0 |
| SiO2 | 33.82 | 32.97 | 0.1 | 0.11 | 30.58 | 31.6 | 0.15 | 0.12 | 97.18 | 96.68 | 3.78 | 0.23 | 27.87 | 27.61 | 0.13 | 0.15 | 0.1 | 0.06 | 52.05 | 52.28 | 33.78 | 43.92 | 94.95 | 0.49 |
| MgO | 1.73 | 1.65 | 1.65 | 1.7 | 1.64 | 1.26 | 1.13 | 1.11 | 0.01 | 0.01 | 0.39 | 0.82 | 2.81 | 2.6 | 1.3 | 1.21 | 1.74 | 0.88 | 0.09 | 0.09 | 18.6 | 14.52 | 0.01 | 0.26 |
| Al2O3 | 8.23 | 8.15 | 0.42 | 0.38 | 1.34 | 5.28 | 0.55 | 0.57 | 0.33 | 0.15 | 12.46 | 11.13 | 0.22 | 0.4 | 53.26 | 52.32 | 0.13 | 0.11 | 29.86 | 28.49 | 0 | 1.79 | 0.12 | 0.72 |
| P2O5 | 1.13 | 1.1 | 0.02 | 0.01 | 1.27 | 1.24 | 0.04 | 0.01 | 0 | 0.01 | 0.32 | 0.02 | 0.69 | 1.15 | 0 | 0 | 0.01 | 0.01 | 0 | 0.01 | 0 | 0.05 | 0.01 | 0.03 |
| K2O | 3.32 | 3.25 | 0 | 0 | 0.42 | 2.11 | 0 | 0 | 0.05 | 0.02 | 0.13 | 0 | 0 | 0 | 0 | 0 | 0 | 0 | 0.19 | 0.23 | 0 | 0.13 | 0.02 | 0 |
| CaO | 17.19 | 16.5 | 0.18 | 0.17 | 28.57 | 23.4 | 0.03 | 0.09 | 0.05 | 0.06 | 0.41 | 0.03 | 0.28 | 0.26 | 0.03 | 0.03 | 0.04 | 0.03 | 13.92 | 12.43 | 0.22 | 7.84 | 0.02 | 0.05 |
| TiO2 | 0.16 | 0.16 | 0.2 | 0.21 | 0.07 | 0.11 | 0.12 | 0.15 | 0.01 | 0 | 24.5 | 25.66 | 0.27 | 0.36 | 2.67 | 2.86 | 51.05 | 50.1 | 0.08 | 0.09 | 0.04 | 0.46 | 0.05 | 30.57 |
| FeOT | 26.8 | 28.64 | 91.57 | 90.86 | 33.31 | 30.78 | 95.06 | 93.68 | 1.17 | 0.97 | 57.79 | 58.96 | 65.71 | 61.74 | 41.98 | 42.56 | 44.86 | 46.02 | 0.44 | 0.68 | 47.25 | 28.88 | 0.11 | 60.06 |
| MnO | 4.63 | 4.51 | 4.37 | 4.33 | 1.63 | 2.1 | 1.47 | 1.85 | 0.01 | 0.01 | 0.3 | 0.29 | 0.69 | 0.59 | 0.27 | 0.26 | 0.58 | 0.51 | 0.01 | 0.01 | 0.56 | 0.49 | 0.03 | 0.4 |
| Cr2O3 | 0.02 | 0.01 | 0.02 | 0.02 | 0 | 0.02 | 0.01 | 0.02 | 0 | 0.01 | 0 | 0.36 | 0 | 0.01 | 0.03 | 0.01 | 0.04 | 0.02 | 0 | 0.01 | 0 | 0.01 | 0 | 0.1 |
| NiO | 0 | 0.02 | 0.01 | 0.02 | 0.1 | 0.02 | 0 | 0.01 | 0.07 | 0.03 | 0.03 | 0.02 | 0 | 0.01 | 0 | 0 | 0 | 0.01 | 0 | 0.02 | 0.06 | 0.04 | 0 | 0.1 |
| ZnO | 0.03 | 0.03 | 0.08 | 0.03 | 0 | 0.03 | 0 | 0.03 | 0.07 | 0.04 | 0 | 0.03 | 0.03 | 0.04 | 0.05 | 0.05 | 0.11 | 0.1 | 0 | 0.03 | 0.02 | 0.07 | 0 | 0.31 |
| BaO | 0.13 | 0.05 | 0 | 0 | 0 | 0.14 | 0 | 0 | 0 | 0 | 0 | 0 | 0 | 0 | 0 | 0 | 0 | 0 | 0 | 0 | 0 | 0 | 0 | 0 |
| SO2 | 1.78 | 2.04 | 0 | 0.02 | | | | | | | 0 | 0.01 | 0.03 | 0.03 | 0 | 0 | 0.01 | 0.01 | 0.03 | 0.01 | 0 | 0.01 | 0.02 | 0.04 |
| Total | 99.9 | 100.04 | 98.62 | 97.87 | 99.61 | 99.15 | 98.59 | 97.67 | 98.94 | 98 | 100.16 | 97.61 | 98.69 | 94.87 | 99.73 | 99.45 | 98.72 | 97.88 | 100.55 | 98.99 | 100.52 | 98.56 | 95.36 | 93.16 |
| O Basis | 4 | 4 | 1 | 1 | 4 | 4 | 1 | 1 | 2 | 2 | 32 | 32 | 4 | 4 | 32 | 32 | 6 | 6 | 32 | 32 | 4 | 4 | 2 | 32 |
| F | | | | | | | | | | | | | | | | | | | | | | | | |
| Na | 0.05 | 0.05 | 0 | 0 | 0.04 | 0.06 | 0 | 0 | 0 | 0 | 0 | 0.01 | 0 | 0 | 0 | 0.01 | 0 | 0 | 1.37 | 1.65 | 0 | 0.02 | 0 | 0 |
| Si | 0.98 | 0.96 | 0 | 0 | 0.94 | 0.96 | 0 | 0 | 0.99 | 0.99 | 1.04 | 0.06 | 0.94 | 0.96 | 0.03 | 0.04 | 0.01 | 0 | 9.44 | 9.63 | 1 | 1.19 | 1 | 0.16 |
| Mg | 0.07 | 0.07 | 0.03 | 0.03 | 0.08 | 0.06 | 0.02 | 0.02 | 0 | 0 | 0.16 | 0.36 | 0.14 | 0.13 | 0.46 | 0.43 | 0.13 | 0.07 | 0.02 | 0.02 | 0.82 | 0.59 | 0 | 0.13 |
| Al | 0.28 | 0.28 | 0.01 | 0.01 | 0.05 | 0.19 | 0.01 | 0.01 | 0 | 0 | 4.02 | 3.81 | 0.01 | 0.02 | 14.79 | 14.64 | 0.01 | 0.01 | 6.39 | 6.18 | 0 | 0.06 | 0 | 0.27 |
| P | 0.03 | 0.03 | 0 | 0 | 0.03 | 0.03 | 0 | 0 | 0 | 0 | 0.07 | 0.01 | 0.02 | 0.03 | 0 | 0 | 0 | 0 | 0 | 0 | 0 | 0 | 0 | 0.01 |
| K | 0.12 | 0.12 | 0 | 0 | 0.02 | 0.08 | 0 | 0 | 0 | 0 | 0.05 | 0 | 0 | 0 | 0 | 0 | 0 | 0 | 0.04 | 0.05 | 0 | 0.01 | 0 | 0 |
| Ca | 0.53 | 0.51 | 0 | 0 | 0.95 | 0.76 | 0 | 0 | 0 | 0 | 0.12 | 0.01 | 0.01 | 0.01 | 0.01 | 0.01 | 0 | 0 | 2.71 | 2.45 | 0.01 | 0.22 | 0 | 0.02 |
| Ti | 0 | 0 | 0 | 0 | 0 | 0 | 0 | 0 | 0 | 0 | 5.05 | 5.61 | 0.01 | 0.01 | 0.47 | 0.51 | 1.95 | 1.95 | 0.01 | 0.01 | 0 | 0.01 | 0 | 7.37 |
| Fe | 0.65 | 0.7 | 0.91 | 0.91 | 0.86 | 0.78 | 0.95 | 0.94 | 0.01 | 0.01 | 13.23 | 14.33 | 1.86 | 1.79 | 8.27 | 8.45 | 1.91 | 1.99 | 0.07 | 0.1 | 1.17 | 0.68 | 0 | 16.1 |
| Mn | 0.11 | 0.11 | 0.04 | 0.04 | 0.04 | 0.05 | 0.01 | 0.02 | 0 | 0 | 0.07 | 0.07 | 0.02 | 0.02 | 0.05 | 0.05 | 0.02 | 0.02 | 0 | 0 | 0.01 | 0.01 | 0 | 0.11 |
| Cr | 0 | 0 | 0 | 0 | 0 | 0 | 0 | 0 | 0 | 0 | 0 | 0.08 | 0 | 0 | 0 | 0 | 0 | 0 | 0 | 0 | 0 | 0 | 0 | 0.03 |
| Ni | 0 | 0 | 0 | 0 | 0 | 0 | 0 | 0 | 0 | 0 | 0.01 | 0.01 | 0 | 0 | 0 | 0 | 0 | 0 | 0 | 0 | 0 | 0 | 0 | 0.03 |
| Zn | 0 | 0 | 0 | 0 | 0 | 0 | 0 | 0 | 0 | 0 | 0 | 0.01 | 0 | 0 | 0.01 | 0.01 | 0 | 0 | 0 | 0 | 0 | 0 | 0 | 0.07 |
| Ba | 0 | 0 | 0 | 0 | 0 | 0 | 0 | 0 | 0 | 0 | 0 | 0 | 0 | 0 | 0 | 0 | 0 | 0 | 0 | 0 | 0 | 0 | 0 | 0 |
| S | 0.05 | 0.06 | 0 | 0 | | | | | | | 0 | 0 | 0 | 0 | 0 | 0 | 0 | 0 | 0 | 0 | 0 | 0 | 0 | 0.01 |
| Total | 2.88 | 2.89 | 0.99 | 0.99 | 3.01 | 2.97 | 0.99 | 0.99 | 1.01 | 1.01 | 23.82 | 24.37 | 3.02 | 2.97 | 24.1 | 24.14 | 4.04 | 4.04 | 20.05 | 20.12 | 3 | 2.78 | 1 | 24.3 |

**Table 2**
Geochemical data of Luna Samples (Major Oxides, Trace, Rare Earth and Platinum Group of Elements).

| Sample | IL-1 | IL-2A | IL-3 | IL-4 | IL-5 | IL-6 | IL-12 | IL-13 | IL-16 | GSR4 (OV) | GSR4 (CV) | GSR4 (OV) | WMG1 (CV) | WMG1 (OV) | WMG1 (OV) |
|---|---|---|---|---|---|---|---|---|---|---|---|---|---|---|---|
| | Major Oxides (wt%) | | | | | | | | | | | | | | |
| $SiO_2$ | 26.89 | 63.84 | 63.57 | 26.62 | 20.77 | 53.16 | 32.31 | 31.27 | 45.78 | | | | | | |
| $Al_2O_3$ | 0.76 | 12.99 | 11.85 | 5.55 | 3.37 | 0.31 | 5.63 | 4.49 | 14.30 | | | | | | |
| $Fe_2O_3$ | 61.70 | 6.83 | 6.55 | 30.87 | 54.90 | 41.23 | 25.49 | 41.11 | 17.37 | | | | | | |
| MnO | 0.03 | 0.10 | 0.09 | 0.54 | 0.25 | 0.01 | 0.53 | 0.54 | 0.19 | | | | | | |
| MgO | 0.19 | 2.85 | 2.48 | 0.36 | 0.01 | 0.27 | 0.37 | 0.11 | 3.76 | | | | | | |
| CaO | 1.66 | 7.61 | 7.39 | 21.43 | 8.76 | 0.24 | 21.03 | 10.88 | 10.12 | | | | | | |
| $Na_2O$ | 0.02 | 1.37 | 1.36 | 0.03 | 0.02 | 0.01 | 0.12 | 0.01 | 1.51 | | | | | | |
| $K_2O$ | 0.14 | 2.90 | 2.71 | 1.70 | 1.23 | 0.05 | 1.73 | 1.83 | 0.70 | | | | | | |
| $TiO_2$ | 0.51 | 0.74 | 0.68 | 1.44 | 0.67 | 0.14 | 1.47 | 0.88 | 2.81 | | | | | | |
| $P_2O_5$ | 1.90 | 0.18 | 0.20 | 8.60 | 6.98 | 1.11 | 8.85 | 6.41 | 1.32 | | | | | | |
| LOI | 6.43 | 0.45 | 1.41 | 3.06 | 3.10 | 3.43 | 3.21 | 3.29 | 2.82 | | | | | | |
| Total | 100.23 | 99.86 | 98.29 | 100.2 | 100.06 | 99.96 | 100.74 | 100.82 | 100.68 | | | | | | |
| Trace and Rare Earth Elements (ppm) | | | | | | | | | | | | | | | |
| Sc (45) | 4.07 | 50.43 | 13.81 | 30.26 | 30.25 | 2.12 | 30.63 | 30.92 | 47.03 | 4.14 | 4.20 | 4.11 | | | |
| V (51) | 101.87 | 449.94 | 101.56 | 270.41 | 191.90 | 56.78 | 267.34 | 204.70 | 409.17 | 36.19 | 33.00 | 36.13 | | | |
| Cr (53) | 60.41 | 149.46 | 48.43 | 69.37 | 61.70 | 149.66 | 64.00 | 39.54 | 128.41 | 23.10 | 20.00 | 22.99 | | | |
| Co (59) | 18.18 | 72.58 | 16.02 | 13.38 | 21.72 | 10.45 | 13.68 | 64.77 | 66.81 | 6.47 | 6.40 | 6.45 | | | |
| Ni (60) | 9.67 | 57.83 | 22.89 | 17.90 | 8.41 | 35.53 | 15.22 | 22.12 | 31.39 | 16.50 | 16.60 | 16.38 | | | |
| Cu (63) | 15.69 | 171.90 | 24.40 | 25.10 | 50.34 | 27.31 | 28.74 | 103.27 | 153.58 | 19.06 | 19.00 | 18.97 | | | |
| Zn (66) | 7.26 | 43.01 | 17.96 | 15.46 | 11.67 | 13.75 | 26.03 | 11.39 | 25.83 | 20.30 | 20.00 | 20.26 | | | |
| Ga (71) | 4.53 | 40.41 | 18.17 | 6.73 | 5.24 | 2.76 | 6.92 | 5.53 | 38.01 | 5.19 | 5.30 | 5.11 | | | |
| Rb (85) | 5.46 | 156.46 | 131.81 | 6.99 | 6.61 | 2.19 | 7.59 | 10.53 | 141.16 | 29.17 | 29.00 | 29.14 | | | |
| Sr (88) | 40.50 | 367.37 | 173.98 | 672.57 | 595.49 | 27.22 | 697.82 | 744.48 | 342.35 | 57.70 | 58.00 | 57.73 | | | |
| Y (89) | 6.24 | 58.54 | 26.47 | 62.29 | 149.78 | 15.06 | 62.38 | 86.13 | 54.10 | 21.33 | 21.50 | 21.26 | | | |
| Zr (90) | 105.17 | 537.16 | 189.66 | 243.19 | 123.18 | 75.39 | 247.35 | 121.98 | 492.71 | 212.19 | 214.00 | 210.47 | | | |
| Nb (93) | 4.62 | 28.92 | 15.85 | 10.12 | 3.71 | 0.93 | 9.59 | 4.98 | 27.43 | 5.82 | 5.90 | 5.77 | | | |
| Cs (133) | 0.34 | 12.13 | 10.06 | 0.33 | 0.37 | 0.15 | 0.36 | 0.64 | 11.11 | 1.79 | 1.80 | 1.83 | | | |
| Ba (137) | 76.60 | 555.10 | 399.63 | 623.98 | 1078.20 | 42.85 | 616.37 | 1084.88 | 509.37 | 144.23 | 143.00 | 144.60 | | | |
| La (139) | 7.55 | 49.62 | 37.02 | 31.03 | 28.87 | 5.53 | 31.16 | 22.59 | 45.46 | 21.32 | 21.00 | 21.21 | | | |
| Ce (140) | 15.65 | 103.73 | 73.54 | 45.21 | 47.87 | 14.46 | 45.53 | 35.22 | 94.73 | 48.16 | 48.00 | 48.23 | | | |
| Pr (141) | 1.67 | 12.95 | 8.70 | 7.60 | 7.28 | 2.52 | 7.66 | 5.66 | 11.90 | 5.39 | 5.40 | 5.35 | | | |
| Nd (146) | 6.03 | 51.61 | 32.03 | 32.03 | 32.47 | 13.55 | 32.23 | 24.89 | 47.29 | 21.10 | 21.00 | 21.01 | | | |
| Sm (147) | 1.18 | 11.31 | 6.23 | 7.37 | 8.87 | 3.90 | 7.33 | 6.49 | 10.28 | 4.70 | 4.70 | 4.61 | | | |
| Eu (153) | 0.25 | 3.02 | 1.27 | 2.50 | 3.53 | 0.98 | 2.49 | 2.54 | 2.79 | 1.01 | 1.02 | 1.00 | | | |
| Gd (157) | 1.11 | 11.05 | 5.36 | 9.11 | 14.28 | 4.14 | 9.09 | 9.26 | 10.18 | 4.45 | 4.50 | 4.32 | | | |
| Tb (159) | 0.19 | 1.86 | 0.87 | 1.61 | 2.81 | 0.68 | 1.61 | 1.75 | 1.72 | 0.78 | 0.79 | 0.78 | | | |
| Dy (163) | 1.24 | 11.46 | 5.12 | 10.54 | 20.34 | 4.02 | 10.47 | 12.27 | 10.66 | 4.04 | 4.10 | 4.00 | | | |
| Ho (165) | 0.28 | 2.44 | 1.08 | 2.30 | 4.84 | 0.82 | 2.30 | 2.83 | 2.26 | 0.71 | 0.75 | 0.72 | | | |
| Er (166) | 0.82 | 6.74 | 2.97 | 6.46 | 14.54 | 2.17 | 6.50 | 8.35 | 6.18 | 1.95 | 2.00 | 1.93 | | | |
| Tm (169) | 0.13 | 0.99 | 0.44 | 0.96 | 2.32 | 0.31 | 0.98 | 1.30 | 0.90 | 0.31 | 0.32 | 0.30 | | | |
| Yb (172) | 0.85 | 6.57 | 2.84 | 6.54 | 15.88 | 1.99 | 6.50 | 9.06 | 5.96 | 1.84 | 1.92 | 1.83 | | | |
| Lu (175) | 0.12 | 0.94 | 0.40 | 0.96 | 2.36 | 0.28 | 0.94 | 1.36 | 0.86 | 0.29 | 0.30 | 0.29 | | | |
| Hf (178) | 3.03 | 16.21 | 5.81 | 6.53 | 3.44 | 2.32 | 6.60 | 3.53 | 14.96 | 6.46 | 6.60 | 6.36 | | | |
| Ta (181) | 0.44 | 2.93 | 1.20 | 1.13 | 0.46 | 0.11 | 0.96 | 0.71 | 3.17 | 0.43 | 0.42 | 0.42 | | | |
| Pb (208) | 5.76 | 13.34 | 6.74 | 2.75 | 2.69 | 4.26 | 4.71 | 3.37 | 7.89 | 7.50 | 7.60 | 7.57 | | | |
| Th (232) | 4.53 | 16.33 | 14.38 | 3.56 | 2.69 | 1.17 | 3.63 | 2.59 | 14.96 | 6.80 | 7.00 | 6.84 | | | |
| U (238) | 1.32 | 2.76 | 2.31 | 6.07 | 3.22 | 4.96 | 6.10 | 3.45 | 2.63 | 2.02 | 2.10 | 2.01 | | | |
| Platinum Group of Elements and Au (ppb) | | | | | | | | | | | | | | | |
| Ru (101) | 14.76 | 9.78 | 24.35 | 24.13 | 26.30 | 25.79 | 25.87 | 6.57 | 13.67 | | | | 35.00 | 34.35 | 34.37 |
| Rh (103) | 2.55 | 1.95 | 3.62 | 3.52 | 4.30 | 4.22 | 3.84 | 1.31 | 25.77 | | | | 26.00 | 25.50 | 25.70 |
| Pd (105) | 4.59 | 10.02 | 11.91 | 11.65 | 8.19 | 7.38 | 2.45 | 5.48 | 14.48 | | | | 382.00 | 368.72 | 377.31 |
| Os (189) | 4.55 | 6.60 | 6.20 | 6.09 | 8.21 | 7.36 | 8.99 | 2.72 | 3.57 | | | | 24.00 | 23.94 | 23.58 |
| Ir (193) | 8.07 | 4.58 | 16.10 | 15.83 | 12.76 | 12.85 | 16.01 | 3.25 | 6.27 | | | | 46.00 | 45.95 | 45.42 |
| Pt (195) | 13.35 | 30.89 | 16.97 | 16.71 | 17.43 | 24.74 | 10.66 | 8.26 | 25.76 | | | | 731.00 | 731.41 | 720.98 |
| Au (197) | 122.78 | 44.65 | 12.505 | 22.36 | 21.14 | 17.03 | 12.51 | 14.68 | 20.54 | | | | 110.00 | 109.82 | 108.24 |

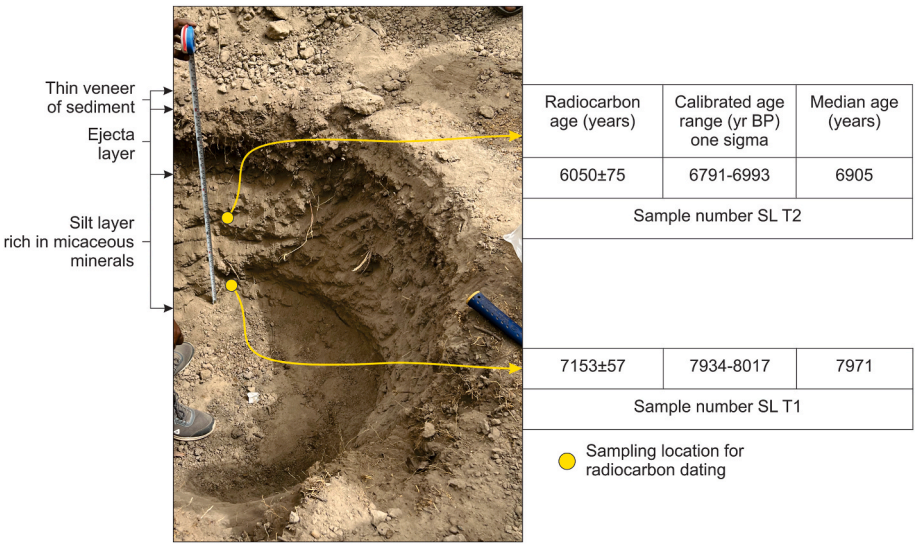


**Fig. 5.** Trench at (C). Ejecta layer forming sharp contact with underlying sediment can be seen. Sample location selected for radiocarbon dating and the ages are shown.

differentiated achondrites, irons and stony-irons (Fig. 7c). Luna Ir concentrations are markedly lower than Gebel Kamil and Morasko Irons. Ir concentrations of Luna samples depict values between that of complex older crater impactites (Rochechouart (201 ± 2 Ma, Kenkmann, 2021), Sääksjärvi (602 ± 17, Mänttäri et al., 2004), Ilyinets, (445 ± 10 Ma; Pesonen et al., 2004), Gardnos (546 ± 5 Ma; Kalleson et al., 2009)) and the younger simple crater impactites (Barringer (0.0611 ± 0.0048 Ma, Barrows et al., 2019), Wabar (290 ± 38 years, Prescott et al., 2004)). Hence, Fig. 7c helps in ruling out both chondrites and primitive achondrites as projectiles at Luna.

Ir–Cr ratios of impactites are reliable in determining the projectile type, owing to variation in elemental concentrations amongst meteorite groups and terrestrial settings (Tagle and Hecht, 2006) (Fig. 7d). A majority (five, Cr/Ir = 4742) of Luna samples are constrained to the iron meteorite zone (IMZ), meanwhile three (IL2A, IL6, IL16; Cr/Ir = 19,240) occur in the target-bolide mixing zone (TBMZ) and one does not fall into any of zones. Both IL6 and IL16 occur in the zone of intersection between IMZ and TBMZ. It is noted that impactites from the younger craters are in IMZ, meanwhile impactites of older craters (Rochechouart (Tagle et al., 2009), Sääksjärvi (Tagle et al., 2009), Ilyinets (Gurov et al., 1998), Gardnos (Goderis et al., 2009)) belong to either TBMZ or remain unclassified. The latter observation is attributed to the wide variation in Ir/Cr ratios of impactites of older complex craters (Tagle et al., 2009; Gurov et al., 1998; Goderis et al., 2009). Yet, as no impactites of older craters fall in the true terrestrial zone (TTZ), the extra-terrestrial nature of the same are re-emphasized and add to the credibility of the Ir–Cr classification criteria. The higher Cr concentrations of the Luna impactites and other crater impactites stem majorly from terrestrial contributions as iron and stony-iron projectiles are Cr-depleted (Fig. 7d). The Luna impactites are associated with low Cr-high Ir values in contrast to the high Cr-low Ir of achondrite and high Cr-high Ir values of chondrite. Cr concentrations of Luna impactites indicate that the potential impactor is either an iron or stony-iron meteorite.

### 5.2. Extent of target-projectile interactions

Based on the siderophile and PGE concentrations, the extent of target-projectile interactions can be estimated. Luna impactites depict Cr/Ir ratios and PGE concentrations that are intermediate to impactites of the older and younger craters (Fig. 6a). For older craters, the Cr/Ir ratios are in $10^5$-$10^6$ range. The average ratio of Cr/Ir is 112,658 for Rochechouart (Tagle et al., 2009); 53,104 for Ilyinets (Gurov et al., 1998); 114,992 for Gardnos (Goderis et al., 2009) and 142,270 for Sääksjärvi (Tagle et al., 2009) (Supplementary Material 5). For younger craters, the Cr/Ir ratios are relatively less, i.e., 253 for Barringer (Mittlefehldt et al., 2005) and 221 for Wabar (Mittlefehldt et al., 1992). Lastly, the Cr/Ir ratio for the meteorite fragments of Morasko Irons is 24 (Pillai et al., 2017) ((Fig. 6a, Supplementary Material 5). The observed variations can be attributed to two reasons. Firstly, older craters have been exposed longer time (>200 million years) to geological agents and hence, terrestrial contributions of Cr tend to be higher; a contradiction to younger craters with lesser exposure time to terrestrial processes. Furthermore, as all the older craters are complex, a wider range of Cr and Ir concentrations could be expected owing relatively to larger spatial extent of target involved in the shock melting (Dence, 1971; Grieve and Cintala, 1992; French, 1998), wherein local target heterogeneity can also influence the elemental concentrations. In contrast, relatively smaller spatial extent of target is exposed to shock effects for simple craters (Dence, 1971; Grieve and Cintala, 1992; French, 1998), and therefore, more uniform and narrower Cr and Ir concentrations are noted. Secondly, projectile contribution to impact melt formation across individual cratering events also vary owing to target lithology, impactor type, projectile velocity, impact energy among others factors (French, 1998; Tagle and Hecht, 2006). At Rochechouart and Sääksjärvi, projectile contribution to melt products is estimated at 0.1 wt% (Tagle et al., 2009), meanwhile Wabar registers approximately 7–17 wt% projectile contribution (Mittlefehldt et al., 1992) and Barringer registers 14 wt% (Mittlefehldt et al., 2005). As Cr/Ir ratios ($10^4$-$10^5$) and age (at most 6.9 ka) of Luna impactites lie between the limits set by older and younger craters, it can be assumed that projectile contributions are between 0.1 and 7 wt%.

Usually, the impact melt compositions are often linked to the target compositions. As the target is not exposed at Luna, we cannot ascertain the target contributions at Luna. Dressler and Reimold (2001) noted that a significant proportion of impact melts (1764 nos.) reflect compositions comparable with that of the average continental crust. For example, at Luna $SiO_2$ concentrations (33.82 wt%; except IL2A and IL3) is lower than the composition of the crust (66 wt%) and impact melt (62.01 wt%) (cf. Dressler and Reimold, 2001). Similarly, all samples (except IL2A and IL3), depicts lower $Al_2O_3$ (4.91 wt%) and higher $FeO_T$ (35.05 wt%) than crustal (15.2, 4.5 wt%) and melt counterparts (15.49, 5.11 wt%) (Dressler and Reimold, 2001).

Moreover, the target interaction with the projectile is non-uniform at Luna as depicted by the bimodal distribution for Cr/Ir ratios in the

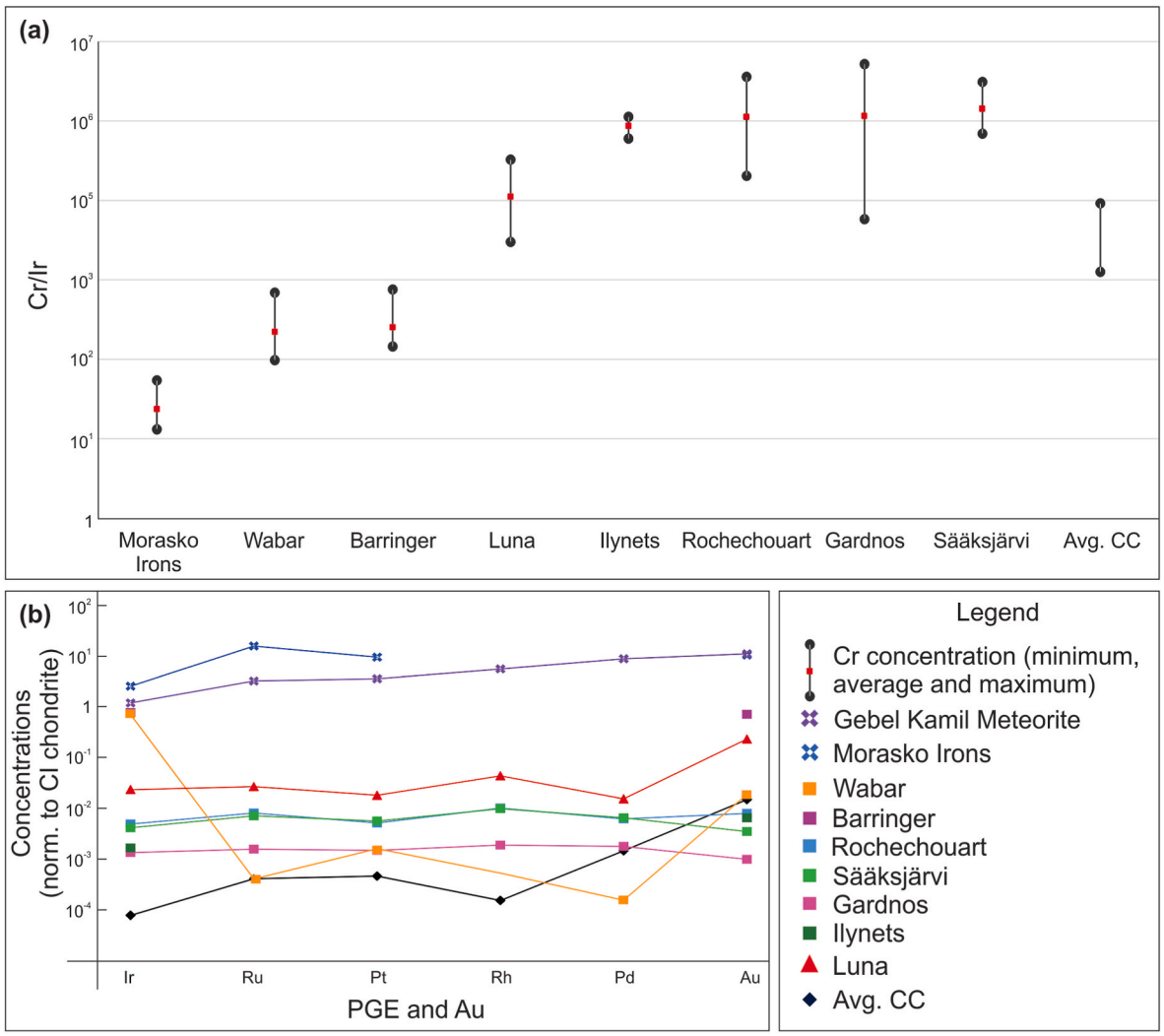


**Fig. 6.** (a) Dumbbell chart showing Cr concentration of Luna samples, terrestrial impactites, Morasko iron and average continental crust (b) Chondrite normalized PGE patterns of Luna samples, other iron-bolide resulted impactites, and average continental crust (avg. CC).

impactites. The Luna impactites in pure iron meteorite field have higher Cr/Ir ratios (avg.: 4742) in contrast to IL2A, IL6, IL13, IL16 (avg.: 19,240). $SiO_2$ contents also depict a bimodal variation, wherein IL2A, IL3, IL6, IL16 has higher concentrations (56.59 wt%) than remaining samples (27.57 wt%). Furthermore, the samples IL2A and IL3 depict compositional similarity to BKR sediments, in terms of $Fe_2O_3$, $Na_2O$ and $K_2O$ (Supplementary Material 4). In all Luna samples, except IL2A, Ru and Rh (immobile elements) are high by virtue of the projectile contribution. From the observations, it is noted that IL2A has the closest affinity to target material and has been subjected to relatively lesser extent of shock processes. In conjunction to the above, it is noted that IL6 and IL16 underwent appreciable impact effects, but do not depict chemical affinity to the remaining Luna impactites. Therefore, Luna samples depict different geochemical signatures resulting from non-uniform exposure to impact shock effects. Hence, based on the diverse set of evidences, the impact origin of the Luna structure is confirmed.

### 5.3. Constraints on age of the impact event and its implications

The Luna Impact Crater has an age <6905 years. Of the 25 craters with formation ages <120,000 years, 21 resulted from iron or stony-iron projectiles (Schmieder and Kring, 2020; Kenkmann, 2021). These 21 craters are simple as well. Additionally, younger impact craters tend to preserve the melt-rocks, as the former has not been exposed to longer durations of geological processes. Karanth et al. (2006) had suggested a younger age for Luna crater; approximated at 4000–5000 years. Our results concur to this. And with this age, probably Luna impact might have hindered or halted the Harappan civilization (7000-1900 BP; Possehl, 2002; Makwana et al., 2021), at least for a short stint of time.

## 6. Conclusion

The study can be summarized with the following conclusions:

i. The Luna Impact Crater resulted from an impact event younger than 6.9 ka.
ii. The structure has a diameter of 1.5–1.8 km.
iii. The impact products manifest as melts containing minerals such as kirschsteinite (>450 °C), wüstite (>570 °C), hercynite (1000–1600 °C) and ulvöspinel.

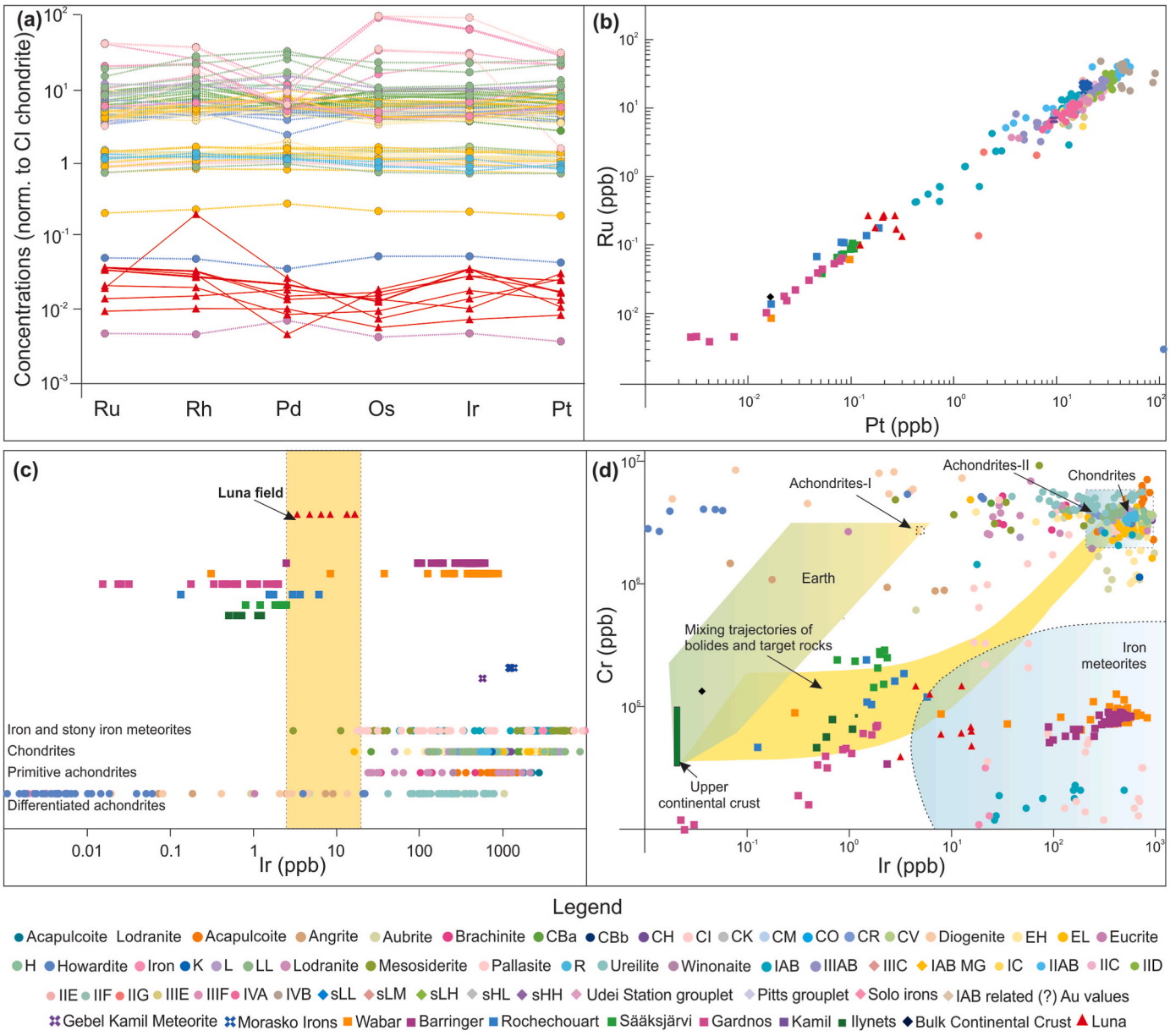


**Fig. 7.** (a) Chondrite-normalized PGE pattern for different meteorite groups and Luna impactites (source: MetBase) (b) Pt–Ru plot of Luna melt rock and several meteorite classes (c) Ir concentrations variation across Luna impactites, terrestrial impactites and different meteorites (d) Ir–Cr plot depicting terrestrial and different meteoritic fields.

iv. The target at Luna is Quaternary sediments of Banni Plains, dominant in clay, with elevated calcium (organic content) and silica (sand/silt) content.
v. Kirschsteinite and hercynite points to silica-undersaturated target/melts meanwhile wüstite, ulvöspinel and ilmenite points to prevalence of a reducing environment during impact.
vi. An iron or stony-iron bolide is the potential impactor at Luna as the differentiated PGE pattern rules out chondrites.

A limitation of our present study is the absence of diagnostic indicators of shock metamorphism, specifically shatter cones, planar deformation features (PDFs) and planar fractures (PFs). Although, these diagnostic features are not recovered from this study, the presence of the above are not overruled since a significant portion of Luna impactites are yet to be discerned. Detailed investigation is required to identify the same, given the inaccessibility of Luna Crater and the pervasiveness of the Banni sediments. Since, our study is the first in-depth report on the Luna Impact Crater with robust evidences, we will cover additional aspects in future studies.

## CRediT authorship contribution statement

**K.S. Sajinkumar:** Conceptualization, Funding acquisition, Investigation, Methodology, Supervision, Writing – review & editing. **S. James:** Formal analysis, Methodology, Resources, Software, Validation, Visualization, Writing – original draft, Writing – review & editing. **G.K. Indu:** Conceptualization, Data curation, Investigation, Methodology, Validation. **Saranya R. Chandran:** Conceptualization, Formal analysis, Methodology, Visualization. **Devika Padmakumar:** Data curation, Methodology, Resources, Writing – original draft. **J. Aswathi:** Conceptualization, Data curation, Validation, Visualization. **S. Keerthy:** Conceptualization, Data curation, Validation, Visualization. **M.N. Praveen:** Supervision, Validation, Visualization, Writing – review & editing. **N. Sorcar:** Investigation, Supervision, Validation. **J.K. Tomson:**

Investigation, Supervision, Validation. **Anil Chavan:** Investigation, Supervision, Validation. **Subhash Bhandari:** Investigation, Supervision, Validation. **M. Satyanarayanan:** Investigation, Supervision, Validation. **R. Bhushan:** Investigation, Supervision, Validation. **A. Dabhi:** Investigation, Supervision, Validation. **Y. Anilkumar:** Investigation, Supervision, Validation.

## Declaration of competing interest

The authors declare that they have no known competing financial interests or personal relationships that could have appeared to influence the work reported in this paper.

## Data availability

Data will be made available on request.

## Acknowledgments

Sajinkumar thanks the University of Kerala for granting funds to do fieldwork and sample analysis. James thanks the Barringer Crater Company for providing the 2022 Barringer Family Award for Meteorite Impact Crater. James also acknowledges the University of Kerala for funding the Ph.D. research, Saranya thanks the Kerala State Council for Science and Technology (KSCSTE) and Aswathi express gratitude to the eGrantz, Government of Kerala for funding their researches. Authors thank Prof. John G. Spray for providing the SEM EDS data and characterizing the mineralogy of the melt rock. Thanks to TanDEM-X team for providing DEM for free of cost under TanDEM-X Science proposal DEM_HYDR3435. This paper commemorates the Diamond Jubilee (1963-2023) celebrations of the Department of Geology, University of Kerala. Authors thank Dr Maria Cristina De Sanctis (Editor-in-Chief), Prof. Gordon Osinski (Reviewer) and another anonymous reviewer for the constructive remarks.

## Appendix A. Supplementary data

Supplementary data to this article can be found online at https://doi.org/10.1016/j.pss.2023.105826.

## References

Abbott, D., Biscaye, P., Cole-Dai, J., Breger, D., 2005, December. Evidence from an ice core of a large impact circa 1443 AD. AGU Fall Meeting Abstracts 2005. PP31C-05.

Aneeshkumar, V., Chandran, S.R., James, S., Santosh, M., Padmakumar, D., Aswathi, J., Keerthy, S., Anilkumar, Y., Praveen, M.N., Satyanarayanan, M., Sajinkumar, K.S., 2022. Meteorite impact at Ramgarh, India: Petrographic and geochemical evidences, and new geochronological insights. Lithos 426-427, 106779.

Badyukov, D.D., Raitala, J., 2012. Ablation spherules in the Sikhote Alin meteorite and their genesis. Petrology 20, 520–528.

Balaram, V., Mathur, R., Banakar, V.K., Hein, J.R., Rao, C.R.M., Rao, T.G., Dasaram, B., 2006. Determination of the Platinum–Group Elements (PGE) and Gold (Au) in Manganese Nodule Reference Samples by Nickel Sulfide Fire-Assay and Te Coprecipitation with ICP-MS.

Barrows, T.T., Magee, J., Miller, G., Fifield, L.K., 2019. The age of wolfe creek meteorite crater (kandimalal), western Australia. Meteoritics Planet Sci. 54 (11), 2686–2697.

Bhushan, R., Yadava, M.G., Shah, M.S., Raj, H., 2019a. Performance of a new 1MV AMS facility (AURiS) at PRL, Ahmedabad, India. Nucl. Instrum. Methods Phys. Res. Sect. B Beam Interact. Mater. Atoms 439, 76–79.

Bhushan, R., Yadava, M.G., Shah, M.S., Banerji, U.S., Raj, H., Shah, C., Dabhi, A.J., 2019b. First results from the PRL accelerator mass spectrometer. Curr. Sci. 116 (3), 361–363.

Biswas, S.K., 2016, November. Tectonic framework, structure and tectonic evolution of Kutch Basin, western India. In: Conference GSI, pp. 129–150.

Biswas, S.K., 2016, Novembe. Mesozoic and tertiary stratigraphy of kutch*(kachchh) A review. In: Conference GSI, pp. 1–24.

Bruce, D., Hancock, P., 1969. Note on the temperature stability of wüstite in surface oxide films on iron. Br. Corrosion J. 4 (4), 221–222. https://doi.org/10.1179/000705969798325361.

Cameron, E.N., 1970. Opaque minerals in lunar samples. Science 167 (3918), 623–625.

Canup, R.M., Asphaug, E., 2001. Origin of the Moon in a giant impact near the end of the Earth's formation. Nature 412 (6848), 708–712.

Chandran, S.R., James, S., Aswathi, J., Padmakumar, D., Binoj Kumar, R.B., Chavan, A., Vivek Bhore, Krishna Kajale, Bhandari, S., Sajinkumar, K.S., 2022. Lonar Impact Crater, India: The best-preserved terrestrial hypervelocity impact crater in a basaltic terrain as a potential Global Geopark. Geoheritage 14, 130.

Chandran, S.R., James, S., Aswathi, J., Padmakumar, D., Sadeeda, M.T., Binoj Kumar, R. B., Chavan, A., Bhandari, S., Sajinkumar, K.S., 2023. A compendium of the best-preserved terrestrial hypervelocity impact crater in a basaltic terrain: the Lonar, India. Earth Sci. Rev. 243, 104508.

Chavan, A., Sarkar, S., Thakkar, A., Solanki, J., Jani, C., Bhandari, S., et al., 2022. Terrestrial martian analog heritage of kachchh basin, western India. Geoheritage 14 (1), 33.

Cox, M.A., Cavosie, A.J., Ferrière, L., Timms, N.E., Bland, P.A., Miljković, K., et al., 2019. Shocked quartz in polymict impact breccia from the Upper Cretaceous Yallalie impact structure in Western Australia. Meteoritics Planet Sci. 54 (3), 621–637.

D'Orazio, M., Folco, L., Zeoli, A., Cordier, C., 2011. Gebel Kamil: the iron meteorite that formed the Kamil crater (Egypt). Meteoritics Planet Sci. 46 (8), 1179–1196.

Dabhi, M., Chavan, A., Thakkar, A., Chauhan, G., Bhagora, R., Chauhan, N., et al., 2022a. Climatic history from early Weichselian (MIS 5D-C) valley-fill deposits and associated factors for basin sedimentation, mainland Kachchh, western India. Quat. Int. 642, 17–28.

Dabhi, M., Thakkar, A., Chavan, A., Chauhan, G., Bhagora, R., Chauhan, N., et al., 2022b. Mid-late Holocene climatic reconstruction from coastal dunes of the western Kachchh, India. Quat. Int. 642, 29–40.

Daly, R.A., 1946. Origin of the Moon and its topography. Proc. Am. Phil. Soc. 90 (2), 104–119.

Deer, W.A., Howie, R.A., Zussman, J., 2013. An Introduction to the Rock-Forming Minerals. Mineralogical Society of Great Britain and Ireland.

Dence, M.R., 1971. Impact melts. J. Geophys. Res. 76 (23), 5552–5565.

Desai, B.G., Biswas, S.K., 2018. Postrift deltaic sedimentation in western Kachchh Basin: insights from ichnology and sedimentology. Palaeogeogr. Palaeoclimatol. Palaeoecol. 504, 104–124.

Ding, Y., Veblen, D.R., 2004. Impactite from Henbury, Australia. Am. Mineral. 89 (7), 961–968.

Dressler, B.O., Reimold, W.U., 2001. Terrestrial impact melt rocks and glasses. Earth Sci. Rev. 56 (1–4), 205–284.

Dressler, B.O., Crabtree, D., Schuraytz, B.C., 1997. Incipient melt formation and devitrification at the Wanapitei impact structure, Ontario, Canada. Meteoritics Planet Sci. 32 (2), 249–258.

Folco, L., Mellini, M., 1997. Crystal chemistry of meteoritic kirschsteinite. Eur. J. Mineral 9 (5), 969–973.

French, B.M., 1998. Traces of Catastrophe: A Handbook of Shock-Metamorphic Effects in Terrestrial Meteorite Impact Structures. No. LPI-Contrib-954).

Ganino, C., Libourel, G., 2017. Reduced and unstratified crust in CV chondrite parent body. Nat. Commun. 8 (1), 261.

Ganino, C., Libourel, G., Jacomet, S., Tottereau, O., 2017, March. Formation of secondary Ca-Fe-rich minerals assemblages in CV chondrites. In: 48th Annual Lunar and Planetary Science Conference, vol. 1964, p. 1396.

Goderis, S., Kalleson, E., Tagle, R., Dypvik, H., Schmitt, R.T., Erzinger, J., Claeys, P., 2009. A non-magmatic iron projectile for the Gardnos impact event. Chem. Geol. 258 (3–4), 145–156.

Goderis, S., Paquay, F., Claeys, P., Osinski, G., Pierazzo, E., 2013. Projectile identification in terrestrial impact structures and ejecta material. Impact Cratering: Processes and Products. Wiley-Blackwell, New York, pp. 223–239.

Gottwald, M., Kenkmann, T., Reimold, W.U., 2020. Terrestrial Impact Structures. The TanDEM-X Atlas, vol. 1. Verlag Dr. Friedrich Pfeil, München. Africa, North/Central America, South America. Vol. 2: Asia, Australia. *Europe*.

Govindaraju, K., 1994. Compilation of working values and sample description for 383 geostandards. Geostand. Newsl. 18, 1–158.

Grieve, R.A., 1987. Terrestrial impact structures. Annu. Rev. Earth Planet Sci. 15 (1), 245–270.

Grieve, R.A., 2001. The terrestrial cratering record. In: Accretion of Extraterrestrial Matter throughout Earth's History. Springer US, Boston, MA, pp. 379–402.

Grieve, R.A., 2005. Economic natural resource deposits at terrestrial impact structures. Geological Society, London, Special Publications 248 (1), 1–29.

Grieve, R.A., Cintala, M.J., 1992. An analysis of differential impact melt-crater scaling and implications for the terrestrial impact record. Meteoritics 27 (5), 526–538.

Grieve, R.A., Kring, D.A., 2007. The Geologic Record of Destructive Impact Events on Earth. Comet/asteroid impacts and human society: an interdisciplinary approach, pp. 3–24.

Gurov, E.P., Koeberl, C., Reimold, W.U., 1998. Petrography and geochemistry of target rocks and impactites from the Ilyinets Crater, Ukraine. Meteoritics Planet Sci. 33 (6), 1317–1333.

Hamann, C., 2018. *Projectile-target Interaction and Rapid, High-Temperature Geochemical Processes in Impact Melts* (Doctoral Dissertation).

Henrichs, L.F., Kontny, A., Reznik, B., Gerhards, U., Göttlicher, J., Genssle, T., Schilling, F., 2020. Shock-induced formation of wüstite and fayalite in a magnetite-quartz target rock. Meteoritics Planet Sci. 55 (1), 56–66.

Indu, G.K., James, S., Chandran, S.R., Aneeshkumar, V., Keerthy, S., Oommen, T., Sajinkumar, K.S., 2022. Deriving a denudation index for terrestrial meteorite impact craters using drainages as proxies. Geomorphology 397, 108007.

James, S., Chandran, S.R., Aswathi, J., Padmakumar, D., Sajinkumar, K.S., 2023. Geologic, geomorphic, tectonic, and paleoclimatic controls on the distribution and preservation of Chicxulub distal ejecta: a global perspective. Earth Sci. Rev., 104545

James, S., Chandran, S.R., Aswathi, J., Padmakumar, D., Aneeshkumar, V., Indu, G.K., Sajinkumar, K.S., 2022a. Meteorite impact crater positions based on paleo-positions and its unrestrained latitudinal distribution. Planet. Space Sci. 222, 105575.

James, S., Chandran, S.R., Santosh, M., Pradeepkumar, A.P., Praveen, M.N., Sajinkumar, K.S., 2022b. Meteorite impact craters as hotspots for mineral resources and energy fuels: a global review. Energy Geoscience 3 (2), 136–146.
Jochum, K.P., Nohl, U., Herwig, K., Lammel, E., Stoll, B., Hofmann, A.W., 2005. GeoReM: a new geochemical database for reference materials and isotopic standards. Geostand. Geoanal. Res. 29 (3), 333–338.
Kalleson, E., Corfu, F., Dypvik, H., 2009. U–Pb systematics of zircon and titanite from the Gardnos impact structure, Norway: evidence for impact at 546 Ma? Geochem. Cosmochim. Acta 73 (10), 3077–3092.
Karanth, R.V., 2006. The unusual impact crater of Luna in Kachchh, western India. Geological Society of India 68 (5), 927–928.
Karanth, R.V., Thakker, P.S., Gadhavi, M.S., 2006. A preliminary report on the possible impact crater of Kachchh. Curr. Sci. 91 (7), 877–879. https://www.jstor.org/stable/24094282.
Keerthy, S., Vishnu, C.L., Li, S.S., Reshma, N., Praveen, M.N., Oommen, T., Singh, S.P., Sajinkumar, K.S., 2019. Reconstructing the dimension of Dhala Impact Crater, Central India, through integrated geographic information system and geological records. Planet. Space Sci. 177, 104691.
Kenkmann, T., 2021. The terrestrial impact crater record: a statistical analysis of morphologies, structures, ages, lithologies, and more. Meteoritics Planet Sci. 56 (5), 1024–1070.
Kjær, K.H., Larsen, N.K., Binder, T., Bjørk, A.A., Eisen, O., Fahnestock, M.A., et al., 2018. A large impact crater beneath Hiawatha Glacier in northwest Greenland. Sci. Adv. 4 (11), eaar8173.
Kracher, A., Willis, J., Wasson, J.T., 1980. Chemical classification of iron meteorites—IX. A new group (IIF), revision of IAB and IIICD, and data on 57 additional irons. Geochem. Cosmochim. Acta 44 (6), 773–787.
Krishna, A.K., Murthy, N.N., Govil, P.K., 2007. Multielement analysis of soils by wavelength-dispersive X-ray fluorescence spectrometry. Atomic Spectroscopy-norwalk Connecticut- 28 (6), 202.
Kumar, A., Maurya, D.M., Khonde, N., Phartiyal, B., Arif, M., Giosan, L., Chamyal, L.S., 2021. Holocene paleoenvironmental changes in the marginal marine basin of Great Rann of Kachchh, western India: insights from sedimentological and mineral magnetic studies on ā 60 m long core. Quat. Int. 599, 138–147.
Kyte, F.T., Bostwick, J.A., 1995. Magnesioferrite spinel in Cretaceous/Tertiary boundary sediments of the Pacific basin: remnants of hot, early ejecta from the Chicxulub impact? Earth Planet Sci. Lett. 132 (1–4), 113–127.
Li, S.S., Keerthy, S., Santosh, M., Singh, S.P., Deering, C., Satyanarayanan, M., Praveen, M.N., Aneeshkumar, V., Indu, G.K., Anilkumar, Y., Sajinkumar, K.S., 2018. Anatomy of impactites and shocked zircon grains from Dhala reveals Paleoproterozoic meteorite impact in the Archean basement rocks of Central India. Gondwana Res. 54, 81–101.
Lim, J., Hong, S.S., Han, M., Yi, S., Kim, S.W., 2021. First finding of impact cratering in the Korean Peninsula. Gondwana Res. 91, 121–128.
Lukanin, O.A., Kadik, A.A., 2007. Decompression mechanism of ferric iron reduction in tektite melts during their formation in the impact process. Geochem. Int. 45, 857–881.
Makwana, N., Prizomwala, S.P., Das, A., Phartiyal, B., Sodhi, A., Vedpathak, C., 2021. Reconstructing the climate variability during the last 5000 years from the Banni plains, kachchh, western India. Front. Earth Sci. 9, 679689.
Mänttäri, I., Kohonen, J., Kujala, H., Pihlaja, P., 2004. A revised age for the Sääksjärvi meteorite impact, southwestern Finland: the connexion with a Caledonian foreland basin. IGC Conf 32. *Abstract* (No. 1434).
Maruyama, S., Santosh, M., 2017. Frontiers in early Earth history and primordial life-Part I. Geosci. Front. 8 (2), 211–213.
Maurya, D.M., Tiwari, M., Rajawat, A.S., Kumar, H., Khonde, N., Chamyal, L.S., 2016, November. Geomorphic characterization of the Banni Plain, Kachchh, using orbital imaging radar (RISAT 1C) and optical remote sensing data. In: Conference GSI, pp. 168–178.
Melosh, H.J., 1989. Impact Cratering: A Geologic Process. Clarendon Press, Oxford. New York: Oxford University Press.
Mittlefehldt, D.W., Hörz, F., See, T.H., Scott, E.R., Mertzman, S.A., 2005. Geochemistry of target rocks, impact-melt particles, and metallic spherules from Meteor Crater, Arizona: empirical evidence on the impact process. In: Large Meteorite Impacts III, vol. 384. Geological Society of America Boulder, CO, pp. 367–390.
Mittlefehldt, D.W., See, T.H., Hörz, F., 1992. Dissemination and fractionation of projectile materials in the impact melts from Wabar Crater, Saudi Arabia. Meteoritics 27 (4), 361–370.
Morrison, S.M., Hazen, R.M., 2021. An evolutionary system of mineralogy, Part IV: planetesimal differentiation and impact mineralization (4566 to 4560 Ma). Am. Mineral. 106 (5), 730–761.
Ngangom, M., Bhandari, S., Thakkar, M.G., Shukla, A.D., Juyal, N., 2017. Mid-Holocene extreme hydrological events in the eastern Great Rann of Kachchh, western India. Quat. Int. 443, 188–199.
Osinski, G.R., Pierazzo, E., 2013. Impact cratering: processes and products. Impact Cratering 1–20.
Osinski, G.R., Grieve, R.A., Bleacher, J.E., Neish, C.D., Pilles, E.A., Tornabene, L.L., 2018. Igneous rocks formed by hypervelocity impact. J. Volcanol. Geoth. Res. 353, 25–54.
Osinski, G.R., Grieve, R.A., Ferriere, L., Losiak, A., Pickersgill, A.E., Cavosie, A.J., et al., 2022. Impact Earth: a review of the terrestrial impact record. Earth Sci. Rev. 232, 104112.
Pesonen, L.J., Mader, D., Gurov, E.P., Koeberl, C., Kinnunen, K.A., Donadini, F., Handler, R., 2004. Paleomagnetism and 40 Ar/39 Ar age determinations of impactites from the Ilyinets structure, Ukraine. Cratering in Marine Environments and on Ice, pp. 251–280.
Pillai, A.A., Anoop, A., Sankaran, M., Sanyal, P., Jha, D.K., Ratnam, J., 2017. Mid-late Holocene vegetation response to climatic drivers and biotic disturbances in the Banni grasslands of western India. Palaeogeogr. Palaeoclimatol. Palaeoecol. 485, 869–878.
Plado, J., Hietala, S., Kreitsmann, T., Lerssi, J., Nenonen, J., Pesonen, L.J., 2018. Summanen, a new meteorite impact structure in Central Finland. Meteoritics Planet Sci. 53 (11), 2413–2426.
Possehl, G.L., 2002. The Indus Civilization: a Contemporary Perspective. Rowman Altamira.
Prescott, J.R., Robertson, G.B., Shoemaker, C., Shoemaker, E.M., Wynn, J., 2004. Luminescence dating of the Wabar meteorite craters, Saudi Arabia. J. Geophys. Res.: Planets 109 (E1).
Reimold, W.U., Koeberl, C., Gibson, R.L., Dressler, B.O., 2005. Economic mineral deposits in impact structures: a review. Impact tectonics 479–552.
Roy, B., Merh, S.S., 1982. The Great Rann of Kutch–an intriguing quaternary terrain. National seminar on quaternary environments 1, 100–108.
Rudnick, R.L., Gao, S., 2014. The composition of the continental crust, the crust. Treatise on Geochemistry 3.
Sant, D.A., Parvez, I.A., Rangarajan, G., Patel, S.J., Bhatt, M.N., Salam, T.S., 2017. Subsurface profiling along Banni Plains and bounding faults, Kachchh, Western India using microtremors method. J. Asian Earth Sci. 146, 326–336.
Santosh, M., Arai, T., Maruyama, S., 2017. Hadean Earth and primordial continents: the cradle of prebiotic life. Geosci. Front. 8 (2), 309–327.
Satyanarayanan, M., Balaram, V., Sawant, S.S., Subramanyam, K.S.V., Krishna, G.V., Dasaram, B., Manikyamba, C., 2018. Rapid determination of REEs, PGEs, and other trace elements in geological and environmental materials by high resolution inductively coupled plasma mass spectrometry. Atom. Spectros 39 (1), 1–15.
Schmieder, M., Kring, D.A., 2020. Earth's impact events through geologic time: a list of recommended ages for terrestrial impact structures and deposits. Astrobiology 20 (1), 91–141.
Schulte, P., Alegret, L., Arenillas, I., Arz, J.A., Barton, P.J., Bown, P.R., et al., 2010. The Chicxulub asteroid impact and mass extinction at the Cretaceous-Paleogene boundary. Science 327 (5970), 1214–1218.
Scotese, C.R., Song, H., Mills, B.J., van der Meer, D.G., 2021. Phanerozoic paleotemperatures: the earth's changing climate during the last 540 million years. Earth Sci. Rev. 215, 103503.
Shoemaker, E.M., 1983. Asteroid and comet bombardment of the Earth. Annu. Rev. Earth Planet Sci. 11 (1), 461–494.
Singh, N., Kar, A., 2001. Characteristics of major soils of Banni mudflat in arid western India and their relationship with topography. J. Arid Environ. 48 (4), 509–520.
Sokol, E., Sharygin, V., Kalugin, V., Volkova, N., Nigmatulina, E., 2002. Fayalite and kirschsteinite solid solutions in melts from burned spoil-heaps, South Urals, Russia. Eur. J. Mineral 14 (4), 795–807.
Sorcar, N., Mukherjee, S., Pant, N.C., Dev, J.A., Nishanth, N., 2021. Chemical dating of monazite: testing of analytical protocol for U–Th–total Pb using CAMECA SXFive tactis EPMA at the national Centre for earth science studies, thiruvananthapuram, India. J. Earth Syst. Sci. 130, 1–11.
Svetsov, V.V., 2005. Numerical simulations of very large impacts on the Earth. Planet. Space Sci. 53 (12), 1205–1220.
Tagle, R., Hecht, L., 2006. Geochemical identification of projectiles in impact rocks. Meteoritics Planet Sci. 41 (11), 1721–1735.
Tagle, R., Schmitt, R.T., Erzinger, J., 2009. Identification of the projectile component in the impact structures Rochechouart, France and Sääksjärvi, Finland: implications for the impactor population for the earth. Geochem. Cosmochim. Acta 73 (16), 4891–4906.
Välja, R., Kirsimäe, K., Koeberl, C., Boamah, D., Kirs, J., 2019. Incipient devitrification of impact melt particles at Bosumtwi crater, Ghana: implications for suevite cooling history and melt dispersion. Meteoritics Planet Sci. 54 (10), 2557–2572.
Whitehead, J., Grieve, R.A.F., Spray, J.G., 2002. Mineralogy and petrology of melt rocks from the Popigai impact structure, Siberia. Meteoritics Planet Sci. 37 (5), 623–647.
Wittmann, Axel, Schmitt, Ralf T., Hecht, Lutz, Kring, David A., Reimold, W. Uwe, Povenmire, Harold, Gohn, G.S., Koeberl, C., Miller, K.G., 2009. Petrology of Impact Melt Rocks from the Chesapeake Bay Crater, vol. 458. Special Paper-Geological Association of America, USA, pp. 377–396.
Zahnle, K., Sleep, N.H., 1996. Impacts and the Early Evolution of Life, Comets and the Origin and Evolution of Life PJ Thomas. CF Chyba, pp. 175–208. CP McKay.

## Online resources

MetBase: Meteorite Information Database, 1994-2017. GeoPlatform UG, Germany. http://www.metbase.org.

Icarus 385 (2022) 115118

Contents lists available at ScienceDirect

Icarus

journal homepage: www.elsevier.com/locate/icarus

# Terrestrial martian analogues from the Indian subcontinent: Implications for hydrological activity on Mars

Anil Chavan *, Vivek Bhore, Subhash Bhandari *

*Department of Earth and Environmental Science, K.S.K.V. Kachchh University, Bhuj-370001, India*

ARTICLE INFO

*Keywords:*
Terrestrial Martian analogue
Hydrological activity
Kachchh
Deccan Traps
Himalayas

ABSTRACT

Martian geology and surface geomorphic features are grouped under Noachian, Hesperian, and Amazonian eras, based on the crater retention ages and resurfacing ages by crater densities. Comparing the similarities and differences between Martian landforms and their terrestrial analogues promotes an understanding of how surface processes operated on both planets. The study focusses on the processes responsible for the evolution of fluvial valleys on the flanks of volcanic craters and the fluvial terraces with an objective towards ascertaining the role of changing climate, tectonic, and volcanic conditions. We have studied the channels that developed on the flank of volcanic crater Ceraunius Tholus and compared with the monogenetic volcanic field of Dhinodhar Hill which have been significantly modified by fluvial processes. Similarly, the fluvial basins developed on the Hesperian volcanic units of Echus plateau were compared with the Alaldari drainage of Upper Tapi river basin, showing the development of theater-headed channels and valleys, and relative fluvial features showing the strong influence of catastrophic climate and tectonic, which is also supported by the morphometric analysis in modulating the topography. The fluvial terraces developed in the Nubra and Shyok rivers of Ladakh and Upper and Middle reaches of Satluj in Central Himalayas are compared with Noctis fossae on Mars both developed due to the interplay of tectonism and climate.

## 1. Introduction

The availability of high-resolution images and outcrop-level observation boosts scientists to start concentrating on outcrop-level mapping on Mars rather than comprehensive and conventional regional-scale mapping. The most promising approach of studying local-scale features are through analogue studies. The processes like volcanism, valley formation, impact cratering, catastrophic flooding, lake formation, and the secondary mineral deposits on Mars can be better understood by analogue studies (Baker and Milton, 1974; Baker et al., 1983; Mangold et al., 2004; Irwin et al., 2011; Flahaut et al., 2014; Singh et al., 2016; Paramanick et al., 2021). The study of terrestrial analogues allows researchers to characterize the processes and evolution of the Martian surface as terrestrial landform evolution is often well understood (Hobbs et al., 2014; Chapman et al., 2007). The detailed investigation of the processes such as low viscosity volcanism (e.g., Hawaii, Snake River, Idaho), wrinkle ridges (e.g., Columbia River Plateau), outflow channels (e.g., Channeled Scablands), valley networks (e.g., Colorado Plateau and Devon Island), gullies (e.g., Devon Island, Greenland, and Ladakh, India), paleo-lakes (e.g., Bonneville, Utah and Devon Island), aeolian features (e.g., Southern California and Southwest Egypt), glacial/permafrost features, (e.g., Alaska, Devon Island, and Canada), volcano-ice interactions (e.g., Iceland), fluvial features (e.g., Death Valley, Mojave), banded iron formations (e.g., Canada) (Farr et al., 2002 and references therein; Sinha et al., 2017) have been investigated in detail on terrestrial analogues site. The study of all these features and related formation and evolution processes operating in terrestrial environments and extrapolating how similar processes could have affected the Martian landforms (Farr et al., 2002). Worldwide analogue localities have been marked for their genesis, geomorphological expression, and processes behind their formations; but very few are reported from the Indian subcontinent (Shukla et al., 2014; Sinha et al., 2017; Bhattacharya et al., 2016; Chavan and Bhandari, 2019; Ray et al., 2021; Chavan et al., 2021a, 2022).

This study, thus concentrates on a few potential locations in India, which encompasses the diverse geological milieu such as Kachchh, Deccan Trappean of Western Ghats, and the Himalayas (Fig. 1). The analogue sites selected thus mimics the Martian geomorphological

* Corresponding authors.
*E-mail addresses:* asac.anil@gmail.com (A. Chavan), subhashbhandari@gmail.com (S. Bhandari).

https://doi.org/10.1016/j.icarus.2022.115118
Received 7 December 2021; Received in revised form 11 May 2022; Accepted 29 May 2022
Available online 3 June 2022
0019-1035/© 2022 Elsevier Inc. All rights reserved.

events that occurred throughout its timeframe. And those are the remarkable valleys developed on the flanks of the volcanic crater by hydrodynamic action on the preexisting topography of a shield volcano known as Dhinodhar hill (Biswas and Deshpande, 1973), forming radial drainage pattern. The alluvial fans are the prime markers of fluvial deposits when the stream debouches into the lower elevation gradient. Alluvial fans are also marked on larger and smaller valleys (mapped on the high-resolution CTX and HiRISE data) of Ceraunius Tholus volcano's flank when streams meet the surrounding flat surfaces. The second site has a narrow intermontane valley on the basaltic terrain plateau of Deccan trap along the northwestern ghat cliffs known as Alaldari valley. The geomorphic features such as knickpoint, theater-headed valleys, hanging channels, river terraces, river islands, lakes within the stream, and debris flow deposits indicate an episodic flow of water and catastrophic flooding that occurred within the area. The narrow V-shaped valley has similarities in shape and geomorphology of the canyon on the Hesperian terrain of western Echus plateau, which has also experienced volcanism and fluvial activity (Mangold et al., 2008; Chapman et al., 2010a, 2010b). The morphometric parameter for both the basin implies similar attributes.

The studies of the Martian surface have speculated the role of water in shaping the planetary landscape (McCauley et al., 1972; Carr, 1981, 1996; Hynek and Phillips, 2003). The valley networks are characterized by dendritic to semi-dendritic drainage patterns, which show striking similarities with terrestrial rivers forming clear drainage basins and rivers like networks or lineaments. The fluvial or fluvial-like landforms on Mars have revealed low-lying, elongated troughs surrounded by elevated topographic valleys (Baker, 1982; Baker et al., 1992, 2015). On the same lines, terrestrial fluvial terraces have a striking resemblance with the large channels of Mars (Duran et al., 2019), have been analyzed in the present work. Noctis Fossae, a complicated system having a domino effect of both surface runoff and tectonic episodes (Chavan et al., 2021 (under review)) on its surface, having recorded N-S to NNE-SSW trending channels forming U—V shaped valleys, terraces,

**Fig. 1.** Map of Indian Sub-continent with terrestrial analogue sites 1. Dinodhar hill (Kachchh) 2. Alaldari Valley (Maharashtra) 3. Himalayan analogues: a). Nubra-Shyok, Ladakh; b). Satluj River, Himachal Pradesh.

surfaces, and deep gorges on the Hesperian volcanic rocks is analyzed here for fluvial activities. Prominent glacio-fluvial features have been documented in the Higher Himalayas. This work analyzes the glacio-fluvial valleys from Nubra and Shyok, Ladakh, and lesser Himalayan domain of the middle Satluj Valley, interpreting high glacial and fluvial discharge and correlated with Martian fluvial features.

The presence of well-developed, water-related morphologies like drainage systems makes the area under study interesting from a geological and geomorphological point of view. Our results characterize Martian valley network morphological variability and show that the morphology of most valleys best corresponds to either fluvial or subglacial incision. We complement our analysis with a geomorphological comparison to terrestrial analogues and interpret those similar fluvial processes occurred on both planets, reinforcing the history of water on Mars and constraining the climatic conditions that prevailed for the potential origin of observed fluvial environments on Mars.

## 2. Data and method

A variety of data is available for Mars by different Orbital and Rover missions, which have revolutionized the way we understand the Planet since the inception of space missions from 1970s. Different imaging cameras and spectrometers such as the Viking Orbiter Visual Imaging Subsystems (VIS) (Thorpe, 1976), the Mars Orbiter Camera (MOC) of Mars Global Surveyor (Malin et al., 1998), the Thermal Emission Imaging Systems (THEMIS) (Christensen et al., 2003, 2004) High-Resolution Stereo Camera (HRSC) (Neukum et al., 2004),the Mars Reconnaissance Orbiter's High-Resolution Imaging Science Experiment (HiRISE) (McEwen et al., 2007), Context Imager (CTX) (Malin et al., 2007) on the Mars Reconnaissance Orbiter (MRO), the Compact Reconnaissance Imaging Spectrometer for Mars (CRISM) (Murchie et al., 2007), and Mars Color Camera (MCC) onboard Mars Orbiter Mission (Arya et al., 2015) have acquired images of Mars.

The data used for the present detailed studies consists of Context Camera (CTX) images having ~6 m/pixel resolution and width ~ 30 km (Malin et al., 2007), in the form of pyramidized TIFF files. Thorough studies of the morphology and geometry of valleys and detailed mapping of the geomorphic features have been performed using images available, downloaded from the Mars Image Explorer website of the Arizona State University (http://viewer.mars.asu.edu/viewer/ctx#$T$=0). Image details with product ID and their attributes are provided in Supplementary Tables 1 and 2. These TIFF files have been used to create a mosaic of the study areas to map the geomorphic features (Chavan et al., 2021b) and Craters on the GIS platform (ArcGIS (10.4.1)). These CTX images, mosaicked to create a background map, and is used to prepare a geomorphological map for the Ceraunius Tholus, Valleys on Echus Plateau, and fluvial terraces within Noctis fossae. The data set was processed and mosaicked at a 6 m/pixel resolution to map all geomorphological features within the study area. GIS platform was utilized for map production, data compilation, and mapped information analysis. The linear and other geomorphic features such as major lineaments, grabens, dykes, alluvial fans, gullies, and valleys with small channels were marked manually by using photogrammetric tools, their tonal, shape, size, shadows, albedo, and textural differences as well as elevation gradients in ArcGIS (10.4.1).

Apart from CTX images, for understanding the 3D aspects of an area, MOLA-HRSC DEM/DTM images (~50 to ~100 m/pixel) were utilized. The MOLA-HRSC DEM/DTM data used to make the elevation profile of significant valleys and cross-section profiles are extracted using ArcGIS (10.4.1). The mosaicked CTX images and DEM/DTM data were overlapped using the GIS platform to extract elevation and river profile. The morphometric analysis of all valleys was done using both the data on ArcGIS (10.4.1) platform. The channels/drainages were drawn using the MOLA-HRSC DEM dataset and connected by neglecting the craters younger to the channels with flow continuity model (Stepinski and Collier, 2004) to create the drainage map of the area.

The Survey of India (SOI) toposheets have been used for mapping the terrestrial geomorphic features to delineate drainages, contour maps, and other linear features in the analogue valleys. Further, the drainages have been drawn on high-resolution satellite images using the flow continuity model on the ArcGIS (10.4.1) platform. Additionally, to understand 3D aspects of valleys and streams, SRTM worldwide elevation data (3 arc-seconds resolution) and ASTER GDEM v2 worldwide elevation data (1 arc-seconds resolution) is utilized. These datasets are processed and used in ArcGIS (10.4.1) for the morphometric analysis and for the extraction of longitudinal and cross profiles within the study area. The landforms were marked on the GIS platform, verified, and ground-truthing was done by extensive fieldwork in all selected analogue sites.

## 3. Martian and terrestrial corresponding analogues sites investigated

### 3.1. Valleys on the flank of Volcanic crater

Mars has witnessed volcanic activity from its early evolutionary phase; the largest volcano within our solar system is reported from Mars. The present volcano northeast of the Tharsis rise has a well-developed radial drainage system on its flank, indicating fluvial processes have reshaped the topography. The Ceraunius Tholus (Centered at Lat. 24.001549° and Long. -97.131771°) is a shield (Plescia, 1999), leading to the fissure type of eruption, which dates to the Late Hesperian Epoch (Plescia, 1999 and References therein). A similar fissure type of volcanic crater, Dhinodhar hill (Centered at Lat. 23.455932° and Long. 69.347626°) (Biswas and Deshpande, 1973), has reported a radial drainage pattern within a few sq. km. areas serves as the analogue site for studying geomorphic and fluvial aspects of the processes that occurred on Mars.

#### 3.1.1. Martian case of study: Ceraunius Tholus

Mars has witnessed volcanism and the formation of volcanoes since the early phase of evolution (Carr and Head, 2010). In the present work, we have studied the volcanic crater Ceraunius Tholus. At the northeast of the Tharsis province, three volcanoes Uranius Patera, Ceraunius Tholus, and Uranius Tholus, are observed as a shield (Plescia, 1999) dating back to the Late Hesperian Epoch (Plescia, 1999). Crater frequency for Ceraunius Tholus, with isochrones from Hartmann (2005), suggests a mid to late Hesperian age ~ 3.5 Gyr (Fassett and Head, 2007) for the edifice. The rim of the Ceraunius Tholus caldera is asymmetrical (Crumpler et al., 1996), with the eastern portion of the rim lying more than 1 km below the western rim (Fig. 2). The highest elevation contour in the area is 8500 m at the eastern rim and ~ 7500 m at the western side of the crater forming asymmetrical geometry for the valley initiation. In contrast, the lowest contour at the plain is 2500 m along the crater's circumference (Fig. 2C and D). Further, it lowers down to 1500 m in Rahe Crater. The area's general slope is about ~6°–11°with, a dimension of 125 × 94 km encompassing a volume of 2.2 × $10^4$ $km^3$, and Caldera diameter is measured as 25 × 22 km with 0.5–2.0 km depth. Several linear troughs occur on the flank, forming a channel resulting in the radial drainage system (Figs. 2A and 2B). Lava flows are not observed much often; further, the impact craters lack ejecta material on the flanks, that may be buried or removed by erosional activity. The linear troughs with few tributaries suggest a juvenile drainage system of a relatively short fluvial episode which might have occurred concurrently during the active phase of volcanism.

The width of most of the valleys remains constant, ranging from~200–600 m in 0.6–1 km transect, while very few are more than one kilometer wide. It moderately increases to few meters downstream with the change in slope gradient of the valley floor. The CTX image data allows separate observation from the previously reported probable inferences with the low-resolution dataset. Most valleys extend to the base of the edifice, forming fan deposits at the bottom of the plain, where

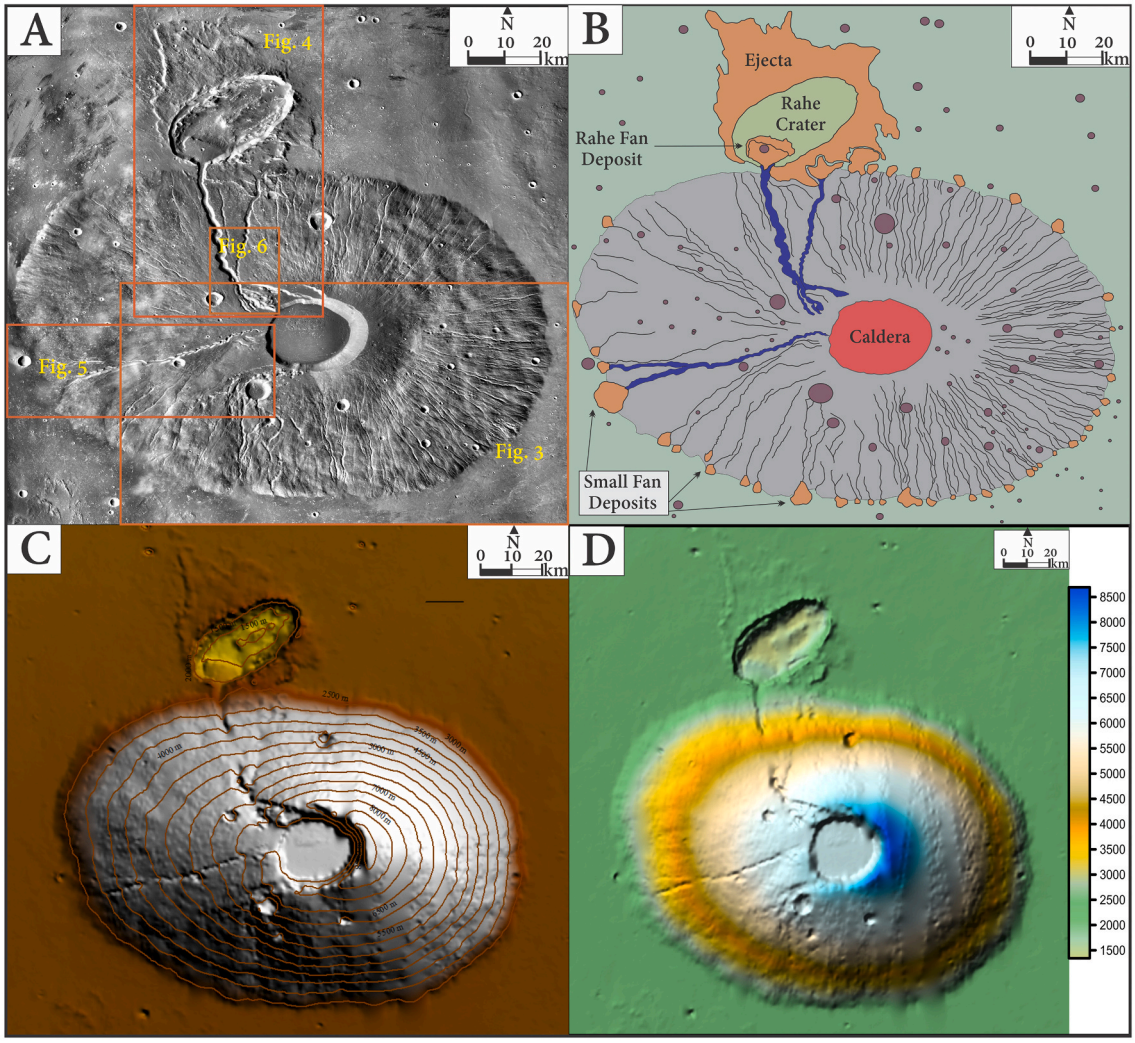


**Fig. 2.** Satellite images of Ceraunius Tholus modified after Chavan et al., 2022. A). CTX image mosaic of Ceraunius Tholus boxed areas showing Figs. 3, 4, 5, and 6 locations; B). Geological, Geomorphological, and drainage map of Ceraunius Tholus (after Fassett and Head, 2007); C). Contour map of Ceraunius Tholus; D). Shaded Relief map of Ceraunius Tholus.

there is a break in slope. The geological history of Ceraunius Tholus is interpreted as a Basaltic shield volcano (Gulick and Baker, 1990; Plescia, 1999).

The valleys on the Ceraunius Tholus are divided into two categories based on the width of the valley 1) Small Valleys and 2) Large Valleys (Figs.3, 4 and 5) (Fassett and Head, 2007). Small valleys incise much of the surface of Ceraunius Tholus. They are less dense on the western flank and become denser on the southern and eastern flanks. These small valleys originate just below the summit rim and extend down the flanks in an approximately subparallel manner, with few tributaries and a small junction angle that is not more than a second-order stream (Strahler, 1957). Further, amongst three more extensive larger valleys, one trend in the *E*-W direction, whereas the other two are in N-S to NNE-SSW direction.

Two types of alluvial fans have been classified around Ceraunius Tholus flank based on the morphology and depositional condition, one where channels open into the Rahe crater at the north, providing accommodation space for sediment (Fig. 4). The Rahe crater becomes a lake, leading to the scarp formation on the floor of Rahe crater (Fig. 3) with sediment load provided by the valley discharge. The other small alluvial fans observed along the crater flank's circumference, where the valleys meet to a much broader area. At this point, the aqueous medium is more widely dispersed, and the sediment load is dropped to form the fan (Figs. 3 and 5).

There are three major valleys (Fig. 4), one flowing from South to North (Figs. 4A and 4B), originating at the caldera rim's summit. The valley's total length is ~70 km and varying width of ~1–3 km (Fig. 4B) from South to North direction. The maximum thickness is observed when the valley meets Rahe crater. The valley erodes the Rahe crater rim and further draws down the sediment load to form an alluvial fan. The crosscutting relationship with the Rahe crater rim indicates that there was fluvial activity after its formation. Valley shape changes from south to north at a higher elevation, the valley has attained a V-shape showing the relatively early stage of its formation. Whereas at lower reaches valley acquires U shape, indicating a higher rate of erosion with an increase in the water supply. The valleys' longitudinal profile (Fig. 4B, Profile AA') indicates few knickpoints along the valley channel. These maybe because of a few pit craters or compositional changes in the lithology. Further down the profile, AA' shows a decline in gradient, like any other terrestrial valleys flowing on uniform lithology. There are few escarpments formed within the Rahe crater and the alluvial fan (Fig. 4B). The other valleys, which are relatively shallow and small in width flow from the SSW-NNE direction, form V—U shaped valleys from the upper reaches to the lower, forming an alluvial fan before meeting flat surfaces. Both the valleys have a cross-cutting relationship amongst themselves (Fig. 6). The older valley has a relatively shallower depth.

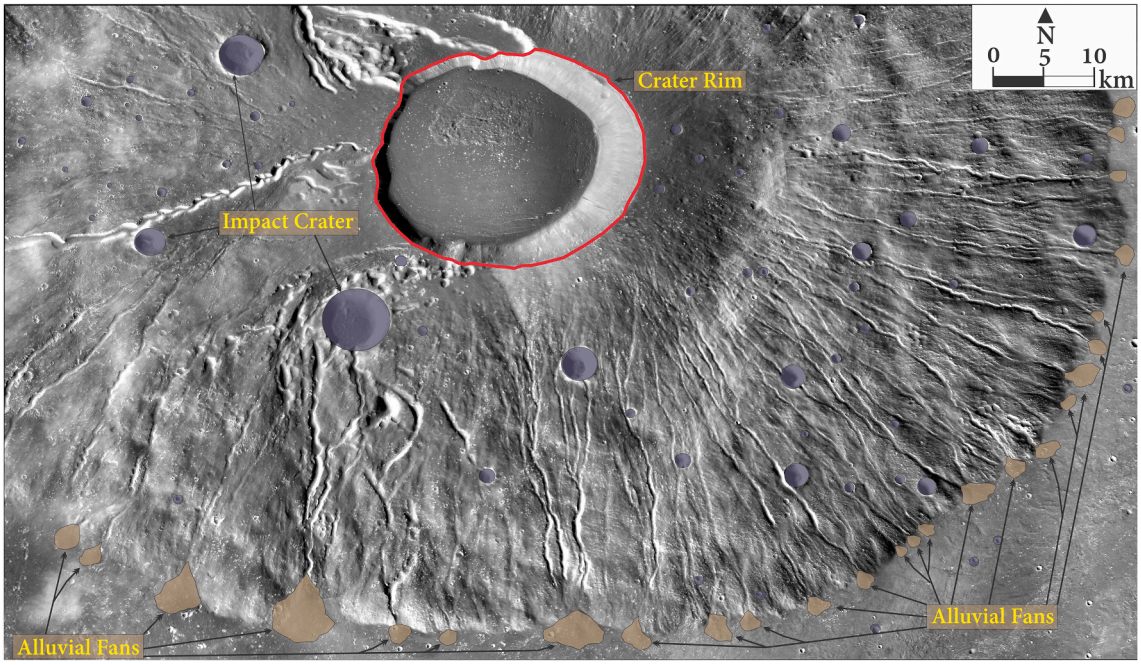


**Fig. 3.** CTX image Mosaic of small valleys with alluvial fans on the flank of Ceraunius Tholus.

The younger valley cut the older valley floor indicating episodic fluvial activity in an area bearing hanging valley and erosional terrace along the bank near the valley curvature.

The third major valley with relatively shallower depth flows from the NEE-SWW direction (Fig. 5A and 5B). This valley starts at 1 km west of the caldera rim from the summit point. The valley has a length of ~72 km and a width of 1–2 km, varying with the slope at upper reaches. The valley maintains V-shape; further, in downslope, it acquires U-shape. Longitudinal profile BB' in Fig. 5 indicate a uniform decline in the slope (Fig. 5B, Profile BB') commonly found in terrestrial river profile with uniform lithology.

The river sinuosity index is calculated for the prominent and pristine valleys on Ceraunius Tholus. River sinuosity index is a ratio of the riverbed's length and the shortest distance between its beginning and end (Mueller, 1968). The attributes for the sinuosity index calculation are given in Table. 1. The sinuosity index is calculated for the eight small valleys (Fig. 2B) and three more extensive valleys (Figs. 4 and 5). The calculated sinuosity index (1.02–1.04) (Table. 1) for the eight smaller valleys (SV1-SV8) (Table.1) on the SW and NE quadrant of Ceraunius Tholus indicate that the valleys are almost straight and run parallel to each other with significantly fewer tributaries. Valleys near the crater's summit in Fig. 3 center-left show little sinuosity next to the impact crater. Similarly, the sinuosity index for the more extensive valleys (LV1-LV3) (Table. 1) is calculated for the valley on the northern flank of Ceraunius Tholus, trending NWW-SEE at upper reaches further changing to SSW-NNE direction. The sinuosity index for this valley is calculated in two segments, and normalized value for both is 1.02, indicating that the valley is straight. Further, the sinuosity index for the other two more extensive valleys, one trending in the N-S direction on the northern flank and the other trending in NEE-SWW direction on the western flank of Ceraunius Tholus, indicate that (1.07 and 1.06) (Table 1) both valleys are sinuous.

### 3.1.2. *Kachchh analogue: Dhinodhar Hill/Than plug*

The conical hills are found in the Northern, Northeastern, and Western peripheral parts of Deccan traps (Sheth et al., 2004) viz. Jabalpur and Pavagadh hills and further interpreted as rootless cones. Similarly, with contemporaneous volcanism associated with the Deccan trap (DT) main event, the early DT flows overlie Mesozoic sedimentary rocks in the Kachchh basin (Biswas and Deshpande, 1973). A similar conical hill along the Kachchh Mainland hill range (Fig. 7) in the form of a volcanic plug is formed by the hardening of melted rocks from the earth's interior (magma) inside an abandoned and eroded volcano (Biswas, 1993). The eruption occurred during the Late Cretaceous period (65–66 Ma) as an eruptive center of Deccan Trap lavas (Pande et al., 1988). It forms the second-highest peak in the Kachchh region, with an altitude of 386 m. The rocks present in this area shows typical pattern of columnar jointing in basaltic lava flows. This unique geomorphic feature originated by the early Deccan trap eruption through preexisting fissures/cracks within the Mesozoic rocks of the Kachchh Basin, provided space to fulfill the magma by the rift generated faulting, namely, along Kachchh Mainland Uplift/Fault (KMU/KMF) (Biswas, 1993).

The southern Kachchh region exposes lava flows and dykes of Deccan tholeiites as well as alkalic basalts (Kshirsagar et al., 2010; Pande et al., 1988; Shukla et al., 2001; Guha et al., 2005). The northern Kachchh exposes many plugs, sills, and dykes of alkali basalt, basanite, and gabbro because of the northern hill range's structural uplifts (Biswas, 1993). These features have been studied in terms of petrology, geochemistry and chronology by several author's (Kshirsagar et al., 2010; Ray et al., 2006; Das et al., 2007; Paul et al., 2008; De, 1981; Mukherjee and Biswas, 1988; Pande et al., 1988; Krishnamurthy et al., 1988, 1999; Simonetti et al., 1998; Karmalkar et al., 2005; Sen et al., 2009). Earlier workers (De, 1964, 1981; Biswas and Deshpande, 1973) considered these to be volcanic craters, noting outward-dipping columnar-jointed lava sheets in the plugs as volcanic vents (Kshirsagar et al., 2010).

The drainage pattern observed at Dhinodhar hill is of radial type (Fig. 8). A characteristic drainage pattern is observed in the volcanic crater where the rim's elevation is highest. Most of the stream starts at the crater's rim. One valley (Fig. 8) flows from the crater's center and further cut through the crater rim at the Eastern flank forming a knickpoint (Fig. 8). Similar drainages are observed with a broader scale on the Ceraunius Tholus volcano on Mars. The observed debris flow valleys (Fig. 7) are formed due to the gravity collapse or influence of water or both activities simultaneously. Similarly, gullies observed constitute three units: Apron, Channel, and Debris deposits (Fig. 7) within a few meters range. Geologically, Mesozoic rocks surround

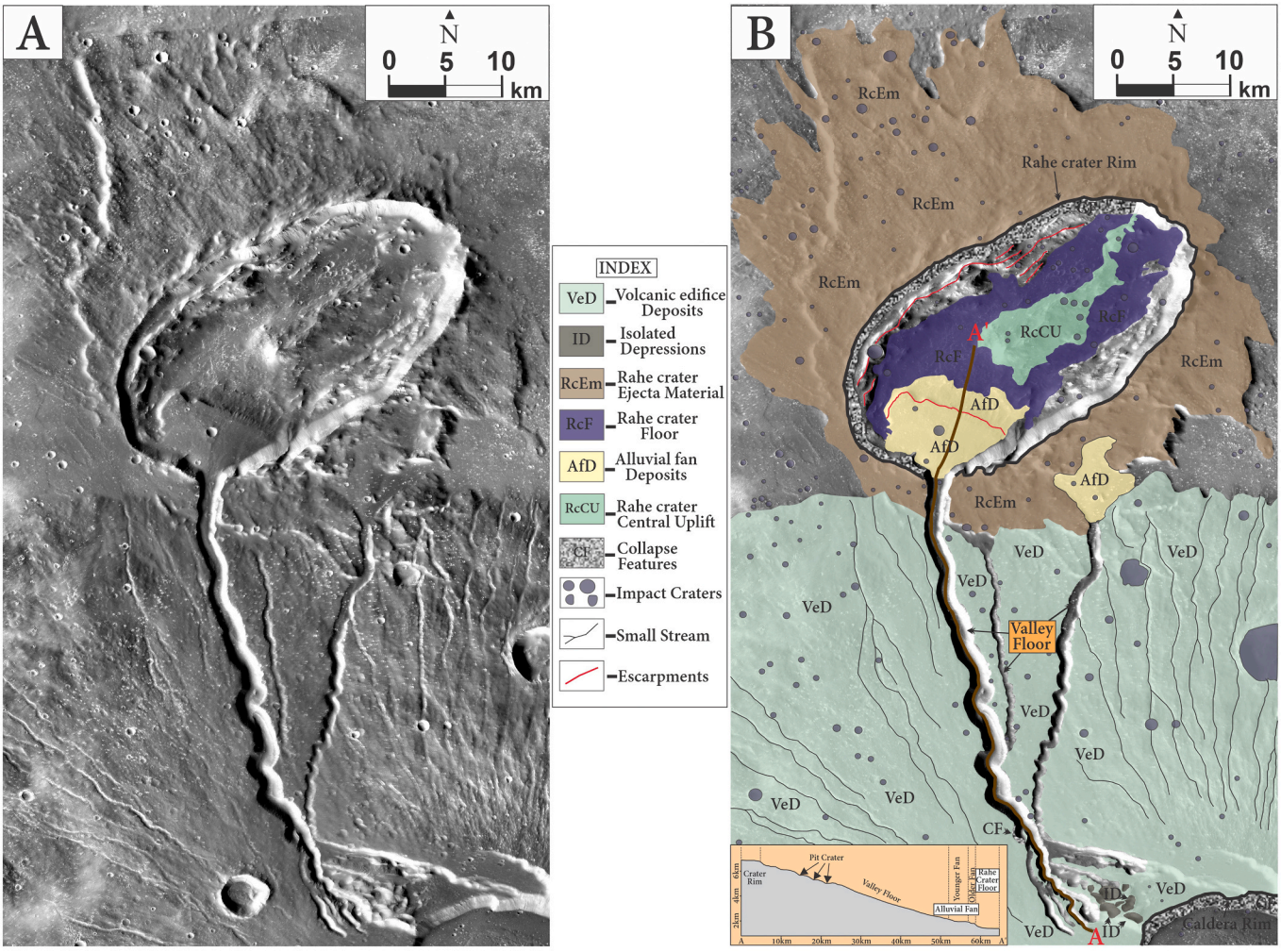


**Fig. 4.** N – NNE flowing large valley and Rahe crater with ejecta material on Northern flank of Ceraunius Tholus. A). CTX image mosaic of the valleys; B). Geomorphic features of North and NNE flowing valleys with a longitudinal profile of central valley AA'.

Dhinodhar hill having a small-scale geomorphic system within a few km$^2$ area; most geomorphic expressions observed give basic information about the factors responsible for formulating the landscape. Crater rim at the upper reaches has nicely preserved columnar joints inclined towards the crater's core. At Dhinodhar Hill, the first order small streams initiate near the crater summit, followed by a debris flow apron at the steep slope gradient. Channels with debris and colluvial fans near the crater rim are also observed. Knickpoints are created when the stream crosses the crater rim at the eastern end, and an alluvial fan has formed when the river debouches into the Banni plain (Fig. 7).

### 3.2. Fluvial valleys and channels on volcanic rocks

Fluvial Martian valleys exhibit various shapes and sizes and have been attributed to the groundwater sapping followed by the flowing of glacial meltwater (Pieri, 1980; Carr, 1981; Baker et al., 1990; Gulick, 1998; Craddock and Howard, 2002; Irwin III and Howard, 2002; Hynek and Phillips, 2003; Stepinski and O'Hara, 2003; Howard et al., 2005a, 2005b; Carr, 2006). One of the east-flowing canyons on the Echus Plateau (Centered at Lat. 2.250398° and Long. 81.481081°) that has experienced four episodes of volcanic activity and four episodes of fluvial activity (Chapman et al., 2010a, 2010b and references therein). Similar geomorphic features with narrow valleys showing analogue lithology are observed in the southern Tapi river highland units (Centered at Lat. 21.107807° and Long. 74.011019°). Besides theater-headed channels, various other geomorphic features within hills of Deccan basalt are formed by the fluvial and tectonic influences through time.

#### 3.2.1. Martian case of study: Canyon on Echus plateau

Martian dichotomy boundary separates the northern plains and the southern highlands (Parker et al., 1993; Kreslavsky and Head, 2002; Fairen et al., 2002). The Noachian and Hesperian outflow complexes with their origin in the Tharsis Volcanic Complex are dominated by the Circum-Chryse outflows (Baker and Milton, 1974; Baker, 1982; Baker et al., 1991), resulting in extensive valley networks in the southern highlands (Harrison and Grimm, 2005). Kasei Valles, with a total flow of $10^5$ to $10^7$ m$^3$ s$^{-1}$ (Bretz et al., 1956; Tanaka and Chapman, 1992; Chapman and Scott, 1989; Williams et al., 2000, 2002), is one of the largest of the Circum-Chryse flows. It extended 3300 km from Echus Chasma into the Chryse-Arcadia basin and formed as the result of multiple fluvial events in the Late Hesperian period (Mosangini and Komatsu, 1998; Williams and Phillips, 1999; Williams et al., 2000; Fairen et al., 2002; Chapman et al., 2007, 2010a, 2010b; Zealey, 2008).

Geographically, the area is located upstream of the Kasei valleys, known as Echus Chasma, and is surrounded by the Echus plateau, composed of basaltic lava flows (Zealey, 2008). It starts flowing towards the north of Kasei valley at the western wall of Echus Chasma. In the study area, the oldest rocks are exposed in the downstream reaches and as isolated patches along the rims of impact craters and its ejecta dating back to Noachian-age (Chapman et al., 2010a). The ~3.7 Ga flood basalt

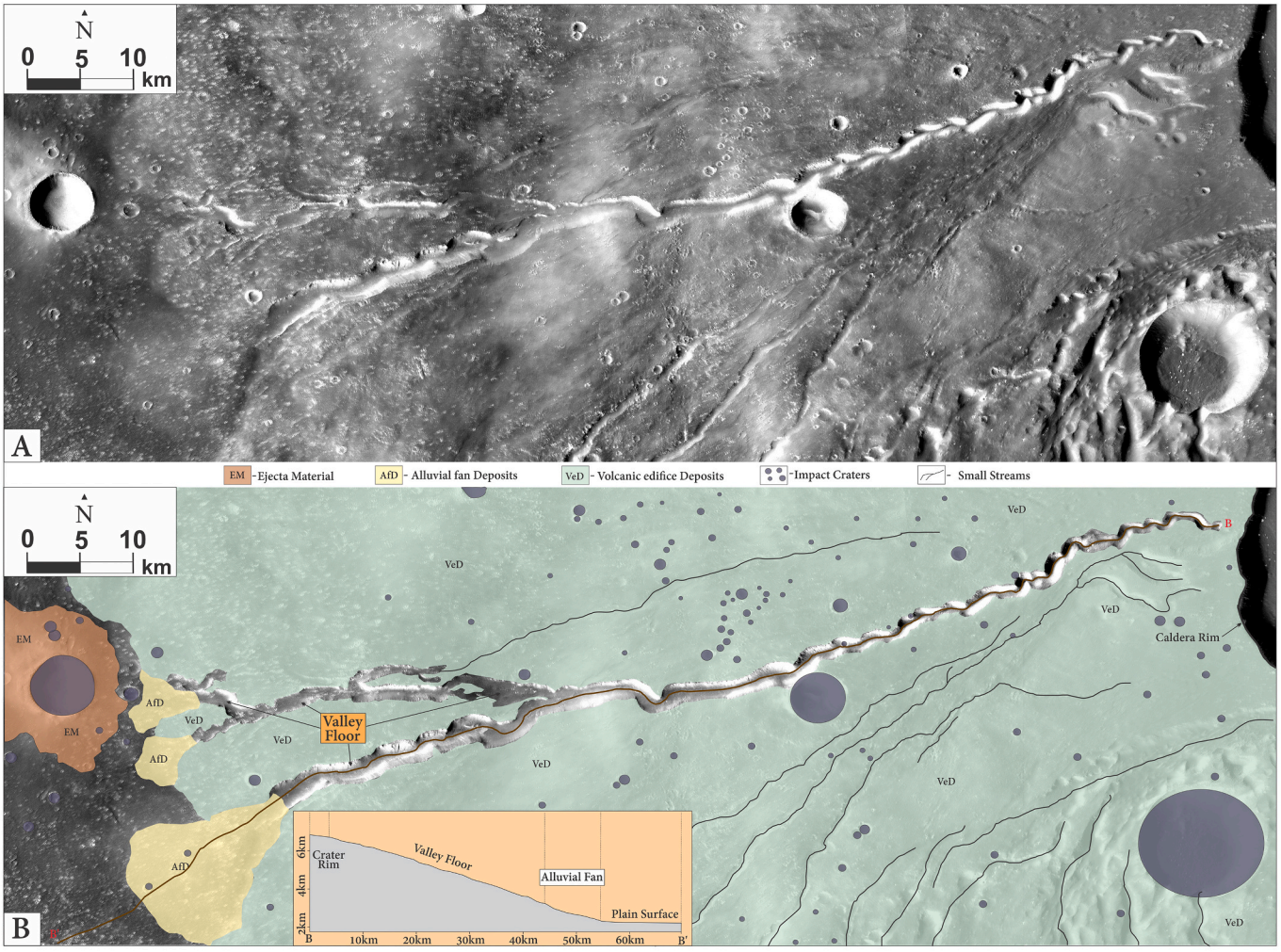


**Fig. 5.** Valley on the Western flank of Ceraunius Tholus. A). CTX image mosaic of the valleys; B). Geomorphic features of NEE-SWW flowing valleys with a longitudinal profile of central valley BB'.

event is the first known widespread volcanic episode in the Kasei Valles and surrounding area; additionally, kipukas of the same flow as remnants of the shield are observed (Chapman et al., 2010a, 2010b). The mapping results show the chasma and valley system cut into Hesperian ridged plains with a base age of 3.73 ± 0.2 Ga (Chapman et al., 2010a; Werner, 2006; Scott and Carr, 1978). Uranius Dorsum, a prominent volcanic ridge at the base of the Kasei floor, marks the end of the first volcanic cycle in the Kasei valley (Chapman et al., 2010a). The Hesperian fractured material with closely spaced graben surrounds Echus Chasma from the South-East side with change in trends from *E*-W, NE-SW, and N-S. Further, the area is fractured by the grabens about the same age (Chapman et al., 2007, 2010a, 2010b). These fractures relate to Valles Marineris formation, subsequently central canyon, and Echus Chasma (Scott and Tanaka, 1986; Witbeck et al., 1991; Rotto and Tanaka, 1995; Chapman and Scott, 1989).

The fracturing and faulting led to the formation of major and minor grabens in Early Hesperian (3.60 Ga ± 0.1), further reactivation took place through time till Amazonian because of the widespread volcanism from the Tharsis and Echus Chasma (1.8 Ga to 190 Ma) (Chapman et al., 2010a, 2010b). The subsidence and collapse formed the voids by the later on tectonic activity, providing space for the movement and ponding of the water. The second episode of volcanism resumed around 3.4 Ga. The related material appears to be of Hesperian Syria Planum Formation lower and middle members, about 800 km to the south of Uranius Dorsum on Echus Chasma's plateau (Chapman et al., 2010a). Chapman et al. (2010a) gave a new classification and designation of the Syria Planum formation as the lower, middle, and upper members (units Hsl, Hsm, and Hsu), respectively, based on crater counting dates and stratigraphical relationships. The third volcanic episode flows in the Northwestern parts of the Kasei valleys dated around 3.38 ± 0.76 Ga to 3.37 ± 0.87 Ga (Chapman et al., 2010a) constitutes lava tubes similar to the terrestrial lava tube. Simultaneously, the carving of the narrow dendritic surface channels started in the middle member of the Syria Planum formation (Hsm) with the release of water from the higher altitudes of Echus plateau's. The channel cutting took place around 2.9 ± 0.26 Ga by crater count dating of the surface of the channel (Chapman et al., 2010a), however as the surface is covered by the upper member of Syria Planum formation, it can be hypothesized that the channeling must have occurred about 3.4 Ga. The fourth and last volcanic cycle overlies all major depositional features of the Echus Chasma floor, where the canyon meets the Chasma floor. This eruption was prolonged in the Late Amazonian, producing a massive output of lava from Tharsis Montes and possibly Echus Chasma (Chapman et al., 2010a), designated as Amazonian platy flow unit Apf (Chapman et al., 2007, 2010a, 2010b) with the relatively flat surface. At the foothill of the Echus plateau the ponded lava lakes were observed (Fig. 10). The narrow channel on the surface of the platy lava flow has Amazonian resurfacing age that overlaps with the average ages of Amazonian flood episode 3 and volcanic episode 4 (Chapman et al., 2010b).

The local ruptures/joints similar to the fractures are observed, which

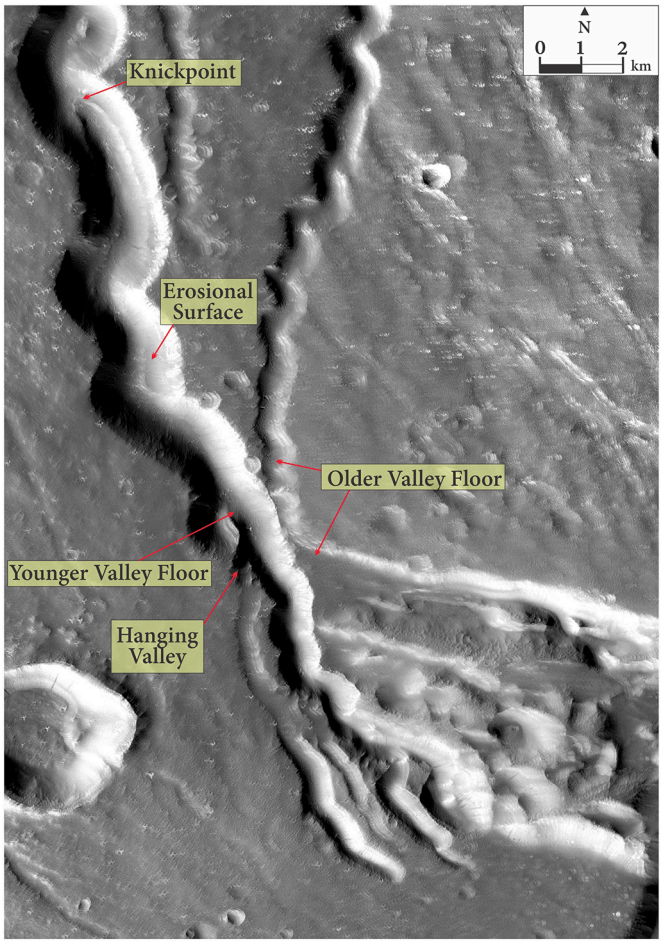


**Fig. 6.** CTX image of the crosscutting relationship of North and NNE trending valleys near the summit of Ceraunius Tholus.

**Table 1**
Attribute table for the length of the river bed, the shortest distance between beginning and end of the valleys, and the sinuosity index with remark for eight smaller valleys and three large valleys.

| Valley No. | Valley length (m) | Straight Length (m) | Sinuosity Index | Remark |
|---|---|---|---|---|
| SV1 | 38,610 | 37,183 | 1.04 | straight |
| SV2 | 35,720 | 34,968 | 1.02 | straight |
| SV3 | 32,412 | 31,399 | 1.03 | straight |
| SV4 | 30,210 | 29,141 | 1.04 | straight |
| SV5 | 28,120 | 27,229 | 1.03 | straight |
| SV6 | 29,820 | 29,252 | 1.02 | straight |
| SV7 | 31,220 | 30,718 | 1.02 | straight |
| SV8 | 29,950 | 28,734 | 1.04 | straight |
| LV1 | 43,611 | 42,795 | 1.02 | straight |
| LV2 | 49,421 | 45,985 | 1.07 | sinuous |
| LV3 | 61,057 | 57,344 | 1.06 | sinuous |

have provided space for the accumulation and flow of lava on the floor of Echus Chasma (Fig. 10) during the Amazonian time. This can be explained as the third cycle of the volcanism in the Northern Kasei valley eruption; subsequent bounding fractures have been formed on the southern Kasei's uplifted block valleys of Echus Chasma, which are filled by the fourth cycle of volcanism.

The Syria Planum formation surrounds the present channels (Fig. 9A). Three-member of the Syria planum formation are exposed in the channel on the northern and southern sides. The Syria Planum Formation lower member (unit Hsl) occurs west of the channel (Chapman et al., 2010a). This material has preserved broad sinuous ridges that trend roughly northeast. The ridges are up to 12 km wide and 150 m high and are capped by resistant material (Zealey, 2007). The crosscutting relationship with sinuous ridges dissected by graben indicates that the unit Hsl is relatively younger than the Hesperian fractured material (unit Hf) (Zealey, 2007). These grabens were active in the Hesperian and then again later in the Amazonian. The broad sinuous ridges on the Hsl unit have been interpreted as possible glacial eskers or sub-ice volcanic "tindar" ridges (Zealey, 2007, 2008). The middle and upper members of the Syria Planum formation overlie the lower member. The contact is very sharp between the members (Fig. 10A), forming cliffs. The incision of the valleys started in the middle member of the Syria Planum formation around 3.4 Ga; this unit was friable, relatively smooth compared to the lower member, and consists of probable ash deposits based on the lack of lava flow structure (Fig. 10A). The crater counting date indicates that the middle member (unit Hsm) was deposited around 3.42 ± 0.9 Ga (Chapman et al., 2010a). This flow thickness varies from 110 to 130 m on both the wall of the canyon, estimated based on the HRSC-MOLA DEM dataset. The deposition of this material marks the end of the second volcanic cycle in the field area. The Hesperian-Noachian undivided units are exposed at the canyon's core, showing flow features similar to the terrestrial flood basalt. The upper member (Hsu) has isolated outcrops of the lobate flows above the middle member near the escarpment between the Echus Chasma and Echus plateau, with an average absolute crater retention age of 3.37 ± 0.8 Ga (Chapman et al., 2010a).

The flooding from the Tharsis Montes has reshaped the canyon. There are at least two older floods that were probably generated from the Tharsis Montes area. The first episode was in the Early Hesperian and is mapped as Hesperian channel with absolute age of 3.61 ± 0.4 Ga by crater counting for this resurfacing unit and marks the first widespread fluvio-glacial episode (Chapman et al., 2010a). The second episode was around 3.4 ± 0.7 Ga, based on the gully's surface dating and corresponds with the onset of glaciation as indicated by the sinuous ridges on the Lower Syria Planum formation, suggesting a second fluvio-glacial episode (Zealey, 2007; Chapman et al., 2010a). Post appearance of the sinuous ridges has initiated dendritic valley formation. The release of water from the upper catchment area formed fluvial features that marked climate change on Mars (van Gasselt, 2007; Hauber et al., 2008), and this represents the third major fluvio-glacial episode in Echus Chasma (Chapman et al., 2010a, 2010b; Milton, 1974; Masursky et al., 1977; Scott and Carr, 1978; Baker and Kochel, 1978, 1979; Carr, 1981; Baker, 1982; Lucchitta, 1982; Chapman and Scott, 1989; Robinson and Tanaka, 1990). The formation of the theater-headed channel occurred along the canyon wall (Fig. 9A). Such features represent the erosional activity developed during the third fluvio-glacial cycle. The ponding within the floor of the Apf unit (Figs. 10A and 11) by subsequent flooding marks the fourth and last fluvioglacial episode dated to be between 54 and 98 Ma Chapman et al. (2010b).

The majority of the channel floor erosion seems to occurred during the Amazonian period, and the floor features can be attributed to a combination of catastrophic flooding and glacial erosion (Chapman and Scott, 1989). It has been suggested that even brines (Brass, 1980; Burt and Knauth, 2003; Chevier and Altheide, 2008) can freeze at typical Martian temperatures forming frazil ice (Baker, 1979), which would eventually consolidate and flow downstream like glacier ice (Lucchitta, 1982).

Based on age relationship it can be argued that the theater-headed channels were formed around 3.4 Ga and continued to evolve through time with episodes of upliftment and regional flooding (Chapman et al., 2010a). The resulting topography has a long narrow, elongated channel with varied geomorphic features. The spectacular fluvial landforms (aggradation and degradation) that are identified in the study area are the hanging valleys, escarpments along the wall of plateaus, incised channel, channel ponding, gully surfaces along the cliff slopes, knickpoints, gorges, and alluvial fan that extend out from the plateau

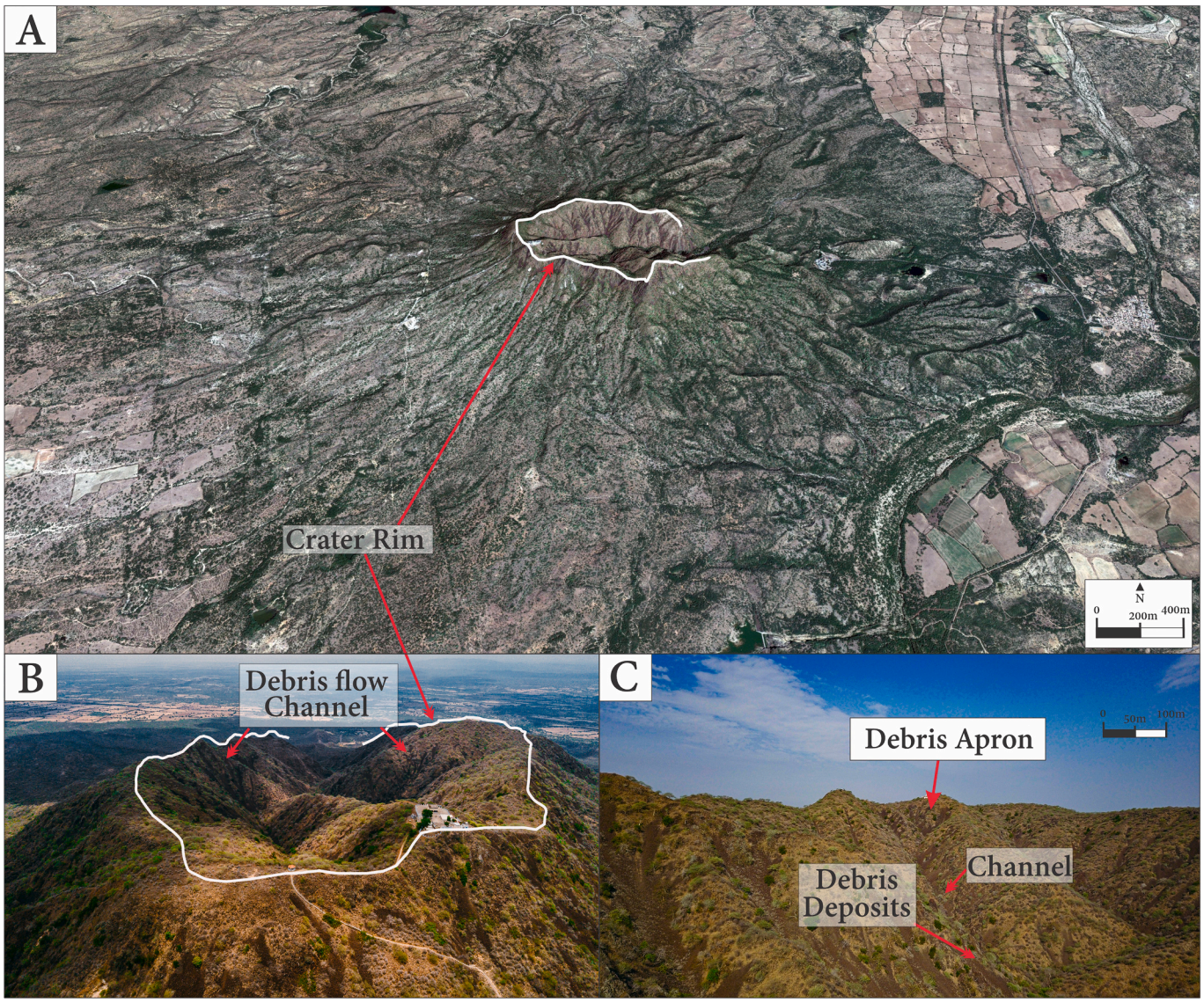


**Fig. 7.** A). Satellite image of Dhinodhar hill (image credit-Google earth); B). Drone image of the caldera; C). Drone image of gullies on the inner wall of the crater.

(Fig. 10A).

The dendritic drainage pattern on steep valleys (Fig. 12A) is sinuous and organized fifth-order streaming without braided contacts. The confluence angle of the streams are perpendicular at few places, with the tributary channels further measured at an acute angle, indicating subsidiary structural influence. On the contrary the voluminous Amazonian flood lavas and catastrophic fluid floods could be the main factor responsible for evolution of dendritic drainage network. The shallower channels are covered with the later aeolian infill as dune's, forming an outline to the valley floor (Mangold et al., 2004). The valley head geometry suggests surface runoff (Mangold et al., 2008). Low cliff and mesas of the volcanic material bound the entrant channel on the plateau wall (Fig. 11).

### 3.2.2. *Alaldari Valley on Northern Deccan Plateau*

The Alaldari valley is a narrow canyon of ~5 km length (Figs. 9B and 10B) is a tributary stream of the Tapi river which originates from Madhya Pradesh and drains into the Arabian Sea. The drainage area is bounded by the Purna river basin in south and Narmada river basin in the north. In the western direction, the stream meets the Tapi river at the reservoir of Ukai dam passing through the Quaternary alluvial plain. Two major peri-continental rift basins bound the passive western margin of the Indian sub-continent, i.e., the Cambay Basin (NNW-SSE) and the Narmada-Tapi (ENE-WSW) graben system formed during early Cretaceous times (Kaila et al., 1981; Biswas, 1982, 1987; Kaila and Krishna, 1992). These rift basins have developed along with the pre-existing major basement fractures and have undergone reactivations periodically from time to time (Biswas, 1982) which has given rise to the horst and graben configuration on a regional scale. The basement faults are cutting across the Deccan Traps, which are also continuing into the Tertiary sediments, have controlled the block structure on a regional scale for the study area (Raju, 1968, 1979; Kaila et al., 1981; Biswas, 1982, 1987). The presence of dyke swarms in the Deccan Trap province (Auden, 1949; Krishnamacharlu, 1972; Karanth and Sant, 1995), the Tapi and associated lineaments (Blanford, 1867; Powar, 1981), fracture-controlled drainage system (Alavi, 1990) indicates the role of tectonism in the formation of the valleys in the area. Dubey and Saxena (1988) have envisaged the role of Quaternary tectonism in the form of fracturing and warping of trappean rocks, dyke emplacements, and tilting of the alluvium.

Geomorphically, the area shows linear ridges (due to the presence of dykes), irregular hills, conical hills, plateaus, escarpments, and valleys. The plateau forms the higher elevated topography within the basaltic terrain extend in the N-S direction, which exhibits flat tableland

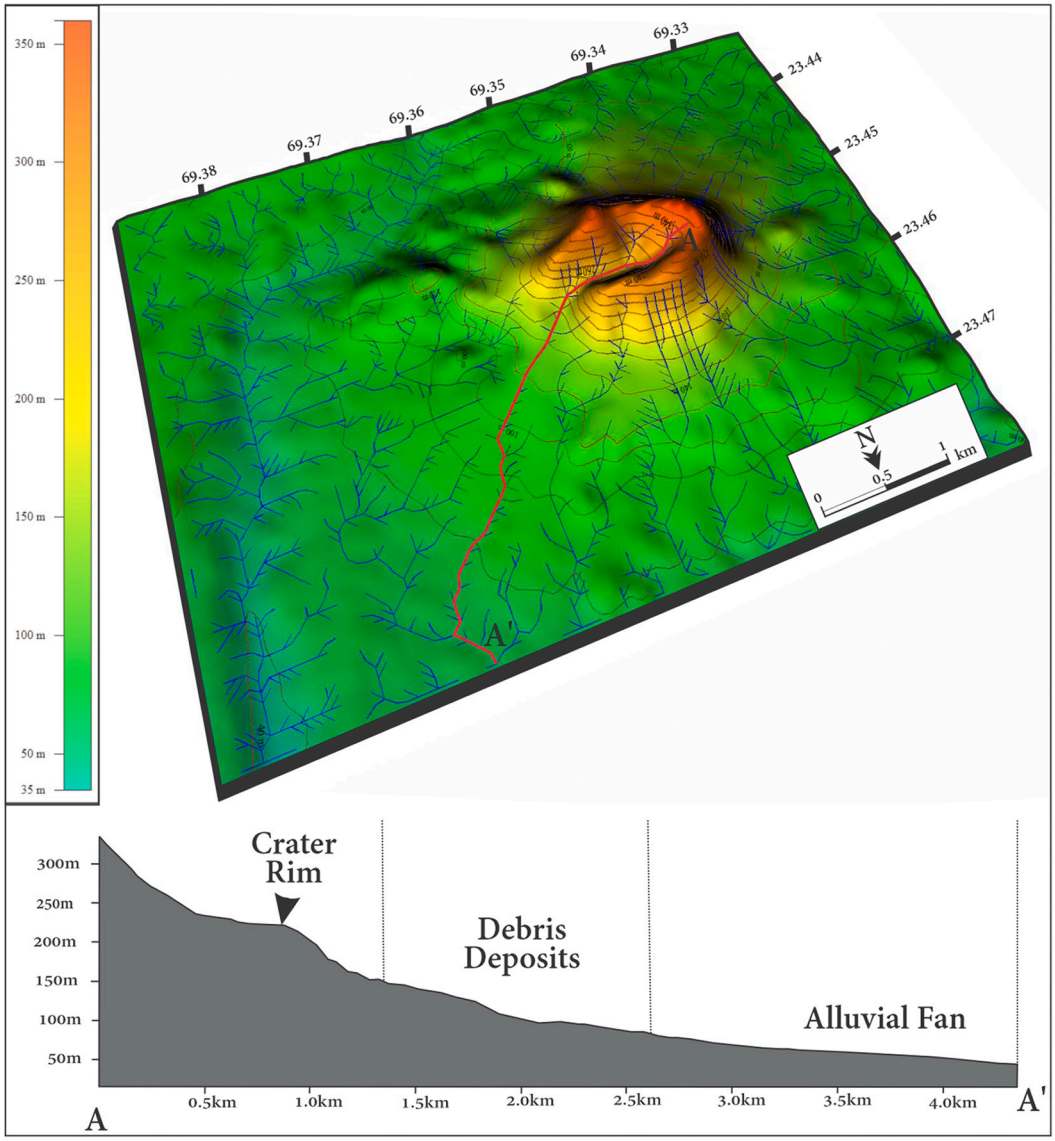


**Fig. 8.** Contour and Drainage map of the Dhinodhar hill derived from DEM and topographic maps with DEM in the background with a longitudinal profile of the stream, which passes from the rim of the crater modified after Chavan et al., 2022.

topography with isolated mounds and comprises steep slopes with a thin cover of soil (Fig. 10B). The plateau separates the alluvial plain from that of the Deccan trap (Western ghat escarpment). The extensive jointing and fracturing of the basaltic lava flows have given rise to weak zones along which broad, flat-bottomed, intermontane valleys have developed. The present canyon is aligned with the major fault trend, i.e., NNE-SSW fault set (Babu, 1984; Rao, 1987) which appears to delineate the trappean highlands (Alavi, 1990). Theater-headed valleys (Fig. 13) as observed on Mars can be seen at the initiation of the canyon at Alaldari. These valleys are considered to be formed by the interplay between post-Deccan trap tectonism, which is primarily caused by the pre-existing basement faulting along the Son-Narmada-Tapi zone (SONATA) (Biswas, 1987) and post-Cretaceous catastrophic climate change that occurred in the Indian subcontinent (Prasad, 2019).

Based on the field study, different flows in the Deccan trap are marked for the Alaldari Valleys. The different flows show variations in the textural and color besides rock variations from the mega-porphyritic, vesicular, amygdaloidal, compact basalt, indicating the differential cooling during their formation. These rocks have a different response to the same *exo*-genetic process, which leads to the formation of knickpoint along the channel. The Quaternary deposits in downstream and along the riverbank in the Alaldari valley directly overlie the Deccan traps; the aggradational terraces are observed along the valley's banks thick debris-flow deposits (Fig. 21). They are deposited by the sub-aerial agencies, and river action, derived from the Deccan Traps and Tertiary rock erosion and denudation controlled by neotectonism and the climatic perturbations (Alavi, 1990; Merh and Chamyal, 1997). During the field study, the climatic and tectonic features were marked (Figs. 10B and 13), such as lake/pond within the channels as an indicator of tectonic activity. The debris deposits on the mainstream bank indicating catastrophic flooding within the area. Further, these debris flow aprons are cut by the erosional activity forming erosional surfaces (Fig. 10). Other features like knickpoint, waterfall (one with 50 m and the other 195 m) which is lithologically controlled, point bar within the channel, hanging valleys on both walls, and jointed rocks trend along the main channel. The mainstream is covered with 1–10 m diameter angular boulders and rounded gravels, pebble and cobbles, and acts as permeable rock aquifer.

The depositional landforms occur as over-bank deposits adjacent to the existing river channels and manifest the present-day seasonal

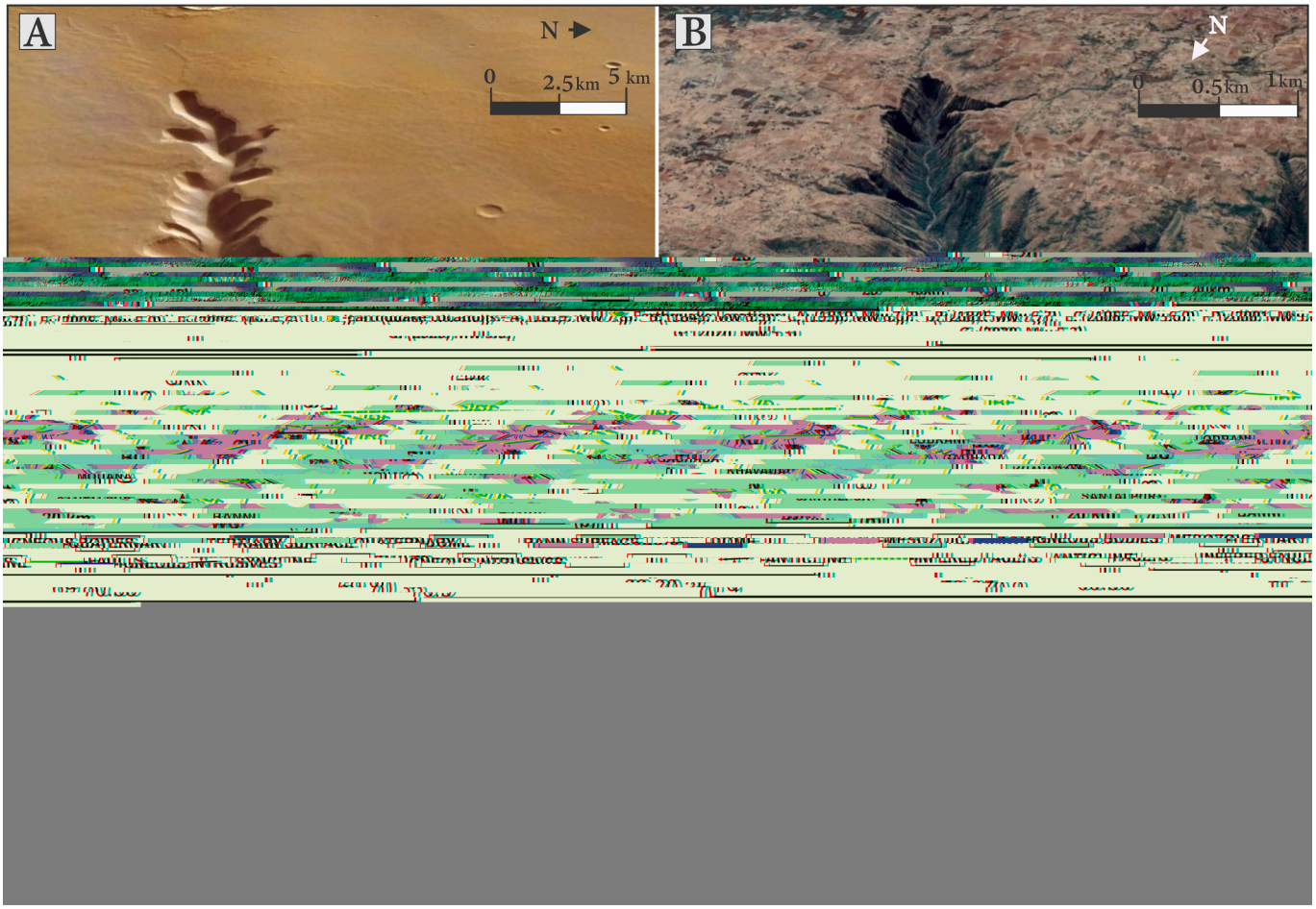


**Fig. 9.** A). Satellite images of valley on Echus plateau; B) Satellite image of Alaldari analogue valley on northern Deccan trap (Google earth).

flooding (Fig. 10B). They are extensively developed along the channel and represent the aggradational phase. The canyon valleys are characterized by three distinct aggradational surfaces in the form of erosional terraces/surfaces ($T_0$, $T_1$ and $T_2$) (Fig. 10B) on both walls of the valleys occurring at varying heights from the riverbeds. Stratigraphically in the Alaldari valley at the base, debris flow deposits are recorded wherein the clast are of sub-rounded basalts with poor sorting supported by matrix. These deposits correlate to the deposition that occurred in semi-arid to sub-humid climatic cycles of regional scale and represent peak flood events (Chamyal et al., 2003; Merh and Chamyal, 1997). The $T_1$ terrace consists of debris and gravelly deposits. The $T_2$ terrace deposits mainly comprise sandy, silty and clayey horizons occurring in the upper part of the sequence and represent overbank and floodplain deposits. The sediments represent decelerating high suspension flows during intermittent floods.

The drainage pattern observed within the short area of basin length of ~10 km and width of ~5 km is dendritic with rectangular at places (Fig. 12C). The stream follows structural lineament, fault, dyke barriers, or lithological control. The study area represents the dominance of two contrasting lithological domains, i.e., the Deccan Traps and alluvium (Fig. 10B), covering large areas over which the existing drainage network is developed. The prevailing fractures strongly control the drainages and joint systems orientation, as represented in the rose diagram (Fig. 12C). The longitudinal profile of a river is controlled by channel discharge, load delivered to the channel, size of the load/debris, flow resistance, velocity, width and depth of the channel, gradient, and tectonism. The inter-relationship of these variables indicates that the area has primary control of tectonics with the prevailing climate conditions as evidenced by the mainstream profile behavior (Figs. 10B and 14).

### 3.2.3. *Morphometric analysis*

According to Schumm et al. (1987), an area's geological history, including information on the structure and surficial conditions, can be deciphered from the study of drainage patterns. The basic morphometric analysis for the Martian and terrestrial basins is performed to better understand the terrain modulation and probable causes of the differential geomorphic feature. A few morphometric parameters are calculated based on the dataset discussed in Section 2, which are stream ordering (Strahler method for ordering drainages) (Supplementary Table. 3), bifurcation ratios, drainage densities, total stream length for main streams, river sinuosity, basin asymmetry factor, valley floor width to height ratios, rose diagram for the first, second and third order stream (Fig. 12A and C). The analysis was done based on the ratios and magnitude-dependent parameters calculated for both the valleys on Earth and Mars to understand the detailed morphological characterization of an area.

*3.2.3.1. Stream ordering.* The three most commonly used ordering systems were proposed by Horton (1945), Strahler (1957), and Shreve (1967); according to Strahler, the first order are the outermost tributaries. Following this method, Alaldari valleys watershed has 225 first-order, 52 second-order, 11 third-order, 3 fourth-order, and 1 fifth-order stream (Supplementary Table. 4) whereas, the Echus plateau valleys has 142 first-order, 30 second-order, 5 third-order, and 1 fourth-order stream (Supplementary. Table. 3).

*3.2.3.2. Bifurcation ratio.* This parameter expresses the ratio of the

$$A_F = 100\ (A_r/A_t)$$

Ar is the basin area to the right (facing downstream) of the trunk stream, and $A_t$ is the total area of the drainage basin. For most stream networks that formed and continue to flow in stable settings, $A_F$ should equal about 50 (Cox, 1994). The $A_F$ is sensitive to tilting perpendicular to the trend of the trunk stream. Values of $A_F$ significantly greater or less than 50 may suggest tilt. $A_F > 50$ implies tilt down to the left of the basin. $A_F$ values for the Alaldari valley and Echus plateau valley are 60.2 and 46.9, implying tilt down to the left and right side, respectively.

*3.2.3.7. Ratio of valley floor width to valley height.* The ratio of valley floor width to valley height ($V_f$) may be expressed as.

$$V_f = 2V_{fw}/[(E_{ld} - E_{sc}) + (E_{rd} - E_{sc})]$$

$V_{fw}$ is the valley floor's width; $E_{ld}$ and $E_{rd}$ are elevations of the left and right valley divides, respectively; and Esc is the elevation of the valley floor (Bull, 1977, 1978). The VF values are calculated from the mountain front to a distance at three places (Supplementary Table. 5) for the Alaldari valley, which are 0.433, 0.22, and 0.287. The lower values of $V_f$ are associated with the V shape of valleys which reflects deep valleys with streams that are actively incising and are commonly associated with uplift. Similarly, for the Echus plateau basin the $V_f$ values come out to be 0.197, 0.33, 0.43; indicate deeply incised V-shaped valleys associated with uplift.

*3.2.3.8. Rose diagrams for First, Second, and Third-order stream.* The trends of First, Second, and Third-order streams are plotted in a rose diagram, grouping it by its order-based on the rose diagram (Figs. 12A and 12C). The higher-order channels mostly follow the trends of the lineaments, which are clearly identified by their pattern. The higher-order streams are mainly trellis, indicating that the drainage is structurally controlled on both basins (Fig. 12).

### 3.3. Terraces formation on Mars and their Himalayan analogues

The southern highlands of Mars are dissected by valley network, showing that water has sculpted the surface in the past (Galofre et al., 2020; Carr, 1995; Craddock and Howard, 2002; Howard et al., 2005a; Hynek et al., 2010; Alemanno et al., 2018). Fluvial terraces on Mars have been marked along the channels in relation with the Martian global sea (Duran and Coulthard, 2020). The fluvial terraces of Noctis fossae (Centered at Lat. 4.829141° and Long. 81.481081°) (Fig. 14) are studied for the valley-terrace development. The area has developed north-flowing valleys resulting from the probable episodic glacial melt leading to fluvial action and the Tharsis-related volcanism-induced tectonics. Similar features are observed in Nubra and Shyok Valley, Ladakh, Higher Himalayas (Centered at Lat. 34°51′12.10″N and Long. 77°29′16.03″E; Lat. 34°46′34.75″N and Long. 77° 9′20.14″E; Lat. 34°48′13.25″N and Long. 77° 6′17.70″E), and in the lesser Himalayan domain of the middle Satluj Valley (Centered at Lat. $31^0$4′ 57.08″ and Long. $31^0$14′58.82"N; Lat. $77^0$4′55.33″ and Long. $77^0$7′21.87″E) (Fig. 1). The basin illustrates U-shaped valleys followed by V-shaped valleys and various geomorphic features pertaining to glacio-fluvial terrain.

#### 3.3.1. Martian case of study: fluvial terraces in Noctis Fossae

Mars, a very dry, cold, and fluvially inactive planet, has preserved different types of fluvial valley network largely represented by longitudinal and dendritic valleys. Presence of branching channel systems (valley networks) indicate past flowing water (Hynek et al., 2010a, 2010b), majorly documented in the southern highlands. The highlands of Mars have recorded extensive fluvial erosion evidenced by incised channels during the Noachian period, which extended to the early Hesperian (Hartmann, 2005; Stepinski and Stepinski, 2005). Most valley networks are assumed to be of the Noachian Period, which coincides well with the hypothesis of warm and wet climatic conditions prevailing during this Martian era.

The area of interest, i.e., Noctis Fossae fall between $0^0$ - $6^0$S Lat. and $95^0$ - $105^0$W Long. (Fig. 14 A), is located in the Southern Highlands (Tanaka and Davis, 1988) of Mars, placed in the north of Noctis Labyrinthus is an example of valley networks showing large drainage systems with erosional activity by surface runoff on pre-existing grabens (Chavan and Bhandari, 2017). The higher elevation in area, varies from ~8500 m to ~4000 m, gradually diminishing in the north. Noctis Fossae has witnessed three faulting episodes: Syria Planum centered faulting followed by Pavonis-I Center faulting and Pavonis-II Center faulting (Chavan and Bhandari, 2017; Tanaka and Davis, 1988). The fluvial system was set-up in the region because the glacial melt existing on the highlands eroding the weaker zones of the pre-existing grabens formed due to Tharsis rise (Chavan et al., 2021 (under review)). The regional Martian structural deformation has led to highly fractured upsided and subsided blocks leading to the development of large grabens within the same lithological domain. Extensively broad valleys and grabens are identified on the surface at elevations of 8.5–4.0 km, sloping towards the north with a depth of 4.0 km in the southern part and 1.5 km in the northern region, as derived from the MOLA-HRSC DEM dataset. The valley bottom lessens from the south to north direction with the change in the elevation gradient. The valleys are U—V shaped and form deep gorges in the Hesperian volcanic rocks (Tanaka et al., 2014a, 2014b) (Fig. 14). The large Martian channels in the area have been subject to tensional forces at their primary stage of genesis (Schumm, 1974), followed by fluvial erosion. Larger channels in the area trending NNE-SSW cut across by the younger secondary linear grabens, which are almost transverse to the central valley network of Noctis Fossae. The valleys from the region meet to the plain surface of AHv (Amazonian-Hesperian volcanic Unit) up north. As observed in the Noctis Fossae, the geomorphic features may result from the Tharsis bulge and its migration (Cheung and King, 2014; Gulick and Baker, 1989; Gulick, 2001; Dohm and Tanaka, 1999; Carr and Head, 2003).

Like Earth's fluvial system, Noctis Fossae hosts aggradational and degradational fluvial terraces $T_0$, $T_1$, $T_2$, $T_3$ or $S_0$, $S_1$, $S_2$, $S_3$ surfaces (Fig. 14C), indicating surface water flow in huge amount probably around Mid-Late Hesperian to Early Amazonian time (Carr, 1996). These terraces/surfaces may be developed by the major Martian tectonics (McCauley et al., 1972; McCauley, 1979; Masursky, 1973; Masursky et al., 1978; Carr et al., 1973; Carr, 1974; Masson, 1979; Blasius and Cutts, 1976; and Blasius et al., 1977) at the time of early Tharsis Rise when Syria Planum was uplifting (Masson, 1979) and simultaneously fluvial action was carving the surface. The terraces documented in the valleys have shaped the landscape formed due to climatic and tectonic perturbation. The meltwater from higher altitudes acted as a primary agent to carve the valleys in the downstream region. A higher slope gradient in the, upstream forms deeper valleys and associated terraces, while downstream, at a lower slope gradient, these valleys become shallower and form braided channels trending in NNE direction.

#### 3.3.2. Himalayan analogues

*3.3.2.1. Nubra-Shyok Valley.* The river Nubra flows along the Karakoram right-lateral strike-slip fault (Searle and Phillips, 2007) (Fig. 15). The Karakoram Fault (KF) determines the river course, which trends almost parallel to the western Himalayas from Pamir to Kailash in southern Tibet and merges with the Indus-Tsangpo Suture (Murphy et al., 2000). The Karakoram right-lateral strike-slip fault in conjunction with Shyok suture along with Khalsar thrust (Weinberg et al., 2000) brought together three terrains of different lithologies and ages viz. Ladakh terrain to the south and the overlying Khardung volcanics (Weinberg et al., 2000); the Saltoro terrain, towards the north-west (Weinberg et al., 2000; Lacassin et al., 2004) (Fig. 15A and B).

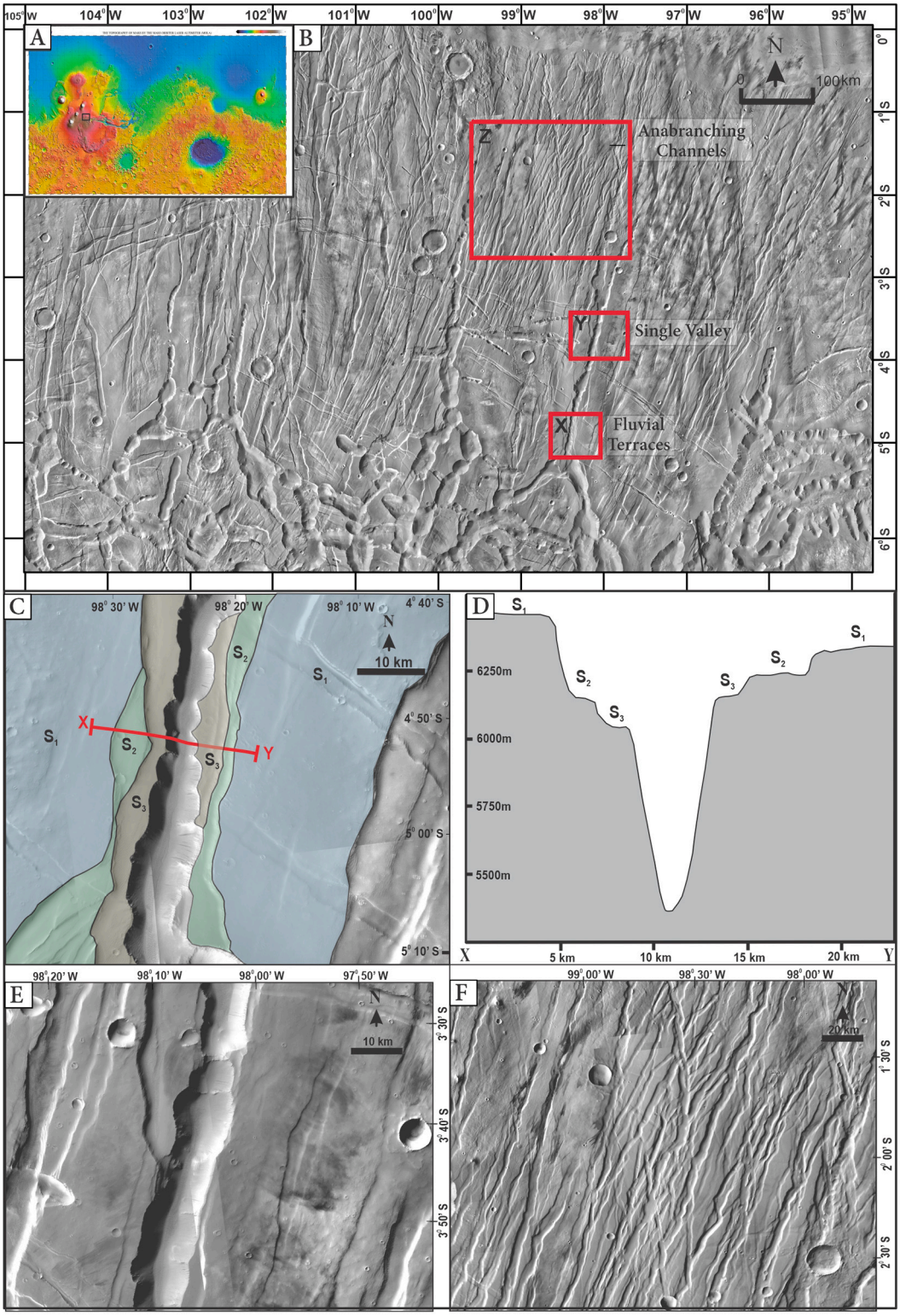


**Fig. 14.** A). MOLA shaded relief map of Noctis Fossae, Noctis Labyrinthus, and Northern portion of Syria Planum. Inset: Topographic Map of Mars showing the location of the area studied; B). High-Resolution CTX camera Image mosaic of Noctis Fossae region showing various channels running parallel to each other. The rivers also show anabranching channels. Box X, Y and Z shows the location of Fig. 14C, E and F having detailed geomorphic features; C). The early to late Hesperian surfaces S1, S2, S3, indicating surface water runoff in huge amounts; D). Cross profile of X-Y shows deep V-shaped valley of more than 1000 m depth having unpaired fluvial terraces; E). Single valley observed in the central reaches of Noctis Fossae; F). Anabranching channels observed in lower reaches of Noctis Fossae.

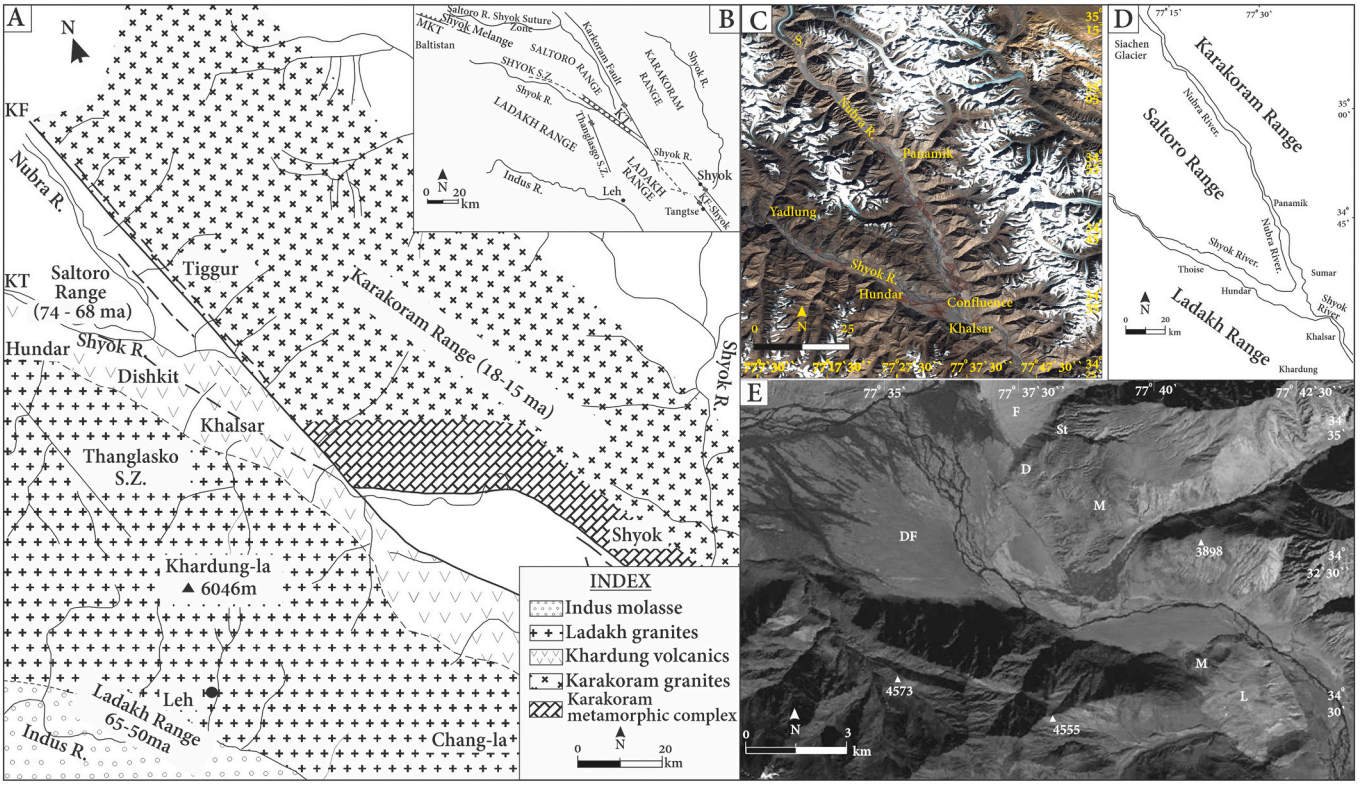


**Fig. 15.** A and B). Geological and Structural map of the study area (after Searle and Phillips, 2007 and Weinberg et al., 2000). KF: Karakoram Fault, KT: Khalsar Thrust; C). Imagery showing river Shyok and Nubra and related glacial features (Google earth); D). Sketch map of river Shyok and Nubra; E). Nubra-Shyok confluence; lacustrine deposits (L) superimposed on moraine (M); Shyok emerges from a narrow outlet and forms a delta like deposit at the confluence; southern basin wall has a crescentic shape. The main channel can be seen towards the left flank intertwined with numerous channels. Various geomorphic features like Glacial Striations (St), Drumlins (D), Alluvial Fans (F) and Delta Fans (DF) are also marked with benchmark heights.

Evidence suggests that the Karakorum fault remained active throughout the Quaternary and is still active (Brown et al., 2002; Chevalier et al., 2005; Searle and Phillips, 2007). Field evidence suggests that mid to late Pleistocene glacial moraines are displaced along the KF (Chevalier et al., 2005; Raterman et al., 2007). Similarly, levees of debris flows show offset of many meters during the terminal Pleistocene and early

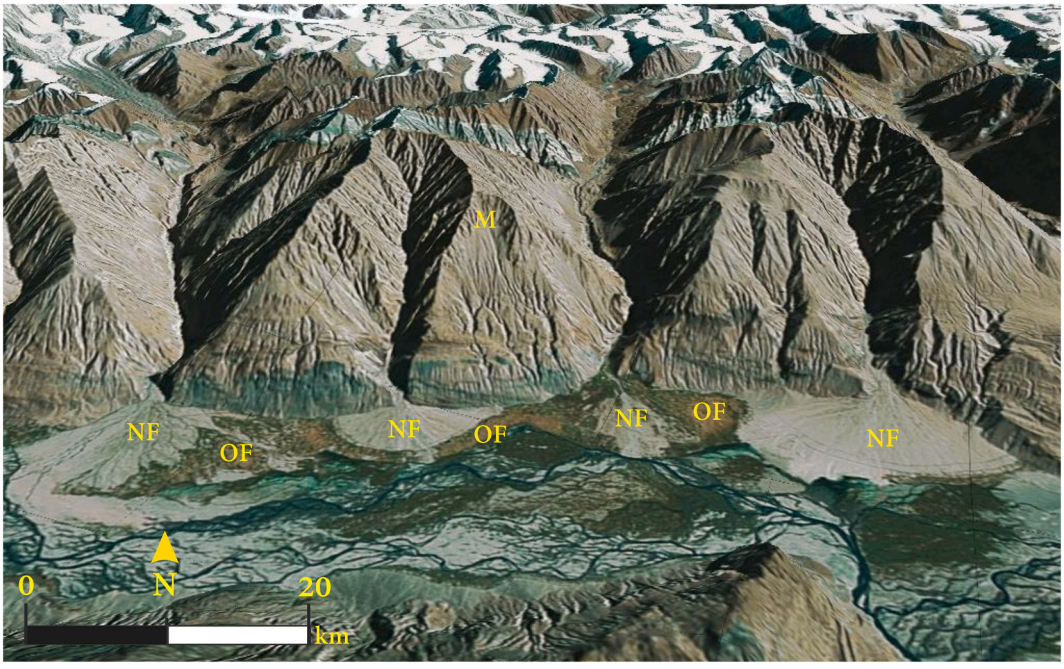


**Fig. 16.** Colluvial fans on the left flank of the river Nubra. The light colored fan of recent origin (NF) and the consolidated old ones are of darker in color (OF). M: moraines. The river Nubra in the foreground shows a wide span having intertwined braided channels.

Holocene (Brown et al., 2002). Right-laterally displaced fluvial moraines (Chevalier et al., 2005) and terraces are also observed along the Karakoram fault (Raterman et al., 2007).

Nearly parallel scarps and tension cracks form a small graben west of the high scarp, indicating extension perpendicular to the valley near Panamik (Brown et al., 2002). In addition, tension cracks on the steep part of fans vary in orientation from N-S to *E*-W (Brown et al., 2002). Remotely sensed data shows comparable features near Panamik. The valley wall has sets of parallel stepwise fractures oriented obliquely in the N—S direction, and the streams on either side of the cracks have deeply carved channels having straight vertical faces. Transverse cracks are wide at the top and taper down, with the depth having V-shaped cross-sections. Tops are smoothly rounded and polished under the glacial environment. The morphology of the tensional cracks suggests these were produced after the glacier's retreat. A series of tensional cracks between Panamik and Tirit show a string of debris flow fans emanating from the base of cracks. The other factors that need to be noted are the numerous successive debris flow chutes and fans on the bank of the river Nubra (Fig. 16). The left flank is occupied with broad-based debris flow fans with sharp apexes (Fig. 16). Invariably light-colored fans rest on top of well-stabilized dark-colored ones (Fig. 16), suggesting a pulsating depositional environment. The bed of the river Nubra is presently occupied by colossal sand and gravel bars intertwined with numerous small streams along with the main meandering stream. The main channel is preferentially confined to the right flank of the basin. The vertical rock facets, deeply entrenched streams, discontinuous moraines appear stepwise, the debris chutes and numerous multiple debris flow fans, and associated tensional cracks are clear indications of vertical uplift. The causative factors for the genesis of these surface features may be found in the climate that caused glaciations in Karakoram.

The Quaternary deposits along rivers Nubra and Shyok follow the Karakoram right-lateral strike-slip fault (KF). Because of the elevated topography, glaciers are the major geomorphic agents in shaping the landscape. The presence of moraines in wide 'U'-shaped valleys suggests that the terrain has witnessed multiple events of glaciation (Sharma et al., 2016 and references therein). The phases of deglaciation are represented by the well-developed flood plains and terrace sequences (Owen et al., 2006; Pant et al., 2005). In addition, evidence of seasonal thawing and freezing (e.g. frost heave) can be observed on slopes covered with obstacle dunes (Pant et al., 2005; Juyal, 2014). River Nubra debouches into the Shyok river and has created a huge delta-like fan that covers most of the floodplain with a network of braided channels (Figs. 15 and 16). The main channel of the river Nubra appears to have been pushed westwards at the distal end of the fan, and the narrow channels of river Shyok meet the north-south trending channel of river Nubra at right angles (Figs. 15 and 16).

The confluence has an exceptionally wide span (~5 km), having an extensive dune field studded with shallow water bodies. The valley on the left has a smooth vertical crescentic wall dipping westward. Looking north, the river Nubra has carved a wide U-shaped basin (with an average span of ~3 km; Fig. 17) having braided and sluggish meandering streams that appear misfit within the wide river span. The basin can be classified as misfit having underfit streams. The bed of the river Nubra is presently occupied by huge sand and gravel bars intertwined with numerous small streams along with main meandering

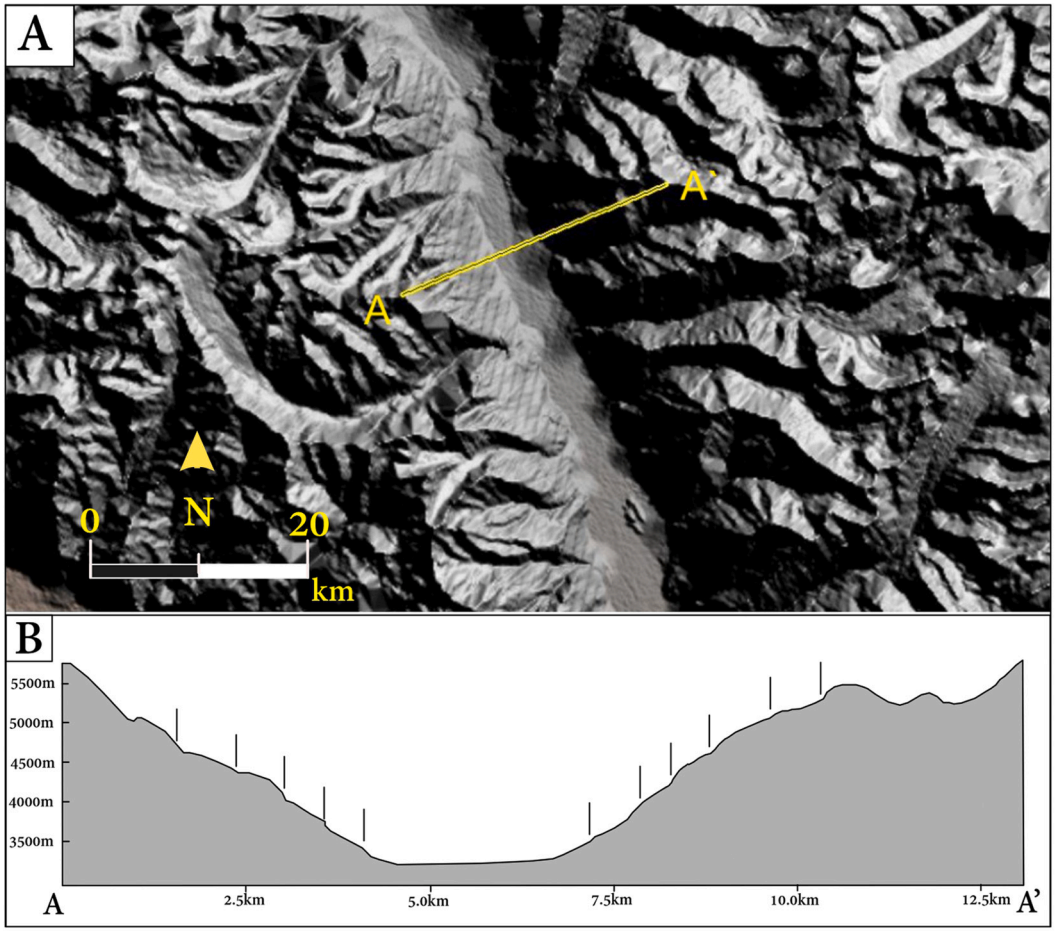


**Fig. 17.** Cross-section across river Nubra shows a perfect U-shaped profile showing deposition of moraines on the either flank. The slope on the left flank appears gradual with milder breaks as opposed to those on the right flank where the breaks are sharper and narrowly spaced.

channel.

The river has a gradual slope from the snout of the Siachin glacier located at 3600 m msl to the Nubra-Shyok confluence at 3100 m msl, an altitudinal drop of 500 m within ~80 km distance between the snout and the confluence. River Shyok has recorded a gradual drop of 100 m between the confluence and Yadlung - a distance of ~50 km. Moraines could be traced up to Hunder. Based on the remotely sensed data, valley cross-sections were extracted to locate the maximum extent of glaciation from Hunder to Yadlung. The moraines could be traced in patches up to Yadlung. U-shaped valley cross-profile persists till Yadlung, indicating glacial action (Fig. 18A). In the downstream at Yadlung V-shaped fluvial profile (Fig. 18B) can be seen. The valley widens at Yadlung, and the river is deflected northwards, creating a wide valley base. It appears that the glacier extended up to the point where the river Shyok suddenly deflected northwards and has the widest base. This observation is further supported by the valley cross-section and absence of moraines downstream.

*3.3.2.2. Satluj River.* The Satluj River is the largest tributary of the Indus River and drains the third largest catchment area in the Himalaya. The river drains through the Tibetan plateau in the north followed by the Tethyan Himalayan Sequence (THS), the Higher Himalaya Crystalline Sequence (HHCS), the Lesser Himalayan metasedimentary Sequence (LHMS), and the Sub-Himalaya Siwalik group of rocks before the river debounces into the alluvial plain (Vannay et al., 2004; Miller et al., 2000; Vannay and Grasemann, 1998; Thiede et al., 2004, 2006). In the upper reaches of the Tibetan Plateau region, large alluvial fans are formed at the base of the hill slopes, which provide abundant sediments that can be easily mobilized by increased river discharge or rainstorms resulting due to glacial and periglacial processes eroding the layered and densely fractured metasedimentary rocks (Wulf et al., 2012; Heimsath and McGlynn, 2008; Molnar et al., 2007). Large fluvial terraces and alluvial fans characterize the lower-elevation Satluj River and tributaries (Bookhagen et al., 2006; Sharma et al., 2016). Based on morphology and sediment assemblages, five major landforms are identified in the Satluj river. These are: (i) the fluvial terraces (valley-fill and strath), (ii) debris flows/landslide deposits, (iii) alluvial fans, (iv) paleoflood deposits, and (v) relict valleys and epigenetic gorges (Fig. 19). However, we have restricted our studies to fluvial terraces, debris flows, and alluvial fans, keeping the martian geomorphic scenario in view.

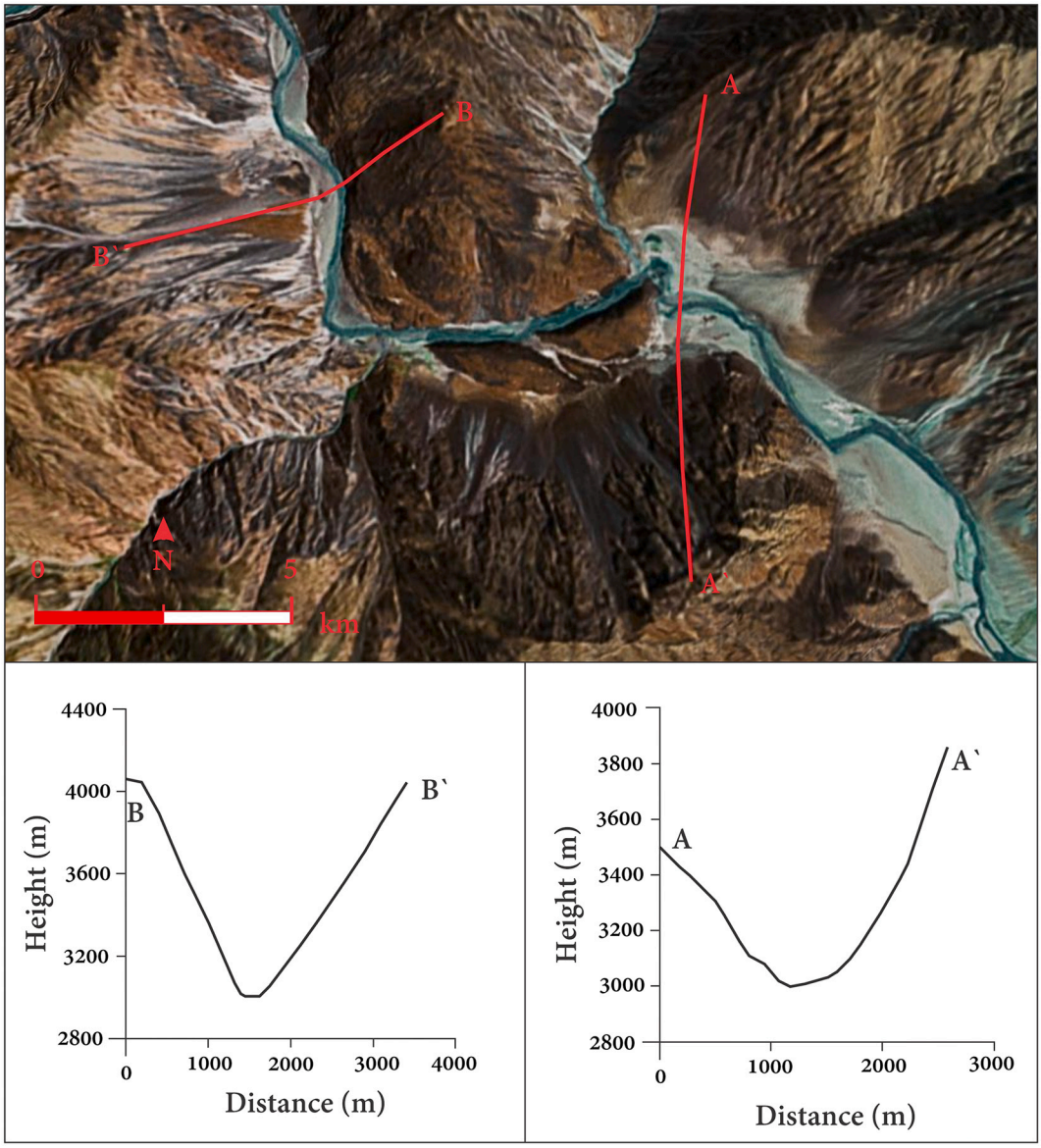


**Fig. 18.** Cross-section across the structurally controlled course of the river Shyok near Yadlung show two different profiles. The cross-section at A – A′ is typical U-shaped glacial profile whereas slightly down stream at B – B′, it becomes V-shaped typical fluvial profile.

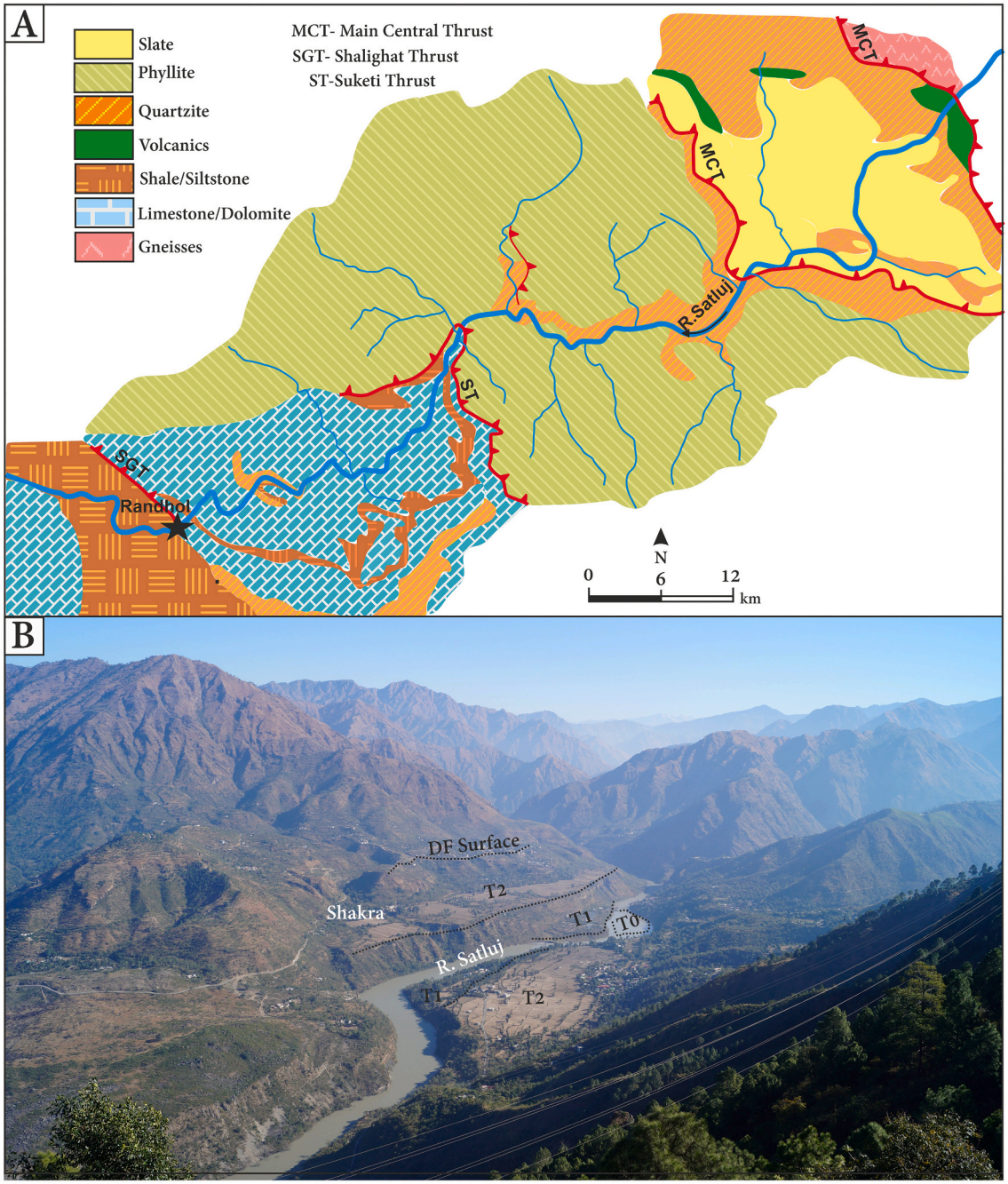


**Fig. 19.** A). Regional geological map of the middle Satluj valley (modified after GSI memoirs 1976 and Thakur and Rawat, 1992) star indicates the location of Shakra; B). Panoramic view of the Satluj valley around Shakra with two aggradation surfaces (valley-fills T2 and T1) and debris flow deposits (DF) (PC- Dr. Shubhra Sharma, BHU, Varanasi).

Two aggradational phases (Terrace $T_1$ and $T_2$) in asymmetrically paired terraces are identified in the wider valley segments of the middle Satluj valley (Fig. 19A). The terrace sediments overlie the bevelled bedrock strath surfaces of variable thickness (Fig. 19A). The older aggradation surface (T2) is classified as valley-fill terrace, whereas, the younger aggradation surface ($T_1$) is identified as a strath terrace based on Bull (1991). The older aggradational phase ($T_2$) having a distinct tabletop topography comprised of weak to moderately lithified gravels indicating that the $T_2$ surface was laid down due to changes in sediment-water ratio because of fluctuating discharge during its deposition. However, the younger aggradational surface ($T_1$), extensive in the middle Satluj valley, appears as a flat-topped surface incising the bedrock at places mainly covered by recent to sub-recent flood sediments. The deposition of $T_1$ terrace also suggests a phase of relative tectonic stability. Also due to the partial sediment supply from the upper catchment and adjoining valley slopes results in the fluvial energy being utilized for the bedrock incision (Sharma et al., 2016; Pratt et al., 2002).

The debris flows in the middle Satluj river (Fig. 19B) mainly comprise of gravity-driven, highly concentrated mixtures of sediment and water, commonly composed of poorly sorted lithoclast, matrix-supported sediments ranging in size from clay to cobbles and boulders. The debris flows in the study area are mainly associated with first or second-order tributary streams, wherein a drastic drop in gradient is observed when it opens into the mainstream. The lithoclasts are dominated by dolomite and slate with subordinate quartzite. Based on the degree of lithification/cementation and various textural properties,

three major generations of debris flows are identified, named DF3 (oldest) to DF1 (youngest) (Sharma et al., 2016).

The alluvial fans in the upper and middle Satluj basin are mainly linked with the second and higher order tributary streams of Satluj river. Morphologically, the deposits appear as fans (cones) radiating downslope from tributary valleys due to the sediment mobilization during episodic rainfall events (Blair and McPherson, 1994). Two generations of alluvial fans are identified based on morpho-stratigraphic position, sedimentary architecture, and degree of weathering/lithification. The older alluvial fan deposits comprise of matrix-supported, moderately lithified, and sorted sediments with crudely fining upward succession with interlay of swelling and pinching silty-sand layers. Younger alluvial fan sediments comprise of non-lithified, poorly sorted, clast dominated, sub-angular lithoclasts with occasional boulders embedded in the silty-sand matrix.

## 4. Discussion

### 4.1. Channels on the volcanic crater and its terrestrial analogue

The linear troughs dissect the entire flank of the Ceraunius Tholus (CT) are interpreted to be the result of fluvial processes by previous workers. The combination of surface runoff and possible sapping, are the constituent agents behind shaping the topography (Gulick and Baker, 1990; Sharp and Malin, 1975). Similarly, channels on the flanks of other volcanoes, such as Hecates Tholus and Alba Patera have been interpreted as fluvial (Mouginis-Mark et al., 1982, 1988; Gulick and Baker, 1989, 1990). There has been much speculation regarding the origin of the large valley on CT (Figs. 4 and 5) and its associated fans, which includes (1) volcanic density flows (e.g., Reimers and Komar, 1979) (2) lava flow with the valley being a lava channel (e.g., Carr, 1974), (3)

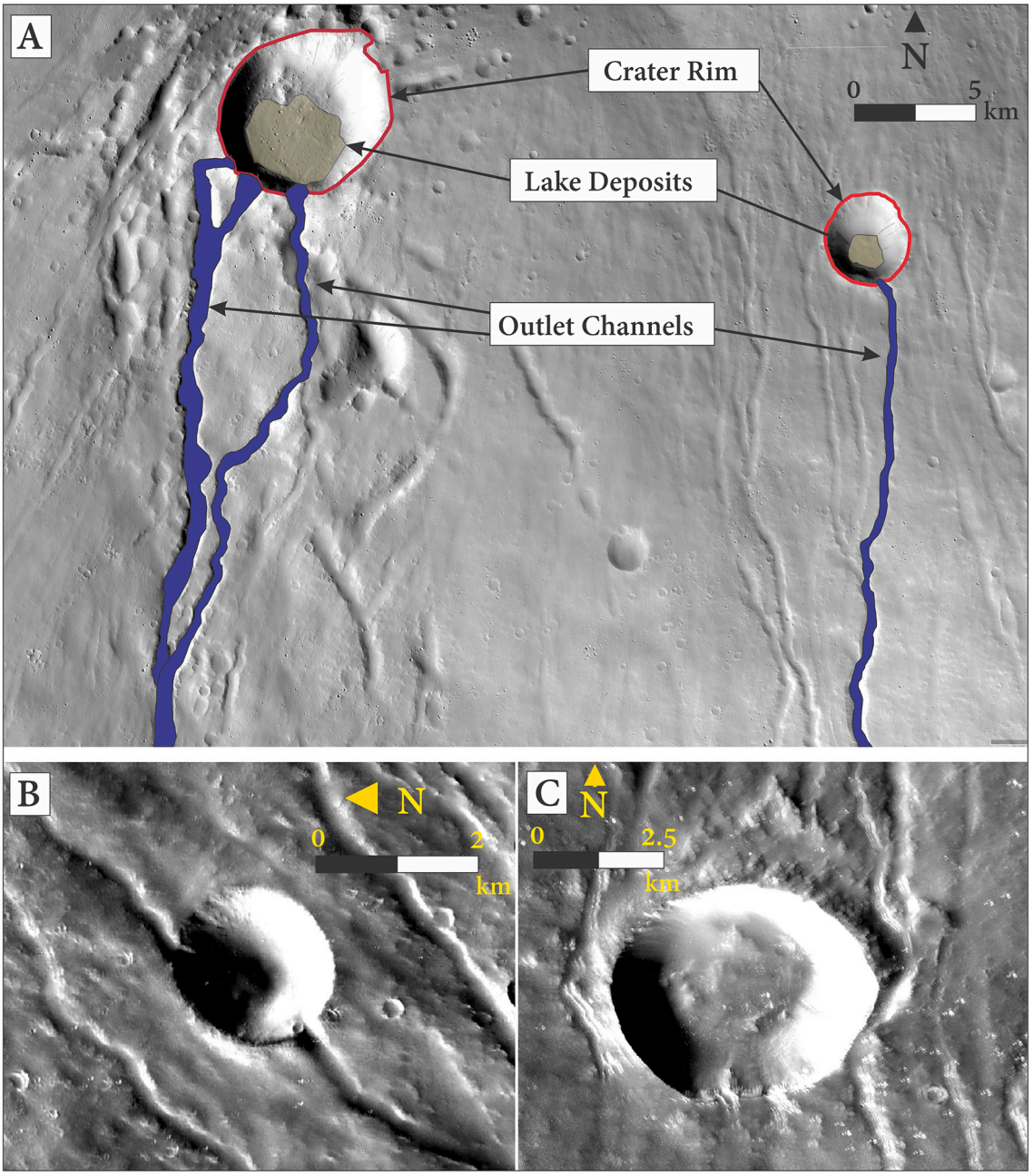


**Fig. 20.** A). Crater Lake on the flank of Ceraunius Tholus with outlet channel probably of Amazonian age fluvial activity; B). Impact crater with inlet and outlet channel on NW flank of Ceraunius Tholus; C). Modified crater rim by fluvial valleys Northern flank of Ceraunius Tholus.

glacial melt-induced surface water flow (e.g., Fassett and Head, 2007), (4) collapse (e.g., Caplinger, 2001), (5) fluvial action (e.g., Gulick and Baker, 1989), and/or (6) combination of these processes. Strath terraces observed along the north-flowing major channel indicate an episodic flow of water probably by the melting of glaciers. Surface water in the channels may also be induced by groundwater flow similar to the terrestrial environment scenarios on Earth. Radial drainage on the flanks of the crater has carved valleys that is reminiscent of strong evidence of fluvial processes (Gulick and Baker, 1989).

Three large canyon-like valleys lie on the northwest flank of Ceraunius Tholus (Figs. 4 and 5). The biggest of these three is a north-trending valley that is comparatively youngest based on crosscutting relationships evident near the crater summit (Fig. 6). This valley is deepest with V-shape near Ceraunius Tholus's summit (Figs. 4 and 5) and becomes U-shape near its base (Figs. 4 and 5), below which lies a substantial fan just inside the rim of the oblong crater Rahe. When the valley debouches into the Rahe crater, it forms a large alluvial fan, wherein the crater acts as a lake/basin, leading to scarp formation within the alluvial fan (Fig. 4). Two different depositional sequences have been documented in the fan that is the older and younger fan indicating two episodes of deposition. The other valleys trending in the West and NNE direction (Figs. 4 and 5) have maintained V-shape near the summit which extends to U-shape in the downstream direction. The Rahe crater precede the formation of major large valleys on the northern flank of Ceraunius Tholus, evidenced by alluvial fan and valley flowing through the crater rim. The small valleys on the crater flank also maintain a V-shape near the crater summit and further U-shape downstream, forming alluvial fans at the edifice base. A number of small craters appear to have been filled with water and then drained into the downslope rim.

The impact craters on the flank of CT have been classified into three groups based on the influence of fluvial activity, mapped at 1:100,000 scale on CTX image mosaic. One, which clearly predates the fluvial activity on the CT, e.g., Rahe crater, has a clear inlet channel with a well-preserved alluvial fan similar to the terrestrial alluvial fan. Further, six such craters are marked with diameters between 1 and 4 km range, and they have both the inlet and outlet channel (Fig. 20), indicating that there is recharge and discharge of water. The relationship of valleys with a crater and its ejecta suggests that valleys were active both before and after the impact event. The second type is where only an outlet channel is preserved (Fig. 20A), indicating that they probably have groundwater-induced water flow forming crater lakes. Seven such impact craters have been marked in the area. The third type of impact craters are widespread on the flank of CT where there is a modification of the crater rim by the adjacent channel (Fig. 20C). Several such types of impact craters are observed with varying diameters from 1 to 5 km range. These relationships with the impact crater provide basic information about small valley formation in multiple episodes or over an extended period.

The valley formation on CT may have taken place around 3.0 Gyr (Fassett and Head, 2007). The characteristics of the fan are not similar to the other fans described on Mars formed when the highland valleys drained into preexisting impact crater (Malin and Edgett, 2003; Moore et al., 2003; Fassett and Head, 2005; Irwin et al., 2005) because of its unique relationship with Rahe crater. The valley enters the Rahe crater cutting the entire rim forming a large alluvial fan, which is only possible when the river carries a huge sediment load. Deposition of sediment in Rahe crater alluvial fan (Fig. 4) is subaqueously allowing to form delta plain, delta front, and pro-delta plain (Malin and Edgett, 2003; Moore et al., 2003; Fassett and Head, 2005).

There is none or obscured tectonic activity in CT area. The knick points along the north-flowing large valley are thought to be generated because of the differential flows during the eruption, which is often found in the terrestrial volcanoes on earth. The evolutionary history, tectonic and climate conditions, stream formation, drainage characteristics, and further gullies and knick point formation within the streams on the CT flank suggests that multiple processes have played a hand-in-hand role in the modulation of the terrain.

Dhinodhar hill, a hydro-volcanic vent in the Deccan Traps with a monogenetic volcanic field implying limited, periodic magma supply and low-degree mantle cooling in Kachchh mainland volcanics (Biswas and Deshpande, 1973). Therefore, Dhinodhar hill is considered a typical example of the volcanic crater formation in the terrestrial environment. The characteristic radial drainage pattern observed from the flanks of the crater of Dhinodhar hill is similar to the drainages observed on a broader scale on the Ceraunius Tholus volcano on Mars (Fig. 2B). The debris flow valleys observed at the inner wall of Dhinodhar crater (Fig. 3A and B) and Ceraunius Tholus seems to have formed by the gravity collapse or influence of water, or a combination of both. The region has developed a small-scale geomorphic system wherein the first-order stream initiation is observed at the summit of the hill, followed by debris flow aprons due to a steep slope gradient. As the rivers flowing from the Dhinodhar hill debouches into the Banni plain, the alluvial fan formation due to gradient loss takes place similar to Ceraunius Tholus volcano setting on Mars (Fig. 2A and B).

Overall, the major geomorphic processes in Dhinodhar hill indicate a fluvio-erosional and depositional system consisting of radial drainage patterns, colluvial deposits, valleys, knick points, and alluvial fan at the lower reaches. The system developed at Dhinodhar hill provides a basic idea of the processes behind shield volcanoes, which can further be extrapolated to the shield volcanoes on planets like Mars.

### 4.2. *Fluvial basin on Hesperian volcanic units and their analogue valleys from Deccan volcanic province*

The theater-headed channels on the Echus plateau comprising of basaltic rocks required differential climatic and tectonic settings. Similar valleys are also observed on the south rim of Valles Marineris, analogous to glacially eroded theater-headed channels on Devon Island (Lee, 2000). Echus plateau valley has reported four episodes of volcanic activities and four flooding episodes with one major structural deformation in Hesperian time (Chapman et al., 2010a), summarized in Table 2 (Fig. 21A-F). The responsible factor for the fluvial activity in the area is both the spring sapping and glacial erosion leading to the development of theater-headed valleys on the basaltic lava flow terrain. Similar valleys are observed on the northwestern Deccan traps from the Tapi River highland units flowing from East-West.

On the regional scale in the Tapi River highlands, the basement block structure is controlled by the basement faults, which are cutting across the Deccan Traps, further continuing into the Tertiary sediments along with the trend of the Son-Narmada-Tapi rift. (Mathur and Kohli, 1963; Mathur and Evans, 1964; Raju, 1968, 1979; Chandra and Chowdhary, 1969; Rao, 1969; Markevich, 1976; Chaube, 1980; Kaila et al., 1981; Biswas, 1982, 1987; Kaila and Krishna, 1992). The extensive jointing and fracturing of the basaltic lava flows have given rise to the primary erosion along which broad, flat-bottomed, intermontane valleys have developed. The presence of dyke swarms in the north of the area and a few at the mouth of the Alaldari valley (Fig. 10B) (Auden, 1949; Krishnamacharlu, 1972; Karanth and Sant, 1995), the Tapi and associated lineaments (Blanford, 1867; Powar, 1981), fracture controlled drainage system (Alavi, 1990) indicate the role of tectonism in the formation of the valleys in the area (Fig. 21G-I). Further, Dubey and Saxena (1988) envisaged the tectonic effect during the Quaternary time in the form of fracturing and warping of trappean rocks, dyke emplacements, and tilting of the alluvium. The dykes within and surrounding areas show strong preferred orientation, with an average trend of $N88^0$ (Ray et al., 2007 and references therein). According to Ray et al. (2007), the dykes are not emplaced along faults or pre-existing fractures. The measured width of dyke within the study area is 4.7 m, composed of doleritic material. The major knickpoints are formed because of the lithological control within the area along the theater head wall valleys with two specific measured heights (one with 50 m and the other 195 m). A set of geomorphic features are also observed along the channel and on the wall of the presently flowing channel, which indicates the strong

**Table 2**
Major events occurred within Echus plateau canyon valleys (Chapman et al., 2010a, 2010b; Zealey, 2007, 2008; Duran and Coulthard, 2020, and references therein).

| Age | Volcanism/Structural deformations | Flooding |
|---|---|---|
| Noachian materials likely crop out at the core of valleys as wall rocks which is designated as Hesperian Noachian undivided (HNu) units deep erosion of the Echus plateau and older strata are exposed in wall rocks | | |
| 3.7 Ga | Deposition of flood basalts which has formed the Hesperian ridged plains (unit Hr) marks the first volcanic episode to affect the area | |
| 3.61 Ga ± 0.4 | | First widespread fluvio-glacial episode |
| 3.60 Ga ± 0.1 | Fracturing and faulting leads to the formation of major and minor grabens in Early Hesperian reactivation took place through time till Amazonian | |
| 3.4 Ga | Emplacement volcanic of Hesperian Syria Planum formation lower members and the ash deposits of middle members marks the second episode of the volcanism | |
| 3.4 ± 0.7 Ga | | The sinuous ridges on the Lower Syria Planum formation marks the second fluvio-glacial period |
| 3.38 to 3.37 Ga | The third episode of volcanism mostly have deposits in Norther Kasei valleys the area is affected by the lava tubes similar to the terrestrial lava tube and deposition of Upper member of Syria Planum formation | Carving of the narrow dendritic surface channels started in middle member of the Syria Planum formation (Hsm) with release of water from downslope of the Echus plateau formation of the theater-headed channel occurred along the canyon wall |
| Amazonian time | Amazonian platy flow unit Apf. These flows has the ponded lava lakes observed at the foothill of the Echus plateau | |
| 54 and 98 Ma | | Ponding within the floor of the Apf unit |

influence of tectonics and catastrophic climate in modulating the topography of an area.

Overall, drainage of Alaldari shows the westerly flow, and their trends are controlled by the ENE - WSW fractures, i.e., the basement fracture trends (Powar, 1981). Whereas for the Echus plateau canyon, the drainages are easterly flowing following the Hesperian unit's fractures trend (Chapman et al., 2010a). The first-order streams show dendritic drainages while the higher-order contacts are rectangular, indicating the influence of the tectonics within the area for both the basin. However, the role of lithology is equally essential and cannot be ruled out. Two lakes are observed in the lower reaches of the Echus plateau canyon along the channel, suggesting that the lakes may have sustained the water within them until the last phase of drying on Mars. Similar sag ponds and river lakes are observed in Alaldari valley; detailed studies of this lake sediment and microbial life within this lake will provide a simulated environment for the astrobiological studies. Chandrasekharam (2000) has identified seven geothermal provinces of India, amogst those three of which are located in and around the Tapi river basin. The presence of geothermal springs in an area indicates high heat flow, steep geothermal gradients, and very fragile and sensitive nature of the crust (Tandon and Chaudhry, 1968; Lee and Rayleigh, 1969; Singh et al., 1975: Ravishanker and Dubey, 1984; Ravishanker, 1987). The presence of hot-spring along the strike of these valleys serves as the analogue hydrothermal setting for Martian hot springs (Brakenridge et al., 1985). The derived morphometric parameters including stream ordering, bifurcation ratios, drainage density, mean stream length, river sinuosity, basin asymmetry factor, the ratio of valley floor width to valley height for both the fluvial basin (Table. 3), the inferences are reported in Section 3.2.3 of this paper.

On the broader scale, both the basin have experienced tectonic and catastrophic flooding through time, leading to the idea of the variation in climate, and the tectonism has played a significant role in bringing up present-day scenarios on Earth, and that can to be extrapolated for Mars (Fig. 21).

### 4.3. Fluvial terraces

The valleys on Mars have preserved evidences of warm and wet climatic conditions, just like Earth's terrestrial fluvial valleys. The aerial distribution of these valleys indicates a huge amount of water discharge. It is most likely expected that most of the channels/valleys result from persistent water flow on the surface of Mars, and the same can be inferred for Noctis Fossae. In Noctis Fossae region, the Early-Late Hesperian surface experienced large-scale fluvial erosion along with the major fault system (Plescia and Saunders, 1982). The valleys of Noctis Fossae have attained the base level by the fluvial erosion with the formation of fluvial terraces along the major valley/channels. The channels on the northern side are shallower and branched, running parallel to each other, further disturbed by the later impact crater (Fig. 11). The long narrow valleys subjected to large scale fluvial activity forming U—V shaped valleys arising due to glacial melt from higher ranges wherein U-shaped valleys depict glacial erosion and the V-shape show extensive episodic fluvial activity. The formation of the fluvial terraces in the Noctis Fossae is influenced by the post-early Hesperian tectonics and episodic melting of the glaciers. The span of fluvial activity was superficially present during early to late Hesperian period and later on it became concentrated to Noctis Labyrinthus troughs forming lake during early Amazonian period.

It is evident that the Nubra basin once supported largest and voluminous glacier in the entire Himalayan range (Ganju et al., 2018) which are also hypothised to be present in southern Highlands of Mars (Conway et al., 2018). The enormity of the glacier, is borne by its large span (~3 km average) that has a maximum width (~5 km) at the confluence. The morphology of the Nubra basin suggests that it was glacially scooped and has a typical U-shaped valley, a similar type of U-shaped valleys are documented in the upstreams of Noctis Fossae (Fig. 18). Furthermore, it has longest moraines extending up to ~80 km from the snout of the Siachen to the confluence (Ganjoo et al., 2018) where the Shyok glacier contributed its might to push the glacier at least up to Yadglung all along the Shyok suture ~50 km downstream (Fig. 15). This glacial advances occurred in two stage and can be called as Stage-1 or Yadlung Advance. The second advance is represented by the drumlins and glacial striations on the valley wall near Tirit on the Nubra (Ganjoo et al., 2018) (Fig. 15).

Two important factors contributing to glaciations are (i) low temperature and (ii) moisture. The ideal altitude for the development for glaciers is 5000 m and above as the temperature drops with the altitude at the rate of ~6.5 °C/km$^2$. It is likely that Karakoram has already attained the required altitude to host a glacier of Siachen's magnitude during the early Quaternary. In addition to low temperature, moisture is another important factor that forms the glacier ice. Enormous amount of moisture will be required to generate a glacier of the Nubra and Shyok magnitude. The evidence suggests that heavy buildup of snow and ice over Ladakh and Tibetan plateau may require long term cold climate to

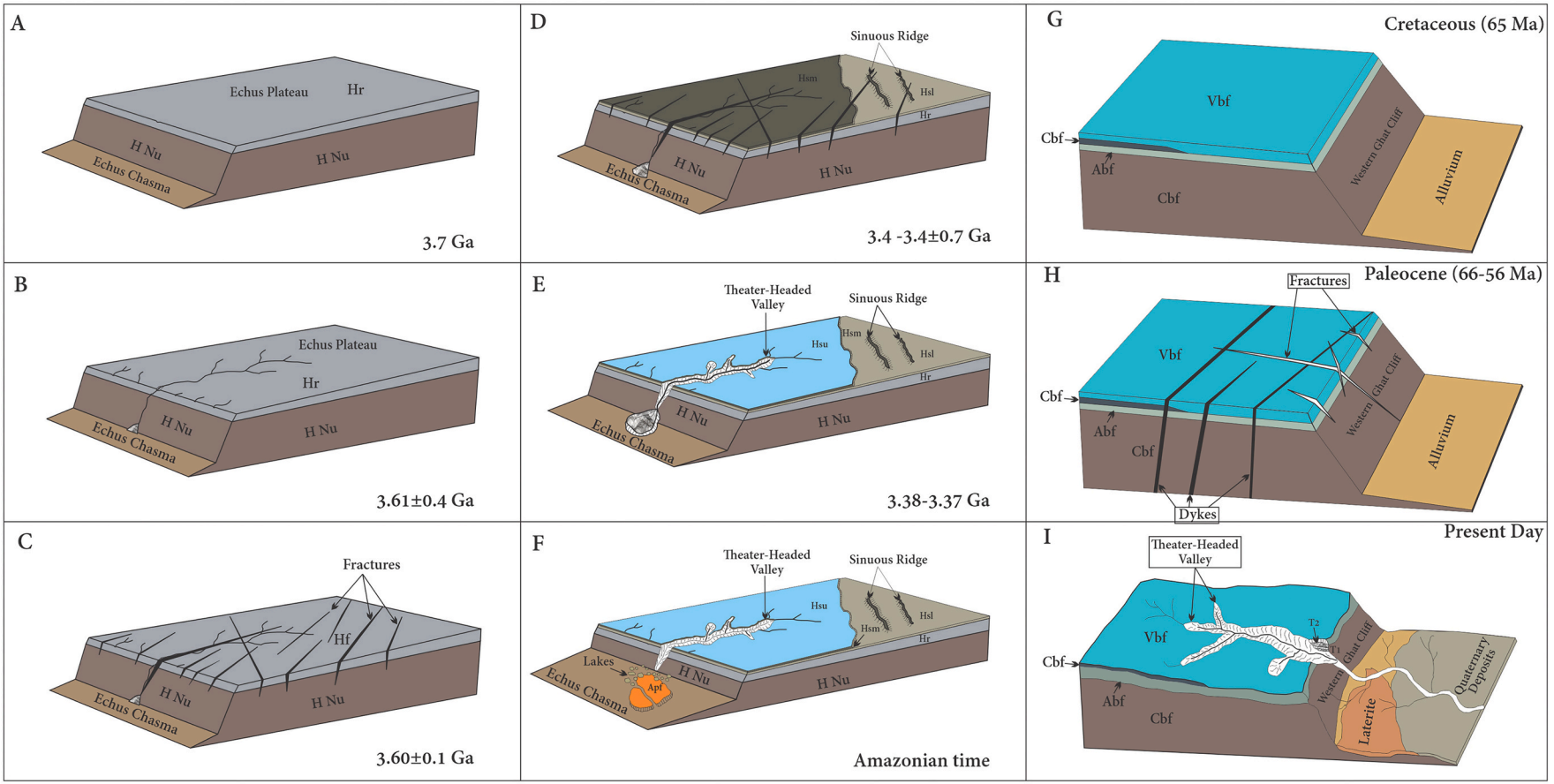


**Fig. 21.** A-F). Evolutionary model of the Theater headed valley on Echus Plateau through time. HNu- Hesperian Noachian units, Hr- Hesperian ridge plain, Hf- Hesperian Fractured units, Hsl- Lower Syria Planum formation, Hsm- Middle Syria Planum formation, Hsu- Upper Syria Planum Formation, G-I).Evolutionary model of Alaldari valley from Cretaceous to present. Cbf- Compact basaltic flow, Abf- Amygdaloidal basaltic flow, Vbf- Vesicular basaltic flow.

**Table 3**
Morphometric parameters/indices for the fluvial basin on Echus plateau canyon and their analogue intermontane valleys from Deccan trap cliff (Alaldari Valleys).

| Sr. No. | Morphometric Parameters/ Indices | Valleys on Echus Plateau | Alaldari Valleys |
|---|---|---|---|
| 1 | Stream ordering | | |
| | 1st | 142 | 225 |
| | 2nd | 30 | 52 |
| | 3rd | 5 | 11 |
| | 4th | 1 | 3 |
| | 5th | | 1 |
| 2 | Bifurcation ratio | 5.24 | 3.92 |
| 3 | Drainage Density | 3.26 $Km^{-1}$ | 0.568 $Km^{-1}$ |
| 4 | Main Stream Length | 62.3 km | 6.32 km |
| 5 | River Sinuosity | 1.03 | 1.05 |
| 6 | Basin Asymmetry factor | 46.9 | 60.2 |
| 7 | Ratio of Valley Floor Width to | 0.43 | 0.197 |
| | Valley Height | 0.22 | 0.33 |
| | | 0.287 | 0.43 |

sustain glaciations in the region. The existence of glaciers in Kashmir and Ladakh (Brown et al., 2002; Owen et al., 2005; Taylor and Mitchell, 2000) indicates that moisture was available for the growth of glaciers. Tibet was glaciated during the Quaternary, which is evident by the existence of relict moraines and ice-caps that have provided valuable information on the climate change. It can therefore be concluded that the Karakoram receives moisture exclusively through the westerlies that feeds the Siachen glacier. It is likely that the Siachen advanced to give rise to the Nubra – Shyok glaciations, with the expansion of the Northern Hemispheric ice sheet during the Quaternary. Same scenario can be postulated for the glaciation in higher reaches of Noctis Fossae.

The fluvial dynamics plays a vital role in the style and pace of landscape evolution in the areas that fall outside the regime of glaciers. In actively deforming mountain belts, rivers flowing continuously incise with insignificant sediment storage (similar to present-day Satluj River) (Sharma et al., 2016; Tinkler and Wohl, 1998). The discontinuous records of valley-fills, alluvial fans, and debris-flow deposits in the river suggest that incision was interrupted by climatically driven pulses of aggradation (Sharma et al., 2016; Pratt-Sitaula et al., 2004). Out of the two distinct phases of aggradations observed in the middle Satluj, the older phase of aggradation ($T_2$), suggests deposition during the post-glacial revival of Indian Summer Monsoon (ISM) (Sirocko et al., 1993; Schulz et al., 1998) supported by high sediment flux.

The second phase of aggradation continued beyond Holocene and probably till early mid-Holocene (Bookhagen et al., 2006; Sharma et al., 2016). The youngest aggradation phase is represented dominantly by a strath surface and suggests reduced sediment supply from the catchment area (Sharma et al., 2016). However, abnormal uplift is recorded in the proximity of major and minor structures at a local scale to modify the river profile (Tyagi et al., 2009). An expression of relative displacement (differential uplift?) is observed in the older aggradation (T2) juxtaposed by a laterally persistent strath terrace and associated gorge downstream, which is ascribed to a river crossing a fault (Sharma et al., 2016; Whittaker et al., 2007) and can be related to tectonic instability after the older aggradation phase. On the other hand, the surface structure of the younger aggradation phase (T1) dominated by the strath surface, can be construed to evidence of relatively enhanced bedrock uplift after ~0.4 ka (Sharma et al., 2016) (Fig. 19). In the middle reaches of Noctis Fossae comparable terraces have been documented, which are formed due to fluvial runoff supported by Hesperian tectonic activity (Tanaka and Davis, 1988).

## 5. Conclusions

The present study identified three new terrestrial analogue sites located in the different geological domain of the Indian sub-continent which can be used to understand the fluvial and glacial landform evolution on the Martian surface. Based on the geomorphology and morphometry following broad inferences can be drawn.

- Though no planetary analogue environment is perfect, the extremely dry and hyper-arid climate, the occurrence of hydrated mineral, analogue iron concretions (Martian blueberries), hypersaline lakes, brines, and poorly vegetated landscape makes Kachchh basin of western India the most relevant analogue site for understanding geomorphology and mineralogy of Mars (Bhattacharya et al., 2016; Chavan and Bhandari, 2019; Ray et al., 2021; Chavan et al., 2022; Chavan and Bhandari, 2022). The valleys developed on the flank of volcanic crater Ceraunius Tholus show strong fluvial processes, robustly equating to the hydro-volcanic monogenetic volcanic field of Dhinodhar hill, Kachchh, as illustrated by similar volcanic rocks, drainage patterns, and fluvial activity. The set of geomorphic features such as debris flow channels, colluvial fans, cross-cutting channels, alluvial fans, and strath terraces along the channels indicate the episodic flow of water played a vital role in formulating topography on Mars and Earth.
- The valleys developed on the basaltic rocks of Deccan trap in the upper reaches of the Tapi river (Alaldari drainage), showing the development of theater-headed valleys. These features are similar to the one observed on the Hesperian volcanic units of the Echus plateau. Thus we tend to suggest that the primary element for opening these valleys is tectonic activity in both areas. The channel indicates the strong influence of catastrophic climate and tectonism, which is also supported by the morphometric analysis in modulating the topography of the Martian Echus plateau and the Alaldari valley area. This observation indicates that the Martian tectonism influenced the origin and evolution of the theater-headed valleys in Echus plateau and the south rim of Valles Marineris.
- The fluvial terraces developed in the Nubra and Shyok rivers of Ladakh and Upper and Middle reaches of Satluj in Central Himalayas and Noctis fossae on Mars are all developed due to interplay of tectonism and climate. The channels/valleys result from persistent water flow on the surface with a huge amount of water discharge wherein the upper reaches had glacial preservance, and the lower reaches had dominance of fluvial developed deposits. All the above-mentioned features suggest a complex interplay of climate and tectonics in the development of glacial and fluvial valley in Nubra-Shyok and Satluj rivers of Ladakh and Himachal Pradesh which can be extrapolated to the development of valley systems in Noctis Fossae region of Mars and also deepens our knowledge on the fluvial geomorphology of the area.
- Finally it can be hypothesized that the stream dynamics and terrace formation reflect the major fluvial and glacial activities on Mars (Chapman et al., 2010a and b; Duran et al., 2019; Duran and Coulthard, 2020). Valley networks on Mars show morphological features that suggest an origin due to ancient precipitation and surface runoff. A variety of fluvial features, ranging from valley networks, drainage basins, river terraces, and valley morphology, suggest that the persistent past climate and tectonics have played a crucial role in the development of studied martian landforms and their earth analogues.

## Declaration of Competing Interest

The authors declare that they have no known competing financial interests or personal relationships that could have appeared to influence the work reported in this paper.

## Acknowledgment

The study is funded by ISRO (Indian Space Research Organization), MOM-AO Project ISRO/SSPO/MOM-AO/2016-17. This work forms a part of the doctoral thesis of Mr. Anil Chavan. The authors acknowledge Mr. Sachin Gavit and Mr. Vishal Kokani for helping in the fieldwork at Alaldari. We are thankful to the CTX, MOLA, and HRSC teams support in making their data available. Dr. Navin Juyal is thanked for his critical suggestions in improving the paper. Dr. Nawal Kishor Sharma is acknowledged for his help in improving written English. The authors are grateful to the anonymous reviewers for their constructive and insightful suggestions, improving our paper in its present form.

## Appendix A. Supplementary data

Supplementary data to this article can be found online at https://doi.org/10.1016/j.icarus.2022.115118.

## References

Alavi, S.A., 1990. Morphotectonic Analysis of South Gujarat Landscape. Unpubl. Ph.D. thesis. M.S. University of Baroda, Vadodara, p. 203.

Alemanno, G., Orofino, V., Mancarella, F., 2018. Global map of Martian fluvial systems: age and total eroded volume estimations. Earth Space Sci. 5, 560–577. https://doi.org/10.1029/2018EA000362.

Arya, A.S., Sarkar, S.S., Srinivas, A.R., Manthira Moorthi, S., Patel, Vishnukumar D., Singh, Rimjhim B., Kiran Kumar, A.S., 2015. Mars colour camera: the payload characterization/calibration and data analysis from earth-imaging phase. Curr. Sci. 109 (06), 1076–1086.

Auden, J.B., 1949. Dykes in Western India. Trans. Nat. Inst. Sci. India 3, 123–157.

Babu, P.V.L.P., 1984. A structural synthesis of the Lower Narmada River Basin and its bearing on the Mesozoic oil prospects. Petrol. Asia J. VII (1), 97–101.

Baker, V.R., 1979. Martian channel morphology: Maja and Kasei Valles. J. Geophys. Res. 84, 7961–7983.

Baker, V.R., 1982. The Channels of Mars. Univ. of Texas, Austin, p. 198.

Baker, V.R., Carr, M.H., Gulick, V.C., Williams, C.R., Marley, M.S., 1992. Channels and valley networks on Mars. In: Univ. of Ariz. Press, Tucson, pp. 493–522.

Baker, V.R., Hamilton, c.w., Burr, D.M., Gulick, V.C., Komatsu, G., Luo, W., Rodriguez, J. A.P, 2015. Fluvial geomorphology on Earth-like planetary surfaces: A review. Geomorphology 245, 149–182. https://doi.org/10.1016/j.geomorph.2015.05.002.

Baker, V.R., Kochel, D.J., 1978. Morphometry of streamlined forms in terrestrial and Martian channels. In: Proc. Lunar Planet. Sci. Conf. 9th, pp. 3193–3203.

Baker, V.R., Kochel, D.J., 1979. Martian channel morphology: Maja and Kasei Valles. J. Geophys. Res. 84, 7961–7984.

Baker, V.R., Milton, D.J., 1974. Erosion by catastrophic floods on Mars and earth. Icarus 23 (1), 27–41. https://doi.org/10.1016/0019-1035 (74)90101-8.

Baker, V.R., Boothroyd, J.C., Carr, M.H., Cutts, J.A., Komar, P.D., Laity, J.E., Patton, P.C., 1983. Channels and valleys on Mars. Bull. Geol. Soc. Am. 94 (9), 10351054.

Baker, V.R., Kochel, R.C., Laity, J.E., Howard, A.D., 1990. Spring sapping and valley network development. In: Higgins, C.G., Coates, D.R. (Eds.), Groundwater Geomorphology; The Role of Subsurface Water in Earth-surface Processes and Landforms, Geological Society of America Special Paper, vol. 252, pp. 235–265.

Baker, V.R., Strom, R.G., Gulick, V.C., Kargel, J.S., Komatsu, G., Kale, V.S., 1991. Ancient oceans, ice sheets and the hydrological cycle on Mars. Nature 352, 589–594.

Bhattacharya, S., Mitra, S., Gupta, S., Jain, N., Chauhan, P., Parthasarathy, G., Ajai, P., 2016. Jarosite occurrence in the Deccan Volcanic Province of Kachchh, western India: spectroscopic studies on a Martian analog locality. J. Geophys. Res. Planet 121. https://doi.org/10.1002/2015JE004949.

Biswas, S.K., 1982. Rift basins in the western margin of India and their hydrocarbon prospects. Bull. Am. Assoc. Pet. Geol. 66 (10), 1497–1513.

Biswas, S.K., 1987. Regional tectonic framework, structural and evolution of western marginal basins of India. Tectonophysics 135, 315–327.

Biswas, S.K., 1993. Geology of Kachchh. KD Malaviya Institute of Petroleum Exploration, Dehradun, p. 450.

Biswas, S.K., Deshpande, S.V., 1973. A note on the mode of eruption of the Deccan Trap lavas with special reference to Kutch. Geol. Soc. India 14 (2), 134–141.

Blair, T.C., McPherson, J.G., 1994. Alluvial fan processes and forms. In: Geomorphology of Desert Environments. Springer, Dordrecht, pp. 354–402.

Blanford, W.T., 1867. On the geology of Tapti and Narbudda valleys and some adjoining districts. Mem. Geol. Surv. India VI (part 3).

Blasius, K.R., Cutts, J.A., 1976. Shield volcanism and lithospheric structure beneath the That-ala Plateau, Mars. In: Proc.Lunar Sci. Conf.7th, pp. 3561–3573.

Blasius, K.R., Cutts, J.A., Guest, J.E., Masursky, H., 1977. Geology of the Valles Marineris: first analysis of imaging from the Viking 1 orbiter primary Mission. J. Geophys. Res. 82 (28), 4067–4091. https://doi.org/10.1029/JS082i028p04067.

Bookhagen, B., Fleitmann, D., Nishiizumi, K., Strecker, M.R., Thiede, R.C., 2006. Holocene monsoonal dynamics and fluvial terrace formation in the northwest Himalaya, India. Geology 34 (7), 601–604.

Brakenridge, G.R., Newsom, H.E., Baker, V.R., 1985. Ancient hot springs on Mars: origins and paleoenvironmental significance of small Martian valleys. Geology 13 (12), 859–862.

Brass, G.W., 1980. Stability of brines on Mars. Icarus 42, 20–28.

Bretz, J.H., Theodore, H., Smith, U., Neff, G.E., 1956. Channeled scabland of Washington; new data and interpretations. Geol. Soc. Am. Bull. 67, 957–1049.

Brown, E.T., Bendick, R., Bourle's, D.L., Gaur, V., Molnar, P., Raisbeck, G.M., Yiou, F., 2002. Slip rates of the Karakorum Fault, Ladakh, India, determined using cosmic ray exposure dating of debris flows and moraines. J. Geophys. Res. 107, 2192–2205.

Bull, W.B., 1977. Tectonic Geomorphology of the Mojave Desert. U.S. Geological Survey Contract Report 14-08-001-G-394. Office of Earthquakes, Volcanoes, and Engineering, Menlo Park, CA.

Bull, W.B., 1978. Geomorphic tectonic classes of the south front of the San Gabriel Mountains, California. In: U.S. Geological Survey Contract Report 14–08-001-G-394. Office of Earthquakes, Volcanoes, and Engineering, Menlo Park, CA.

Bull, W.B., 1991. Geomorphic Responses to Climatic Change. Oxford University Press, New York, p. 326.

Burt, D.M., Knauth, L.P., 2003. Electrically conducting, Ca-rich brines, rather than water, expected in the Martian subsurface. J. Geophys. Res. 108, 9951–9973.

Caplinger, M.A., 2001. High-resolution imaging of Ceraunius Tholus, Mars. Lunar Planet. Sci. 32 (Abstract 1342).

Carr, M.H., 1974. The role of lava erosion in the formation of lunar rilles and martian channels. Icarus 22, 1–23.

Carr, M.H., 1981. The Surface of Mars. Yale Univ. Press, New Haven, Conn, p. 232.

Carr, M.H., 1995. The Martian drainage system and the origin of valley networks and fretted channels. J. Geophys. Res. Planet. 100, 7479–7507.

Carr, M.H., 1996. Water on Mars. Oxford Univ. Press, New York.

Carr, M.H., 2006. The Surface of Mars. Cambridge University Press, 307 pp.

Carr, M.H., Head, J.W., 2003. Oceans on Mars: an assessment of the observational evidence and possible fate. J. Geophys. Res. 108, 5042.

Carr, M.H., Head, J.W., 2010. Geologic history of Mars. Earth Planet. Sci. Lett. 294 (3–4), 185–203. https://doi.org/10.1016/j.epsl.2009.06.042.

Chamyal, L.S., Maurya, D.M., Raj, R., 2003. Fluvial systems of the drylands of western India: a synthesis of Late Quaternary environmental and tectonic changes. Quat. Int. 104 (1), 69–86.

Chandra, P.K., Chowdhary, L.R., 1969. Stratigraphy of the Cambay basin. Bull. ONGC 6 (2), 37–50.

Chandrasekharam, D., 2000. Geothermal energy resources of India: Country Update. In: Proc. World Geothermal Congr. 2000, Japan, pp. 133–142.

Chandrashekar, H., Lokesh, K.V., Sameena, M., Roopa, J., Ranganna, G., 2015. Coastal and Ocean Engineering (Mangalore). In: Dwarakish, G.S. (Ed.), Proc. Int. Conf. Water Resources, 4. Elsevier Procedia, pp. 1345–1353.

Chapman, M.G., Scott, D.H., 1989. Geology and hydrology of the north Kasei Valles area, Mars. In: Lunar Planet. Sci. Conf., 19th, Proceeds., Part 1, pp. 367–375.

Chapman, M.G., Neukum, G., Werner, S.C., Gasselt, S., Dumke, A., Zuschneid, W., Michael, G., 2007. Echus Chasma and Kasei Valles, Mars: New Data and Geologic Interpretations. 37th Lunar and Planetary Science Conference (#1407).

Chapman, M.G., Neukum, G., Dumke, A., Michael, G., Van Gasselt, S., Kneissl, T., Masson, P., 2010a. Noachian – Hesperian Geologic History of the Echus Chasma and Kasei Valles System on Mars : New Data and Interpretations, 294, pp. 256–271. https://doi.org/10.1016/j.epsl.2009.11.032.

Chapman, M.G., Neukum, G., Dumke, A., Michael, G., Van Gasselt, S., Kneissl, T., Zuschneid, W., Hauber, E.N.M., 2010b. Amazonian geologic history of the Echus Chasma and Kasei Valles system on Mars: new data and interpretations. Earth Planet. Sci. Lett. 294 (3–4), 238–255. https://doi.org/10.1016/j.epsl.2009.11.034.

Chaube, A.N., 1980. Geologic framework of the oil and gas fields of the Indian platform. In: Energy Conference, Honolulu.

Chavan, A.A., Bhandari, S., 2017. Fluvio geomorphic set-up of Noctis Fossae in Noctis Labyrinthus of Syria-Planum Provenance, Mars. In: AGU Fall Meeting Abstracts, vol. 2017 pp. P41C-2849.

Chavan, A.A., Bhandari, S., 2019. Potential terrestrial geomorphic analogues from Kachchh rift basin, western India to Mars. In: 9th Internal. Conf. on Mars, Lunar Planet. Sci. Contrib. Rept. 2089, p. 6076.

Chavan, A.A., Sarkar, S., Bhandari, S.L., 2021. Episodic and declining fluvial processes in Noctis Fossae, Syria Planum Province, Mars. Adv. Space Res. Submitted for publication.

Chavan, A., Bhandari, S., 2022. Volcanic craters and cones in central Kachchh mainland, western India: potential analogue for the Martian studies? J. Earth Syst. Sci. 131 (3). In press.

Chavan, A.A., Bhore, V.K., Bhandari, S.L., 2021a. Morphometric analysis of Alaldari Valley Western Deccan Traps: implications for the Martian analogue studies. LPI Contrib. 2595, 8056.

Chavan, A.A., Sarkar, S., Thakkar, A.C., Bhandari, S.L., 2021b. A new method of mosaicking context camera (CTX) images for the geomorphological study of Martian landscape. Open J. Geol. 11, 373–380.

Chavan, A., Sarkar, S., Thakkar, A., Solanki, J., Jani, C., Bhandari, S., Bhattacharya, S., Desai, B.G., Ray, D., Shukla, A.D., Sajinkumar, K.S., Mitra, S., Gupta, S., Chauhan, G., Thakkar, M.G., 2022. Terrestrial Martian Analog Heritage of Kachchh Basin, Western India. Geoheritage 14 (1), 1–26.

Cheung, K.K., King, S.D., 2014. Geophysical evidence supports migration of Tharsis volcanism on Mars. J. Geophys. Res. E Planet 119 (5), 1078–1085.
Chevalier, M.L., Ryerson, F.J., Tapponnier, P., Finkel, R.C., Van der Woerd, J., Li, H.B., Liu, Q., 2005. Sliprate measurements on the Karakorum fault may imply secular variations in fault motion. Science 307, 411–414.
Chevier, V.F., Altheide, T.S., 2008. Low-Temperature Aqueous Fluids on Mars. Abstracts submitted to the Lunar Planet. Sci. Conf. 39th, #1176.
Christensen, P.R., Bandfield, J.L., Bell, J.F., Gorelick, N., Hamilton, V.E., Ivanov, A., Wyatt, M.B., 2003. Morphology and composition of the surface of Mars: Mars odyssey THEMIS results. Science 300 (5628), 2056–2061. https://doi.org/10.1126/science.1080885.
Christensen, P.R., Jakosky, B.M., Kieffer, H.H., Malin, M.C., Mcsween, H.Y., Nealson, K., Ravine, M., 2004. The thermal emission imaging system (THEMIS) for the Mars 2001 odyssey mission. Space Sci. Rev. 110 (1), 85–130. https://doi.org/10.1023/B:SPAC.0000021008.16305.94.
Conway, S.J., Butcher, F.E., de Haas, T., Deijns, A.A., Grindrod, P.M., Davis, J.M., 2018. Glacial and gully erosion on Mars: a terrestrial perspective. Geomorphology 318, 26–57.
Cox, R.T., 1994. Analysis of drainage basin symmetry as a rapid technique to identify areas of possible Quaternary tilt-block tectonics: an example from the Mississippi Embayment. Geol. Soc. Am. Bull. 106, 571–581.
Craddock, R.A., Howard, A.D., 2002. The case for rainfall on a warm, wet early Mars. J. Geophys. Res. 107 https://doi.org/10.1029/2001JE001505.
Crumpler, L.S., Head, J.W., Aubele, J.C., 1996. Calderas on Mars: Charac- teristics, structural evolution, and associated flank structures. In: McGuire, W.C., Jones, A.P., Neuberg, J. (Eds.), Volcano Instability on the Earth and Other Planets, vol. 110. Geol. Soc. of London Special Publication, pp. 307–348.
Das, B., Paul, D.K., Chaudhary, A.K., Ray, A., Patil, S.K., Biswas, S.K., 2007. Petrology and geochemistry of basanite dikes and gabbro from northern Kachchh, western India: implications on source rock characteristics. J. Geol. Soc. India 70, 771–779.
De, A., 1964. Iron–titanium oxides of the alkali olivine basalts, tholeiites, and acidic rocks of the Deccan Trap series and their significance. In: Int Geol Congr 24th Sess, 7, pp. 126–138.
De, A., 1981. Late Mesozoic-Lower Tertiary magma types of Kutch and Saurashtra. In: Subbarao, K.V., Sukheswala, R.N. (Eds.), Deccan Volcanism and Related Basalt Provinces in Other Parts of the World, 3. Geol Soc Ind Mem, pp. 327–339.
Dohm, J.M., Tanaka, K.L., 1999. Geology of the Thaumasia region, Mars: plateau development, valley origins, and magmatic evolution. Planet. Space Sci. 47, 411–431.
Dubey, R., Saxena, R.K., 1988. Thermal springs and associated tectonics of Tapi basin area, districts Dhule and Jaigaon, Maharashtra. Rec. Geol. Surv. India 115, 150–174.
Duran, S., Coulthard, T.J., 2020. The Kasei Valles, Mars : a unified record of episodic channel flows and ancient ocean levels. Sci. Rep. 1–7 https://doi.org/10.1038/s41598-020-75080-y.
Duran, S., Coulthard, T.J., Baynes, E.R.C., 2019. Knickpoints in Martian channels indicate past ocean levels. Sci. Rep. 1–7 https://doi.org/10.1038/s41598-019-51574-2.
Fairen, A.G., Ruiz, J., Angula, F., 2002. An origin for the linear magnetic anomalies on Mars through accretion of terrains: implications for dynamo timing. Icarus 160, 220–223.
Farr, T.G., et al., 2002. Terrestrial analogs to Mars. In: Sykes, M.V. (Ed.), The Future of Solar System Exploration, 2003–2013. Community Contributions to the NRC Solar System Exploration Decadal Survey, Astron. Soc. Pac. Conf. Series, vol. 272, pp. 35–76.
Fassett, C.I., Head, J.W., 2005. Fluvial sedimentary deposits on Mars: ancient deltas in a crater lake in the Nili Fossae region. Geophys. Res. Lett. 32.
Fassett, C.I., Head, J.W., 2007. Valley formation on martian volcanoes in the Hesperian: evidence for melting of summit snowpack, caldera lake formation, drainage and erosion on Ceraunius Tholus, Mars. Icarus 189, 118–135. https://doi.org/10.1016/j.icarus.2006.12.021.
Flahaut, J., Massé, M., Le Deit, L., Thollot, P., Bibring, J.P., Poulet, F., Quantin, C., Mangold, N., Michalski, J., Bishop, J.L., 2014. Sulfate-rich deposits on Mars: a review of their occurrences and geochemical implications. In: Eighth International Conference on Mars 1791, p. 1196.
Fort, M., Burbank, D.W., Freytet, P., 1989. Lacustrine sedimentation in a semi-arid alpine setting: An example from Ladakh, northwestern Himalaya. Quat. Res. 31 (3), 332–350.
Galofre, A.G., Jellinek, A.M., Osinski, G.R., 2020. Valley formation on early Mars by subglacial and fluvial erosion. Nat. Geosci. 13 (10), 663–668.
Ganju, A., Nagar, Y.C., Sharma, L.N., Juyal, N., 2018. Luminescence chronology and climatic implication of the late quaternary glaciation in the Nubra valley, Karakoram Himalaya, India. Palaeogeogr. Palaeoclimatol. Palaeoecol. 502, 52–62.
Guha, D., Das, S., Srikarni, C., Chakraborty, S.K., 2005. Alkali basalt of Kachchh: its implication in the tectonic framework of Mesozoic of western India. J. Geol. Soc. India 66, 599–608.
Gulick, V.C., 1998. Magmatic intrusions and a hydrothermal origin of fluvial valleys on Mars. J. Geophys. Res. 103, 19365–19388.
Gulick, V.C., 2001. Origin of the valley networks on Mars: a hydrologic perspective. Geomorphology 37, 241–268.
Gulick, V.C., Baker, V.R., 1989. Fluvial valleys and martian paleoclimates. Nature 341, 514–516. Gulick and Baker 1989.
Gulick, V.C., Baker, V.R., 1990. Origin and evolution of valleys on martian volcanoes. J. Geophys. Res. 95, 14325–14344.
Harrison, K.P., Grimm, R.E., 2005. Groundwater-controlled valley networks and the decline of surface runoff on early Mars. J. Geophys. Res. 110 (E12), E12S16.
Hartmann, W.K., 2005. Martian cratering. Isochron refinement and the chronology of Mars. Icarus 174, 294–320.
Hauber, E., van Gasselt, S., Chapman, M.G., Neukum, G., 2008. Geomorphic evidence for former lobate debris aprons at low latitudes on Mars: indicators of the Martian paleoclimate. J. Geophys. Res. 113, E02007. https://doi.org/10.1029/2007je002897.
Heimsath, A.M., McGlynn, R., 2008. Quantifying periglacial erosion in the Nepal high Himalaya. Geomorphology 97 (1–2), 5–23.
Hobbs, S.W., Paull, D.J., Clarke, J.D., 2014. A comparison of semiarid and subhumid terrestrial gullies with gullies on Mars: implications for Martian gully erosion. Geomorphology 204, 344–365. https://doi.org/10.1016/j.geomorph.2013.08.018.
Horton, R.E., 1932. Drainage basin characteristics. Trans. Amer. Geophys. Union 13, 350–360.
Horton, R.E., 1945. Erosional development of streams and their drainage basins: hydrophysical approach to quantitative morphology. Geol. Soc. Am. Bull. 56 (3), 275–370.
Howard, A.D., Moore, J.M., Irwin III, R.P., 2005a. An intense terminal epoch of widespread fluvial activity on Mars: 1. Valley network incision and associated deposits. J. Geophys. Res. 110, E12S14. https://doi.org/10.1029/2005JE002459.
Howard, A.D., Moore, J.M., Irwin III, R.P., Craddock, R.A., 2005b. A sedimentary platform in Margaritifer Sinus, Meridiani Planum and Arabia? Lunar Planet. Sci. 36, 1545 (abstract).
Hynek, B.M., Phillips, R.J., 2003. New data reveal mature, integrated drainage systems on Mars indicative of past precipitation. Geology 31, 757–760.
Hynek, B.M., Beach, M., Hoke, M.R.T., 2010a. Updated global map of Martian valley networks and implications for climate and hydrologic processes. J. Geophys. Res. 115 (E9), 1–14.
Hynek, B.M., Beach, M., Hoke, M.R., 2010b. Updated global map of Martian valley networks and implications for climate and hydrologic processes. J. Geophys. Res. Planet. 115, E090008.
Irwin III, R.P., Howard, A.D., 2002. Drainage basin evolution in Noachian Terra Cimmeria. Mars. J. Geophys. Res. 107 https://doi.org/10.1029/2001JE001818.
Irwin, R.P., Howard, A.D., Craddock, R.A., Moore, J.M., 2005. An intense terminal epoch of widespread fluvial activity on early Mars. 2. Increased runoff and paleolake development. J. Geophys. Res. 110 https://doi.org/10.1029/2005JE002460. E12S15.
Irwin, R.P., Craddock, R.A., Howard, A.D., Flemming, H.L., 2011. Topographic influences on development of Martian valley networks. J. Geophys. Res. E Planet 116 (2). https://doi.org/10.1029/2010JE003620.
Juyal, N., 2014. Ladakh: The High-Altitude Indian Cold Desert. In Landscapes and Landforms of India. Springer, Dordrecht, pp. 115–124.
Kaila, K.L., Krishna, V.G., 1992. Deep seismic sounding studies in India and major discoveries. Curr. Sci. 62, 117–154.
Kaila, K.L., Krishna, V.G., Mall, D.M., 1981. Crustal structure along Mehmedabad -Bijlimora profile in the Cambay basin, India, from deep seismic soundings. Tectonophysics 76, 99–130.
Karanth, R.V., Sant, D.A., 1995. Lineaments and dyke swarms of lower Narmada valley and southern Saurashtra, Western India. In: Memoir Geol. Soc. India. No. 33, pp. 425–434.
Karmalkar, N.R., Rege, S., Griffin, W.L., O'Reilly, S.Y., 2005. Alkaline magmatism from Kutch, NW India: implications for plume- lithosphere interaction. Lithos 81, 101–119.
Kreslavsky, M.A., Head, J.W., 2002. Fate of outflow channel effluents in the northern lowlands of Mars: the Vastitas Borealis Formation as a sublimation residue from frozen ponded bodies of water. J. Geophys. Res. 107, 5121. https://doi.org/10.1029/2001JE001831.
Krishnamacharlu, T., 1972. Dyke around Dediapada, Broach dist. Gujarat. Bull. Volcanol. 35, 947–956.
Krishnamurthy, P., Pande, K., Gopalan, K., Macdougall, J.D., 1988. Upper mantle xenoliths in alkali basalts related to Deccan Trap volcanism. In: Subbarao, K.V. (Ed.), Deccan Flood Basalts, 10. Geol Soc Ind Mem, pp. 53–67.
Krishnamurthy, P., Pande, K., Gopalan, K., Macdougall, J.D., 1999. Mineralogical and chemical studies on alkaline basaltic rocks of Kutch, Gujarat, India. In: Subbarao, K.V. (Ed.), Deccan Volcanic Province, 43(2). Geol Soc Ind Mem, pp. 757–783.
Kshirsagar, P.V., Sheth, H.C., Shaikh, B., 2010. Mafic Alkalic Magmatism in Central Kachchh, India: A Monogenetic Volcanic Field in the Northwestern Deccan Traps, pp. 595–612. https://doi.org/10.1007/s00445-010-0429-9.
Lacassin, R., Valli, F., Arnaud, N., Leloup, P.H., Paquette, J.L., Haibing, L., Tapponnier, P., Chevalier, M.L., Guillot, S., Maheo, G., Xu, Z.Q., 2004. Largescale geometry, offset and kinematic evolution of the Karakorum fault, Tibet. Earth Planet. Sci. Lett. 219, 255–269.
Lee, P., 2000. Cold-based glaciations on Mars: Landscapes of glacial selective linear erosion on Devon Island, Nunavut, Arctic Canada, as a possible analog. In: 2nd Internatl. Conf. on Mars Polar Science and.
Lee, W.H.K., Rayleigh, C.B., 1969. Fault plane solution of the Koyna (India) earthquake. Nature 223, 172–173.
Lucchitta, B.K., 1982. Ice sculpture in the Martian outflow channels. J. Geophys. Res. 87 (B12), 9951–9973.
Malin, M.C., Edgett, K.S., 2003. Evidence for persistent flow and aqueous sed- imentation on early Mars. Science 302, 1931–1934.
Malin, M.C., Carr, M.H., Danielson, G.E., Davies, M.E., Hartmann, W.K., Ingersoll, A.P., Warren, J.L., 1998. Early views of the Martian surface from the Mars orbiter camera of Mars global surveyor. Science 279 (5357), 1681–1685. https://doi.org/10.1126/science.279.5357.1681.
Malin, M.C., Bell, J.F., Cantor, B.A., Caplinger, M.A., Calvin, W.M., Clancy, R.T., Wolff, M.J., 2007. Context camera investigation onboard the Mars reconnaissance

orbiter. J. Geophys. Res. E Planet 112 (5), 1–25. https://doi.org/10.1029/2006JE002808.
Mangold, N., Quantin, C., Ansan, V., Delacourt, C., Allemand, P., 2004. Evidence for precipitation on Mars from dendritic valleys in the Valles Marineris area. Science 305, 78–81.
Mangold, N., Ansan, V., Masson, P., Quantin, C., Neukum, G., 2008. Geomorphic study of fluvial landforms on the northern Valles Marineris plateau, Mars. J. Geophys. Res. E Planet 113 (8), 1–23. https://doi.org/10.1029/2007JE002985.
Markevich, V.P., 1976. Prognostic Assessment of Oil and Gas Prospects of India and Main Guidelines for Future Exploration (ONGC Report).
Masson, Ph., 1979. Structure pattern analysis of the Noctis Labyrinthus-Valles Marineris region of Mars. Icarus 30, 49–62.
Masursky, H., 1973. An Apollo view of lunar geology. In: Chamberlain, J.W., Watkins, C. (Eds.), Lunar Science, vol. 4. Lunar Science Institute, Houston, Tex, pp. 511–512.
Masursky, H., Boyce, J.M., Dial Jr., A.L., Schaber, G.G., Strobell, M.E., 1977. Classification and time of formation of Martian channels based on Viking data. J. Geophys. Res. 82, 4016–4038.
Masursky, H., Dial, A.L., Strobel, M.H., 1978. Geologic Map of the PhoenicisLacusQuadrangle of Mars, Misc. Inv. Map 1-896. U.S. Geol. Surv., Reston, Va.
Mathur, L.P., Evans, P., 1964. Oil in India. In: 22nd Int. Geol. Congr. New Delhi, Spec. Pap., pp. 1–87.
Mathur, L.P., Kohli, G., 1963. Exploration and development for oil in India. In: 6th World Pet. Congr. Frankfurt, Proc. Sec., 1, pp. 633–658.
McCauley, J.F., 1979. Geologic Map of the Coprates Quadrangle of Mars, Misc. Inv. Map 1-897, U.S. Geol. Surv., Reston, Va.
McCauley, J.F., Carr, M.H., Cutts, J.A., Hartmann, W.K., Masursky, H., Milton, D.J., Wilhelms, D.E., 1972. Preliminary mariner 9 report on the geology of Mars. Icarus 17 (2), 289–327.
McEwen, A.S., Eliason, E.M., Bergstrom, J.W., Bridges, N.T., Hansen, C.J., Delamere, W. A., Grant, J.A., Gulick, V.C., Herkenhoff, K.E., Keszthelyi, L., Kirk, R.L., 2007. Mars reconnaissance orbiter's high resolution imaging science experiment (HiRISE). J. Geophys. Res. Planet 112 (E5). https://doi.org/10.1029/2005JE002605.
Merh, S.S., Chamyal, L.S., 1997. The Quaternary Geology of Gujarat Alluvial Plains. Monog. Ind. Nat. Sci. Acad, New Delhi, 98p.
Miller, C., Klötzli, U., Frank, W., Thöni, M., Grasemann, B., 2000. Proterozoic crustal evolution in the NW Himalaya (India) as recorded by circa 1.80 Ga mafic and 1.84 Ga granitic magmatism. Precambrian Res. 103 (3–4), 191–206.
Milton, D.J., 1974. Geologic map of the Lunae Palus quadrangle of Mars. In: U.S. Geol. Surv. Misc. Invest. Ser. Map I-894, 1:5,000,000-scale.
Molnar, P., Anderson, R.S., Anderson, S.P., 2007. Tectonics, fracturing of rock, and erosion. J. Geophys. Res. Earth Surf. 112 (F3).
Moore, J.M., Howard, A.D., Dietrich, W.E., Schenk, P.M., 2003. Martian lay- ered fluvial deposits: implications for Noachian climate scenarios. Geo- Phys. Res. Lett. 30 https://doi.org/10.1029/2003GL019002. 2292.
Mosangini, C., Komatsu, G., 1998. Geomorphology of Kasei Valles and Scale of Flooding Episodes. In Proceedings of the 29th Annual Lunar and Planetary Science Conference, Abstract no. 1779.
Mouginis-Mark, P.J., Wilson, L., Head, J.W., 1982. Explosive volcanism on Hecates Tholus, Mars: investigation of eruption conditions. J. Geophys. Res. 87, 9890–9904.
Mouginis-Mark, P.J., Wilson, L., Zimbelman, J.R., 1988. Polygenic eruptions on Alba Patera, Mars. Bull. Vocanol. 50, 361–379.
Mueller, J.E., 1968. An introduction to the hydraulic and topographic sinuosity indexes. Ann. Assoc. Am. Geogr. 58 (2), 371. https://doi.org/10.1111/j.1467-8306.1968.tb00650.x.
Mukherjee, A.B., Biswas, S., 1988. Mantle-derived spinel lherzolite xenoliths from the Deccan volcanic province (India): implications for the thermal structure of the lithosphere underlying the Deccan Traps. J. Volcanol. Geotherm. Res. 35, 269–276.
Murchie, S., Arvidson, R., Bedini, P., Beisser, K., Bibring, J.P., Bishop, J., Wolff, M., 2007. Compact reconnaissance imaging spectrometer for Mars (CRISM) on Mars reconnaissance orbiter (MRO). J. Geophys. Res. 112, E05S03. https://doi.org/10.1029/2006JE002682.
Murphy, M.A., An, Yin, Kapp, P., Harrison, T.M., Ding, Lin, 2000. Southward propagation of the Karakoram fault system, Southwest Tibet: timing and magnitude of slip. Geology 28, 451–454.
Neukum, G., Jaumann, R., the HRSC Co-Investigator and Experiment Team, 2004. HRSC: The High Resolution Stereo Camera of Mars Express, 1240. Eur. Space Agency Spec. Publ, pp. 17–35.
Owen, L.A., Finkel, R.C., Barnard, P.L., Haizhou, M., Asahi, K., Caffee, M.W., Derbyshire, E., 2005. Climatic and topographic controls on the style and timing of Late Quaternary glaciation throughout Tibet and the Himalaya defined by 10Be cosmogenic radionuclide surface exposure dating. Quat. Sci. Rev. 24, 1391–1411.
Owen, L.A., Caffee, M.W., Bovard, K.R., Finkel, R.C., Sharma, M.C., 2006. Terrestrial cosmogenic nuclide surface exposure dating of the oldest glacial successions in the Himalayan orogen. Ladakh Range, northern India. Geol. Soc. Am. Bull. 118, 383–392.
Pande, K., Venkatesan, T.R., Gopalan, K., Krishnamurthy, P., Macdougall, J.D., 1988. 40Ar-39Ar ages of alkali basalts from Kutch, Deccan volcanic province, India. In: Subbarao, K.V. (Ed.), Deccan Flood Basalts, 10. Geol Soc Ind Mem, pp. 145–150.
Pant, R.K., Phandtare, N.R., Chamyal, L.S., Juyal, N., 2005. Quaternary deposits in Ladakh and Karakoram Himalaya: a treasure trove of the palaeoclimate records. Curr. Sci. 88, 1789–1798.
Paramanick, S., Rajesh, V.J., Praveen, M.N., Sajinkumar, K.S., Bhattacharya, S., 2021. Spectral and chemical characterization of Copiapite-Rozenite from Padinjarathara in Wayanad, southern India: implications for secondary sulphate occurrences on Mars. Chem. Geol. https://doi.org/10.1016/j.chemgeo.2020.120043.
Parker, T.J., Gorsline, D.S., Saunders, R.S., Pieri, D.C., Schneeberger, D.M., 1993. Coastal geomorphology of the Martian northern plains. J. Geophys. Res. 98, 11,061–011,078.
Paul, D.K., Ray, A., Das, B., Patil, S.K., Biswas, S.K., 2008. Petrology, geochemistry and palaeomagnetism of the earliest magmatic rocks of Deccan volcanic province, Kutch, Northwest India. Lithos 102, 237–259.
Pieri, D.C., 1980. Geomorphology of martian valleys. In: NASA Tech. Memo. 81979, pp. 1–160.
Plescia, J.B., 1999. Geology of the Uranius group volcanic constructs: Uranius Patera, Ceraunius Tholus, and Uranius Tholus. Icarus 143, 376–396.
Plescia, J.B., Saunders, R.S., 1982. Tectonic history of the Tharsis Region, Mars. J. Geophys. Res. 87 (B12), 9775.
Powar, K.B., 1981. Lineament fabric and dyke pattern in the western part of the Deccan volcanic province. In: Geol. Soc. Mem., No. 3, pp. 45–57.
Prasad, V., 2019. Late cretaceous climate of the Indian subcontinent. Open J. Geol. 9 (10), 692.
Pratt, B., Burbank, D.W., Heimsath, A., Ojha, T., 2002. Impulsive alluviation during early Holocene strengthened monsoons, Central Nepal Himalaya. Geology 30 (10), 911–914.
Pratt-Sitaula, B., Burbank, D.W., Heimsath, A., Ojha, T., 2004. Landscape disequilibrium on 1000–10,000 year scales Marsyandi River, Nepal, central Himalaya. Geomorphology 58 (1–4), 223–241.
Raju, A.T.R., 1968. Geological evolution of Assam and Cambay Tertiary basins of India. Am. Assoc. Pet. Geol. Bull. 52, 2422–2437.
Raju, A.T., 1979. Basin analysis and petroleum exploration with some examples in Indian sedimentary basins. J. Geol. Soc. India 20, 47–60.
Rao, K.L.N., 1969. Litho-stratigraphy of Paleogene succession for southern Cambay basin. Bull. ONGC 6 (1), 24–37.
Rao, K.L.N., 1987. Geological Study of the Northern Cambay Basin with Special Reference to its Tectonic Framework and Depositional Environments. Unpubl. Ph. D. Thesis. M. S. University of Baroda.
Raterman, N.S., Cowgill, E., Lin, D., 2007. Variable structural style along the Karakoram fault explained using triple-junction analysis of intersecting faults. Geosphere 3 (2), 71–85.
Ravishanker, S., 1987. Neotectonic activity along the Tapti Satpura lineament in Central India. Ind. Miner. 41 (1), 19–30.
Ravishanker, S., Dubey, R., 1984. Landforms, neotectonism and geothermal activity in part of Tapi basin, District Jalgaon, Maharashtra A study. Rec. Geol. Surv. India 113 (6), 70–85.
Ray, A., Patil, S.K., Paul, D.K., Biswas, S.K., Das, B., Pant, N.C., 2006. Petrology, geochemistry and magnetic properties of Sadara sill: evidence of rift related magmatism from Kutch basin, Northwest India. J. Asian Earth Sci. 27, 907–921.
Ray, R., Sheth, H.C., Mallik, J., 2007. Structure and emplacement of the Nandurbar – Dhule mafic dyke swarm, Deccan Traps, and the tectonomagmatic evolution of flood basalts. Bull. Volcanol. 69, 537–551. https://doi.org/10.1007/s00445-006-0089-y.
Ray, D., Shukla, A.D., Bhattacharya, S., Gupta, S., Jha, P., Chandra, U., 2021. Hematite concretions from the Late Jurassic Jhuran sandstone, Kutch, western India: implications for sedimentary diagenesis and origin of "blueberries" on Mars. Planet. Space Sci. 197, 105–163.
Reimers, C.E., Komar, P.D., 1979. Evidence for explosive volcanic density currents on certain martian volcanoes. Icarus 39, 88–110.
Robinson, M.S., Tanaka, K.L., 1990. Magnitude of a catastrophic flood event at Kasei Valles, Mars. Geology 18, 902–905.
Rotto, S., Tanaka, K.L., 1995. Geologic/Geomorphic map of the Chryse Planitia region of Mars. U.S. Geol. Surv. Misc. Invest. Ser. Map I-2441, Scale 1:5,000,000.
Schulz, H., von Rad, U., Erlenkeuser, H., 1998. Correlation between Arabian Sea and Greenland climate oscillations of the past 110,000 years. Nature 393 (6680), 54–57.
Schumm, S.A., 1974. Structural origin of large Martian channels. Icarus 22 (3), 371–384.
Schumm, S.A., Mosley, M.P., Weaver, W., 1987. Experimental fluvial geomorphology. John Wiley and Sons, New York, p. 413.
Scott, D.H., Carr, M.H., 1978. Geologic map of Mars. In: U.S. Geological Survey Misc. Inv. Map I 1083.
Scott, D.H., Tanaka, K.L., 1986. Geologic map of the western equatorial region of Mars. In: U.S. Geol. Surv. Misc. Invest. Ser., pp. Map I-1802-A.
Searle, M.P., Phillips, R.J., 2007. Relationships between right-lateral shear along the Karakoam fault and metamorphism, magmatism, exhumation and uplift: evidence from the K2–Gasherbrum–Pangong ranges, North Pakistan and Ladakh. J. Geol. Soc. Lond. 164, 439–450.
Sen, G., Bizimis, M., Das, M., Paul, D.K., Ray, A., Biswas, S., 2009. Deccan plume, lithosphere rifting, and volcanism in Kutch, India. Earth Planet. Sci. Lett. 27, 101–111.
Sharma, S., Bartarya, S.K., Marh, B.S., 2016. Post-glacial landform evolution in the middle Satluj River valley, India: implications towards understanding the climate tectonic interactions. J. Earth Syst. Sci. 125 (3), 539–558.
Sharp, R.P., Malin, M.C., 1975. Channels on Mars. Geol. Soc. Am. Bull. 86, 593–609.
Sheth, H.C., Mathew, G., Pande, K., Mallick, S., 2004. Cones and Craters on Mount Pavagadh, Deccan Traps : Rootless Cones ?, 4, pp. 831–838.
Shreve, R.L., 1967. Infinite topologically random channel networks. J. Geol. 75 (2), 178–186.
Shukla, A.D., Bhandari, N., Kusumgar, S., Shukla, P.N., Ghevariya, Z.G., Gopalan, K., Balaram, V., 2001. Geochemistry and magneto- stratigraphy of Deccan flows at Anjar, Kutch. Proc. Ind. Acad. Sci. Earth Planet Sci. 110, 111–132.
Shukla, A.D., Ray, D., Pande, K., Shukla, P.N., 2014. Formation of paleosol (fossil soil) in Deccan Continental Flood Basalt: Alteration style and implications towards aqueous environment of early Mars. In: 8th Internal. Conf. on Mars, Lunar Planet. Sci. Contrib. Rept, p. 1194.

Simonetti, A., Goldstein, S.L., Schmidberger, S.S., Viladkar, S.G., 1998. Geochemical and Nd, Pb, and Sr isotope data from Deccan alkaline complexes—inferences for mantle sources and plume- lithosphere interaction. J. Petrol. 39, 1847–1864.
Singh, D.D., Rastogi, B.K., Gupta, H.K., 1975. Surface wave radiation pattern and source parameters of the Koyna earthquake of Dec. 10, 1967. Bull. Seism. Soc. Am. 65, 711–731.
Singh, M., Rajesh, V.J., Sajinkumar, K.S., Sajeev, K., Kumar, S.N., 2016. Spectral and chemical characterization of jarosite in a palaeo-lacustrine depositional environment in Warkalli Formation in Kerala, South India and its implications. Spectrochim. Acta A Mol. Biomol. Spectrosc. 168, 86–97.
Sinha, R.K., Vijayan, S., Shukla, A.D., Das, P., Bhattacharya, F., 2017. Gullies and debris-flows in Ladakh Himalaya, India : a potential Martian analogue. Geol. Soc. Lond., Spec. Publ. 467 (1), 315–342. https://doi.org/10.1144/SP467.9.
Sirocko, F., Sarnthein, M., Erlenkeuser, H., Lange, H., Arnold, M., Duplessy, J.C., 1993. Century-scale events in monsoonal climate over the past 24,000 years. Nature 364 (6435), 322–324.
Stepinski, T.F., Collier, M.L., 2004. Extraction of Martian valley networks from digital topography. J. Geophys. Res. E Planet 109 (11), 1–9. https://doi.org/10.1029/2004JE002269.
Stepinski, T.F., O'Hara, W.J., 2003. Vertical analysis of martian drainage basins. Lunar Planet. Sci. 35, 1659.
Stepinski, T.F., Stepinski, A.P., 2005. Morphology of drainage basins as an indicator of climate on early Mars. J. Geophys. Res. 110, E12S12.
Strahler, A.N., 1957. Quantitative analysis of watershed geomorphology. EOS Trans. Am. Geophys. Union 38 (6), 913–920.
Tanaka, K.L., Chapman, M.G., 1992. Kasei Valles, Mars-interpretation of canyon materials and flood sources. In: Abstract from the Proceedings of Lunar and Planetary Science Conference, vol. 22, pp. 73–83.
Tanaka, K.L., Davis, P.A., 1988. Tectonic history of the Syria Planum province of Mars. J. Geophys. Res. Solid Earth 93 (B12), 14893–14917.
Tanaka, K.L., Skinner Jr., J.A., Dohm, J.M., Irwin III, R.P., Kolb, E.J., Fortezzo, C.M., Platz, T., Michael, G.G., Hare, T.M., 2014a. Geologic Map of Mars, U.S.G.S. Scientific Investigations Map 3292. U.S. Geological Survey, Flagstaff, AZ. Available online at. http://pubs.usgs.gov/sim/3292/pdf/sim3292_map.pdf.
Tanaka, K.L., Skinner, J.A.J., Dohm, J.M., Irwin, R.P., Kolb, E.J., Fortezzo, C.M., Platz, T., Michael, G.G., Hare, T.M., 2014b. Geologic map of Mars. In: U.S. Geological Survey Scientific Investigations Map 3239, Scale 1:20,000,000, p. 43.
Tandon, A.N., Chaudhry, H.M., 1968. Koyna Earthquake of December 1967, India Meteorological Dept. Scientific Report, No. 59.
Taylor, P.J., Mitchell, W.A., 2000. The Quaternary glacial history of the Zanskar Range, north-west Indian Himalaya. Quat. Int. 65 (66), 81–99.
Thiede, R.C., Bookhagen, B., Arrowsmith, J.R., Sobel, E.R., Strecker, M.R., 2004. Climatic control on rapid exhumation along the Southern Himalayan Front. Earth Planet. Sci. Lett. 222 (3–4), 791–806.
Thakur, V.C., Rawat, B.S., 1992. Geological map of the Western Himalaya. Survey of India.
Thiede, R.C., Arrowsmith, J.R., Bookhagen, B., McWilliams, M., Sobel, E.R., Strecker, M. R., 2006. Dome formation and extension in the Tethyan Himalaya, Leo Pargil, Northwest India. Geol. Soc. Am. Bull. 118 (5–6), 635–650.
Thorpe, T., 1976. The Viking orbiter cameras' potential for photometric measurement. Icarus 27 (2), 229–239. https://doi.org/10.1016/0019-1035(76)90006-3.
Tinkler, K.J., Wohl, E., 1998. Rivers over Rock: Fluvial Processes in Bedrock Channels (No. 107). American Geophysical Union.
Tyagi, A.K., Chaudhary, S., Rana, N., Sati, S.P., Juyal, N., 2009. Identifying areas of differential uplift using steepness index in the Alaknanda basin, Garhwal Himalaya, Uttarakhand. Curr. Sci. 1473–1477.
van Gasselt, S., 2007. Cold-Climate Landforms on Mars (PhD. Dissertation). Shaker Verlag, Aachen, Germany, 264 pp.
Vannay, J.C., Grasemann, B., 1998. Inverted metamorphism in the High Himalaya of Himachal Pradesh (NW India): phase equilibria versus thermobarometry. Schweiz. Mineral. Petrogr. Mitt. 78, 107–132.
Vannay, J.C., Grasemann, B., Rahn, M., Frank, W., Carter, A., Baudraz, V., Cosca, M., 2004. Miocene to Holocene exhumation of metamorphic crustal wedges in the NW Himalaya: evidence for tectonic extrusion coupled to fluvial erosion. Tectonics 23 (1).
Vijith, H., Satheesh, R., 2006. GIS based morphometric analysis of two major upland sub-watersheds of Meenachil river in Kerala. J. Indian Soc. Remote Sens. 34 (2), 181–185.
Vittala, S.S., Govindaiah, S., Gowda, H.H., 2004. Evaluation of groundwater potential zones in the sub-watersheds of north pennar river basin around Pavagada, Karnataka, India using remote sensing and GIS techniques. J. Indian Soc. Remote Sens. 33, 351–362.
Weinberg, R.F., Dunlap, W.J., Whitehouse, M.J., 2000. New field, structural and geochronological data from the Shyok and Nubra valleys, northern Ladakh: linking Kohistan to Tibet. In: Khan, M.A., Treloar, P.J., Searle, M.P., Jan, M.Q. (Eds.), Tectonics of the Nanga Parbat Syntaxis and Western Himalaya, 170. Geol. Soc., London. Sp. Publ., pp. 253–275
Werner, S.C., 2006. Major Aspects of the Chronostratigraphy and Geologic Evolutionary History of Mars. PhD. Dissertation. Freie University, Cuvillier Verlag, Göttingen, Germany, 153 pp.
Whittaker, A.C., Cowie, P.A., Attal, M., Tucker, G.E., Roberts, G.P., 2007. Bedrock channel adjustment to tectonic forcing: implications for predicting river incision rates. Geology 35 (2), 103–106.
Williams, R.M., Phillips, R.J., 1999. Flow rates and duration within Kasei Valles, Mars. In: Proceedings of the 30th Annual Lunar and Planetary Science Conference, Abstract No. 1417.
Williams, R.M., Phillips, R.J., Malin, M.C., 2000. Flow rates and duration within Kasei Valles, Mars: implications for the formation of a Martian Ocean. Geophys. Res. Lett. 27 (7), 1073–1076.
Williams, R.M.E., Malin, M.C., Edgett, K.S., 2002. Possible late-stage mudflows in Kasei Valles. In: Proceedings of the 33rd Annual Lunar and Planetary Science Conference, Abstract No.1807.
Witbeck, N.E., Tanaka, K.L., Scott, D.H., 1991. Geological map of the Valles Marineris region, Mars (east half and west half), scale 1:2,000,000, U.S. Geol. Surv. Misc. Invest. Ser., I-2010.
Wulf, H., Bookhagen, B., Scherler, D., 2012. Climatic and geologic controls on suspended sediment flux in the Sutlej River Valley, western Himalaya. Hydrol. Earth Syst. Sci. 16 (7), 2193–2217.
Zealey, W.J., 2007. Glacial, periglacial and glacio-volcanic structures on the Echus plateau, upper Kasei Vallis. In: 7th Internal. Conf. on Mars, Lunar Planet. Sci. Contrib. Rept. 1353, #3002.
Zealey, W.J., 2008. Glacial, Periglacial and Glacio-Volcanic Structures on the Echus Plateau, Upper Kasei Valles, 57, pp. 699–710. https://doi.org/10.1016/j.pss.2008.08.007.

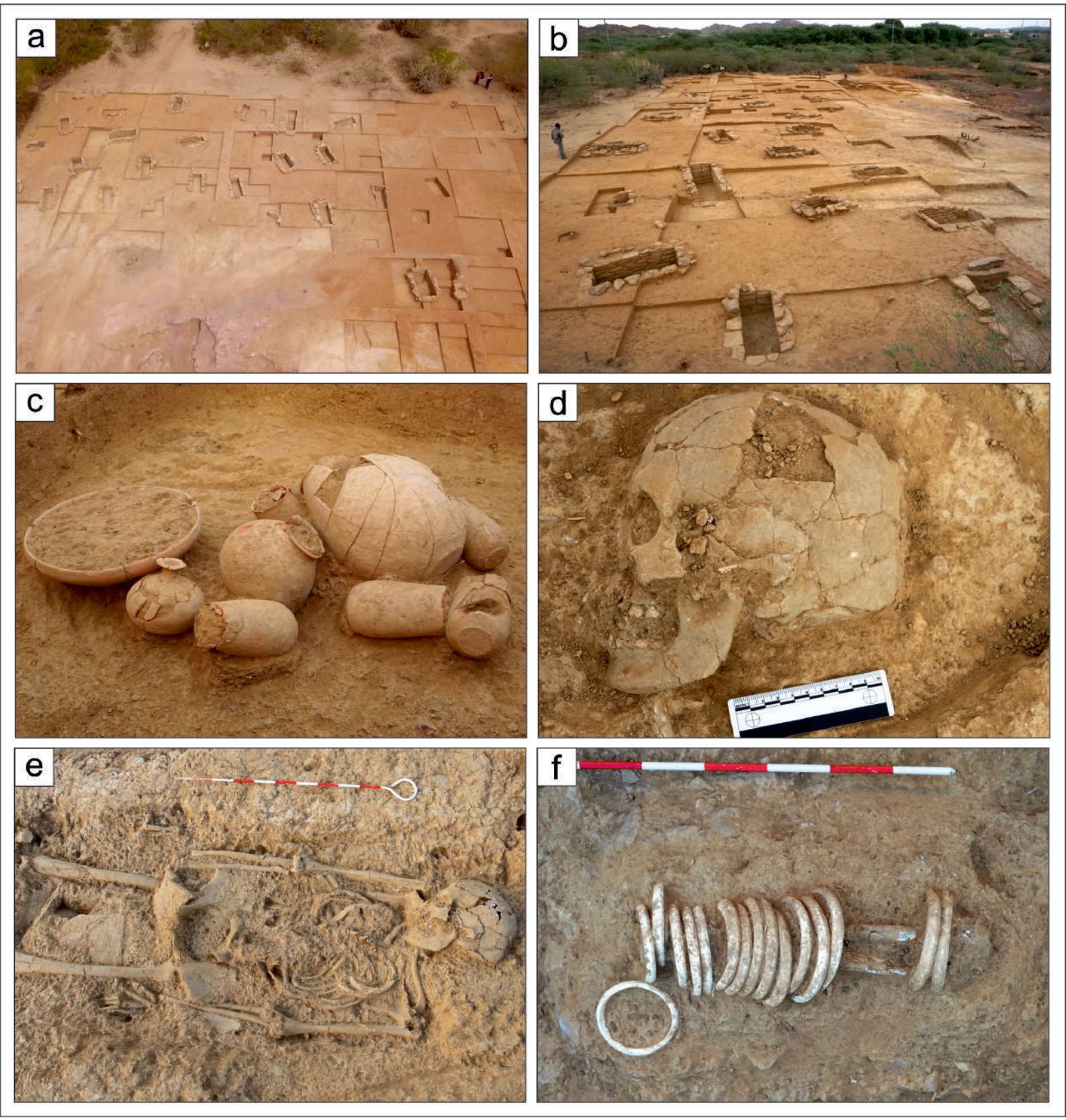
a
b
c
d
e
f

realme Shot on realme 10 Pro 5G 108MP
2023 10 30 08:39